Proceedings

International Conference on Nuclear Science and Technology

Nuclear Society Of Iran | Atomic Energy Organization of Iran | Nuclear Sciences and Technologies Research Institute

Papers on:

Radiation Measurements

*In this booklet, you will find the selected papers presented at the **First International Conference on Nuclear Science and Technology**, held from May 6-8, 2024, in Isfahan, Iran.*
We hope you find it informative and enjoyable!

ICNST 2024

Contact and Accessibility

icnst2024.com
registration@icnst2024.com


بسم الله الرحمن الرحیم

The Conference President's Message
ICNST 2024

Attendees, guests, and colleagues

I would like to warmly welcome you to the first International Conference on Nuclear Science and Technology (ICNST 2024). It has been a real honor and privilege to serve as the president of this conference. The conference this year has brought together an incredible diversity of authors and speakers from universities, government, and industry to share ideas and new perspectives on a wide range of radiation applications, nuclear reactors, particle accelerators, radiation measurements, fusion and plasma, stable and radioactive isotopes, radiation safety and security, nuclear agriculture, fuel cycle, lasers, education and training and nuclear governance.

Climate change, a new topic which has been added to this year's agenda as an important worldwide issue. a matter that has been brought up as a critical concern at the majority of IAEA conferences and nuclear scientific assemblies in recent years.

Panel discussions and exhibitions are being introduced as side activities in an attempt to keep this scientific meeting from becoming one-dimensional and increase its effectiveness.

More than 520 complete papers have been approved for this conference; when combined with the additional panels, get-togethers, and side activities, it is anticipated that over 1000 people will attend in person in the historical and touristic city of Isfahan. We look forward to welcoming participants to share their practical ideas and to enjoy an academical and cultural three days in Isfahan.

I'll close by wishing you everyone an incredible, instructive, and transformative experience during ICNST2024 and I hope that this conference can pave the route for academic materials to be used in industry and everyday life.

Prof. Javad Karimi-Sabet
President of ICNST2024
Javad Karimi-Sabet

welcome statment of scientific secretary ICNST 2024

"In the name of God, the Merciful,

Prior to giving the stage to address this distinguished forum, let me take this opportunity to express our deep gratitude, on behalf of all attendees, for His Excellency Mr. Islami's scientific, educational, and motivational remarks, as well as for his excellent organization of this conference.

I would also like to express our appreciation to His Excellency Dr. Mortazavi, Governor-General of Isfahan Province, for his constructive and useful support in enabling this meeting to take place.

This is a great pleasure and honor to extend a warm greeting to each and every one of you for the International Conference on Nuclear Science and Technology, scheduled from May 6th to May 8th, 2024, in the historic city of Isfahan, Iran.

With the aim of advancing our knowledge of nuclear science and technology, this conference is a major global convergence of experts, researchers, and practitioners. It is a platform for the sharing of creative concepts, the presentation of state-of-the-art research, and the formation of cooperative alliances.

As the scientific secretary of this prestigious event, I am particularly excited about the diverse array of participants expected to grace us with their presence. From the esteemed scientists and engineers of Russian universities and research centers to representatives from Islamic countries, friendly nations, and beyond, this conference promises to be a melting pot of perspectives, experiences, and expertise.

The extensive coverage of this conference is another aspect of its uniqueness. We have nearly 900 participants representing 22 countries around the world. Of the 900 participants, 620 are authors covering 13 major topics. There are 421 papers for oral and poster presentations, with additional documents for publication in ISC journals. There will be 3 plenary sessions, 16 panel discussions, 20 parallel oral presentation sessions, and 3 poster sessions.

Prof. Hosein Afarideh
Scientific Secretariat of ICNST2024

Organizers

Nuclear Society Of Iran (NSI)

Atomic Energy Organization of Iran (AEOI)

Nuclear Science and Technology Research Institute (NSTRI)

Scientific Partnership

International Atomic Energy Agency (IAEA)

Isfahan University

Sharif University

Kurchatov Institute

Amirkabir University of Technology (Tehran Polytechnique)

Shahid Beheshti University

Isfahan University of Technology

Shiraz University

Islamic Azad University

K. N. Toosi University of Technology

Ferdowsi University of Mashhad

Kerman Graduate University of Technology

Sahand University of Technology

University of Tabriz

Islamic World Scieence Citation Center

Journal of Nuclear Science and Technology (JonSat)

Radiation Physics and Engineering journal

Nuclear Watch

Cooperative Organization

Isfahan Governorate

Isfahan Municipality

Abbasi Hotel

Iran Atomic Energy Production & Development Co.

Iran's Nuclear Raw Materials & Fuel Production Co.

Radiation Application Development Co.

Ofogh Consulting Engineers Co.

Nuclear Power Plant Safety Development & Promotion Co.

Nuclear Power Plant Engineering & Construction Co.

Engineering & Design of Industrial Simulator Co.

Energy Industry Development Engineering Co

Atomic Power Plant Pepair & support

Nuclear Reactors Fuel Co.

Iran Radioactive Waste Management Co.

Mesbah Energy Co.

Iran Gharb Industrial, Mining and Energy Co.

Pars Isotope Co.

Center for Laser Science & Technology of Iran

Centrifuge Production of Iran Co.

Plasma Technology Development Co.

Rasa Technology and Innovation Center

Behyaar Sanaat Sepahan Co.

Nuclear Data Base of Iran (NDB)

Parto think tank (strategic studies of nuclear industry development)

International Conference Alerts

Local Scientific Board

RAW	NAME	ROLE	AFFILIATION
1	**Prof. Hossein Afarideh**	**Chairman of Local Scientific Board**	**Amirkabir University of Technology (Tehran Polytechnique)(AUT)**
2	**Prof. Mohammad Ghanadi Maragheh**	**Member of The Local Scientific Board**	**Nuclear Science and Technology Research Institute of Iran (NSTRI)**
3	**Prof. Mohammad Lamei Rashti**	**Member of The Local Scientific Board**	**Nuclear Science and Technology Research Institute of Iran (NSTRI)**
4	**Prof. Mohammad Bagher Ghofrani**	**Member of The Local Scientific Board**	**Sharif University of Technology (SUT)**
5	**Prof. Hosein Faghihian**	**Member of The Local Scientific Board**	**University of Isfahan (UI)**
6	**Prof. Javad Rahighi**	**Member of The Local Scientific Board**	**Institute for Research in Fundamental Sciences (IPM)**
7	**Prof. Seyed Amirhossein Feghhi**	**Member of The Local Scientific Board**	**Shahid Beheshti University (SBU)**

Scientific Committee

RAW	NAME	ROLE	AFFILIATION
1	**Prof. Ali Akbar Salehi**	**Member of The Scientific Committe**	**Sharif University of Technology (SUT)**
2	**Prof. Seyyed Javad Ahmadi**	**Member of The Scientific Committe**	**Nuclear Science and Technology Research Institute of Iran (NSTRI)**
3	**Prof. Farhoud Ziaee**	**Member of The Scientific Committe**	**Nuclear Science and Technology Research Institute of Iran (NSTRI)**
4	**Prof. Saeed Hamidi**	**Member of The Scientific Committe**	**University of Arak**
5	**Prof. Seyedzafarollah Kalantari**	**Member of The Scientific Committe**	**Isfahan University of Technology (IUT)**
6	**Prof. Naser Bagheri Moghaddam**	**Member of The Scientific Committe**	**National Research Institute for Science Policy (NRISP)**
7	**Prof. Naser Vosoghi**	**Member of The Scientific Committe**	**Sharif University of Technology (SUT)**
8	**Prof. Seied Rabi Mahdavi**	**Member of The Scientific Committe**	**Iran University of Medical Sciences**
9	**Prof. Meisam Torab Mostaedi**	**Member of The Scientific Committe**	**Nuclear Science and Technology Research Institute of Iran (NSTRI)**
10	**Prof. Fereydoun Abbasi Davani**	**Member of The Scientific Committe**	**Shahid Beheshti University (SBU)**
11	**Prof. Seyed Farhad Masoudi**	**Member of The Scientific Committe**	**K.N.Toosi University of Technology**
12	**Prof. Rasool Ruknizadeh**	**Member of The Scientific Committe**	**University of Isfahan (UI)**
13	**Prof. Gholamreza Raeesali**	**Member of The Scientific Committe**	**Nuclear Science and Technology Research Institute of Iran (NSTRI)**
14	**Prof. Asghar Sedighzadeh**	**Member of The Scientific Committe**	
15	**Prof. Hossein Kazeminejad**	**Member of The Scientific Committe**	**Nuclear Science and Technology Research Institute of Iran (NSTRI)**
16	**Prof. Seyyed Jaber Safdari**	**Member of The Scientific Committe**	**Nuclear Science and Technology Research Institute of Iran (NSTRI)**

17	**Prof. Omid Reza Kakuee**	**Member of The Scientific Committe**	**Nuclear Science and Technology Research Institute of Iran (NSTRI)**
18	**Prof. Alireza Keshtkar**	**Member of The Scientific Committe**	**Nuclear Science and Technology Research Institute of Iran (NSTRI)**
19	**Prof. Fereshte Haj esmail Beigi**	**Member of The Scientific Committe**	**Nuclear Science and Technology Research Institute of Iran (NSTRI)**
20	**Prof. Masoud Mahjour-shafiei**	**Member of The Scientific Committe**	**Nuclear Science and Technology Research Institute of Iran (NSTRI)**
21	**Prof. Mahmoud Payami Shabestar**	**Member of The Scientific Committe**	**Nuclear Science and Technology Research Institute of Iran (NSTRI)**
22	**Prof. Ali Bahrami Samani**	**Member of The Scientific Committe**	**Nuclear Science and Technology Research Institute of Iran (NSTRI)**
23	**Dr. Farhanaz Motamedi**	**Member of The Scientific Committe**	**Nuclear Science and Technology Research Institute of Iran (NSTRI)**
24	**Dr. Faezeh Rahmani**	**Member of The Scientific Committe**	**K.N.Toosi University of Technology**
25	**Dr. Ebrahim Moghiseh**	**Member of The Scientific Committe**	**Nuclear Science and Technology Research Institute of Iran (NSTRI)**
26	**Dr. Iraj Jabari**	**Member of The Scientific Committe**	**University of Isfahan (UI)**
27	**Dr. Nima Ghal-Eh**	**Member of The Scientific Committe**	**Ferdowsi University of Mashhad**
28	**Dr. Mitra Athari Alaf**	**Member of The Scientific Committe**	**Islamic Azad University Science and Research Branch**
29	**Dr. Gholamreza Etaati**	**Member of The Scientific Committe**	
30	**Dr. Amir Movafeghi**	**Member of The Scientific Committe**	**Nuclear Science and Technology Research Institute of Iran (NSTRI)**

Executive Committee

RAW	NAME	ROLE
1	Dr. Farshad Ghasemi	Chairman of the Executive Committee
2	Dr. Ehsan Molazadeh	Member of The Executive Committee
3	Dr. Seyyed Ghasem Biniaz	Member of The Executive Committee
4	Mr. Aliakbar Aminidoust	Member of The Executive Committee
5	Mr. Mohammad Hosein Arkannia	Member of The Executive Committee
6	Ms. Fatemeh Zamani	Member of The Executive Committee
7	Ms. Mahya Pazoki	Member of The Executive Committee
8	Mr. Hosein Maleki	Member of The Executive Committee
9	Mr. Maziar Dalili	Member of The Executive Committee
10	Mr. Shojaei	Member of The Executive Committee
11	Ms. Fatemeh Rezaei	Member of The Executive Committee
12	Mr. Reza Rafiei	Member of The Executive Committee
13	Ms. Seyyedeh Elham Ebrahimi	Member of The Executive Committee

Radiation Measurements Papers

ICNST 2024
International Conference on Nuclear Science and Technology
6- 8 MAY 2024 | Isfahan, Iran

Radiation Measurements

ICNST 2024
International Conference on Nuclear Science and Technology
6- 8 MAY 2024 | Isfahan, Iran

Determining Detector Dead Time by Statistical Analysis of Detector Counts (Paper ID: 1012)

Jalilzadeh H. Correspondent[1*], Ashrafi S. Co-Author[1, 2], Ariafar H. Co-Author [1]

[1]Faculty of Physics, University of Tabriz, Tabriz, Iran

[2]*Research institute for Applied Physics & Astronomy, University of Tabriz, Tabriz, Iran*

Abstract

Dead time in the Geiger-Mueller detector can cause detector counts to be lost. Statistical parameters such as variance and distribution of time intervals of counts are affected. This distorts the Poisson distribution of counts and changes its statistical parameters. In this study, the dead time of the detector has been investigated using these changes. The variance-to-mean ratio is one method used to determine dead time by measuring the degree of deviation of the Poisson statistic from the measured count compared to the real count. This study is carried out for a paralyzable model and a non-paralyzable model for the Geiger-Mueller detector using Python programming language. Due to the randomness of the time intervals between the emitted radiations, the Monte Carlo method was used in the simulation. This study investigated two different microsecond dead times for each of the models. The results of the simulation for the counts and variances showed an acceptable agreement with the results of the existing analytical relationships for paralyzable and non-paralyzable models. Thus, the dead time was obtained using these results for two ideal models (P and NP models). The difference between the dead time obtained from the simulation results and the dead time input to the program was less than 2 percent.

Keywords: Time interval distribution, Geiger-Mueller detector, Paralyzable model, Non- paralyzable model, Hybrid model, Mont Carlo simulation

Introduction

The Poisson distribution is characterized by the equality of its variance and mean. In the case of the Geiger-Mueller detector, counts follow a Poisson distribution, if all the particles reaching thedetector are counted, the variance will be equal to the expected value. This can be concluded based on the fact that the variance and mean are equal in the Poisson distribution [1-5].

To estimate the dead time, the recommended method is Variance To Mean Ratio (VTMR) [2]. If all particles reaching the detector are counted, VTMR = 1 . However, the presence of dead time in the detector prevents the counting of all particles, especially at high count rates. As a result, some events will always be lost, depending on the dead time of the detector.

There are two models for dead time correction: the non-paralyzable (NP) model and the paralyzable (P) model. In the NP model, the dead time cannot be extended, and only events are lost. On the other hand, in the P model, in addition to event loss, the particle will cause the dead time to be extended by the amount of the dead time. These models represent two extremes for the behavior of an ideal detection system. However, real counting systems exhibit behavior that falls between these two extremes. Hybrid models have been developed to address this behavior, which are a combination of the ideal models [6-7]. The different models for dead time are illustrated in Figure 1 [4].

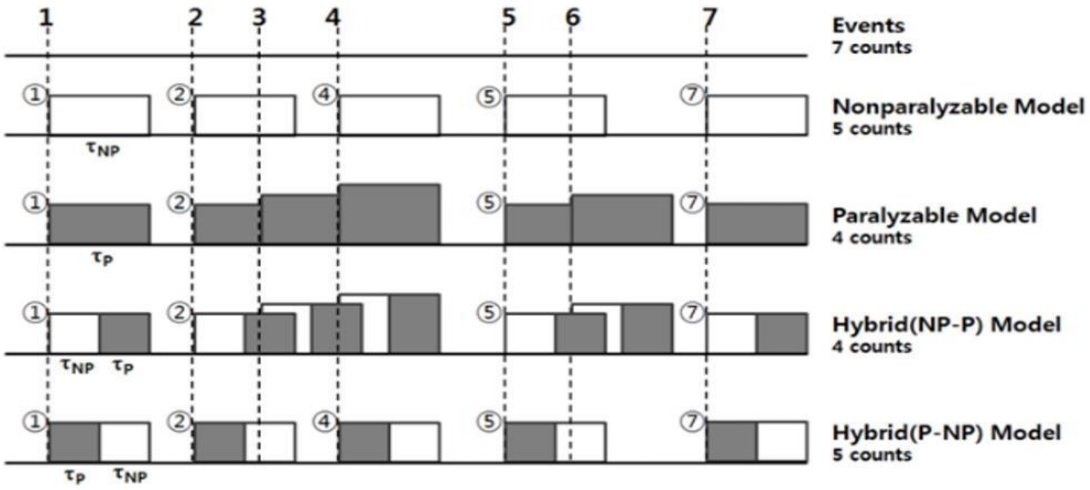

Fig. 1. Illustration of counts registered by NP, P and hybrid dead time models.

Research Theories

As previously stated, a portion of the real count rate is not accounted for. In light of this, a mathematical expression has been put forth for both the non-paralyzable and paralyzable models,

outlining the correlation between the observed counts and the true counts [8,9]. In the case of the non-paralyzable model, the relationship is defined as follows:.

$$\boldsymbol{m} = \frac{\boldsymbol{n}}{\mathbf{1}+\boldsymbol{\tau_{NP}n}} \qquad (1)$$

where m is measured count rate, $\boldsymbol{n}$ is real count rate at which counts are actually measured in counts per second and $\boldsymbol{\tau NP}$ is dead time of non-paralyzable model.

For the paralyzable model, this relationship is given as:

$\boldsymbol{m} = \boldsymbol{n}.\ \boldsymbol{exp}(-\boldsymbol{\tau N n})$, (2)

Where $\boldsymbol{\tau N}$ is dead time of paralyzable model.

In order to derive our findings based on statistical parameters such as variance and mean, it is imperative to calculate the variance of the measured counts for each of the models at hand. Previous studies conducted by Muller and Kosten have successfully determined the variance for these specific models [1,2]. Specifically, the variance to mean ratio for the nonparalyzable dead time model can be expressed as:

$$\boldsymbol{VTMR} = \frac{\boldsymbol{\sigma^2(mt)}}{\boldsymbol{mt}} = \mathbf{1} - \mathbf{2}\boldsymbol{\tau_{NP}m} + \boldsymbol{\tau^2}\ \boldsymbol{m^2}_{\boldsymbol{NP}} \qquad (3)$$

The aforementioned equation is derived by dividing the Muller relationship by the mean value. In this equation, $\sigma 2(mt)$ represents the variance of the measured count, mt denotes the mean of the measured count, and t signifies the measurement time. Additionally, the VTMR (Variance-to-Mean Ratio) for the paralyzable dead time model can be expressed as:

$$\boldsymbol{VTMR} = \frac{\boldsymbol{\sigma^2(mt)}}{\boldsymbol{mt}} = \mathbf{1} - \mathbf{2}\boldsymbol{\tau_p m} + \frac{\boldsymbol{\tau^2 m}}{\boldsymbol{t}}_{\boldsymbol{P}} \qquad (4)$$

The performance and operations of the Geiger-Mueller detector are extensively examined by analyzing the distribution of time intervals between consecutive counts. This distribution, which typically follows a Poisson distribution, is widely employed to model random events. By utilizing the Poisson distribution, we can gain insights into the likelihood of an event occurring within a specific time interval. In the case of the Geiger-Mueller detector, these events correspond to the generation of electrical pulses resulting from the interaction between radioactive particles and the detector. Each electrical pulse represents the entry of a radioactive particle into the detector, and these pulses are independent of one another and unaffected by the timing of previous pulses. As a result, the time distribution in the Geiger-Mueller detector is commonly represented using the Poisson and exponential distribution. This modeling approach allows us to accurately predict and analyze the probability of electrical pulse occurrences across different time intervals [10].

Experimental

In this study, the statistical parameters of counts and time intervals were generated using the Monte Carlo method. The Geiger-Mueller detector simulator was developed in the Python programming environment for this purpose. To obtain observed (measured) total counts, count rates, and their statistical parameters, the program requires input data such as detector dead times and true count rates. In order to facilitate a more accurate comparison, a fixed measurement time of 1 second was used for all models in this research article. Within the simulator, radiation is emitted randomly, and the time interval between two radiation events (t) is sampled from a well- known interval distribution [4]:

$$\boldsymbol{f(t)dt = n.exp(-n.t)\,dt} \qquad (5)$$

The investigation involved analyzing both the paralyzable and non-paralyzable models under two different total dead times, namely 150 μs and 300 μs. As a result, four different cases were simulated. These simulations yielded a total of 23 entries, representing the true count. Furthermore, the obtained simulation results were compared to the results obtained from analytical relations (1), (2), (3), and (4).

Results and Discussion

Table 1 shows the results of simulation and analytical (VTMRs and count rates) for the dead time of 150 μs for two paralyzable and non-paralyzable models. The value of VTMR for GMSIM is obtained using the values obtained for the observed counts through simulation and relations (3) and (4).

Table 1. Comparison of VTMRs resulted in GMSIM to Mueller formula (eq. (3)) for non-paralyzable model; and to Kosten formula (eq. (4)) for paralyzable model.

	Count rate (cps)		**Variance to mean ratio**			
Input/ true	**Measured**		τ_{NP} = **150 μs**		τ_P = **150 μs**	
	NP	**P**	**GMSIM**	**Eq. (3)**	**GMSIM**	**Eq. (4)**
20	19.95	19.95	0.994	0.994	0.994	0.994
40	39.85	39.7	0.988	0.988	0.988	0.988
60	59.85	59.35	0.982	0.982	0.982	0.982
80	79	79.2	0.976	0.976	0.976	0.976
100	99.05	98.2	0.971	0.971	0.971	0.970
200	194.1	193.65	0.943	0.943	0.942	0.942
300	287.45	286.4	0.916	0.916	0.914	0.914
400	377.95	378.35	0.890	0.890	0.887	0.887
500	466.75	467.2	0.865	0.865	0.860	0.861
600	547.1	546.2	0.843	0.842	0.836	0.836
700	632.7	626.5	0.819	0.819	0.812	0.811
800	717.65	711.05	0.796	0.797	0.787	0.787
900	793.55	781.6	0.776	0.776	0.766	0.764
1000	869.4	859.6	0.756	0.756	0.742	0.742
2000	1543.2	1483.55	0.591	0.592	0.555	0.556
3000	2048.8	1916.85	0.480	0.476	0.425	0.426
4000	2496.55	2199.75	0.391	0.391	0.340	0.341
5000	2866	2396.3	0.325	0.327	0.281	0.292
6000	3146.8	2424.55	0.279	0.277	0.273	0.268
7000	3400.4	2438.85	0.240	0.238	0.268	0.265
8000	3649.95	2423.7	0.205	0.207	0.273	0.277
9000	3834.35	2351.4	0.180	0.181	0.295	0.300
10000	3980.05	2206.2	0.162	0.160	0.338	0.331

The simulation results obtained for the variance-to-mean ratio (GMSIM) are very close to the results obtained from equation (3) for the non- paralyzable model and equation (4) for the paralyzable model using the results obtained from relations (1) and (2). Therefore, these results can be used to obtain the dead time.

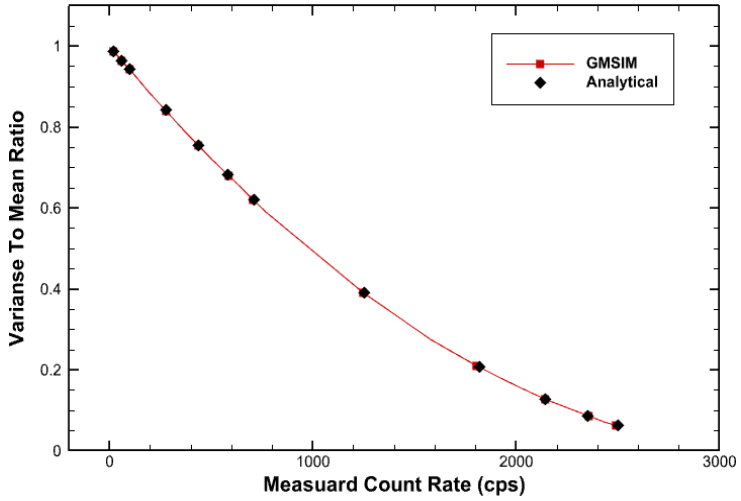

Fig. 2. GMSIM variance to mean ratio for non-paralyzable model (τ_{NP} = 300 μs).

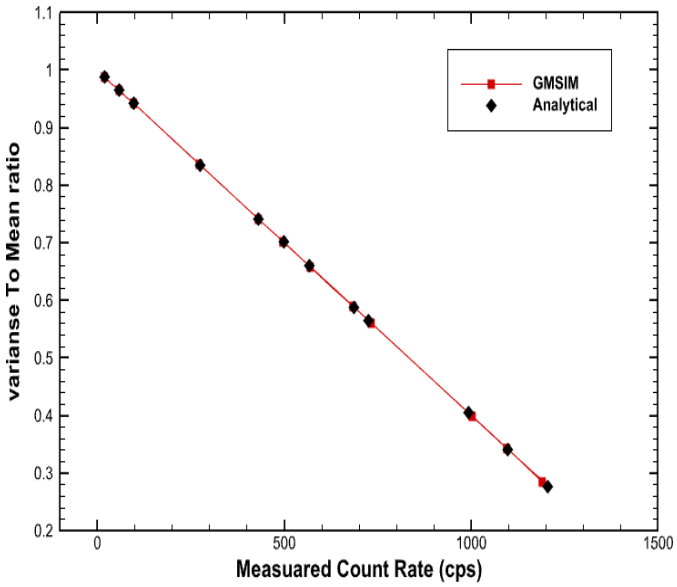

Fig. 3. GMSIM variance to mean ratio for paralyzable model (τP = 300 μs).

In Fig. 2. and Fig. 3. "Analytical" shows the results obtained from Eq. (3) and Eq. (4).

By fitting the results of the GMSIM, dead time can be determined which are: 152±2 μs, 303±3 μs for nonparalyzable model using dead time input parameter of 150 μs and 300 μs, while for paralyzable model, the GMSIM results are 152±2 μs, and 302±2 μs, using same dead time input parameter as nonparalyzable model.

Conclusions

In this article, considering that we used the Monte Carlo method for simulation, it was observed that the results for the observed counts and statistical parameters are in good agreement with the results obtained from the analytical relationships. These results were successfully used to determine the dead time of the Geiger-Mueller detector. Therefore, the Monte Carlo method is an efficient method for this simulation.

Considering the success of the simulation done in the article, further development of the simulator program can help future research in the field of detector counts.

References

[1] Kosten, L. (1943). on the frequency distribution of the number of discharges counted by a Geiger-Müller counter in a constant interval. Physica, 10: 749-756.

[2] K. Hashimoto, K. Ohya, and Y. Yamane. (1996). Dead-Time Measurement for Radiation Counters by Variance-to-Mean Method, Journal of Nuclear Science and Technology, Vol. 33, No. 11, pp: 863-868.

[3] Müller, J.W. (1973). Dead-time problems. Nuclear Instruments and Methods, 112: 47-57.

[4] S.H. Lee, R.P. Gardner, J.A.E. Moosung. (2007). Non-Poisson Counting Statistics of a Hybrid G–M Counter Dead Time Model, Nucl. Instr. and Method in Physics Research B 263

[5] N.S. Syam, S. Maeng, M.G. Kim, S.Y. Lim, S.H. Lee. (2018). Statistical Parameter Study of Time Interval Distribution for Nonparalyzable, Paralyzable, and Hybrid Dead Time Models, Journal of Korean Physics Society, Vol. 72, No. 10: 1133 – 1188.

[6] Lee, S. H., Gardner, R. P., & Jae, M. (2004). Determination of dead times in the recently introduced hybrid GM counter dead time model. Journal of Nuclear Science and Technology, 41(sup4): 156-159.

[7] Patil, A. (2010). Dead time and count loss determination for radiation detection systems in high count rate applications. Missouri University of Science and Technology.

[8] Feller, W. (2015). RETRACTED CHAPTER: On Probability Problems in the of Counters. In Selected Papers I (pp. 751-759). Springer, Cham.

[9] Evans, R. D., & Evans, R. D. (1955). The atomic nucleus (Vol. 582). New York: McGraw-Hill.

[10] M. Arkani, G. Raisali. (2015). Measurement of Dead Time by Time Interval Distribution Method, Nuclear Instruments and Methods in Physics Research No. A774: 151–158

ICNST 2024
International Conference on Nuclear Science and Technology
6- 8 MAY 2024 | Isfahan, Iran

An improved model for dead time correction of G-M detector (Paper ID: 1018)

Ariafar H. Correspondent[1*], Ashrafi S. Co-Author[1,2], *, Jalilzadeh H. Co-Author[1,2].

[1]*Faculty of Physics, University of Tabriz, Tabriz, Iran*

[2]*Research institute for Applied Physics & Astronomy ,, University of Tabriz, Tabriz, Iran*

Abstract

Due to the long dead time, the application of the G-M counter is limited to relatively low count rates. To extend the range of application of these counters, the hybrid dead time model is used. This hybrid model is based on two paralyzable and non-paralyzable dead time models. The new model involves two parameters, which are paralyzable and non-paralyzable dead times. The dead times used in the model are very closely related to the physical dead time of the G-M tube and its resolving time. The use of this hybrid model provides the possibility of performing accurate corrections on G-M tube counts and expands the scope of the detector's application. In this work, to find paralyzable and non-paralyzable dead time values, the experimental method of two sources has been used. The radioactive source used is 226Ra . Also to correct the counts in this work, the non-linear least square algorithm method has been used. In the count rate of 5090 cps, the paralyzable and non-paralyzable dead times are respectively equal to $\tau_P = 43.316\ \mu s$ and $\tau_{NP} = 54.006\ \mu s$. Additionally in the count rate of 4053 cps, $\tau_P = 45.941\ \mu s$ and $\tau_{NP} = 54.818\ \mu s$. In the new hybrid model, the dead time of the paralyzable and non paralyzable system in these counting rates are equal to $\tau_P = 0.0068\ \mu s$ and $\tau_{NP} = 54.181\ \mu s$.

Keywords: G-M counter, hybrid model, paralyzable model, non-paralyzable model, non-linear least square algorithm

Introduction

G-M detectors have been used in nuclear physics for almost a hundred years and have a wide range of applications. These detectors have several advantages, including high sensitivity to various types of radiation, high pulse height, and low price. However, they also have some disadvantages, such as the inability to measure the energy of radiation particles and a long dead time compared to other radiation detectors [1]. The dead time of a detection system refers to the time it takes for the system to process one event before it can process another. Any events that occur during this dead time are lost [2]. At

high count rates, the dead time becomes a significant limitation for the applications of any detection system.

To expand the useful count rates of G-M detectors, it is important to accurately describe the dead time and its components and develop a correction model [3]. The traditional one-parameter dead time models, such as the paralyzable and nonparalyzable models, are not sufficient to properly represent the dead time response of a detection system [2]. To address this limitation, a new two-parameter dead time model based on a hybrid approach is proposed in this research. This model combines both paralyzable and non-paralyzable dead time components. By using this new dead time model, accurate corrections can be made for G-M counters with high counting rates, leading to a significant increase in the usable range of these counters.

Research Theories

In the non-paralyzable model proposed by Feller and Evans, the dead time is not extended and any radiation events that happen during the detector's dead times are not included in the count [4], [5]. The relationship between the actual counting rate and the observed counting rate is significant and can be describe as follows:

$$m = \frac{n}{1+\tau_N} \quad (1)$$

In the non-paralyzable model, the observed counting rate (m) is the rate at which counts are actually measured in counts per second (cps). The true counting rate (n) is the actual rate at which counts are occurring in cps. The non-paralyzable dead time (τN) is the time it takes for the detector to recover after each count in microseconds (μs). When a radiation event happens during the dead time, it is not counted, but the dead time is extended [4], [5]. The relationship between the true and observed counting rates can be expressed as follows:

$$m = n\exp(-n\tau_P) \quad (2)$$

Where (m) is the observed count rate, (n) is true count rate and τ_p is the paralyzable dead time in μs. Equation (2) cannot be easily solved, so this model is transformed into the following form using the inverse method and approximation with Taylor expansion:

$$n = \left(\frac{8\tau_P^3 m^4}{3}\right) + \left(\frac{3\tau_P^2 m^3}{2}\right) + (\tau_P m^2) + m \quad (3)$$

The paralyzable and non-paralyzable models have achieved some success, but it has been proposed that the actual dead time characteristics of the G-M counter lie somewhere in between these models [6]. Lee and Gardner have introduced a new hybrid model that combines the best of both models.

$$m = \frac{n \exp(-n\tau_P)}{1+n\tau_N} \quad (4)$$

In this model, the non-paralyzable dead time refers to the time when a G-M tube is unable to detect the next radiation event. On the other hand, the paralyzable dead time is the time between the end of the non-paralyzable dead time and when a pulse larger than the discriminator level can be developed (Fig1).

When radiation enters and creates an electron-ion pair in the G-M tube, the electron is accelerated towards the anode, causing a series of electron avalanches along the anode wire. While electrons quickly gather at the anode, ions tend to stay longer around the anode due to their slower mobility. This ion space charge blocks the electric field needed for developing avalanches, effectively pausing the G-M discharge for a certain period of time (τN).

As the positive ions drift towards the cathode, the space charge becomes less concentrated, allowing the electric field to gradually recover to its original strength. If a second radiation event happens during this recovery period (τP), a partially developed pulse may be generated. Whether or not this pulse is registered by the counting system depends on the discriminator level of the system [5].

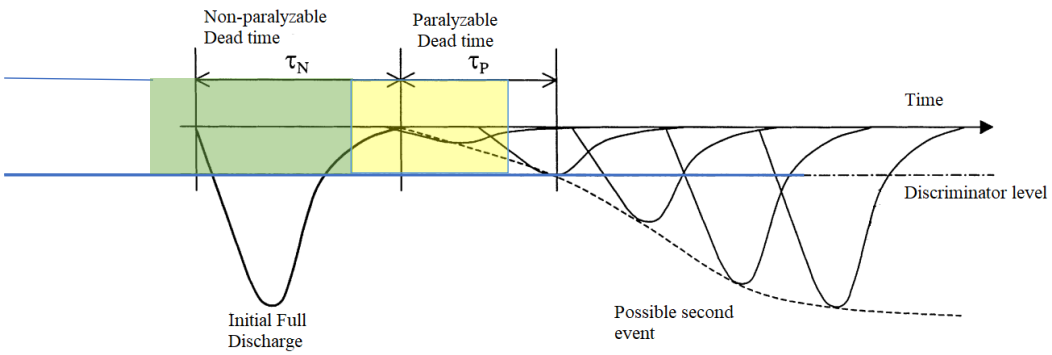

Fig.1. Illustration of the dead time behavior of the G-M detector on an oscilloscope.

Experimental

To ensure the accuracy of the results, it is crucial to conduct experimental verification. In order to do this, we utilize experimental data from two decaying sources. $226Ra$ sources are placed in front of a G-M tube, and measurements are taken every ten seconds.

The general geometry of this experiment is as follows:

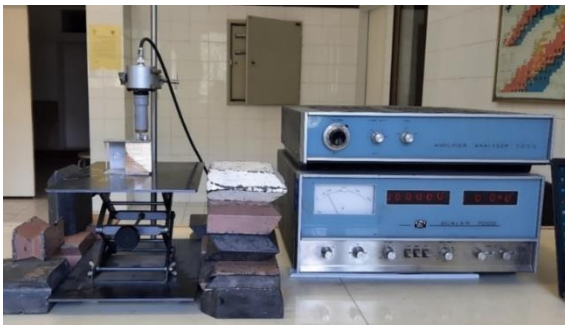

Fig.2. The general geometry.

This geometry includes a G-M tube to detect the rays, a scalar counter, two $226Ra$ sources(the half-life of $226Ra$ is 1600 years, and its activity is $9\mu ci$), a base made of aluminum to keep the sources stable to prevent possible errors from losing the count, and an artificial source to prevent dispersion from surrounding environment.

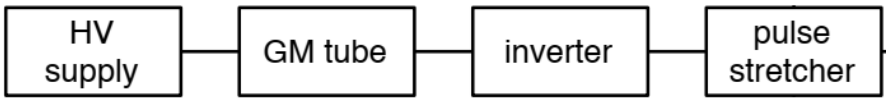

Fig.3. Basic structure of the G-M counter.

A block diagram for the G-M counter we can be building is given above. The purpose of these blocks are as follows:

HV supply: Converts the 220 V urban electricity voltage to the 400 V needed by the G-M tube.

G-M tube: Detects ionizing radiation: emits a current pulse whenever a ionization event occurs inside the tube.

Inverter: Converts the current from the G-M tube into an inverted voltage pulse.

Pulse stretcher: Converts the very short pulse from the inverter into 1.5 ms pulse.

To determine the dead times of the hybrid model, a method involving two sources is recommended. This is because the hybrid model includes an additional parameter, requiring an extra split source compared to the usual split source method.We denote each set of split sources as a and b, with 12 representing the combined sum source, and 1 or 2 indicating individual split sources. In order to maintain the conservation of true counting rates, six formulas are used for the six measurements of split and combined sum sources.

$$m_{a1} = \frac{n_{a1} exp(-n_{a1}\tau_P)}{1+n_{a1}\tau_{NP}} \quad (5)$$

$$m_{a2} = \frac{n_{a2} exp(-n_{a2}\tau_P)}{1+n_{a2}\tau_{NP}} \quad (6)$$

$$m_{a12} = \frac{\left(n_{a1}+n_{a2}\right) exp(-\left[n_{a1}+n_{a2}\right]\tau_P)}{1+(n_{a1}+n_{a2})\tau_{NP}} \quad (7)$$

$$m_{b1} = \frac{n_{b1} exp(-n_{b1}\tau_P)}{1+n_{b1}\tau_{NP}} \quad (8)$$

$$m_{b2} = \frac{n_{b2}\, exp\left(-n_{b2}\tau_P\right)}{1+n_{b2}\tau_{NP}} \quad (9)$$

$$m_{b12} = \frac{\left(n_{b1}+n_{b2}\right) exp(-\left[n_{b1}+n_{b2}\right]\tau_P)}{1+(n_{b1}+n_{b2})\tau_{NP}} \quad (10)$$

The system equations involve six unknowns, including two dead times (τP and τNP) and four split true counts ($na1$, $na2$, $nb1$, and $nb2$) [6]. The set (a) corresponds to counts (5090.5±71.34 cps, 2968.6±54.48 cps, and 2933.1±54.15 cps), while the set (b) corresponds to the counts (4053.9±63.67 cps, 2325±48.21 cps, and 2235.4 ± 47.28 cps).

Since the equations have a transcendental nature, a numerical iterative scheme is necessary. In this study, the non-linear least square algorithm method is employed to solve these equations. Subsequently, the iterative methods are used to calculate the dead times from the six measurements data obtained from two source methods, which satisfy equations (5) through (10). The calculated dead times are then compared to the original ideal G-M counter characteristics.

Results and Discussion

The data we collected from our experiments revealed some interesting findings. We measured the paralyzable and non-paralyzable dead times of our system for different counts. For counts $m12$, $m1$, and $m2$, we obtained values of 5090.5±71.34 cps, 2968.6±54.48 cps, and 2933.1±54.15 cps, respectively. The corresponding dead times were τP = 43.316 μs and τNp = 54.006 μs.

We also measured the dead times for a different set of counts: $m12$, $m1$, and $m2$. The values we obtained were 4053.9±63.67 cps, 2325±48.21 cps, and 2235.4 ± 47.28 cps, respectively. The dead times for these counts were τP = 45.941 μs and τNp = 54.818 μs in addition in the new hybrid model, the dead time of the paralyzable and non paralyzable system in these counting rates are equal to $\tau_P = 0.0068\ \mu s$ and $\tau_{NP} = 54.181\ \mu s$.

When we applied the hybrid model, we found that the paralyzable dead time was very small compared to the overall dead time of our detection system. This suggests that our G-M system follows the non-paralyzable model for these counts.

Based on the results presented in Table (1), we can conclude that our proposed hybrid model provides more accurate corrections compared to the non-paralyzable and paralyzable models. This model can be used to correct the counts obtain from our G-M system and estimate any count losses.

Table 1. Corrections of counts.

Observed count rates	Corrections		
	Hybrid model	Non-paralyzable model	Paralyzable model
Counts/S	Counts/S	Counts/S	Counts/S
m_{a1} 2968 ± 71	3539 ± 78	3535 ± 78	3447 ± 105
m_{a2} 2933 ± 54	3489 ± 77	3485 ± 77	3398 ± 103
m_{a12} 5091 ± 71	7028 ± 136	7021 ± 138	6845 ± 245
m_{b1} 2325 ± 48	2658 ± 64	2665 ± 63	2623 ± 61
m_{b2} 2235 ± 47	2541 ± 62	2547 ± 61	2508 ± 59
m_{a12} 4054 ± 64	5198 ± 105	5212 ± 106	5131 ± 99

The results we obtained show that our hybrid model is better at making accurate corrections compared to both the non-paralyzable and paralyzable models. This model can be used to correct G-M system counts and estimate the number of losses. Our system adhered to the non-paralyzable model, but this newly presented model can be used for any other type of G-M system that may follow either the paralyzable model or both the non-paralyzable model and the paralyzable model, considering the contribution of the paralyzable model

Conclusions

In this paper, we have shown that in the two source method, it is important to keep the test geometry intact and stable. To ensure accurate counting rates, the combined intensity of split sources should be equal to the sum intensity of the sources. Additionally, it is crucial to keep the background counts very low, as they are not taken into account.

Further research can explore the use of higher count rates. The focus of this paper was on the relationship between observed and true counting rates, and how they are compared through measurements. However, it was found that due to dead time effects, the observed events deviate from the Poisson random statistic.

To estimate dead times, a variance-to-mean ratio model can be used. This involves repeating measurements at different count rates and comparing the degree of deviation of the Poisson statistic from the measured count to estimate the true count.

References

[1] [1] Lee, S. H., & Gardner, R. P. (2000). A new G–M counter dead time model. Applied Radiation and Isotopes, 53(4-5), 731-737.

[2] [2] Feller, W. (2015). RETRACTED CHAPTER: On Probability Problems in the Theory of Counters. In Selected Papers I (pp. 751-759). Springer, Cham.

[3] [3] Evans, R. D., & Evans, R. D. (1955). The atomic nucleus (Vol. 582). New York: McGraw-Hill.

[4] [4] Lee, S. H., Gardner, R. P., & Jae, M. (2004). Determination of dead times in the recently introduced hybrid GM counter dead time model. Journal of Nuclear Science and Technology, 41(sup4), 156-159.

[5] [5] Patil, A. (2010). Dead time and count loss determination for radiation detection systems in high count rate applications. Missouri University of Science and Technology.

[6] [6] Lee, S. H., Gardner, R. P., & Jae, M. (2004). Determination of dead times in the recently introduced hybrid GM counter dead time model. Journal of Nuclear Science and Technology, 41(sup4), 156-159.

ICNST 2024
International Conference on Nuclear Science and Technology
6- 8 MAY 2024 | Isfahan, Iran

Comparative Performance Analysis of 3D Pixel Detector and Commonly Used Radiation Detectors in High Energy Physics and Imaging (Paper ID: 1044)

M.M. Bahjat Haghighi[1], M. Mohamadian[1*]
[1]Amirkabir University of Technology, Physics and Energy Engineering Department
[*]mohamadian@aut.ac.ir

Abstract

In high energy physics experiments and imaging systems, the accurate detection and measurement of radiation is crucial for understanding fundamental particles and their interactions. This study presents a comprehensive comparison of the performance of 3D pixel detectors with other commonly used radiation detectors in the fields of high energy physics and imaging. The focus is on evaluating the efficiency, resolution, and sensitivity of 3D pixel detectors in comparison to traditional radiation detectors such as scintillators, semiconductor detectors, and gas-filled detectors. The research methodology involves experimental characterization of each detector type under various radiation sources and energy levels, as well as simulations to assess their performance in different operating conditions.

The results of this study provide valuable insights into the strengths and limitations of 3D pixel detectors compared to other radiation detectors, offering significant information for researchers and engineers in selecting the most suitable detector for specific applications in high energy physics and medical imaging. Additionally, the findings contribute to advancing the development and optimization of radiation detection technologies for improved performance and reliability in demanding scientific and medical environments.

Keywords: 3D pixel detector, high energy physics, imaging, performance analysis, radiation detectors.

Introduction

Radiation detectors are essential tools for the detection and measurement of high energy particles and radiation in various fields, including high energy physics experiments and medical imaging applications. The development of advanced detectors with improved performance characteristics is crucial for enhancing the accuracy and efficiency of these applications. In recent years, the 3D pixel detector has emerged as a promising technology with potential advantages over commonly used radiation detectors such as scintillation detectors and semiconductor detectors. 3D pixel detectors are a type of semiconductor radiation detectors that have electrodes penetrating through the bulk of the

sensor, creating a three-dimensional array of pixels [1]. They offer several advantages over conventional planar detectors, such as higher radiation hardness, lower leakage current, faster charge collection, and reduced pixel capacitance [1-2]. This paper presents a comparative performance analysis of the 3D pixel detector and commonly used radiation detectors, aiming to evaluate their respective capabilities in high energy physics experiments and imaging.

The principles of radiation detection and measurement have been extensively studied and applied in various scientific and technological fields. In high energy physics, the accurate detection of high energy particles is essential for studying fundamental particles and their interactions. Similarly, in medical imaging, radiation detectors are used to capture images for diagnostic and therapeutic purposes. Commonly used radiation detectors include scintillation detectors, which utilize the emission of light when struck by radiation, and semiconductor detectors, which rely on the generation of electron-hole pairs in a semiconductor material.

The 3D pixel detector is a relatively new technology that offers several potential advantages over traditional radiation detectors. It is based on a three-dimensional array of small pixel sensors, which allows for precise spatial resolution and efficient charge collection. The 3D pixel detector also exhibits high radiation hardness and energy resolution, making it a promising candidate for high energy physics experiments and medical imaging applications.

Several studies have investigated the performance characteristics of the 3D pixel detector and compared it with commonly used radiation detectors. These studies have highlighted the potential advantages of the 3D pixel detector in terms of spatial resolution, energy resolution, efficiency, and radiation hardness. However, a comprehensive comparative analysis of the performance of the 3D pixel detector and commonly used radiation detectors is necessary to provide a clear understanding of their capabilities and limitations.

In this paper, we present a thorough comparative performance analysis of the 3D pixel detector and commonly used radiation detectors, aiming to provide valuable insights into their respective capabilities in high energy physics experiments and imaging applications. The findings of this analysis will contribute to the advancement of detector technologies and inform the selection of suitable detectors for specific applications in high energy physics and medical imaging.

Comparison of Different Features of Semiconductor Detectors

When comparing the performance of 3D pixel detectors with other types of radiation detectors commonly used in high energy physics experiments, imaging and especially medical imaging, several factors be highlighted such as; Spatial resolution, Energy resolution, Radiation tolerance, Efficiency and Material budget.

Spatial Resolution

3D pixel detectors typically offer excellent spatial resolution due to their fine segmentation and precise position measurement capabilities. This can be compared with the spatial resolution of other detectors such as scintillation detectors or gas-based detectors. For instance, J. balibrea et al. at investigated five different models to reconstruct the 3D-ray hit coordinates in five large LaCl3(Ce) monolithic crystals optically coupled to pixelated silicon photomultipliers [3]. They report that the average resolutions close to 1-2 mm FWHM are obtained in the transverse crystal plane for crystal thicknesses between 10 mm and 20 mm using analytical models. For thicker crystals, average resolutions of about 3-5 mm FWHM are obtained. While for example Lanza, R C et al. [4] discuss the use of gas scintillators for imaging of low energy isotopes. They report that the spatial resolution has been measured at 3-4 mm FWHM.

The spatial resolution of a detector refers to its ability to accurately determine the position of radiation interactions. In high energy physics experiments, spatial resolution is essential for identifying the location of particle interactions and reconstructing their trajectories. Amlan Datta et al. also discusses the development of high spatial resolution X-ray detectors using solution-processable two-dimensional hybrid perovskite single-crystal scintillators grown inside microcapillary channels. These detectors demonstrate excellent spatial resolution and have the potential for low-cost large-area ultrahigh spatial resolution high frame rate X-ray imaging. The detectors are capable of detecting thermal and fast neutrons too. Furthermore, they reported that the spatial resolution of the PEALPB detectors was determined to be ~ 32% better than micro columnar CsI detectors. [5]

Therefore, compared to scintillation detectors or gas-based detectors, 3D pixel detectors offer significantly higher spatial resolution due to their fine segmentation and precise position measurement capabilities. Scintillation detectors, as an illustration, typically have a spatial resolution in the range of millimeters to centimeters, while gas-based detectors have a resolution of a few hundred micrometers.

In contrast, 3D pixel detectors can achieve spatial resolutions of tens of micrometers or even better [5].

The high spatial resolution of 3D pixel detectors is due to their small pixel size, typically in the range of 50-100 micrometers. This fine segmentation allows for precise position measurement and localization of radiation interactions. In addition, the 3D design of the detector allows for charge sharing between adjacent pixels, further improving the spatial resolution [5-6].

The improved spatial resolution of 3D pixel detectors has significant implications for high energy physics experiments, where precise position measurement is essential for identifying particle interactions and reconstructing particle trajectories.

In medical imaging application, mostly high spatial resolution is important for accurately localizing and characterizing tumors or other abnormalities. Additionally, all of the aforementioned features are identical for this area.

Energy Resolution

The energy resolution of a detector is vital for accurately measuring the energy of radiation interactions. 3D pixel detectors are known for their excellent energy resolution, especially for charged particles. Comparing this with the energy resolution of semiconductor detectors or calorimeters can provide insights into their relative performance. This is due to their ability to precisely localize the interaction point of the incoming radiation within the detector volume, resulting in improved spatial resolution and subsequently enhanced energy resolution. In comparison to traditional semiconductor detectors, 3D pixel detectors often exhibit narrower FWHM values, indicating higher energy resolution. The energy resolution of 3D pixel detectors can vary depending on the specific design, material, and application. However, typical energy resolutions for 3D pixel detectors can range from around 1% to 0.1% FWHM for X-ray and gamma-ray detection. In some cases, even better energy resolutions have been achieved in research and development settings. It's important to note that these values are approximate and can vary based on the specific implementation and conditions.

Mele F et al. conducted a study on advancements in High-Energy-Resolution CdZnTe Linear Array Pixel Detectors with Fast and Low Noise Readout Electronics, achieving an energy resolution of approximately 0.96% FWHM [6]. In a separate study, Wen Li et al. investigated the energy resolution limiting factors of multi-pixel events in 3D position-sensitive CZT gamma-ray spectrometer, achieving

an energy resolution of about 1.8~1.9% FWHM at 662 keV [7]. Moreover, Seiichi Yamamoto et al. explored an ultrahigh spatial resolution radiation-imaging detector using 0.1 mm × 0.1 mm pixelated GAGG plate combined with a 1 mm channel size Si-PM array, achieving a 0.31-mm FWHM for Am-241 [8]. Gu Y et al. studied a high-resolution, 3D positioning cadmium zinc telluride detector for PET, achieving a spatial resolution of 0.44±0.07 mm in the direction orthogonal to the electrode planes. Measurements based on coincidence electronic collimation yielded a point spread function with 0.78 ± 0.10 mm FWHM [9]. Furthermore, William R. Kaye, in his Ph.D. thesis, reported the performance of HPGe at approximately 0.2% FWHM at 662keV. And further, the energy resolution of pixelated CdZnTe for gamma rays was found to be 0.36% FWHM at 2614 keV [10].

Energy resolution of pulsed neutron beam provided by the ANNRI beamline at the J-PARC/MLF in the single-bunch mode, is better than about 1% between 1 meV and 10 keV at a neutron source operation of 17.5 kW [11]. Yvan A. Boucher in his thesis reported A137Cs spectrum from the HPGe detector showing an energy resolution of 0.30% FWHM at 662 keV [12]. In addition, the spatial resolution of semiconductor pixel detector in [13] is 99.3 μm which is according to detection efficiency about 0.1% for 4MeV neutrons. Also, with the state-of-the-art readout technology, the Orion Group at the University of Michigan consistently achieves single-pixel events energy resolutions below 0.40% FWHM at 661.7 keV for most direct-attachment CdZnTe detectors. Hence, it is possible to reduce the weight and size of hand-held, 3-D CdZnTe devices at a small cost of energy resolution (<0.1%) and calibration time [14].

However, there are some other semiconductor detectors with energy resolutions below 1% FWHM include:

— Silicon Drift Detectors (SDD) which are semiconductor detectors commonly utilized in X-ray spectroscopy and other applications requiring high energy resolution. The energy resolution of SDDs has been the subject of various research papers. As a case in point, Strüder L. et al [15] discusses the development of SDDs for electron microscopy applications, reporting that the energy resolution of an SDD was enhanced from 152 eV at Mn K α, with a 3.5 mm2 small SDD operated at -20°C, to less than 5 electrons (rms) in 2008 at 100,000 counts per second for a 10 mm2 active area [15-16].

— Germanium Detectors: High-purity germanium (HPGe) detectors are known for their excellent energy resolution, making them suitable for gamma-ray spectroscopy in nuclear physics and materials analysis. Roques, J. P. et al discusses the radiation hardness of 3D silicon radiation detectors and their

use in High Energy Physics (HEP) experiments. They highlight the superior radiation tolerance of 3D detectors compared to planar sensors, among other advantages [17]. Another researcher Lee, I Y explains that Germanium detectors provide significantly improved energy resolution in comparison to sodium iodide detectors, as explained in the preceding discussion of resolution. Germanium detectors produce the highest resolution commonly available today [18]. Additionally, Zeng, Z. compares the energy resolution of a broad-energy germanium detector with semi-coaxial HPGe detectors. They show that the broad-energy germanium detector can achieve a better energy resolution than semi-coaxial HPGe detectors [19].

— CdZnTe Detectors: Cadmium Zinc Telluride (CdZnTe) detectors are used in medical imaging, security screening, and nuclear spectroscopy due to their high energy resolution and room temperature operation. Mele F et al discusses the development of CdZnTe detectors for medical, astrophysical, or industrial applications. They report that the energy resolution of a CdZnTe detector was measured to be 782 eV FWHM (1.3%) on the 59 keV line at room temperature (+20 °C) using an uncollimated 241 Am [20]. Another researcher Wang, S. et al. reports that the energy resolution of a CdZnTe detector was better than 5% (FWHM) at 59.5 keV and better than 1.2% (FWHM) at 662 keV [21].

— Scintillation Detectors with Photomultiplier Tubes (PMTs) can achieve energy resolutions below 1% FWHM, making them useful in gamma-ray and X-ray spectroscopy. These detectors are commonly used in various fields such as medical imaging, materials analysis, and nuclear physics due to their high energy resolution capabilities.

For 3D pixel detectors, as mentioned previously, the energy resolution is often better than 1 %, even reaching 0.1%. For example, Robertson JG et al. proposed a universal energy response model for determining the energy resolution of a detector based on the assumption that the energy response can be described by a Gaussian function. The model was tested on various detectors, including high-purity germanium, sodium iodide, and liquid argon detectors, with results showing that the model is accurate and can be used to determine the energy resolution of a detector with an uncertainty of less than 1% [22, 23]. Moreover, Oonuki, K. et al. developed a thick CZT detector with a thickness of 0.5 cm for rare event and low-background searches, including neutrino less double beta ($0\nu\beta\beta$) decay, low-energy nuclear recoils, and coherent elastic neutrino-nucleus scattering. The detector features an excellent energy resolution, low detection thresholds down to the sub-keV range, and enhanced background rejection capabilities. The energy resolution of these detectors is about 0.1% FWHM in the region of

interest around Qββ = 2039 keV [24] (Fig. 1). Besides, a P-type point contact (PPC) germanium detector used in rare event and low-background searches also achieved an energy resolution of about 0.1% FWHM, with similar results to those mentioned previously [24, 25].

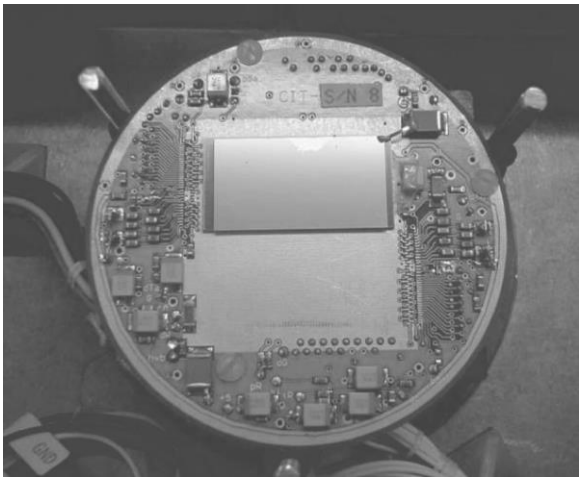

Fig. 1. Photo of the pixel detector. The detector has dimensions of 23.7 × 13.0 mm^2 and a thickness of 0.5 mm. The cathode surface is shown in the picture [25].

To comparing this feature, a universal energy response model has been proposed for determining the energy resolution of a detector. The model is based on the assumption that the energy response of a detector can be described by a Gaussian function. The model has been tested on a variety of detectors, including a high-purity germanium detector, a sodium iodide detector, and a liquid argon detector [22].

Radiation Tolerance

High energy physics experiments often involve high radiation levels. Comparing the radiation tolerance of 3D pixel detectors with other detectors, such as silicon strip detectors or gas-filled detectors, can demonstrate their suitability for use in such environments.

Dalla Betta G-F et al. discuss the radiation hardness of 3D silicon radiation detectors and their application in High Energy Physics (HEP) experiments, emphasizing the superior radiation tolerance of 3D detectors compared to planar sensors, along with other advantages [26]. Also, Dalla Betta G-F et al. present another study reviewing silicon radiation detectors, with a focus on fabrication aspects. They discuss the evolution of silicon radiation detectors from planar to 3D sensors and emphasize the advantages of 3D sensors, including their superior radiation tolerance [2]. Y. Dieter et al. compare the radiation tolerance of passive CMOS sensors with conventional planar sensors, demonstrating that passive CMOS sensors are radiation tolerant and can withstand a fluence of 1 × 1016 neq/cm2, the expected fluence for the future innermost ATLAS pixel detector layer. They also show that the

performance of passive CMOS sensors in terms of noise and hit-detection efficiency is comparable to that of conventional planar sensors [27].

Efficiency

The efficiency of a detector in capturing and registering radiation events is an important performance metric. Comparing the efficiency of 3D pixel detectors with other detectors, can highlight their relative performance in detecting radiation.

van der Sar et al. discusses the potential silicon photomultiplier (SiPM)-based scintillation detectors in photon-counting computed tomography (PCCT) scanners, as an alternative to CdTe and CZT detectors. They investigate fast SiPM-based scintillation detectors for X-ray photon-counting applications and compares their energy response and count rate performance with other detectors. The results demonstrate that the SiPM-based scintillation detectors exhibit higher detection efficiency than scintillation detectors and photomultiplier tubes [28]. Furthermore, in another study, van der Sar et al. review silicon radiation detectors, focusing on fabrication aspects. They discuss the evolution of silicon radiation detectors from planar to 3D sensors and highlight the advantages of 3D sensors, including their superior radiation tolerance. However, they do not compare the efficiency of 3D pixel detectors with other detectors [29]. Additionally, Iida, H. et al. compares the performance of a pixelated CdZnTe detector with a conventional scintillation detector, demonstrating that the CdZnTe detector exhibits higher energy resolution and detection efficiency than the scintillation detector [30].

Material Budget

In high energy physics experiments, minimizing the material budget of detectors is essential to reduce multiple scattering and energy loss. Comparing the material budget of 3D pixel detectors with other detectors, such as wire chambers or calorimeters, can demonstrate their advantages in minimizing material interactions [31].

In comparing the material budget of 3D pixel detectors with other detectors such as wire chambers or calorimeters, it's important to consider the amount of material present in the detector system, as this can affect the interactions of particles and the overall performance of the detector [32].

3D pixel detectors typically have a low material budget due to their compact design and use of semiconductor materials. The thin active layers of the detector contribute to minimizing the amount of

material particles must traverse before interacting with the detector. This low material budget is advantageous in high-energy physics experiments as it reduces multiple scattering and energy loss, allowing for more accurate measurements of particle trajectories and energies [33].

In contrast, wire chambers, which consist of arrays of thin conducting wires, and calorimeters, which absorb and measure the energy of particles, can have higher material budgets. Wire chambers contain a larger amount of structural material due to the wires and support structures, while calorimeters often incorporate dense absorber materials such as lead or tungsten [34].

The lower material budget of 3D pixel detectors can be particularly beneficial in experiments where minimizing material interactions is critical for achieving precise measurements of particle properties and interactions. Additionally, in applications where space is limited or minimizing the impact of the detector on the particles being measured is important, the low material budget of 3D pixel detectors can be advantageous [35-36].

For high-energy physics experiments and other applications where material budget is a concern, the comparison of material budgets between 3D pixel detectors, wire chambers, and calorimeters is an important factor in selecting the most suitable detector technology for the specific experimental requirements.

By comparing these performance factors, we can evaluate the strengths and limitations of 3D pixel detectors relative to other commonly used radiation detectors in high energy physics experiments. This comparison can inform the selection of detectors based on the specific requirements of the experiment and contribute to the advancement of radiation detection technologies in the field.

Discussion

Medical Imaging and Industrial Applications

3D pixel detectors can be used for various medical imaging modalities, such as X-ray, computed tomography (CT), positron emission tomography (PET), and single photon emission computed tomography (SPECT). These modalities use different types of radiation sources and detection mechanisms to produce images of the internal structures and functions of the human body [1].

The choice of one clinical device over another is influenced by technical disparities among the equipment, such as detection medium, shorter scan time, patient comfort, cost-effectiveness, accessibility, greater sensitivity and specificity, and spatial resolution [1].

In [2] Silicon radiation detectors, a special type of microelectronic sensor, are reviewed for their fabrication aspects. They can directly convert radiation into an electrical signal, ready to be processed by an electronic circuit. In conventional planar detection structures, photon absorption efficiency is limited by the thickness of the detector, which is itself limited by charge transport properties in the chosen material [37]. The evolution of detector technologies has been mainly driven by the ever-increasing demands for frontier scientific experiments [2]. The effectiveness and precision of disease diagnosis and treatment have increased, thanks to developments in clinical imaging over the past few decades. This is due to the huge development and progression of science steadily in imaging modalities [1]. AI has been incorporated with diagnostic and treatment techniques, including imaging systems. Its applications aided in manipulating sophisticated data in imaging processes and increased imaging tests' accuracy and precision during diagnosis [1,37,38].

DESIGN AND FABRICATION

Beside comparing the performance of 3D pixel detectors with other types of radiation detectors, other features and fabrication methods could also be compared as follow.

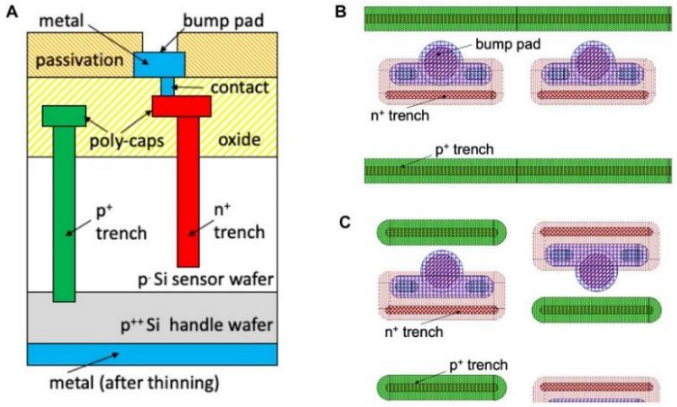

Fig. 2. 3D-trenched-electrode pixel: (A) schematic cross-section; layouts of two adjacent pixels of 55 × 55 μm2 size in (B) existing device and (C) proposed device [39].

Boughedda A. et al. discusses a design modification to an existing 3D-trenched pixel detector aimed at improved fabrication yield (Fig. 2). The device concept is studied and its performance is evaluated by TCAD simulations, in comparison to the existing one. The modified design features a less uniform electric field distribution but is expected to yield good timing performance and high radiation tolerance. The results show potential for the proposed design but besides highlight some drawbacks, such as less uniform electric field distribution [39].

Anderlini L. et al. reports on the development, production, and characterization of innovative 3D diamond sensors achieving 30% improvement in both space and time resolution with respect to sensors from the previous generation (Fig. 2). This is the first complete characterization of the time resolution of 3D diamond sensors and combines results from tests with laser, β rays and high energy particle beams (Fig. 3) [40].

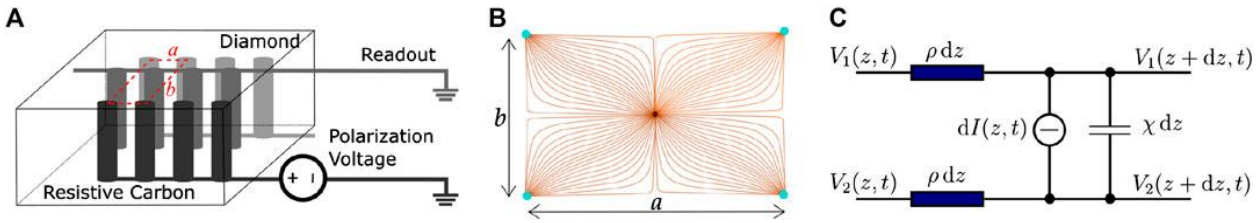

Fig.3. (A) schematic representation of the generic 3D a×b rectangular elementary cell. (B) projection of the cell on the transverse plane. (C) electrical model of a single cell [40].

G. W. Deptuch et al. discusses the vertically integrated photon imaging chip (VIPIC1) pixel detector (Fig. 4), a stack consisting of a 500-µm-thick silicon sensor, a two-tier 34-µm-thick integrated circuit, and a host printed circuit board (PCB) [41].

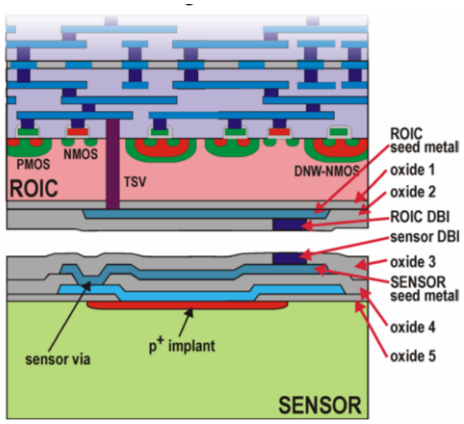

Fig. 4. A cross-section of the Ni-DBI bonding connection between the sensor diode and the pixel electronics of the VIPIC1 chip [41].

Liu, P. et al., introduces a new technique for luminosity measurement using 3D pixel modules. The technique has been tested using 2016 and 2017 ATLAS data at a collision energy of 13 TeV, and its integration into the comprehensive luminosity analysis is progressing well [42].

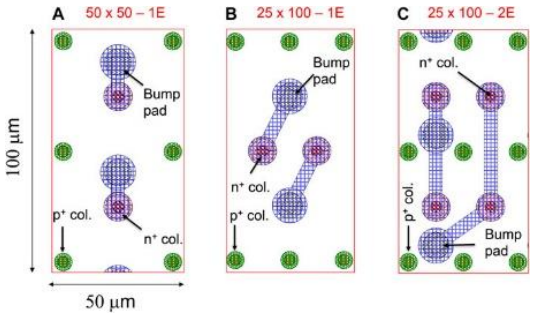

Fig. 5. 3D pixel layouts, showing pairs of adjacent pixels [43].

3D pixel detectors have shown some unexpected and notable outcomes in various applications. For instance, the fabrication yield improved by a design modification to an existing 3D-trenched pixel detector at [39]. Also, the 3D silicon sensor technology has been chosen to instrument the innermost pixel layer of the ATLAS Inner Tracker at CERN, which is the most exposed to radiation damage. This is due to its superior radiation hardness [43]. In addition, three foundries (CNM, FBK, and SINTEF) have developed and fabricated novel 3D pixel sensors to meet the specifications of the new ITk pixel detector for ATLAS Inner Tracker Upgrade (Fig. 5). These are produced in a single-side technology on either Silicon On Insulator (SOI) or Silicon on Silicon (Si-on-Si) bonded wafers by etching both n- and p-type columns from the same side [43]. Furthermore, different applications have benefited from advancements in 3D detector technologies. For instance, new micro-dosimeters that can measure the linear energy transfer (LET) of ionizing particles at cellular levels were developed recently (Fig. 6). At the same time, highly efficient neutron detectors with trenches or 3D detectors made in diamond were developed by several research groups around the world too [44-46].

The emerging technologies and future trends in 3D pixel detector radiation detection technology include advancements in detector materials, such as the development of novel semiconductor materials with improved radiation detection capabilities and reduced noise levels. Additionally, there is ongoing research in the optimization of readout electronics to enhance the sensitivity and precision of radiation detection. Furthermore, advancements in data acquisition systems are enabling higher data throughput and improved signal processing for more accurate and efficient radiation detection. These developments are driving the evolution of 3D pixel detector technology towards higher performance and broader applications in fields such as medical imaging, security screening, and scientific research (Fig. 7).

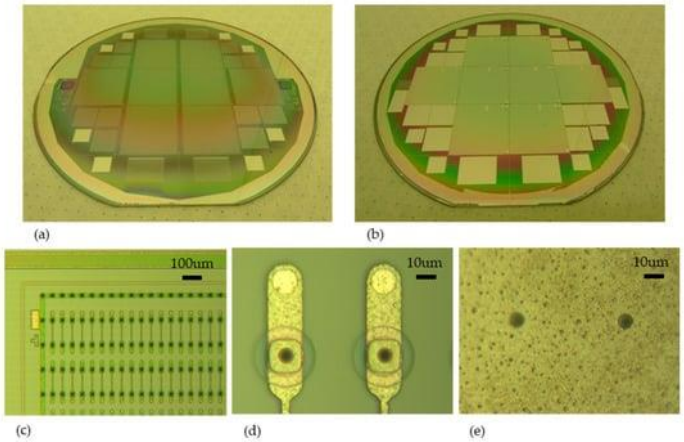

Fig. 6. Front side (**a**) and backside (**b**) photographs of IBL wafers. View of FE-I4 devices, front side (**c**,**d**) and backside (**e**) from ATLAS Forward Proton(AFP) production [44].

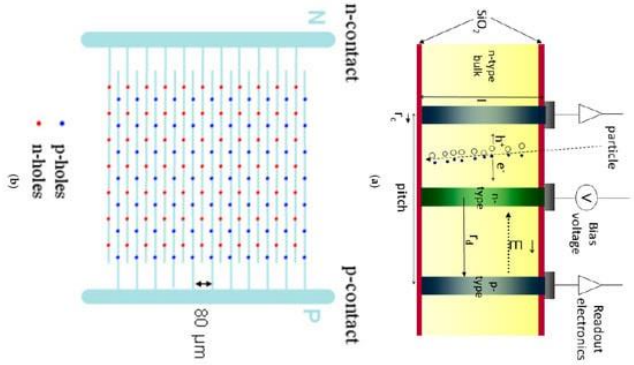

Fig. 7. Sketch of the cross-section (**a**) and frontside (**b**) of an ultra-thin 3D diode (U3DTHIN) [45].

Conclusion

In conclusion, the comparative performance analysis of 3D pixel detectors and commonly used radiation detectors in high energy physics and imaging demonstrates the potential advantages of 3D pixel detectors in terms of spatial resolution, radiation hardness, and efficiency. The results suggest that 3D pixel detectors show promise for improving the precision and quality of data acquisition in high energy physics and imaging applications. However, further research and development are needed to fully realize their potential and address any remaining challenges. Overall, this analysis contributes to the ongoing exploration of advanced detector technologies for enhancing scientific research and medical imaging.

References

[1] Usanase, N., Uzun, B., Ozsahin, D.U. et al. A look at radiation detectors and their applications in medical imaging. Jpn J Radiol 42, 145–157 (2024).

[2] Dalla Betta G-F, Ye J. Silicon Radiation Detector Technologies: From Planar to 3D. Chips. 2023; 2(2):83-101.
[3] Balibrea-Correa, J., Lerendegui-Marco, J., Babiano-Suárez, V., Caballero, L., Calvo, D., Ladarescu, I., Domingo-Pardo, C. (2021). Machine Learning aided 3D-position reconstruction in large LaCl3 crystals. Nuclear Instruments and Methods in Physics Research Section A: Accelerators, Spectrometers, Detectors and Associated Equipment, 1001, 165249.
[4] Lanza, R. C., Rideout, W., Fahey, F., & Zimmerman, R. E. (1987). Gas scintillators for imaging of low energy isotopes. IEEE Transactions on Nuclear Science, 34(1), 406-409.
[5] Datta, A., Fiala, J., Motakef, S. (2021). 2D perovskite-based high spatial resolution X-ray detectors. Scientific Reports, 11(1), 22897.
[6] Mele F, Quercia J, Abbene L, Benassi G, Bettelli M, Buttacavoli A, Principato F, Zappettini A, Bertuccio G. Advances in High-Energy-Resolution CdZnTe Linear Array Pixel Detectors with Fast and Low Noise Readout Electronics. Sensors. 2023; 23(4):2167.
[7] Wen Li, Yanfeng Du, B. D. Yanoff, J. S. Gordon, Energy resolution limiting factors of multi-pixel events in 3D position sensitive CZT gamma-ray spectrometer, 2008 IEEE Nuclear Science Symposium Conference Record, Dresden, Germany, 2008, pp. 496-502.
[8] Seiichi Yamamoto, Jun Kataoka, Kei Kamada, Akira Yoshikawa, Nuclear Instruments and Methods in Physics Research Section A: Accelerators, Spectrometers, Detectors and Associated Equipment, Volume 919, 1 March 2019, Pages 125-133, An ultrahigh spatial resolution radiation-imaging detector using 0.1 mm × 0.1 mm pixelated GAGG plate combined with 1 mm channel size Si-PM array
[9] Gu Y, Matteson JL, Skelton RT, Deal AC, Stephan EA, Duttweiler F, Gasaway TM, Levin CS. Study of a high-resolution, 3D positioning cadmium zinc telluride detector for PET. Phys Med Biol. 2011 Mar 21;56(6):1563-84. Epub 2011 Feb 18. PMID: 21335649; PMCID: PMC3274175.
[10] William R.Kaye, Energy and Position Reconstruction in Pixelated CdZnTe Detectors, Ph.D. thesis, 2012.
[11] Kino, K et al., Energy resolution of pulsed neutron beam provided by the ANNRI beamline at the J-PARC/MLF, Nuclear Instruments and Methods in Physics Research A, Volume 736, p. 66-74. 2014
[12] Yvan A. Boucher, Analysis of Cadmium Zinc Telluride Detector Performance and Characteristics for Applications in Gamma-Ray Imaging Spectrometers, Ph.D. thesis, 2013.
[13] J Jakůbek, Semiconductor Pixel detectors and their applications in life sciences, 2009, Journal of Instrumentation, Volume 4, 2009 JINST 4 P03013
[14] Jiawei Xia, Yuefeng Zhu, Zhong He, Efficient temperature corrections for gamma-ray energy reconstruction in 3-D position-sensitive CdZnTe detectors, Nuclear Instruments and Methods in Physics Research Section A: Accelerators, Spectrometers, Detectors and Associated Equipment, Volume 954, 21 February 2020, 161340
[15] Strüder L, Niculae A, Holl P, Soltau H. Development of the Silicon Drift Detector for Electron Microscopy Applications. Microscopy Today. 2020;28(5):46-53.

[16] Lechner, P., Eckbauer, S., Hartmann, R., Krisch, S., Hauff, D., Richter, R., ... & Sampietro, M. (1996). Silicon drift detectors for high resolution room temperature X-ray spectroscopy. Nuclear Instruments and Methods in Physics Research Section A: Accelerators, Spectrometers, Detectors and Associated Equipment, 377(2-3), 346-351.
[17] Roques, J. P., Teegarden, B. J., Lawrence, D. J., & Jourdain, E. (2023). The Use of Germanium Detectors in Space. In Handbook of X-ray and Gamma-ray Astrophysics (pp. 1-44). Singapore: Springer Nature Singapore.
[18] Lee, I. Y. , Deleplanque, M. A., Vetter, K., Developments in large gamma-ray detector arrays, Progress in Physics, Volume 66, Issue 7, pp. 1095-1144 (2003).
[19] Zeng, Z., Mi, YH., Zeng, M. et al. Characterization of a broad-energy germanium detector for its use in CJPL. NUCL SCI TECH 28, 7 (2017).
[20] F. Mele et al., High-energy-resolution CdZnTe linear array pixel detectors with fast and low noise readout electronics, 2023 IEEE Nuclear Science Symposium, Medical Imaging Conference and International Symposium on Room-Temperature Semiconductor Detectors (NSS MIC RTSD), Vancouver, BC, Canada, 2023, pp. 1-1.
[21] Wang, S., Guo, JH., Zhang, Y. et al. High-resolution pixelated CdZnTe detector prototype system for solar hard X-ray imager. NUCL SCI TECH 30, 42 (2019).
[22] Yu, M., Wen, L., Zhou, X. et al. A universal energy response model for determining the energy nonlinearity and resolution of epm and γ in liquid scintillator detectors. Eur. Phys. J. C 83, 403 (223).
[23] Robertson JG. Detector Sampling of Optical/IR Spectra: How Many Pixels per FWHM?, Publications of the Astronomical Society of Australia. 2017;34:e035.
[24] Edzards, F., Hauertmann, L., Abt, I., Gooch, C., Lehnert, B., Liu, X., Mertens, S., Radford, D.C., Schulz, O., Willers, M., Surface Characterization of P-Type Point Contact Germanium Detectors. Particles 2021, 4, 489-511.
[25] Oonuki, K., Inoue, H., Nakazawa, K., Mitani, T., Tanaka, T., Takahashi, T., Harrison, F. A. (2004). Development of uniform CdTe pixel detectors based on Caltech ASIC. In High-Energy Detectors in Astronomy, Vol. 5501, pp. 218-2281. SPIE.
[26] Dalla Betta G-F, Povoli M (2022) Progress in 3D Silicon Radiation Detectors. Front. Phys. 10:927690.
[27] Y. Dieter et al., Radiation tolerant, thin, passive CMOS sensors read out with the RD53A chip Panel, Nuclear Instruments and Methods in Physics Research Section A: Accelerators, Spectrometers, Detectors and Associated Equipment, Vol. 1015, 1 November 2021, 165771,
[28] van der Sar, S. J., Leibold, D., Brunner, S. E., & Schaart, D. R. (2022, October). LaBr3: Ce and silicon photomultipliers: towards the optimal scintillating photon-counting detector. In 7th International Conference on Image Formation in X-Ray Computed Tomography (Vol. 12304, pp. 55-60). SPIE.
[29] van der Sar, S. J., & Schaart, D. R. (2021). Silicon Photomultiplier-Based Scintillation Detectors for Photon-Counting X-Ray Imaging. In Radiation Detection Systems (pp. 289-312). CRC Press.

[30] Iida, H., Ogawa, K. Comparison of a pixelated semiconductor detector and a non-pixelated scintillation detector in pinhole SPECT system for small animal study. Ann Nucl Med 25, 143–150 (2011).
[31] D Ascenzo, N., Marrocchesi, P. S., Moon, C. S., Morsani, F., Ratti, L., Saveliev, V., Xie, Q. (2014). Silicon avalanche pixel sensor for high precision tracking. Journal of instrumentation, 9(03), C03027.
[32] Dalla Betta, G. F., Boscardin, M., Mendicino, R., Ronchin, S., Sultan, D. M. S., & Zorzi, N. (2015, October). Development of new 3D pixel sensors for phase 2 upgrades at LHC. In 2015 IEEE Nuclear Science Symposium and Medical Imaging Conference (NSS/MIC) (pp. 1-4). IEEE.
[33] Munker, M., Benoit, M., Dannheim, D., Fenigstein, A., Kugathasan, T., Leitner, T., ... & Snoeys, W. (2019). Simulations of CMOS pixel sensors with a small collection electrode, improved for a faster charge collection and increased radiation tolerance. Journal of Instrumentation, 14(05), C05013.
[34] Pernegger, H. (2015). The Pixel Detector of the ATLAS experiment for LHC Run-2. Journal of Instrumentation, 10(06), C06012.
[35] Mapelli, A., Catinaccio, A., Daguin, J., Van Lintel, H., Nuessle, G., Petagna, P., & Renaud, P. (2011). Low material budget microfabricated cooling devices for particle detectors and front-end electronics. Nuclear Physics B-Proceedings Supplements, 215(1), 349-352.
[36] Heggelund, A. L., & Atlas Collaboration. (2023). Overview of the ATLAS ITk pixel detector. Journal of Instrumentation, 18(02), C02014.
[37] M. Ruat, E. G. d'Aillon, L. Verger, 3D semiconductor radiation detectors for medical imaging: Simulation and design, 2008 IEEE Nuclear Science Symposium Conference Record, Dresden, Germany, 2008, pp. 434-439.
[38] Korotcenkov, G., Vatavu, S. (2023). Medical Applications of II-VI Semiconductor-Based Radiation Detectors. In: Korotcenkov, G. (eds) Handbook of II-VI Semiconductor-Based Sensors and Radiation Detectors. Springer, Cham.
[39] Boughedda A, Latreche S, Lakhdara M, Dalla Betta G-F (2022) A Modified 3D-Trench Pixel Detector: Proof of Concept by TCAD Simulations. Front. Phys. 10:957089.
[40] Anderlini L et al., (2020) Fabrication and Characterisation of 3D Diamond Pixel Detectors With Timing Capabilities. Front. Phys. 8:589844.
[41] G. W. Deptuch et al., Fully 3-D Integrated Pixel Detectors for X-Rays, in IEEE Transactions on Electron Devices, vol. 63, no. 1, pp. 205-214, Jan. 2016,
[42] Liu, P., ATLAS Collaboration. (2019). A new technique for luminosity measurement using 3D pixel modules in the ATLAS IBL detector. Nuclear Instruments and Methods in Physics Research Section A: Accelerators, Spectrometers, Detectors and Associated Equipment, 924, 275-278.
[43] Terzo S et al., (2021) Novel 3D Pixel Sensors for the Upgrade of the ATLAS Inner Tracker. Front. Phys. 9:624668.
[44] Quirion D, Manna M, Hidalgo S, Pellegrini G. Manufacturability and Stress Issues in 3D Silicon Detector Technology at IMB-CNM. Micromachines. 2020; 11(12):1126.

[45] Guardiola C, Fleta C, Quirion D, Pellegrini G, Gómez F. Silicon 3D Microdetectors for Microdosimetry in Hadron Therapy. Micromachines. 2020; 11(12):1053.
[46] Shi G, Zheng L, Wang W, Lu K. Non-Scanning Three-Dimensional Imaging System with a Single-Pixel Detector: Simulation and Experimental Study. Applied Sciences. 2020; 10(9):3100.
[47] Liu M, Zhou T, Li Z. Electrical Properties of Ultra-Fast 3D-Trench Electrode Silicon Detector. Micromachines. 2020; 11(7):674.

ICNST 2024
International Conference on Nuclear Science and Technology
6- 8 MAY 2024 | Isfahan, Iran

Measurement of Natural Radioactivity in Some Construction Stones of Neyriz City, with Evaluation of Radiation Dose (Paper ID: 1045)

Maryam Akhtari[1], Zahra Rakeb[1*], Sedigheh Sina[1,2], Reza Faghihi[1,2], F.N. Alizadeh[2]
[1] *Department of Nuclear Engineering, School of Mechanical Engineering, Shiraz University, Shiraz, Iran*
[2] *Radiation Research Center, Shiraz University, Iran*

Abstract

Natural radioactive materials are typically found in the water, air, and soil. In all building materials including concrete, brick, granite, and marble stones, etc., there are natural radionuclides from the K-40, and decay series of U-238, Th-232, and. Measurement of these radionuclides are important for human health and for radiation protection. This study aimed to determine the activity of thorium-232, potassium-40, cesium-137, and radium-226 radionuclides in six samples of granite, and marble stones obtained from Neyriz City, Fars Province.

Neyriz City in the Fars Province has many stone mines. For example, an active marble mine in this city extracts 2,500 tons per month, producing approximately 650–700 tons. The stones produced in this city are exported to most parts of Iran, and also other countries, such as China and India.

In the first step, the stone samples were grounded to obtain a completely uniform sample, they were placed in suitable Marinelli containers and then examined and analyzed using gamma spectroscopy. A high-purity germanium detector was used to measure radionuclides.

The maximum activities measured for Thorium-232, Potassium-40, and Radium-226 are 11.76, 1215.55, and 29.96 Bq/kg, respectively, which were measured in the granite stone sample no.3. For Cesium-137, no activity higher than the minimum detectable activity of the detection system was observed in any stone sample. The maximum effective dose rate absorbed in the air caused by natural radionuclides was calculated in one of the granite stones as 111 nGy/h.

Keywords: HPGe, Granite, Marble, Natural Radioactive, NORM, Gamma Spectroscopy

Introduction

Radioactivity is defined as the process of spontaneous decay and transformation of unstable nuclei into stable nuclei. Radioactive materials can be of natural or artificial origin [1]. Natural radionuclides include the decay chains of U-235, U-238, and Th-232, as well as K-40. Natural materials containing these nuclei are known by the NORM1 [2]. The concentration of natural radioactivity is important

[1] Naturally Occurring Radioactive Material

from the point of view of health physics [3]. Natural radionuclides are found in water, air, and soil, so it is obvious that they are present in all building materials such as concrete, brick, sand, stone, etc.

Marble is a metamorphic stone mainly composed of calcite and other minerals. Any limestone with a polishable surface is called marble and is mostly used as a wall and floor covering in houses. Because this stone is generally composed of sediments, it may contain some amount of radioactive material. Granite is a hard igneous stone that usually has a medium to coarse grain. Granites are suitable as construction and decorative materials for internal and external use [4].

Granite and marble are widely used as building materials in Iran and the world. Due to the presence of natural radionuclides in them, it is important to determine the activity concentration of these substances and to determine the radiation exposure of people. In the field of determining natural radioactivity, many investigations have been conducted in Iran, including in Golestan province, Fars province, the fields of the Parsian operational area, around Tehran city, Arak, Hoviezeh, Kerman, and Ramsar [5-12].

Similar investigations have been conducted in other countries of the world, including the Netherlands, Bangladesh, Ireland, Iraq, and Qatar, to determine the natural activity in soil or building materials [13-17]. There are three natural radioactive chains in nature, which are Uranium-235, Uranium-238, and Thorium-232[18]. Radon gas which is produced in natural decay chains, is the most important cause of internal exposure to people. Internal exposure to alpha particles occurs through inhalation of radon gas. Radium-226 is present in all rocks and soils in varying amounts. the activity of 226Ra in natural samples is determined by measuring the γ ray emitted from its progeny, like 214Bi, and 214Pb, provided that the 226Ra- 222Rn secular equilibrium has been established [19].

The purpose of this research was to determine the amount of natural, and artificial radioactivity of marble and granite stones used in Neyriz city of Fars province and also to evaluate the dose of people in the houses where these stones were used for their construction.

Research Theories

Gamma Spectroscopy:

The stone samples were prepared from Neyriz city, which included three samples of marble and three samples of granite. The collected samples were crushed and dried to remove moisture and passed

through a mesh of a specific size and homogenized. Each sample was weighted and transferred to a clean and dry Marinelli container. Then they were sealed and kept for 8 weeks to reach equilibrium. Efficiency calibration was done by using a reference material, provided by the International Atomic Energy Agency, i.e. RGTh. The background measurement was performed for 327,600 seconds in the absence of any radiation source using an HPGe detector.

The activity of six samples after reaching the secular equilibrium was measured using an HPGe gamma-ray spectroscopy system. The activity value of Ra-226 was calculated from the peaks of Pb-214 and Bi-214. The activity of K-40 was obtained from the peak with the energy of 1461 keV of this radionuclide, and the peaks of Pb-212, Ac-228, and Tl-208 were used to calculate the activity of the Th-232 chain.

Dosimetry quantities:

Quantities to evaluate the amount of natural radiation of building materials:

Radium equivalent activity

It is useful to obtain the radiological risk of the building materials, which is obtained from Eq. 1.

$$Ra_{eq}(\frac{Bq}{kg}) = (A_{Th} * 1.43) + A_{Ra} + (A_k * 0.77) \quad \text{Eq. 1}$$

In this equation, ATh is the specific activity of thorium-232, ARa is the specific activity of radium-226, and AK is the specific activity of potassium-40. The amount of activity equivalent to radium for the samples should be less than 370 Bq/kg [20-22].

Effective absorbed dose rate

The effective absorbed dose rate from natural gamma radiation in the air at a distance of one meter from the ground surface is calculated using Eq. 2.

$$\dot{D}\left(\frac{nGy}{h}\right) = 0.462C_U + 0.604C_{Th} + 0.0417C_K \quad \text{Eq. 2}$$

where the C coefficients of the activity of each substance are in terms of Bq/kg, the permissible limit of this coefficient is 80 nGy/h [23, 24].

Annual effective dose

After calculating the dose using Eq. 2, the annual effective dose can be obtained using Eq. 3.

$$\text{AED}\left(\frac{msv}{y}\right) = \dot{D}\left(\frac{nGy}{h}\right) * 8760\left(\frac{h}{y}\right) * 0.7 * 0.8 * 10^{-6} \quad \text{Eq. 3}$$

That the conversion factor of absorbed dose in the air to effective dose is 0.7 and the occupation factor indoor is 0.8. The amount of AED should be less than 1 millisievert per year [23-25].

Gamma activity concentration index

This index related to the annual dose is due to gamma radiation caused by surface material, whose value should be less than 6 for surface materials such as tiles and less than 1 for bulk materials. This index is obtained using Eq. 4 [26, 27].

$$I_\gamma = \frac{A_{Ra}}{150} + \frac{A_{Th}}{100} + \frac{A_K}{1500} \quad \text{Eq. 4}$$

Internal hazard index

The amount of internal exposure of radon and its daughters is quantified with this coefficient shown in Eq.5. For safe use of material in the building, this quantity should be less than one [28,29].

$$H_{int} = \frac{A_{Ra}}{185} + \frac{A_{Th}}{259} + \frac{A_K}{4810} \quad \text{Eq. 5}$$

External hazard index

The external hazard index can be determined by Eq. 6. If this index is less than one, the risk of natural external exposure will be negligible [28,29].

$$H_{ext} = \frac{A_{Ra}}{370} + \frac{A_{Th}}{259} + \frac{A_K}{4810} \quad \text{Eq. 6}$$

In this section, the summary of the theoretical basis should be given, if any. Here, you can cite handbooks or classical papers in the field, and use equations, if necessary. Do not use equations that are common knowledge.

RESULTS AND DISCUSSION

Based on the results, the MDA values for Th-232, Ra-226, and K-40 were found to be obtained 0.9692, 1.2529, and 1.2056 Bq/kg respectively. The types of detected natural radioactive nuclei and their activity levels are shown in Table 1.

Table 1. Detected natural radioactive nuclei in each sample and their specific activity

Sample	K-40 (Bq/kg)	Th-232 (Bq/kg)	Ra-226 (Bq/kg)
Marble no.1	5.45±2/33	*[2]	20.42±4.52
Marble no.2	7.26±2.69	*	17.48±4.18
Marble	4.4±2.09	*	19.98±4.47

[2]The values marked with * mean that the activity value is less than the minimum detectable activity value.

no.3			
Granite no.1	2.81±1.67	*	*
Granite no.2	7.5±2.74	*	2.71±1.65
Granite no.3	1215.55±34.86	76.11±8.72	29.96±5.47

The highest specific activity of Ra-226 was observed in granite sample no.3 with value of 29.96±5.47 Bq/kg. While in granite sample no.1, the amount of this radionuclide was lower than the minimum detectable activity amount. The activity of the thorium-232 chain in most of the samples was lower than the MDA value, except granite sample no.3. In granite sample no.3, the amount of potassium-40 was significantly high and its value was measured as 1215.55±34.86 Bq/kg, while in other samples it was almost in the average value of 5.5 Bq/kg.

The quantities used to determine the radiation risk and calculate the dose of people due to the natural radiation of building materials are calculated for each sample and listed in Table 2.

Table 2. Evaluated quantities of natural radiation of building materials and their risk

Sample	$Ra_{eq}(\frac{Bq}{kg})$	$\dot{D}(\frac{nGy}{h})$	$AED\left(\frac{msv}{y}\right)$	I_γ	H_{int}	H_{ext}
Marble no.1	24.617 ±4.86	9.661 ±2.07	0.047 ±0.01	0.140 ±0.03	0.112 ±0.02	0.056 ±0.01
Marble no.2	23.070 ±4.66	8.379 ±1.92	0.041 ±0.01	0.121 ±0.03	0.096 ±0.02	0.049 ±0.01
Marble no.3	23.368 ±4.75	9.414 ±2.05	0.046 ±0.01	0.136 ±0.03	0.109 ±0.02	0.055 ±0.01
Granite no.1	2.164 ±1.28	0.117 ±0.07	0.001 ±0.003	0.002 ±0.001	0.001 ±0.003	0.001 ±0.003
Granite no.2	8.485 ±2.67	1.565 ±0.76	0.008 ±0.003	0.023 ±0.01	0.016 ±0.009	0.009 ±0.004
Granite no.3	1074.771 ±127.57	110.500 ±5.98	0.542 ±0.03	1.771 ±0.09	0.709 ±0.04	0.628 ±0.04

In most cases, all parameters are below the limiting levels, except for granite no.3. Although in this sample, the equivalent activity of radium and effective absorbed dose rate are higher than the permissible limit, the annual effective dose rate is lower than the permissible limit for ordinary people. In addition, the Hint and Hext indexes are lower than the limited level for this sample. For granite no.3 the gamma activity concentration index is less than the limited level for surface materials like tiles but this index is higher than the limited level for bulk material. The lowest measured parameters belong to granite sample no.1, all of which are less than limited levels. All parameters for marble stones are almost equal and their variation is negligible.

Conclusions

In this research, the radionuclides present in 6 samples of marble and granite stones used in Neyriz city of Fars province were identified using gamma spectroscopy using HPGe semiconductor detector, and their activities were determined. The maximum activity of Ra-226, Th-232, and K-40 was observed in granite sample number 3, and their values were 29.96±5.47, 76.11±8.72, and 1215.55±34.86 Bq/kg, respectively. Except for one granite sample, the activity of the thorium-232 chain was lower than the MDA value. Also, the activity value of radium-226 in granite sample no. 1 was lower than this value. Values higher than MDA for cesium-137 were not observed in any sample. To check the amount of natural radiation of building materials and determine the amount of risk caused by them, it is recommended to calculate parameters such as radium equivalent activity, annual effective dose rate, gamma activity concentration index, internal hazard index, and external hazard index. Criteria and permissible limits are defined for each of the parameters. These parameters were calculated for each sample of marble and granite, and most of the samples were within the allowed range in terms of the amount of natural radioactivity. Although granite sample no.3 had an activity equivalent to radium exceeding the permissible limit, could be used as a building material due to the annual dose limit being lower than the permissible limit recommended by ICRP-60 for ordinary people. Based on the gamma activity concentration index, granite sample 3 should be used as tiles for the building. It is noticeable, that the granite sample no.3 measurement was repeated due to the significant high natural activity and confidence in the results, and the same results were obtained again. It is suggested that dosimetry be done for the workers and workplace of this stone’s mine to ensure the workers' safety and prevent occupational exposure exceeding the permissible limit.

Acknowledgements

We are grateful to the Radiation Research Center of Shiraz University and the personnel.

References

[1] Friedlander, G., Kennedy, J. W., Macias, E. S., & Miller, J. M. (1981). Nuclear and radiochemistry. John Wiley & Sons.

[2] Gilmore, G. (2008). Practical gamma-ray spectroscopy. John Wiley & Sons

[3] Cember, H. (2009). Introduction to health physics.

[4] Mohamed, R. I., Algamdi, S. K., & Al-Shamani, N. S. (2016). Evaluation of radionuclide concentrations and associated radiological hazard in marble indices and granite used as building materials in Al-Madinah Al-Munawarah. Journal of Taibah University for Science, 10(3), 369-374.

[5] H. Bazrafshan (2018). Determining the radiation concentration of building materials using gamma ray spectroscopy. Golestan University.

[6] R. Faghihi, S. Mehdizadeh, and S. Sina, "Natural and artificial radioactivity distribution In soil of fars province, Iran," Radiat. Prot. Dosimetry, vol. 145, no. 1, pp. 66–74, 2011, doi: 10.1093/rpd/ncq367.

[7] M. J. Shahgolh (2018). Determining the concentration of natural radioactive substances in drilling mud and measuring the dose of workers in Parsian operational area. Shiraz University.

[8] S. Hafezi, J. Amidi, and A. Attarilar, "Concentration of natural radionuclides in soil and assessment of external exposure to the public in Tehran," Iran. J. Radiat. Res., vol. 3, no. 2, pp. 85–88, 2005.

[9] R. Pour Imani, V. Heidari (2017). Investigating environmental radiation in construction materials used in Arak city. Journal of Environmental science and technology, no.3.

[10] R. Pour Imani, S. M. Mortazavi Shahroodi (2019). Investigating environmental radioactivity in the border soils of Hoveyze region. Journal of Environmental science and technology, no.3.

[11] M. Malakotian, M. Sadeghi, A. Nasiri (2014). Investigation of gamma rays in building stones in Kerman city. Scientific Research Journal of Yazd School of Health, pp. 13-21.

[12] E. BavarNegin (2010). Investigating the inventory of radioactive materials and the rate of radon gas emission in construction materials of Ramsar region. Gilan University.

[13] P. De Jong, "Exposure to natural radioactivity in the Netherlands," University of Groningen, 2010.

[14] M. A. Khatun, J. Ferdous, and M. M. Haque, “Natural Radioactivity Measurement and Assessment of Radiological Hazards in Some Building Materials Used in Bangladesh,” J. Environ. Prot. (Irvine,. Calif)., vol. 09, no. 10, pp. 1034–1048, 2018, doi: 10.4236/jep.2018.910064.

[15] E. M. Doorly, “Radioactivity from Building Materials in the Republic of Ireland,” University o f Dublin, 2006.

[16] A. T. Al-bayati, “Determination of the Concentrations for Radioactive Elements Around Al Tuwaitha Center Using Gamma-Ray Spectroscopy and CR-39 Detectors,” University of Baghdad, 2011.

[17] H. A. Al-Sulaiti, “Determination of Natural Radioactivity Levels in the State of Qatar Using High Resolution Gamma-ray Spectrometry,” University of Surrey, 2011.

[18] L. Kölbel, T. Kölbel, U. Maier, M. Sauter, T. Schäfer, and B. Wiegand, “Water–rock interactions in the Bruchsal geothermal system by U–Th series radionuclides,” Geotherm Energy, no. 8, 2020.

[19] Papadopoulos, A., Christofides, G., Koroneos, A., Stoulos, S., & Papastefanou, C. (2013). Radioactive secular equilibrium in 238U and 232Th series in granitoids from Greece. Applied Radiation and Isotopes, 75, 95-104.

[20] Tufail, M. Radium equivalent activity in the light of UNSCEAR report. Environ Monit Assess 184, 5663–5667 (2012). https://doi.org/10.1007/s10661-011-2370-6

[21] Adewoyin, O. O., Omeje, M., Omonhinmin, C., Nwinyi, O., Arijaje, T., & Ayanbisi, O. (2023). Assessment of Radium Equivalent Activity and Total Annual Effective Dose in Cassava cultivated around Ewekoro Cement Factory. Journal of Food Protection, 86(11), 100160.

[22] ICRP, 1991. 1990 Recommendations of the International Commission on Radiological Protection. ICRP Publication 60. Ann. ICRP 21 (1-3).

[23] Papadopoulos, A., Christofides, G., Papastefanou, C., Koroneos, A., & Stoulos, S. (2010). RADIOACTIVITY OF GRANITIC ROCKS FROM NORTHERN GREECE. Bulletin of the Geological Society of Greece, 43(5), 2680-2691.

[24] European Commission, Directorate-General for Environment, Radiological protection principles concerning the natural radioactivity of building materials, Publications Office, 2000.

[25] Charles, M. (2001). UNSCEAR Report 2000: sources and effects of ionizing radiation.

[26] Caño, A., Suárez-Navarro, J. A., Puertas, F., Fernández-Jiménez, A., & Alonso, M. D. M. (2023). New Approach to Determine the Activity Concentration Index in Cements, Fly Ashes, and Slags on

the Basis of Their Chemical Composition. Materials (Basel, Switzerland), 16(7), 2677. https://doi.org/10.3390/ma16072677

[27] Elnobi, Sahar & Harb, Shaban & Khalifa, Nour. (2017). Influence of grain size on radionuclide activity concentrations and Radiological hazard of building material samples. Applied Radiation and Isotopes. 130. 10.1016/j.apradiso.2017.09.021.

[28] A. Sroor & N. Dawood (2011): Evaluation of radiation level and radon exhalation rate of rock samples from Mahd Ad Dahab mine in Saudi Arabia, Radiation Effects and Defects in Solids: Incorporating Plasma Science and Plasma Technology, 166:4, 305-312

[29] Beretka, J., & Matthew, P. J. (1985). Natural radioactivity of Australian building materials, industrial wastes and by-products. Health physics, 48(1), 87–95. https://doi.org/10.1097/00004032-198501000-00007

ICNST 2024
International Conference on Nuclear Science and Technology
6- 8 MAY 2024 | Isfahan, Iran

Comparison of Absorbed Dose Calculation Methods in Adult Female Patients Undergoing Nuclear Medicine Procedures with 99m-Tc Radiopharmaceuticals: Monte Carlo vs. MIRD (Paper ID: 1059)

Ahad Ollah Ezzati[1], Farzane Mohajeri[1*]
[1] Department of Physics, University of Tabriz, 29 Bahman Blvd, Tabriz, Iran.

Abstract

Accurate dosimetry calculations are essential in nuclear medicine for optimizing patient care and safety. This study compares dosimetry calculations using the Monte Carlo (MC) method and the Medical Internal Radiation Dosimetry (MIRD) method for three radiopharmaceuticals administered to an adult female patient undergoing SPECT imaging. The absorbed doses in various organs were evaluated, with the MC method showing higher absorbed doses in the kidneys and liver, while the MIRD method predicted higher absorbed doses in the thymus, liver, and kidneys. The differences in dose estimations between MC and MIRD methods were 11.57% and 1.70% for the 99mTc-HMPAO and 99mTc-DMSA, respectively. The effective doses calculated by the MC method were 13.68mSv and 5.27mSv, while the MIRD method yielded slightly different results with effective doses of 15.47mSv and 5.18mSv. The study concludes that MC calculations provide a more accurate representation of absorbed doses compared to the MIRD method, emphasizing the importance of accurate dosimetry in nuclear medicine. The MC method outperforms the MIRD method in predicting absorbed doses, making it a valuable tool for optimizing radiation therapies and improving patient outcomes.

Keywords: Absorbed Dose, SPECT imaging, 99mTc-HMPAO, 99mTc-DMSA, MIRD method, Monte Carlo simulation.

Introduction

Nuclear medicine is crucial for improving healthcare, particularly in cancer treatment. Tomographic methods are used to determine activity distribution, and as new radiopharmaceuticals are introduced, the importance of nuclear medicine will continue to grow. Internal dosimetry calculates absorbed dose distribution within tissues, with SPECT images providing precise three-dimensional distributions. Biodistribution and imaging techniques are essential for absorbed dose calculations, which must be assessed individually for each patient due to patient-specific parameters[1]. The Medical Internal Radiation Dosimetry (MIRD) committee standardized methods for absorbed dose calculations, but

alternative methods are needed for diagnostic and therapeutic applications[2,3]. The Monte Carlo (MC) method involves computationally intensive calculations, while simpler calculations are used in MIRD methods. Studies have evaluated dosimetry for different radiopharmaceuticals, such as 111In and 90Y, and 18F-FDG for PET imaging, showing differences in calculated doses between MC and MIRD methods. Voxel-based dosimetry methods have been utilized to enhance therapeutic efficacy, and studies have compared different methods for estimating internal doses with promising results.

Flux et al. evaluated the patient's dosimetry for the administered activity of 185 MBq of 111In on day zero, and 7.4–15 MBq/kg of 90Y on day 7. The study found that 90Y remained in the blood and target organs longer than 111In. The red marrow absorbed a median dose of 0.97 Gy for 90Y, and there was no correlation between hematological toxicity and the absorbed dose in the red marrow[1]. Ezzati et al. calculated the dose factors of 18F-FDG for patients undergoing PET imaging, revealing variations in calculated doses between MC and MIRD for different organs[4].

Kim et al. utilized personalized voxel-based dosimetry employing S-value techniques to assess the efficacy of 177Lu-DOTATATE therapy. They compared the accuracy of single- and multiple-voxel S-value methods through MC simulations, and validated the latter using a single-photon emission computed tomography dataset. The precision of the methods increased with the utilization of more dose kernels. The findings revealed that single voxel S-values and 20 voxel S-values exhibited average dose estimation errors of less than 6%, while organ-based dosimetry using OLINDA/EXM had errors of up to 123%. This suggests that voxel-based dosimetry techniques have the potential to enhance the therapeutic outcomes of 177Lu-DOTATATE and facilitate the investigation of tumor dose responses [5].

Accurate dosimetry calculations are crucial for therapeutic effectiveness and reducing radiation exposure, with the S-value and MC methods being commonly used techniques. This study aims to compare the accuracy of the MC and MIRD methods for absorbed dose calculations of specific radiopharmaceuticals in an adult female patient after SPECT imaging, with the goal of improving patient care and radiation safety in nuclear medicine practices.

Research Theories

Monte Carlo Method:

The MCNPX 2.7 code used MC simulation as a dosimetry method to accurately assess absorbed dose distribution by considering radionuclide and tissue density distributions. The study involved a female MIRD phantom undergoing SPECT imaging with 99mTc-HMPAO and 99mTc-DMSA radiopharmaceuticals. The administered activity for each radiopharmaceutical in SPECT imaging was 740 MBq for 99mTc-HMPAO and 185 MBq for 99mTc-DMSA[6-8]. Biokinetic data from ICRP publications were utilized for calculating absorbed doses[9]. The table1 below shows the cumulative distribution of radiopharmaceutical activity for each SPECT imaging. The biokinetic model estimated the distribution and metabolism of each radiopharmaceutical in the body. Each simulation considered 500 million particle histories, and the maximum uncertainty was below 1%.

Table 1. Activity distribution data for 99mTc-HMPAO, and 99mTc-DMSA.

Radiopharmaceutical	**Activity receives**	**Organs**	$\widetilde{A_s}/A_0$ (h) [9]
99mTc-HMPAO	740 MBq	Brain Thyroid Lung Stomach wall Small intestine wall Upper large intestine wall Lower large intestine wall Small intestine contents Upper large intestine Lower large intestine Kidneys Urinary bladder Red marrow Other organs	0.41 0.043 0.71 0.047 0.20 0.065 0.050 0.24 0.32 0.16 0.62 0.46 0.51 3.0
99mTc-DMSA	185 MBq	Kidneys Urinary bladder Liver Spleen Total body (excluding urinary bladder contents)	3.7 0.42 0.40 0.040 6.8

The cumulative activity was determined using Equation 1, where $A(u)$ represents the activity in the source organ at time u.

$$\tilde{A} = \int_0^{\infty} A(u)\, du \qquad (1)$$

The activity distribution of the patient following 99mTc-DMSA injection was obtained using a kidney-bladder biokinetic model. To quantify the cumulative activity in the urinary bladder during the first bladder filling T_V, Equation 2 was used. Calculating the absorbed dose in the bladder is more complex than in a static organ. The ICRP recommends a urinary voiding interval of 3.5 hours for adults. Equation 2 takes into account various factors such as biological constant λ_i, radioactive decay constant λ_p, fraction of excreted activity eliminated through the kidneys f_r, and fraction of administered activity a_i with component i.

$$\tilde{A}_{UB} = f_r \sum_{i=1}^{N} a_i \left(\frac{1-e^{-\lambda_p T_V}}{\lambda_p} - \frac{1-e^{-(\lambda_i+\lambda_p)T_V}}{\lambda_i+\lambda_p}\right)\frac{1}{1-e^{-(\lambda_i+\lambda_p)T_V}} \qquad (2)$$

To calculate the cumulated activity of 99mTc-HMPAO, the gastrointestinal tract, biliary excretion, and liver biokinetics model were applied [9]. It was assumed that the patient did not ingest any activity, and the radiopharmaceutical entered the small intestine via the liver and gallbladder. Equation 3 describes the activity in other organs during radiopharmaceuticals' decline or buildup.

$$\frac{\widetilde{A_S}(t)}{A_0} = F_s \sum_{j=n+1}^{n+m} a_j \sum_{i=1}^{n} \left\{ a_i \frac{T_i}{T_i - T_j}\left[\exp\left(\frac{-ln(2)}{T_{i.eff}}t\right) - \exp\left(\frac{-ln(2)}{T_{j.eff}}t\right)\right]\right\} \qquad (3)$$

Assuming that the total accumulated activity is $\tilde{A}$ (MBq) and the dose for a unit of administered activity is E(MeV/g), the absorbed dose (Gy) in the organs mentioned above was calculated using Equation 4, which can be represented as:

$$\dot{D}_0 = \tilde{A}\, E\left(\frac{MeV}{gs}\right) \times 1.6 \times 10^{-13} \frac{J}{MeV} \times 10^3 \frac{g}{kg} = 1.6 \times 10^{-10} \times \tilde{A}\, E\left(\frac{J}{kg \cdot s}\right) \qquad (4)$$

The whole-body effective dose for the patient is calculated using Equation 5, where W_T represents the tissue weighting factor and H_T represents the equivalent dose to the tissue.

$$H_E = \sum W_T\, H_T \qquad (5)$$

MIRD Method:

In the MIRD method, Equation 6 is used to calculate the dose to an organ that is exposed to radiation from both the activity and surrounding organs:

$$D = \widetilde{A_s}\, S \qquad (6)$$

Here, $\widetilde{A_s}$ represents the cumulative activity, and S is the absorbed dose per unit cumulated activity (S-value). The S-value is determined by the sum of ΔΦ for each organ, as shown in Equation 7:

$$S = \sum \Delta\Phi \qquad (7)$$

The calculation of S involves the summation of y_i, E_i, and $\Phi_i(r_T \leftarrow r_S)$, as given in Equation 8 [10]:

$$S = \sum_i y_i\, E_i\, \Phi_i(r_T \leftarrow r_S) \qquad (8)$$

The Specific Absorbed Fraction (SAF), denoted by $\sum \Delta\Phi$, and the yield y_i (measured in unit $(\frac{1}{Bq \cdot s})$) are presented in reference data using the MIRD formalism. Finally, the dose $D(Gy)$ for several source regions is calculated using Equation 9 [11]:

$$D(Gy) = \sum_S \widetilde{A_s}\,(r_S) \cdot S(r_T \leftarrow r_S) \qquad (9)$$

Each source organ is calculated separately.

Results and Discussion

Monte Carlo Method:

Table 2 displays the absorbed doses of various organs in a patient who has received injections of radioisotopes: 99mTc-HMPAO and 99mTc-DMSA. The doses were determined through MC simulation, indicating that specific organs absorbed higher doses.

Table 2. Absorbed doses (Gy) of patient organs after injection of 99mTc-HMPAO, and 99mTc-DMSA (MC results).

Organs	Absorbed dose (Gy)	
	99mTc-DMSA	**99mTc-HMPAO**
Trunk	1.13E-03	2.88E-03
Head	2.07E-04	5.55E-04
Adrenals	3.46E-03	8.25E-03
Uterus	8.10E-04	4.31E-03
Thymus	4.75E-04	8.66E-04
Spleen	3.12E-03	7.32E-03
Pancreas	2.65E-03	6.08E-03
Kidney	1.99E-02	4.88E-02
Heart	8.11E-04	1.57E-03
Gall bladder	2.18E-03	5.03E-03
Stomach	1.54E-03	3.44E-03
Lung	7.81E-04	1.52E-03
Colon	1.13E-03	3.03E-03
Small intestine	1.43E-03	3.57E-03
Breasts	3.59E-04	6.69E-04
Ovaries	8.22E-04	2.78E-03

Urinary bladder	5.72E-04	1.74E-02
Oesophagus	1.07E-03	2.23E-03
Liver	1.67E-03	3.75E-03
Thyroid	4.62E-04	8.28E-04
Body skin	2.75E-04	6.33E-04
Brain	3.34E-04	3.60E-03
Salivary glands	5.64E-04	1.28E-03
Upper arm bone	6.67E-04	1.29E-03
Lower arm	4.64E-04	1.01E-03
Spine	2.58E-03	5.97E-03
Skull-cranium and Facial skeleton	3.66E-04	2.19E-03
Pelvis, Clavicles and Scapulae	1.18E-03	3.21E-03
Legs up	3.09E-04	5.84E-04
Legs down	1.79E-04	2.87E-04
Rib cage	8.95E-04	1.87E-03
Leg bone up	6.30E-04	1.20E-03
Leg bone down	4.22E-04	6.73E-04

MIRD Method:

Table 3 shows the results from the MIRD method used to calculate absorbed doses in various organs. The MIRD method is a standard way to estimate radiation doses in the human body. The study found that the kidneys, spleen, and adrenal glands had the highest doses of 99mTc-DMSA, and the kidneys, urinary bladder, and gall bladder had the highest absorbed doses of 99mTc-HMPAO.

Table 3. MIRD-calculated organ absorbed doses (Gy) for two gamma decay energies of 99mTc-HMPAO, and 99mTc-DMSA (MIRD results).

Organs		
	99mTc-DMSA	**99mTc-HMPAO**
trunk/muscle	9.82E-04	3.97E-03
adrenals	3.01E-03	6.72E-03
uterus	1.56E-03	7.67E-03
thymus	8.11E-04	4.16E-03
spleen	2.89E-03	5.61E-03
pancreas	2.50E-03	6.73E-03
kidney	1.38E-02	1.32E-02
heart	1.16E-03	5.37E-03
gall bladder	2.34E-03	1.06E-02
stomach	1.61E-03	5.15E-03
lungs	1.01E-03	5.85E-03
large intestine, colon	1.62E-03	9.01E-03
small intestine	1.63E-03	7.53E-03
breasts	5.55E-04	5.04E-03
ovaries	1.36E-03	7.38E-03

urinary bladder & contents	2.42E-03	1.15E-02
liver	2.12E-03	7.47E-03
thyroid	7.57E-04	7.45E-03
skin	5.06E-04	2.12E-03
brain	5.56E-04	5.06E-03
LLI Wall	1.26E-03	7.42E-03
Total Body	1.10E-03	4.36E-03
Red Marrow	1.25E-03	4.64E-03
Bone Surfaces	1.96E-03	8.26E-03

Table 4 compares the effective dose differences between MC simulation and MIRD methods, highlighting the importance of accurate dose calculation methods. It also emphasizes the significance of reliable methods for calculating absorbed doses in the diagnosis and treatment of diseases.

Table 4. The MC and MIRD methods were used to calculate the effective doses of 99mTc-HMPAO, and 99mTc-DMSA.

Calculation method	**Effective dose (mSv)**	
	99mTc-DMSA	**99mTc-HMPAO**
MC	5.27	13.68
MIRD	5.18	15.47
Difference	1.70%	11.57%

Table 4 presents the effective doses calculated using the MC and MIRD methods for 99mTc-HMPAO and 99mTc-DMSA. The MC method yielded effective doses of 13.68 and 5.27, while the MIRD method yielded 15.47 and 5.18 for the same radiopharmaceuticals. The differences in calculated absorbed effective doses for 99mTc-HMPAO and 99mTc-DMSA were 11.57% and 1.70%, respectively. These findings emphasize the importance of selecting the appropriate method for accurate dose calculations in nuclear medicine. Dosimetry results may vary between the MC and MIRD methods due to factors such as the MC method's consideration of tissue heterogeneity, organ geometry, and radiation interactions, in contrast to the simplified mathematical models and assumptions used in the MIRD method. The accuracy of input data, computational algorithms, and energy deposition models can also impact dosimetry results. MC simulations provide more accurate energy deposition models compared to MIRD methods, but the complexity of calculations in the MC method can lead to differences in dosimetry results. Both methods have their own advantages and limitations, and the choice depends on specific application requirements, available resources, and desired accuracy.

The study evaluated the absorbed dose of 99mTc-DMSA and 99mTc-HMPAO using the S-value and MC methods, comparing the percentage difference between the two methods. The use of MC in dosimetry calculations is prioritized due to its higher accuracy, despite the differences in dose estimation. Effective doses calculated using both methods still showed good agreement, as most of the deposited doses were caused by self-irradiation.

Previous studies by Ezzati et al. used MIRD and MC techniques to calculate absorbed doses in patients undergoing diagnostic PET scans using 18F-FDG. The MC method was more accurate in calculating doses compared to the MIRD method, with calculated doses being 13.02% and 11.19% lower than the MC method for EC due to the significant effects of urinary bladder emptying on other organs.

The MCNP simulation was used to generate accurate dosimetry data and determine the best approach for accessing radiation. The simulation results were found to be acceptable in comparison to the measurements in the phantom study, emphasizing the importance of advanced dosimetry methods for accurately estimating absorbed doses and optimizing radiation access.

Conclusion

We accurately calculated internal absorbed doses in adult female patients using MC and MIRD methods for 99mTc-HMPAO and 99mTc-DMSA administration. Our findings showed that the kidney received the highest dose in patients injected with these radiotracers. We also calculated effective doses using both methods. Our study provides important insights into the potential risks of these diagnostic procedures, helping healthcare professionals make more informed decisions for patient care.

References

[1] Flux G, Bardies M, Monsieurs M, Savolainen S, Strand S-E, Lassmann M. The impact of PET and SPECT on dosimetry for targeted radionuclide therapy. Zeitschrift für medizinische Physik. 2006;16(1):47-59.

[2] Guo L. The applications of SPECT in internal dosimetry. Foreign Medical Sciences Section of Radiation Medicine and Nuclear Medicine. 2004;28(2):67-70.

[3] Fisher DR. Perspectives on Internal Dosimetry for Optimized Radionuclide Therapy. Cancer Biotherapy & Radiopharmaceuticals. 2022;37(3):161-3.

[4] Ezzati AO, Mohajeri F. Absorbed dose of 18F-FDG for female patients: Monte Carlo versus MIRD method. The European Physical Journal Plus. 2023;138(1):27.

[5] Kim KM, Lee MS, Suh MS, Selvam HSMS, Tan TH, Cheon GJ, et al. Comparison of voxel S-value methods for personalized voxel-based dosimetry of 177Lu-DOTATATE. Medical Physics. 2022;49(3):1888-901.

[6] De Sadeleer C, Bossuyt A, Goes E, Piepsz A. Renal technetium-99m-DMSA SPECT in normal volunteers. Journal of Nuclear Medicine. 1996;37(8):1346-9.

[7] Juni JE, Waxman AD, Devous MD, Tikofsky RS, Ichise M, Van Heertum RL, et al. Procedure guideline for brain perfusion SPECT using 99mTc radiopharmaceuticals 3.0. Journal of nuclear medicine technology. 2009;37(3):191-5.

[8] Lyra ME, Andreou M, Georgantzoglou A, Kordolaimi S, Lagopati N, Ploussi A, et al. Radionuclides used in nuclear medicine therapy–From production to dosimetry. Current Medical Imaging. 2013;9(1):51-75.

[9] Mattsson S, Johansson L, Leide Svegborn S, Liniecki J, Noßke D, Riklund K, et al. ICRP publication 128: radiation dose to patients from radiopharmaceuticals: a compendium of current information related to frequently used substances. Annals of the ICRP. 2015;44(2_suppl):7-321.

[10] Browne E, Be M-M, Desmond Mac Mahon T, Helmer R. Report on the activities of the Decay Data Evaluation Project. CEA Saclay; 2001.

[11] Mountford P, O'doherty M, Forge N, Jeffries A, Coakley A. Radiation dose rates from adult patients undergoing nuclear medicine investigations. Nuclear medicine communications. 1991;12(9):767-78.

ICNST 2024
International Conference on Nuclear Science and Technology
6- 8 MAY 2024 | Isfahan, Iran

Design and Implementation of a Low-Cost Alpha Radiation Detector Using BPW46 Photodiode and Arduino UNO R3 (Paper ID: 1080)

Ehsan Parsazadeh, Kamal Hadad, Mohammad-Reza Mohammadian-Behbahani*, Ahmad Pirouzmand

Department of Nuclear Engineering, School of Mechanical Engineering, Shiraz University, Shiraz, Iran.

Abstract

The utilization of small-scale radiation detectors is beneficial due to their decreased sensitivity to background radiation and diminished geometrical acceptance, making them suitable for detecting low levels of activity. To develop a compact, portable, and cost-effective radiation detection system, commercial silicon photodiodes, initially intended for detecting photons within the visible, infrared, or ultraviolet ranges of the electromagnetic spectrum, can be employed. This paper presents the design and construction of an alpha detector using the BPW46 photodiode, which features a high sensitivity to alpha particles after removing the plastic layer from its sensitive surface. The readout preamplifier circuit comprises a NE5532P low-noise operational amplifier, while the counter system is based on the Arduino UNO R3.

Keywords: Alpha radiation, Arduino UNO R3, BPW46 photodiode, Radiation detector

Introduction

Semiconductor detectors are devices used to detect and measure ionizing radiation. When radiation interacts with the sensitive volume of a semiconductor detector, it produces a large number of electrons and holes. These charge carriers are then moved under an applied electric field. Semiconductor materials benefit from smaller work functions compared to gas and scintillation detectors, resulting in a higher number of generated charge carriers [1].

In addition to application-specific semiconductor detectors such as Si and Ge detectors made in p-n and p-i-n diode configurations [1][2], there is a possibility to use general-purpose semiconductor devices for detection of ionizing radiation. For example, in previous studies [3-6], optical photodiodes have been examined.

Photodiodes are semiconductor devices that generate electrical signals primarily when exposed to visible light, ultraviolet, or infrared radiation. They consist of an intrinsic (i) semiconductor layer,

sandwiched between two n+ and p+ layers, serving as the radiation-sensitive part of the sensor. This configuration creates a p-i-n diode, as in Figure 1. By the absorption of light photons and the subsequent generation of electrons and holes, the output signal is formed. Similarly, when the photodiode is exposed to ionizing radiation, electron-hole pairs are created through processes such as Coulomb interaction (for charged particles) or photoelectric absorption and Compton scattering (for photons). Like specialized radiation detectors, a photodiode a radiation detector is reverse biased, as shown in Figure 1, to increase the sensitive volume of the detector [7][8].

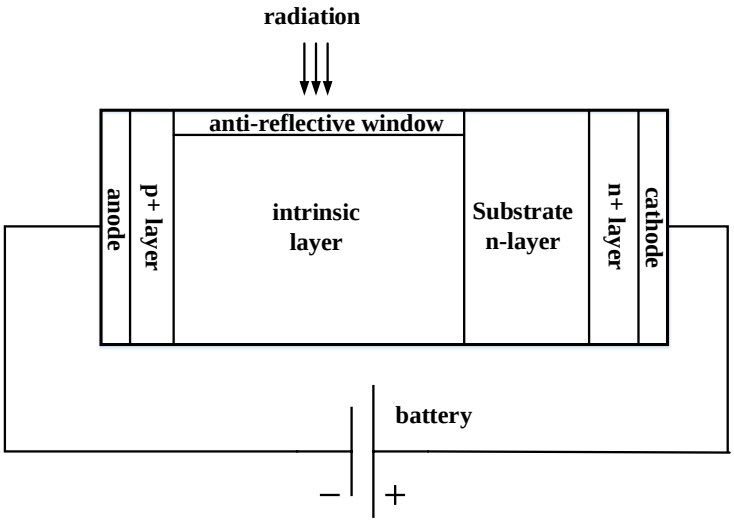

Fig. 1. Schematic of a p-i-n photodiode with an intrinsic semiconductor layer sandwiched between two heavily doped n^+ and p^+ layers. The photodiode is reverse biased by a battery supply. The anti-reflective window provides the optical coupling of the sensor with the environment.

Charged particles, particularly heavy charged particles, may not reach the sensitive volume of the detector due to energy loss through Coulomb interaction in the lens and filter of the photodiode. This is why it is necessary to remove the disturbing layers from the path of radiation through physical or chemical methods.

The energy responses of some low-cost silicon photodiode detectors, applied for various types of radiation, including alpha particles, fission fragments, internal conversion electrons, and X-rays are presented in [9][10]. In reference [11], Hamamatsu PIN silicon diodes, originally designed for detecting ambient light, are repurposed for the detection and spectroscopy of alpha particles, by using a low-noise charge-sensitive preamplifier. Reference [6] describes the application of two low-cost silicon p-i-n diodes, BPX61 and BPW34, as portable radiation counters. The BPW34 chip is used to

detect beta particles, while BPX61 employed to detect alpha particles after removing the entrance glass window. In reference [12], a SFH206K-Osram photodiode and a charge-sensitive preamplifier are proposed for detection and spectroscopy of alpha particles.

The aim of the current study is to design and construct a low-cost alpha radiation counter utilizing the BPW46 [13] photodiode.

Materials and Methods

The signals obtained from the photodiode cannot be measured directly due to their low amplitude. A readout circuit, comprising a logarithmic amplifier followed by a charge-sensitive amplifier, was implemented. This circuit efficiently processes the signals, counting and displaying the number of particles impinging on the photodiode (Figure 2) [15][14]. A comparator circuit was used to generate logic pulses proportional to the particles detected by the sensor, to finally give the number of counts [16]. In the proposed detection system, the threshold voltage can be adjusted using a variable resistor to eliminate electronic noise.

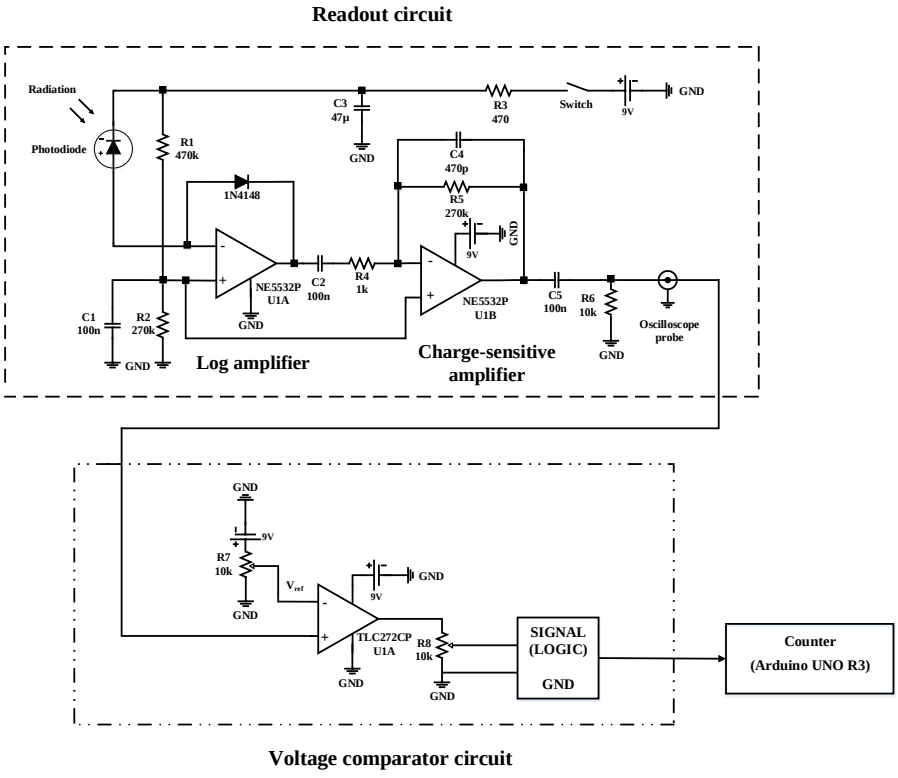

Fig. 2. Readout circuit (top) and voltage comparator (down) for reading out the photodiode output pulses. A photodiode in reverse bias is also shown. Discrimination level is adjusted by a multi-turn potentiometer.

The printed circuit boards were designed using the Altium Designer software with the aim of minimizing noise. The components were arranged as close as practical to reduce the impact of input capacitance caused by cabling, ground loops, or radio-frequency pickups. Figure 3 provides two- and three-dimensional views of the designed preamplifier and discriminator systems. The photodiode and electronic circuit of the preamplifier were encased in a metal box to protect from environmental light and electromagnetic interferences.

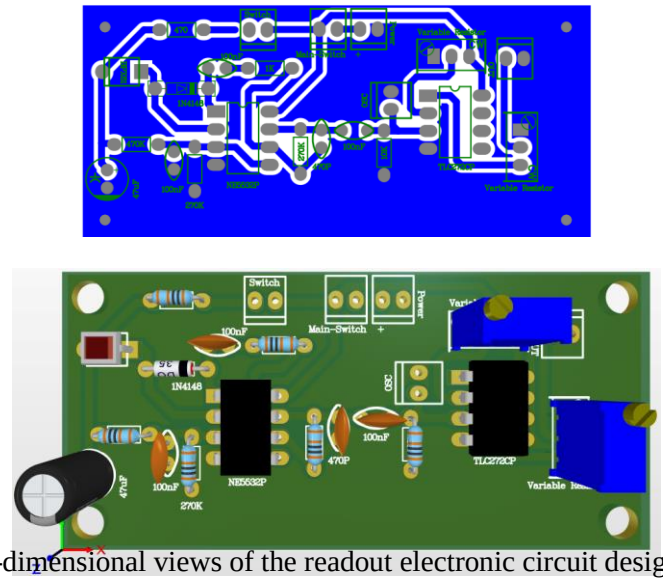

Fig. 3. Two- and three-dimensional views of the readout electronic circuit designed in Altium Designer software version 22.6.1.

In order to quantify the number of logical pulses, an Arduino Uno R3 was programmed in Arduino Integrated Development Environment (IDE) (Table 1). The functionality of the program was validated through the Proteus simulation program.

Table 1. Program for calculating the rate of pulses.

```
// include the library code:
#include <LiquidCrystal.h>
// initialize the library with the numbers of the interface pins
#include <LiquidCrystal.h>
LiquidCrystal lcd(8, 9, 4, 5, 6, 7);
int freqCounter = 0;
long preMillis = 0;

void isr() //interrupt service routine
{
  freqCounter++;
}

void printCounting(){
  lcd.setCursor(6, 1); //6th column and second row
  lcd.print((freqCounter/1000)%10);
  lcd.print((freqCounter/100)%10);
  lcd.print((freqCounter/10)%10);
  lcd.print(freqCounter%10);
  lcd.print(" ");
}
```

```
void setup() {
   // set up the LCD's number of columns and rows:
  lcd.begin(16, 2);
  // Print a message to the LCD.
lcd.print("Alpha detector");
delay(3000);
lcd.clear();
  lcd.print("Count Per Second");
  printCounting();
  delay(10);
  attachInterrupt(0,isr,RISING);  //attaching the interrupt
}
void loop() {

 while((millis()-preMillis)<1000);
 detachInterrupt(0);          //detaches the interrupt
printCounting();
 freqCounter = 0;
 preMillis = millis();
 attachInterrupt(0,isr,RISING);  //attaching the interrupt
again
 }
```

To detect alpha particles using BPW46 photodiode, its protective plastic layer (thickness of 0.7 mm) needs to be removed as it prevents alpha particles from reaching the sensor sensitive area. To have an assessment, let us assume an approximate mass stopping power ($dE/\rho dx$) of 800 MeV.cm2/g for 5.5 MeV alpha particles of Am-241 hitting mylar3. If we approximate the density of mylar to be $\rho = 1.4$ g/cm3, the linear stopping power (dE/dx) would be:

$dE/dx = 800$ MeV.cm2/g $\times$ 1.4 g/cm3 = 1120 MeV/cm which means a 1120 MeV of energy loss for each cm of mylar thickness. The thickness of the coating layer in our work is 0.7 mm, which results in an energy loss of

1120 MeV/cm $\times$ 0.07 cm = 78 MeV

This is much higher than the initial 5.5 MeV energy of the alpha particles. It means that the alpha particles are fully stopped in the coating layer. It should be remarked that the cover layer of the photodiode is made of plastic, not mylar. However, by repeating the calculations for plastic, a similar conclusion is expected.

For the case of gamma rays of C0-60, assume a linear attenuation coefficient of $\mu \approx 0.1$ cm-1 for 1.17 MeV photons of C0-60. By assuming a good geometry, the percent of the gamma-ray flux passing the plastic layer is

$I/I0 = \exp(-\mu x) = \exp(-0.1 \text{ cm}^{-1} \times 0.07 \text{ cm}) = 99.3\ \%$

So we can conclude that the plastic layer is transparent to the gamma rays of Co-60.

[3] www.ortec-online.com: Ortec Experiment 5: Energy Loss with Heavy Charged Particles

Different physical and chemical methods are available to remove the plastic layer for alpha detection. In this study, acetone with a purity of 99.8% was used to effectively soften and eliminate the layer. However, there are limitations in fully removing this layer as the mechanical support of the structure is lost and the very delicate anode wire of the photodiode will be damaged. As a result, only some portion of the plastic layer was removed (Figure 4).

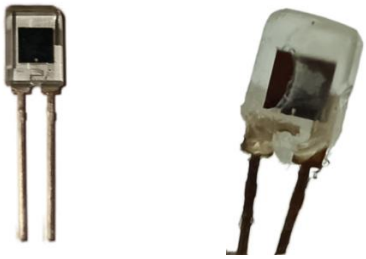

(a) (b)

Fig. 4. BPW46 photodiode (a) before and (b) after removing a portion of the plastic layer.

The whole configuration of the nuclear electronics chain for the proposed detector is illustrated in Figure 5. Upon collision of alpha particles with the photodiode, a significant number of electrons and holes are created which are subsequently collected to form a very weak analog signal. This signal is then processed by the preamplifier circuit, then transferred to a discriminator circuit. The logic output of the discriminator is then sent to a programmed Arduino module, which calculates the pulse rate. Finally, the calculated value is displayed on a Liquid Crystal Display (LCD) screen.

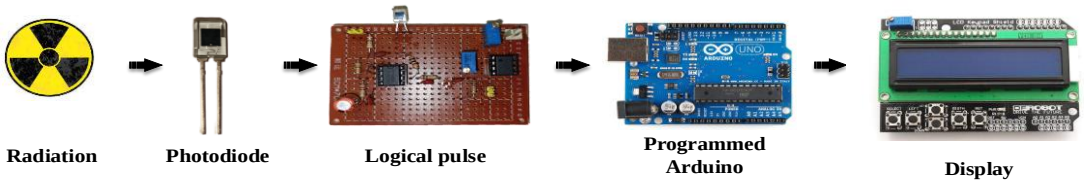

Fig. 5. Scheme of the processing chain of the proposed detector system.

Results and Discussion

First to assess the electronic noise, the output of the detector was observed on an oscilloscope in the absence of radioactive sources (Figure 6-a). The performance of the detector was evaluated by separate check sources emitting alpha particles (Am-241, activity of 0.034 μCi and alpha particle energy of

approximately 5.5 MeV) and gamma-rays (Co-60, activity of 0.71 µCi). Figures 6-b and 6-c display the responses of the sensor to alpha and gamma radiations, respectively.

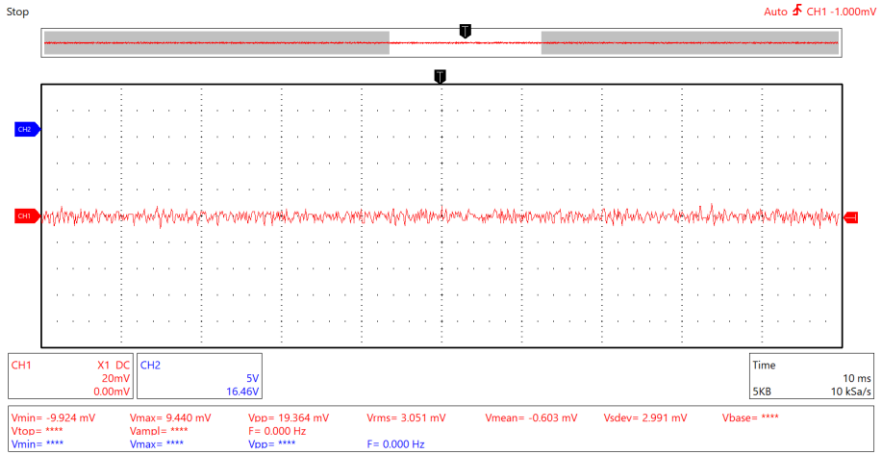

(a)

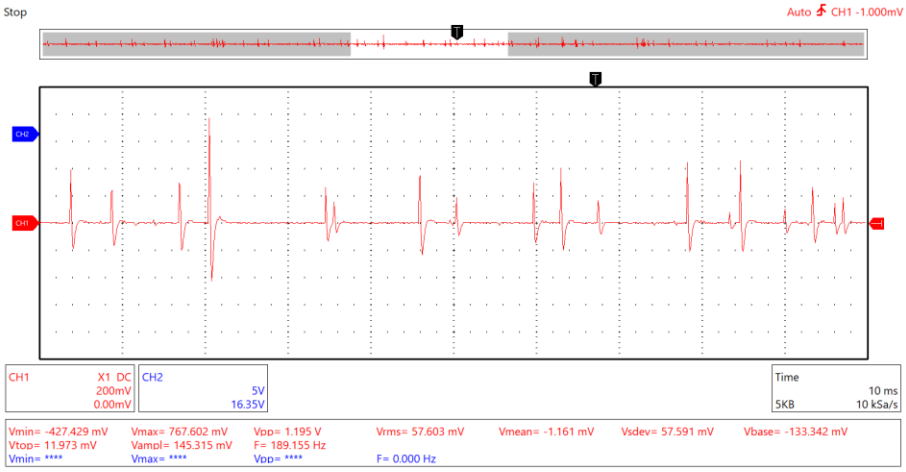

(b)

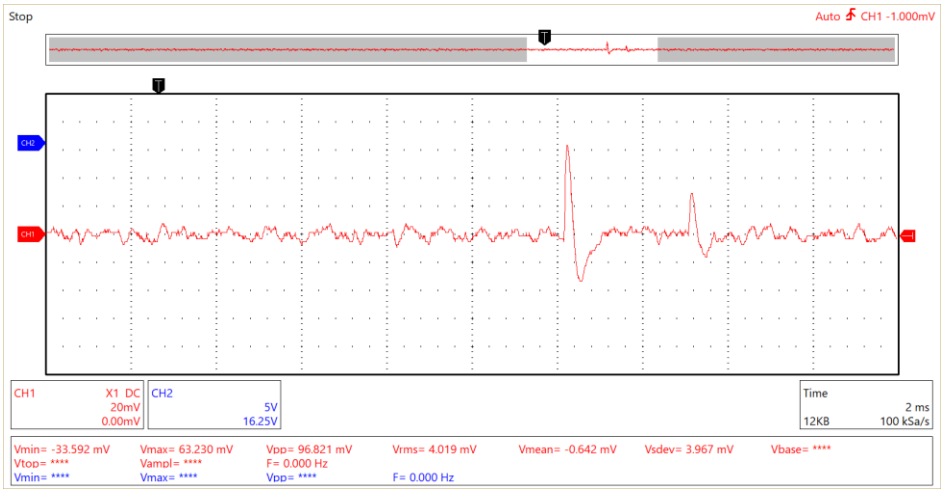

(c)

Fig. 6. (a) Output of the amplifier circuit without radioactive source, (b) in the presence of an Am-241 alpha-emitting source and (c) in the presence of a Co-60 gamma-ray source.

In the absence of a radioactive source, electronic noise signals with a maximum amplitude of approximately 10 mV were observed. After the source is placed, pulses of different amplitudes emerge both for alpha and gamma sources (Figures 6-b and 6-c). This is due to the way gamma and alpha particles interact with the sensitive area of the photodiode. Gamma-rays generally have a low interaction probability with silicon; even in cases of Compton scattering, only a fraction of the gamma-ray energy is transferred to the photodiode. On the other hand, alpha particles can transfer a larger fraction of their energy through Coulomb interaction, resulting in higher-amplitude pulses. However, the amplitude of alpha pulses also depends on the angle at which they hit the sensitive surface of the photodiode [12]. With the alpha source, signals of amplitudes ranging from 50 mV to 1.2 V and a width of approximately 250 μs were observed. The gamma source led to the detection of pulses with amplitudes predominantly less than 60 mV.

The measured average rates of the recorded pulses were about 160 and 70 counts per second (cps) for alpha and gamma sources, respectively. It should be remarked that only nearly one third of the sensitive area of the photodiode is available for detecting charged particles (Figure 4). Utilizing more portions of the photodiode surface can enhance the detection efficiency of the system.

The detection efficiency of the detector was also calculated as follows. The activity of the alpha source is 1258 Bq (=0.034 μCi) with a source surface area of nearly 0.2 cm2. The total surface area of the sensor is 7.5 mm2 and let us assume a sensor sensitive area of 7.5/3 mm2 (with plastic layer partly

removed for alpha detection). Therefore, the rate of particles reaching the detector can be calculated from the ratio of surface areas of the sensor and the source:

$$\frac{(\frac{7.5}{3}) \times 0.01\ \text{cm}^2}{0.2\ \text{cm}^2} \times 1258 \approx 158\ \text{cps}$$

This is in a very good agreement with the mean experimental counting rate of 160 cps which gives an intrinsic detection efficiency of 158/160 ≈ 100% for alpha detection.

For the case of Co-60 source, the total activity is 26270 Bq (= 0.71 µCi). Let us assume that half this value is projected toward the detector. The effective source surface is estimated to be 0.785 cm2, and the sensor is exposed by all its surface area. This gives the rate of gamma rays reaching the detector as:

$$\frac{7.5 \times 0.01\ \text{cm}^2}{0.785\ \text{cm}^2} \times {}^{26270}/_{2} \approx 1255\ \text{cps}$$

with an experimentally-recorded mean count rate of 70 cps, the intrinsic efficiency for gamma detection is calculated: 70/1255 ≈ 6%.

Conclusion

An alpha particle counter based on BPW46 photodiode is reported, which is sensitive to alpha particles after removing its protective plastic layer. The low-cost nature of the detector makes it available to a wider range of users for the applications of radiation monitoring and safety. Improvements can be made in the future works to enhance its sensitivity, to reduce noise, and to minimize the pile-up effects under higher rates. It can also be modified to be applied for the spectrometry of alpha and beta radiations.

References

[1] G. F. Knoll, Radiation detection and measurement. John Wiley & Sons, 2010.

[2] H. Spieler, Semiconductor Detector Systems. Oxford University Press, 2005.

[3] I. Ruiz-García, J. Román-Raya, J. Banqueri, A. J. Palma, D. Guirado, and M. A. Carvajal, “Commercial photodiodes and phototransistors as dosimeters of photon beams for radiotherapy,” Med. Phys., vol. 48, no. 9, pp. 5440–5447, 2021.

[4] O. Van Hoey et al., “Radiation dosimetry properties of smartphone CMOS sensors,” Radiat. Prot. Dosimetry, vol. 168, no. 3, pp. 314–321, 2016.

[5] E. Damulira, M. N. S. Yusoff, A. F. Omar, N. H. Mohd Taib, and N. M. Ahmed, "Application of Bpw34 photodiode and cold white LED as diagnostic X-ray detectors: A comparative analysis," Appl. Radiat. Isot., vol. 170, no. December 2020, p. 109622, 2021, doi: 10.1016/j.apradiso.2021.109622.

[6] O. Keller, M. Benoit, A. Müller, and S. Schmeling, "Smartphone and tablet-based sensing of environmental radioactivity: Mobile low-cost measurements for monitoring, citizen science, and educational purposes," Sensors (Switzerland), vol. 19, no. 19, 2019, doi: 10.3390/s19194264.

[7] G. D. Bett, ADVANCES IN PHOTODIODES. Edited by Gian Franco Dalla Betta. 2011.

[8] L. T. Phan et al., "Manufacture research of the test equipment to measure the dose rate in high radiation medium," 2017.

[9] C. C. Bueno, J. A. C. Gonçalves, and M. D. de S. Santos, "The performance of low-cost commercial photodiodes for charged particle and X-ray spectrometry," Nucl. Instruments Methods Phys. Res. Sect. A Accel. Spectrometers, Detect. Assoc. Equip., vol. 371, no. 3, pp. 460–464, 1996.

[10] C. C. Bueno, A. A. de S. Correa, F. Camargo, J. A. C. Gonçalves, and P. F. P. R. Mendes, "Response of a rad-hard silicon diode for charged particles," Nucl. Instruments Methods Phys. Res. Sect. A Accel. Spectrometers, Detect. Assoc. Equip., vol. 533, no. 3, pp. 435–441, 2004.

[11] P. H. Gooda and W. B. Gilboy, "High resolution alpha spectroscopy with low cost photodiodes," Nucl. Instruments Methods Phys. Res. Sect. A Accel. Spectrometers, Detect. Assoc. Equip., vol. 255, no. 1–2, pp. 222–224, 1987.

[12] K. Pascoalino, F. CAMARGO, J. A. C. GONCALVES, and C. C. Bueno, "Measurement of the insensitive surface layer thickness of a PIN photodiode based on alpha-particle spectrometry," Brazilian J. Radiat. Sci., 2022.

[13] "BPW46 datasheet: Silicon PIN Photodiode," Vishay Intertechnology, Inc., 2014, [Online]. Available: https://www.vishay.com/docs/81524/bpw46.pdf.

[14] "alpha spectroscopy," [Online]. Available: https://stoppi-homemade-physics.de/alphaspektroskopie/.

[15] "Das Elektronik-Labor," pp. 1–5, [Online]. Available: https://www.elektronik-labor.de/Projekte/Alpha4.html.

[16] M. Nakhostin, Signal Processing for Radiation Detectors. John Wiley & Sons, 2017.

ICNST 2024
International Conference on Nuclear Science and Technology
6- 8 MAY 2024 | Isfahan, Iran

Preliminary Test Results of Low-Cost Active Detectors for Radon Gas Monitoring (Paper ID: 1081)

Ehsan Parsazadeh, Kamal Hadad, Mohammad-Reza Mohammadian-Behbahani*, Ahmad Pirouzmand

Department of Nuclear Engineering, School of Mechanical Engineering, Shiraz University, Shiraz, Iran.

Abstract

Radon gas is a significant source of natural radiation exposure in humans. In this research, the responses of three different radiation detectors are compared by preliminary test results for Radon gas detection. First detector is a pulse-mode counter developed by using a BPW34 photodiode. To amplify and read out the output signal of the photodiode, a charge-sensitive preamplifier is designed. A pulse counting circuit is implemented in the following. The second developed detector is a simple current-mode air ionization chamber working at low applied voltages, with output signal enhanced by a current amplifier transistor, read out by an Arduino UNO module. Additionally, an alpha-sensitive Geiger-Mueller counter (model NT-960, Novin Teyf) with a mica entrance window is employed as the third detector. Soil samples containing natural Uranium, in companion with all three detectors were sealed in a chamber to study the detector responses to changing concentrations of Radon gas. Findings indicate that all three detectors exhibit an increasing response as the concentration of Radon gas is increased.

Keywords: Arduino-based ion chamber, Geiger-Mueller counter, Photodiode detector, Radon gas monitoring

Introduction

Radon-222 is a noble gas originating from the radioactive decay chain of Uranium or thorium, both of which found in minimal quantities in the majority of rocks and soils. The concentration of Radon gas varies by geographical region, season, and environmental conditions. Radon-222 undergoes alpha decay with a half-life of 3.82 days, leading to the formation of Polonium-218, which subsequently decays to Lead-214 through alpha decay with a half-life of 3.10 minutes. Alpha particles, having a high linear energy transfer, can inflict serious damage to cells along their path within tissue.

The World Nuclear Association currently identifies Radon as the main cause of radiation exposure in humans. Its invisibility, lack of odor, taste, and color make it difficult to identify without specific tools. Although Radon detectors are commercially available, their affordability may restrict their access. Passive detectors and electret systems are commonly used for long-term measurements of Radon, while systems with continuous function are most often used for online short-term measurements [1-7].

Radon and its decay products may emit alpha particles, beta particles or gamma rays. Hence, a range of alpha, beta, and gamma detectors can be applied: solid and liquid scintillation detectors, nuclear track detectors, electrometers, ionization chambers, semiconductor detectors, and thermo-luminescence detectors [8].

Elísio and Peralta (2020) utilized a SLCD-61N5 low-cost planar photodiode and a charge-sensitive preamplifier, along with an Arduino-based counter system, as an active Radon gas detector [9]. Blanco-Novoa et al. (2018) tested an IoT remote Radon monitoring system for accurate measurement of Radon concentration in various locations including buildings in Galicia, Spain, where high levels of Radon gas are expected [6]. Kim et al. (2016) studied a PIN photodiode Radon sensor by which the measured rate for Radon-emitting soil was 4.38 counts per hour [10]. Bayrak et al. (2013) utilized a low-cost Radon detection system for predicting earthquakes, made of a windowless PS100-7-CER-2 photodiode, in companion with an amplifier and shaper [11].

Břízová et al. (2020) studied an ionization chamber in current-mode to detect alpha particles, equipped with an Arduino module [12]. Studnička et al. (2019) also tested a low-cost current-mode ion chamber developed for monitoring Radon gas, operating at a low voltage. The study reported a minimum measurable activity of approximately 50 Bq/m3 for Radon gas [13].

In the current study, we mainly aim to assess the performance of two detectors: a pulse-mode detector based on a photodiode, and a current-mode ionization chamber. The idea is to monitor the variations in the concentration of environmental Radon gas.

Experimental Setup

In this research, two detectors similar to [13] and [14] were developed: a photodiode detector and a free air ionization chamber (Figures 1 and 2, respectively). Additionally, a Novin Teyf NT-960 Geiger-

Mueller counter [15] was used. This detector, with a thin mica entrance window, is sensitive to alpha particles. All these three detectors were placed in a well-insulated chamber.

The output signals of the photodiode were amplified and processed using a charge-sensitive preamplifier. To achieve this, a two-stage TLC272 operational amplifier was utilized. A discriminator unit was also implemented to produce logic pulses that correspond to the particles detected by the photodiode. Finally, a microcontroller was programmed to calculate the rate of logic pulses and display the result on a LCD screen [16] (Fig. 1). To enhance the detection of beta particles, the protective plastic layer on the photodiode was sanded down to a much lower thickness. The BPW34 photodiode [17], in companion with the preamplifier were enclosed in a metal casing to protect from interfering light or electromagnetic waves. A tiny hole on the metal box permitted the passage of Radon gas, while blocking any environmental light.

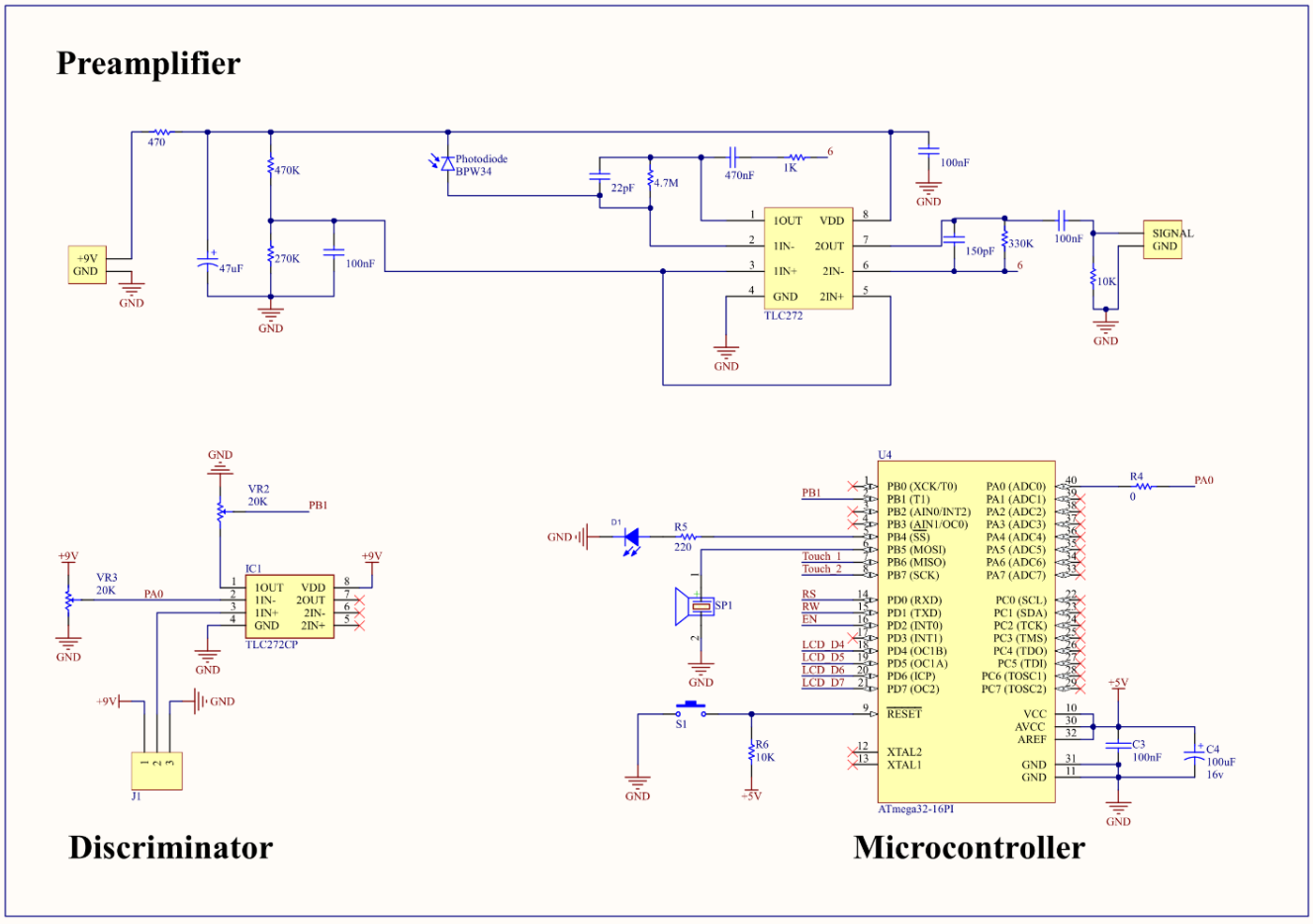

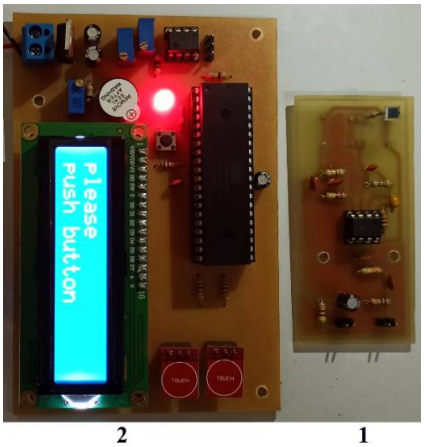

Fig. 1. The photodiode detector. Top: schematic view of the detector designed in Altium Designer software. Down: assembled detector, including (1) the charge-sensitive preamplifier with the BPW34 photodiode, and (2) the counter system.

In the ion chamber, a guard ring is employed to minimize the leakage current. A BC517 NPN Darlington transistor [18] is used to amplify the chamber current signal (Fig. 2). A DC voltage booster module is employed to enhance the applied voltage. To measure the output signal, the analog-to-digital converter of an Arduino UNO board is utilized. The recorded values are then transmitted to an smartphone via a HC-05 Bluetooth module. To prevent from electromagnetic wave interferences, a metal cap envelopes the readout circuit on the top, and a metal grid covers the bottom side of the chamber, where the radiations are allowed to enter via.

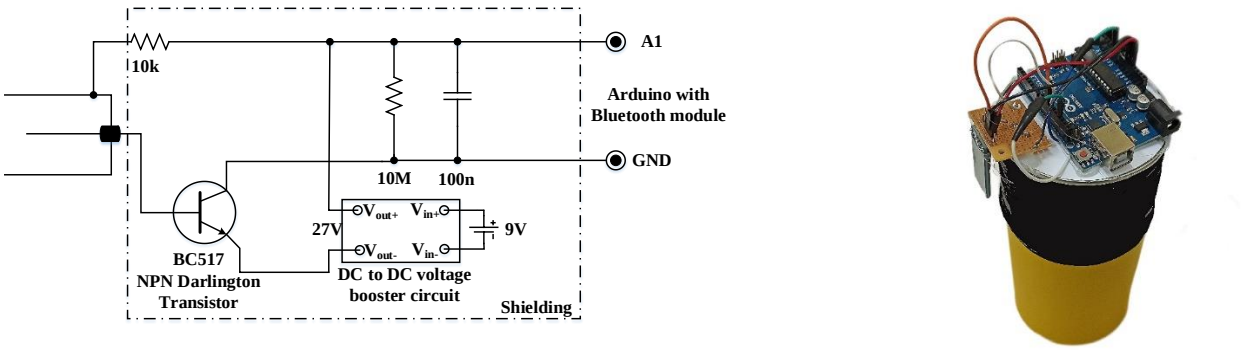

Fig. 2. The current-mode ionization chamber: Left: the detector sensor circuit. Right: the fabricated detector.

The experimental setup is shown in Figure 3, in which there exist two separate chambers: one containing Uranium soil (number 1) and the other, the detectors (number 2). The total volume of these chambers is roughly 40 liters. During the measurements, the room temperature was held at 25 degrees

Celsius. An InstruStar-ISDS205A oscilloscope card was utilized to monitor the outputs of the detectors.

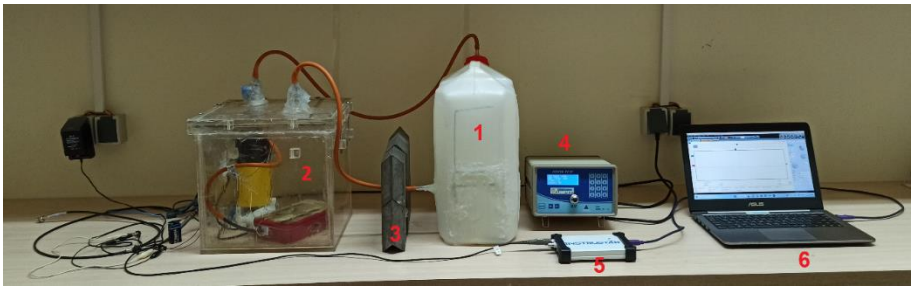

Fig. 3. The experimental setup. (1) An insulated container of Uranium containing ore and soil which produce Radon gas. (2) An insulated chamber where detectors are placed inside. (3) Lead blocks to protect the detectors from direct exposure by gamma rays of Uranium. (4) Power supply and readout system of the Geiger-Mueller detector. (5) InstruStar-ISDS205A oscilloscope card. (6) Laptop for reading the output of the oscilloscope card.

Results and Discussion

First to measure the background values, the Geiger-Mueller detector, the ion chamber, and the semiconductor detector were set up in the absence of Radon gas, and their corresponding values recorded (shown as the data points of day 1 in Fig. 4). The count rates of the Geiger-Mueller and the semiconductor detectors were obtained by averaging the counts recorded over 100-second intervals. Subsequently, the Radon gas was introduced, allowed to enter the chamber for 15 days, which corresponds to roughly four half-lives of Radon. During this period, the Radon concentration built up. In the next phase, the entrance valve was closed so as to evaluate the decrease in Radon concentration. Measured values of each detector were normalized to their corresponding maximum value (reached on day 15), and the concentration curves plotted altogether in Figure 4.

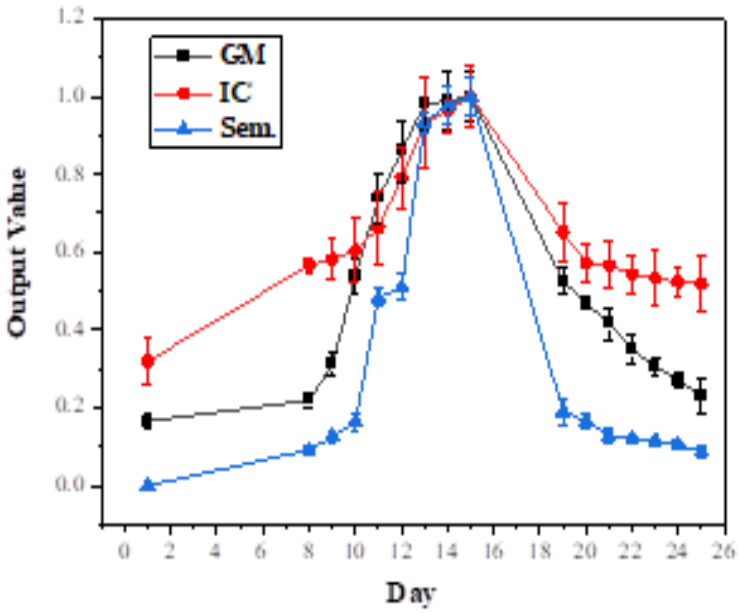

Fig. 4. Normalized concentration curves of the three detectors: the Geiger Mueller (GM) detector, chamber (IC) and the semiconductor detector (Sem.). The Radon entrance valve was close on day 15.

An exponential fitting of the decaying part of the GM curve in Figure 4 gives the half-life (t1/2) of Radon gas acceptably. To this goal, a single exponential function as Eq. 1 was fitted to the data points of days 15-25 of the GM curve.

$$y(t) = y_0 + Ae^{-0.693(t-t_0)/t_{\frac{1}{2}}} \quad (1)$$

where y0 is a bias term, A amplitude, t time in days and t0 = 15 the start time. The fitting result gives a calculated t1/2 of 4.2 days, in acceptable accordance with the true half-life of Radon, 3.82 days. The discrepancy may be attributed to the absence of information on days without measurement, as well as the measurement errors.

While the Geiger-Mueller counter acceptably follows the expected behavior, the semiconductor detector fails due to its quite lower number of counts (due to its lower detection efficiency) and increased statistical fluctuations of the recorded counts. A lower sensitivity for the semiconductor detector is also observed with outputs tending to zero when the activity is low (after day 18 and before day 8). For the case of ion chamber, a relatively large background leakage current (the normalized output level of nearly 0.5 in Fig. 4) is observed from which the curve rises and to which it returns back. This high level of leakage current limits the sensitivity of the ion chamber.

Despite the fact that the results by the ion chamber and the semiconductor detector deviate from the expectations, in general, it can be observed that when the concentration of Radon gas inside the chamber was increased, all three detectors exhibited an increasing trend. Conversely, when the gas valve was closed and the concentration of Radon decreased, all three detectors recorded a decreasing trend of data.

Conclusions

In this study, the design and preliminary test results of a photodiode detector, as well as an ion chamber were reported. These detectors benefit from several advantages including portability, compactness, on-line response (in comparison with passive detectors), low energy consumption and low manufacturing costs. Generally based on experimental tests, it was shown that both detectors, along with a standard Geiger-Mueller counter, could follow the increasing and decreasing trends in Radon gas concentration. Limitations of the proposed detectors include their sensitivity and probable response stability issues.

Acknowledgements

The authors would like to express their gratitude to the Radiation Research Center of Shiraz University for supplying the radioactive sources and facilitating the test conditions. They also wish to thank Mosayeb Dehghani, the laboratory staff at the School of Mechanical Engineering, Shiraz University for his technical assistance.

References

[1] S. Sukanya and S. Joseph, Environmental Radon: A Tracer for Hydrological Studies. Springer Nature, 2023.
[2] Y. Ishimori, K. Lange, P. Martin, Y. S. Mayya, and M. Phaneuf, “Measurement and calculation of radon releases from NORM residues,” 2013.
[3] M. Ćujić et al., “Radon-222: environmental behavior and impact to (human and non-human) biota,” Int. J. Biometeorol., vol. 65, pp. 69–83, 2021.
[4] W. H. Organization, WHO handbook on indoor radon: a public health perspective. World Health Organization, 2009.
[5] U. N. S. C. on the E. of A. Radiation, “Ionizing radiation: sources and biological effects. 1982 report to the general assembly, with annexes,” 1982.

[6] O. Blanco-Novoa, T. M. Fernández-Caramés, P. Fraga-Lamas, and L. Castedo, "A cost-effective IoT system for monitoring indoor radon gas concentration," Sensors (Switzerland), vol. 18, no. 7, 2018, doi: 10.3390/s18072198.
[7] R. Mishra, B. K. Sapra, and Y. S. Mayya, "Development of an integrated sampler based on direct 222Rn/220Rn progeny sensors in flow-mode for estimating unattached/attached progeny concentration," Nucl. Instruments Methods Phys. Res. Sect. B Beam Interact. with Mater. Atoms, vol. 267, no. 21–22, pp. 3574–3579, 2009.
[8] Radon (In Persian). NSTRI Publications, 2017.
[9] S. Elísio and L. Peralta, "Development of a low-cost monitor for radon detection in air," Nucl. Instruments Methods Phys. Res. Sect. A Accel. Spectrometers, Detect. Assoc. Equip., vol. 969, p. 164033, 2020.
[10] G. Kim, T. Oh, and J. Kim, "IMPLEMENTATION OF A PIN PHOTODIODE RADON COUNTER," Glob. J. Eng. Sci. Res., vol. 3, no. January, pp. 58–63, 2016.
[11] A. Bayrak, E. Barlas, E. Emirhan, Ç. Kutlu, and C. S. Ozben, "A complete low cost radon detection system," Appl. Radiat. Isot., vol. 78, pp. 1–9, 2013, doi: 10.1016/j.apradiso.2013.03.054.
[12] L. Břízová, J. Šlégr, and K. Váňová, "Simple alpha particle detector with an air ionization chamber," Phys. Teach., vol. 58, no. 1, pp. 42–45, 2020.
[13] F. Studnička, J. Štěpán, and J. Šlégr, "Low-cost radon detector with low-voltage air-ionization chamber," Sensors, vol. 19, no. 17, p. 3721, 2019.
[14] "alpha spectroscopy," [Online]. Available: https://stoppi-homemade-physics.de/alphaspektroskopie/.
[15] "https://www.novinteyf.ir/nt-960." .
[16] E. Parsazadeh, K. Hadad, M. R. Mohammadian-Behbahani, and A. Pirouzmand, "Design and construction of a beta ray detector using BPW34 photodiode (In Persian)," Iranian Nuclear Society, 2023, [Online]. Available: https://inc.nsi.ir/article_9505.pdf.
[17] "BPW34 datasheet: Silicon PIN Photodiode," Vishay Intertechnology, Inc., 2011, [Online]. Available: https://www.vishay.com/docs/81521/bpw34.pdf.
[18] Onsemi, "BC517 NPN Darlington Transistor," 2017. [Online]. Available: https://static.chipdip.ru/lib/958/DOC003958404.pdf.

ICNST 2024
International Conference on Nuclear Science and Technology
6- 8 MAY 2024 | Isfahan, Iran

Calculation and experimental validation of the energy response of thermoluminescence dosimeter used for measurement of individual dose-equivalent (Paper ID: 1096)

M. Norouzkhani[1], A. Moslehi*[,2], V. Ataeinia[3], M. Sohani[1], S. J. Bizeh[3]

[1] Department of Physics, Shahrood University of Technology, Shahrood, Iran,

[2] Radiation Applications Research School, Nuclear Science and Technology Research Institute, AEOI, Tehran, Iran.

[3] Management of Nuclear Protection, Radiation Protection and HSE, Nuclear Science and Technology Research Institute, AEOI, Tehran, Iran.

Abstract

One of the challenges of individual and environmental dosimetry in Iran is the absence of standard radiation fields with various energies for calibrating the dosimeters. For dosimetry in photon fields, only the standard fields of 60Co (1.25 MeV) and 137Cs (662 keV) sources, located in the Karaj Secondary Standard Dosimetry Lab (SSDL) can be utilized. If response of a given dosimeter is independent of the photon energy in a definite range, its calibration curve obtained in the SSDL can be applied for the other photon fields covering that energy range. Thus, the dose-equivalent measured by the dosimeter is true within an acceptable uncertainty. Otherwise, some large uncertainty would be imposed to the quantity of dose-equivalent measured by the dosimeters. This study aims to determine energy response of a personal thermoluminescence dosimeter (TLD) designed for determining the personal dose-equivalent, Hp(10), in order to investigate whether the calibration curve in the 60Co gamma field can be utilized for assessing the dose-equivalent in the photon fields with different energies. To do this, First, enough number of TLD dosimeters (an appropriate plastic badge including a TLD-100 chip) are irradiated with a few Hp(10) values using the 60Co source in the Karaj SSDL. The badges are placed on a water phantom with dimensions of 30×30×15 cm3, one meter distant from the source. Then, MCNP4C code is used to calculate the energy response at 662 keV and 1.25 MeV energies and are validated with the experimental data. Next, the calculation is carried out for several other energies in the range of 20 keV to 1.25 MeV. Obtained results show that for the energies more than 400 keV, the response of the dosimeter is independent of the photon energy, within 10% uncertainty. But for the energies smaller than 400 keV, a significant dependence on the energy is observed; such that in 40 keV the response is about 2 times larger than that at 1.25 MeV. This means there is an overestimation and uncertainty for the Hp(10) values of those personnel working with low-

energy photons. It can be concluded that some correction factor will be required to be applied for the responses in the low energy region in order to reduce the mentioned uncertainty.

Keywords: Energy response, Thermoluminescence dosimeter, Individual dose-equivalent

Introduction

After the discovery of the thermoluminescence properties of some materials such as lithium fluoride and their potential for use in radiation dosimetry, a large number of investigations have been carried out on the properties and uses of the dosimeters [1-4]. Various studies showed that the radiation energy and angle of radiation have a significant role in the response of TLD dosimeters [5-12].

In the past three years, a thermoluminescence dosimetry system has been established in Nuclear Science and Technology Research Institute (NSTRI) to determine the dose-equivalent of personnel working with photon fields. One of the largest sources of uncertainty in the above system is the energy dependence of the dosimeter. Because there are only two standard photon sources of 60Co and 137Cs located in Karaj (SSDL) are available for calibration. When utilizing the calibration curves obtained in these fields for the dosimeters irradiated in the low energy fields, some uncertainty would be imposed on the dose equivalent values, if the energy response per unit of dose in the measurements and calibration fields are not similar, caused by the dependency of the dosimeter response on the photon energy. In this work, the aim is to determine the energy response of the dosimeter used in NSTRI to find out if it is calibrated in the standard fields of Karaj SSDL, the calibration curve can be used for the dosimeters used in the fields with different energies or not. The results will have an effect on the amount of uncertainty of the dosimetry system.

Experimental

In this section, first the energy response of individual dosimeter is calculated for the energies 662 keV (137Cs) and 1.25 MeV (60Co). The individual dosimeter used in NSTRI is shown in Fig.1. It is a plastic badge equipped with a filter of 1000 mg/cm2 for measurement of HP(10) value. In addition, each badge has a TLD-100 chip as the sensitive volume. In this work, before irradiation five TLDs were annealed and put in their badges. The irradiation was carried out by means of 137Cs and 60Co standard field of Karaj SSDL as shown in Fig. 2 where dosimeters were irradiated with dose-equivalents 0.5, 7.0 and 20 mSv. The badges were placed on a slab phantom (30 cm × 30 cm × 15 cm) in a 100 cm distance from the source. Before irradiation, the TLD-100 dosimeters were annealed in

the oven at 400 °C for 1 hours followed by an extra annealing at 100 °C for 2 hours. After irradiation in the SSDL, the TLDs were preheated at 100 °C for 10 min to eliminate unstable thermoluminescence (TL) signals. Finally, they were read by a Harshaw 4500 TLD reader (Gammasonics, USA) in which the reading procedure started from 50 °C to 300 °C with a rate 25 °C/s. Furthermore, In the measurements, the total TL response (the electric charge given by the reader) modified by the Elemental correction coefficient (ECC) was considered as the desired experimental response.

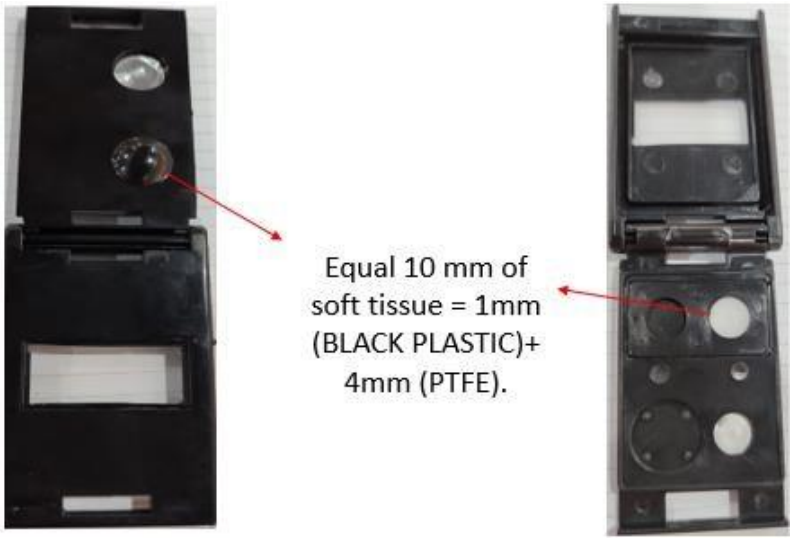

Fig. 1. The individual dosimeter used in NSTRI.

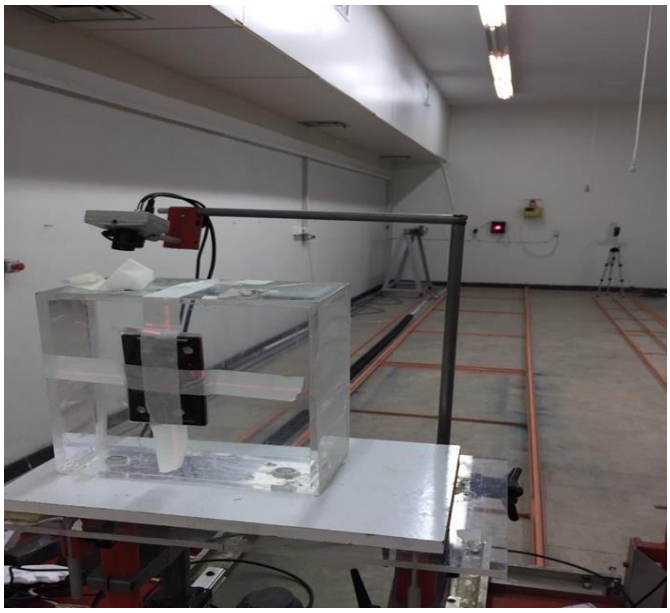

Fig. 2. The irradiation setup used in Karaj SSDL.

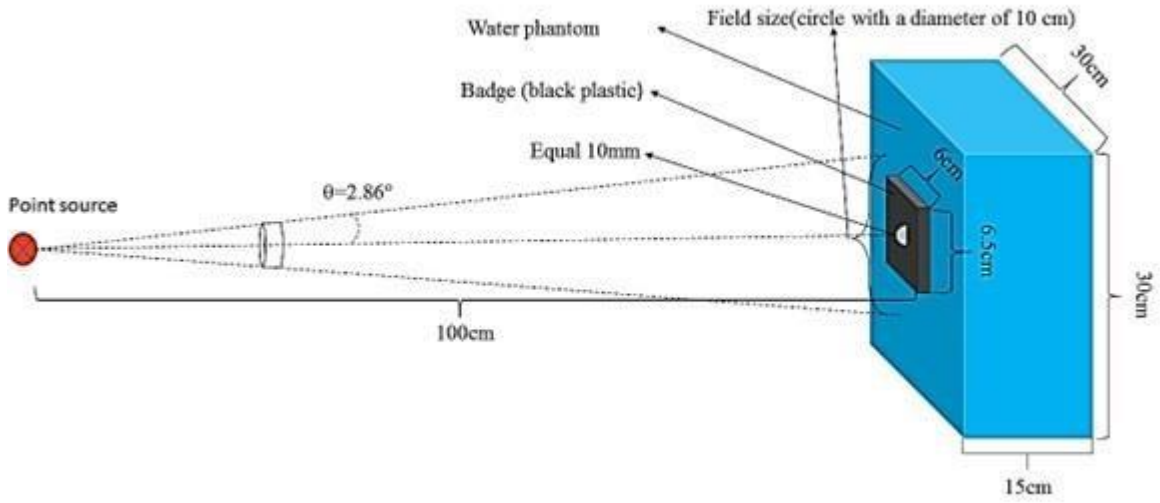

Fig. 3. The geometry simulated in the MCNP4C code.

Simulation

In order to calculate the energy response of the individual dosimeter described in the previous section, Monte Carlo simulations using MCNP4C code were performed. The simulated geometry is shown in Fig. 3 in which the badge containing the TLD and the water phantom were considered. Lithium fluoride (LiF) was chosen as the TLD material. To reduce the computation time, the photons were emitted within a solid angle such that at the place of dosimeter on the phantom surface, the field was surrounded by a circle of 10 cm in diameter. The photon energies from 20 keV to 1.25 MeV were considered. The response at photon energy E was calculated by Eq. (1) [1]:

$$\boldsymbol{R(E)} = \frac{\boldsymbol{r(E)}}{\boldsymbol{X_{air}(E)}} \qquad (1)$$

in which $\boldsymbol{r(E)}$ was the reading of dosimeter at energy E and $\boldsymbol{Xair(E)}$ was the exposure value at this energy. Since the exposure is proportional to the collision KERMA when charged particle equilibrium (CPE) is established, $\boldsymbol{Kc,air(E)}$ was used instead of exposure. Furthermore, From the fact that $\boldsymbol{r(E)}$ is proportional to the total energy deposited in the TLD chip, Eq. (1) changed to

$$\boldsymbol{R(E)} = \boldsymbol{c}\frac{\boldsymbol{E_{dep}(E)}}{\boldsymbol{K_{c,air}(E)}} \qquad (2)$$

when c was the proportionality constant. Finally, the relative energy response was obtained by normalizing the response at any energy to that of 1.25 MeV, i.e.,

$$R_{rel}(E) = \frac{R(E)}{R(1.25\ MeV)} \quad (3)$$

The energy deposit and air KERMA values were calculated by *F8 tally in the TLD and F6 tally in the air, respectively. To obtain the air KERMA, an air sphere with 5 cm diameter was simulated instead of the dosimeter without phantom. It should be notified that to have CPE condition, a PMMA wall was considered surrounding the air sphere. For any energy, the thickness of PMMA wall was selected equal to the range of secondary electrons with energies equal to their primary photons obtained from the NIST [13] library.

In order to validate the simulation, first the energy responses of 662 keV (137Cs) and 1.25 MeV (60Co) gamma rays together with the relative responses (to 60Co) were calculated. The responses were computed per unit of dose-equivalent. Then, the experimental relative responses were determined from the TL responses (i.e., the charge measured by the reader in the unit of nC) measured for three dose-equivalents of 0.7, 5 and 20 mSv. It should be noted that for any dosimeter, the TL response was multiplied by the corresponding ECC value of the TLD chip. Next, the average relative response was compared with the calculated one.

Results and Discussion

Table 1 presents the calculated and experimental relative responses. The uncertainty value (with coverage factor 2) of the measured responses is 25% in the used TLD dosimetry system which is added to the table. The comparison reveals that for the both energies considered (662 keV and 1.25 MeV), the calculated and experimental relative responses are the same (both equal to 1.00). Therefore, the simulation was confirmed by the experimental data.

After validation of the simulation, the energy responses for other energies are computed by Eq. (3) as given in Table 2. The uncertainty values (coverage factor 2) are determined using the error propagation formula. Furthermore, Fig. 4 shows the variation of relative energy response vs. the photon energy. The error bars show the standard deviation of the data. As can be observed, the curve has a peak below 0.4 MeV in which the relative energy response reaches to its maximum value (=1.92) at 40 keV. In this energy range, the photoelectric effect dominates where the absorption coefficients of the dosimeter (including the badge and TLD) are vastly different from that of air. On the other hand, for the energies larger than 0.4 MeV, the response is almost independent of photon energy. Because, in this region

Compton scattering is the dominant interaction where the absorption coefficients of the dosimeter and the air are similar.

As the final point, regarding Fig. 4 and Table 2, one can conclude that for the individual dosimeter using TLD-100 chip some correction is required for the energy response, especially for the energies smaller than 0.4 MeV. The reason is that the calibration in 137Cs or 60Cs fields can be used for the other energies only when the dosimeter response is independent of the photon energy. Otherwise, there would be some error in determining the dose-equivalent especially in the low energy region. Considering the single photon energies, the required correction factors can be defined as the inverse of the relative response values. Table 3 presents the correction factors for different photon energies considered in this work. It is found that their variation with the photon energy is the inverse of that of for the relative responses plotted in Fig. 4.

Table 1. The experimental values of the energy and relative responses for the dosimeters irradiated with dose-equivalents 0.7, 5.0 and 20.0 mSv in with ^{137}Cs and ^{60}Co sources. The calculated values per unit of dose are given for comparison. Two standard deviations of the data are also presented.

$H_p(10)$ (mSv)	$R_{TL,exp}$(nC)	$R_{rel,\ exp}$	$R_{rel,\ exp,\ ave}$	R_{cal}	$R_{rel,\ cal}$
0.7	Cs: 255.81±63.98 Co: 282.31±70.58	0.91±0.32	1.00±0.58	Cs: 1.00±0.02 Co: 1.00±0.02	1.00±0.03
5.0	Cs: 2083.56±520.9 Co: 1964.42±491.1	1.06±0.37			
20.0	Cs: 8362.41±2090.6 Co: 8062.89±2015.62	1.03±0.36			

Table 2. Calculated values of the energy response for different photon energies.

E (MeV)	K_{air} (J/Kg)	E_{dep} (MeV)	$R(E)$	R_{rel}
0.02	1.01E-17	1.08E-09	1.07E+08	0.85±0.04
0.03	4.46E-18	8.99E-10	2.02E+08	1.61±0.06
0.04	2.73E-18	6.58E-10	2.41E+08	1.92±0.04
0.06	2.01E-18	4.63E-10	2.31E+08	1.84±0.08
0.08	2.28E-18	4.39E-10	1.93E+08	1.54±0.06
0.10	2.84E-18	4.89E-10	1.72E+08	1.37±0.02
0.14	4.29E-18	6.72E-10	1.57E+08	1.25±0.02
0.30	1.09E-17	1.43E-09	1.32E+08	1.05±0.04
0.40	1.49E-17	1.89E-09	1.27E+08	1.01±0.04
0.511	1.91E-17	2.41E-09	1.27E+08	1.01±0.04
0.662	2.44E-17	3.05E-09	1.25E+08	1.00±0.02
0.80	2.90E-17	3.60E-09	1.24E+08	0.99±0.04
1.00	3.51E-17	4.28E-09	1.22E+08	0.97±0.04
1.25	4.17E-17	5.23E-09	1.26E+08	1.00±0.02

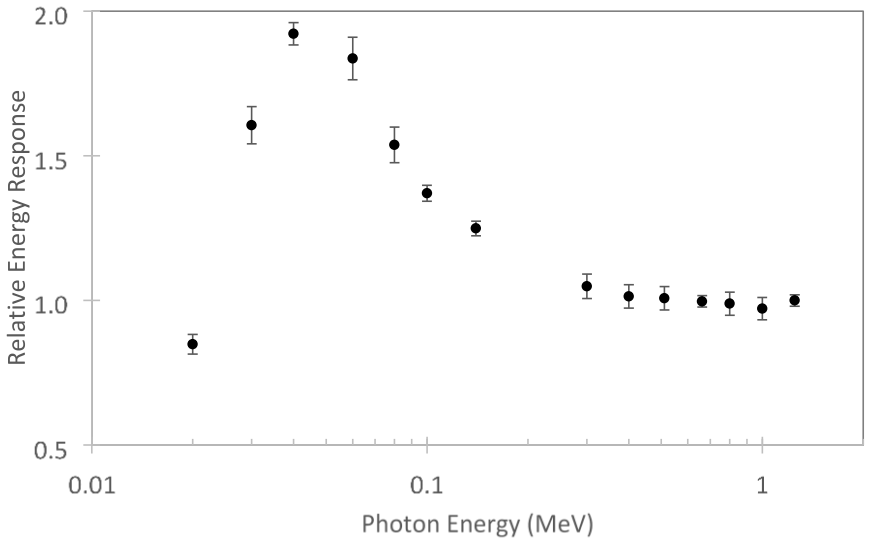

Fig.4. Variation of the relative energy response of the individual dosimeter vs. Photon energy. Error bars show the uncertainty values with the coverage factor 2.

Table 3. The correction factors to be applied for the relative response.

***E* (MeV)**	R_{rel}	**Correction factor**
0.02	0.85±0.04	1.17
0.03	1.61±0.06	0.62
0.04	1.92±0.04	0.52
0.06	1.84±0.08	0.54
0.08	1.54±0.06	0.65
0.10	1.37±0.02	0.73
0.14	1.25±0.02	0.80
0.30	1.05±0.04	0.95
0.40	1.01±0.04	0.98
0.511	1.01±0.04	0.99
0.662	1.00±0.02	1.00
0.80	0.99±0.04	1.01
1.00	0.97±0.04	1.03
1.25	1.00±0.02	1.00

Conclusions

In the present work, the energy response of personal dosimeter based on the TLD-100 chip is calculated in the energy range of 20 keV to 1.25 MeV using the MCNP4C code. The results for 662 keV and 1.25 MeV is validated by the measurements. It is found that there is a dependency on the photon energy in the low energy region (below 400 keV). As a result, in order to use the calibration curve obtained in the 137Cs or 60Cs in the Karaj SSDL (as the only standard fields in the country) for the dosimeters irradiated in the low energy fields, some correction factors are required to obtain the true dose-equivalent values.

References

[1] Attix. F. H (2004). Introduction to Radiological Physics and Radiation Dosimetry, Wiley-VCH Verlog GmbH.

[2] Frederick, F. et al., (1952). Storage of radiation energy in crystalline lithium fluoride and metamict minerals. The Journal of Physical Chemistry, 56(5), 546–548.

[3] Da Silva, T., et al., (1995). Thermoluminescence dosemeter for personal dose equivalent assessment. Radiation protection dosimetry, 58: 17-21.

[4] Olko, P., et al., (2006). Thermoluminescent detectors applied in individual monitoring of radiation workers in Europe—a review based on the EURADOS questionnaire. Radiation protection dosimetry, 120(1-4): 298-302.

[5] Alves, G., et al., (2008). Energy and angular dependence of the personal dosemeter in use at ITN-DPRSN. Radiation Measurements, 43: 641–645.

[6] Carinoua, E., et al., (2008). Energy dependence of TLD 100 and MCP-N detectors. Radiation Measurements 43, 599–602

[7] Zoetelief, J. and Jansen, J.T.M., (1997). Calculated energy response correction factors for LiF thermoluminescent dosemeters employed in the seventh EULEP dosimetry intercomparison. Physics in Medicine & Biology, 42(8): 1491.

[8] Banaee, N. and Nedaie, H.A. (2013). Evaluating the effect of energy on calibration of thermoluminescent dosimeters 7-LiF:Mg,Cu,P (GR-207A). Int. J. Radiat. Res, 11(1): 51-54.

[9] Avila, O., et al., (2014). Energy dependence of TLD-900 dosimeters exposed to low energy X-rays, Radiat. Meas., 71: 127-132.

[10] Herrati, A., et al., (2016). Investigation of TLD-700 energy response to low energy x-rays encountered in diagnostic radiology, Open Phys., https://doi.org/10.1515/phys-2016-0016.

[11] Masterson, M, et al., (2019). Relative response of dosimeters to variations in scattered X-ray energy spectra encountered in interventional radiology, Physica Medica, 67: 141-147.

[12] Benali, A, et al., (2022). Geometrical effects on luminescent dosimeter energy response, J. Instrum., 17: P01035.

[13] Stopping powers and range tables for electrons, protons and heavy ions, https://www.nist.gov

ICNST 2024
International Conference on Nuclear Science and Technology
6- 8 MAY 2024 | Isfahan, Iran

Eu-doped BaMgAl10O17 –a potential scintillation material for charged particles and low energy x-ray detection. (Paper ID: 1097)

Alizadeh V. [1*], Najafi M. [2]

[1]*Department of physics, faculty of Science, Imam Hossein University, Tehran, Iran,*

[2]*Department of Chemistry, Faculty of Science, Imam Hossein University, Tehran, Iran*

Abstract

In this paper, we report Eu2+-doped BaMgAl10O17 nanoparticles (BAM: Eu2+ NPs) which can be used as a suitable candidate to fabricate an efficient scintillator for alpha, beta & low energy x-ray detection. The Eu2+-doped BaMgAl10O17 phosphor is prepared by a new simple solution combustion synthesis (SCS) method. The morphology, luminescence properties, and structural analysis of the synthesized compound are performed by field emission scanning electron microscopy (FE-SEM), photoluminescence (PL) spectra, and X-ray diffraction (XRD) techniques. Synthesized NPs were used to prepare two types of scintillator films. The NPs embedded in transparent adhesive tape to form a composite film and coated by drop coaction to form a thin layer on a PMMA plate. The photoluminescence study showed an intense blue band centered at~447nm caused by Eu2+. The radiation response of the synthesized BAM nanoparticles was measured using 241Am, 230Th alpha, and 90S/90Y beta sources. The scintillation properties of the BAM: Eu2+ NPs indicated that this NPs can be used as a suitable efficient scintillators for alpha, beta & low energy x-ray detection.

Keywords: Scintillation, solution combustion synthesis, nanoparticles, charged particles, BaMgAl10O17: Eu2+, x-ray detection

Introduction

Scintillators are a kind of luminescent material that has the potential to detect highly energetic ionizing radiations such as X-rays, γ rays, β rays, and neutrons. They work as energy transformers: converting high-energy X-ray or gamma rays into ultraviolet/visible (UV/Vis) light. Accordingly, they find various applications ranging from photodynamic therapy (PDT) [1], security [2], well-logging [3], medical imaging [4], etc. The very first scintillator material NaI (Tl) was discovered way back in 1948. Since then, there has been a growing interest in exploring new kinds of scintillators. Several reported representative scintillators include NaI: Tl, LiI: Eu, BaF2: Ce, CaF2: Eu, CeF3, and LaBr3: Ce [5].

Unfortunately, many of these materials are hygroscopic and impose severe limitations on their usage [6].

Recently various phosphor materials have been actively investigated to improve their luminescent properties and to meet the development of different displays, luminescence devices, and modern lighting systems. BaMgAl10O17:Eu2+ NPs are one of the most significant phosphor materials utilized in the plasma snowboards and vogue lighting systems [7-9].

We have previously prepared Eux-doped Ba1-xMgAl10O17 phosphors (where x=0, 0.02, 0.035, 0.055, and 0.07) using a new and simple solution combustion synthesis (SCS) method [10]. Here, in the continuation of our studies, we have reported the scintillation properties of the Ba1-xMgAl10O17: xEu2+ where x=0.06 (B-E-6%) nanoparticles against charged particles and low energy x-ray detection.

Experimental

Eu-doped BaMgAl10O17:Eu2+ NPs were prepared by a new simple solution combustion process. The photoluminescence spectrum of BAM: Eu NPs under 365 nm excitation wavelengths shows a blue emission peak at about 447 ± 2 nm. This result emphasized that the observed blue emission corresponds to Eu2+ ions transitions from the 4f65d first excited configuration state to the 4f7(8S7/2) ground state [11-13]. The details of the process and characteristics of photoluminescence and morphology have been reported in our previous work [10].

The scintillator samples were made either by coating about 7 mg of the BAM NPs on a circular transparent adhesive tape (surface area ~4.52 cm2) (Fig.1 A) or by drop coaction of a nearly homogenized disperse solution of BAM NPs in ethanol (1.5 mg/ml) on surface of a PMMA plate and dried at room temperature(Fig.1B).

Fig. 1. A) BAM NPs has coated on a circular transparent adhesive B) drop coaction of disperse

solution of BAM NPs in ethanol on surface of a PMMA plate

A typical setup for investigation of BAM NPs scintillation properties has been shown in Fig. 2. First, In this setup The scintillation sample (BAM: Eu) coated transparent adhesive tape by using an amount of the optical grease was coupled to a photomultiplier tube (PMT, model R329-02 from Hamamatsu, spectral response 300 to 650 nm and wavelength of maximum response 420 nm). Second, the same procedure was used with the powder (BAM: Eu) was spread into a PMMA Plate. Two alpha radiation source (241Am, 230Th), 90S/90Y as a Beta radiation source and a 241Am with plastic coat as a gamma radiation source used for study of scintillation property of the samples. The properties of radiation sources are shown in Table1.

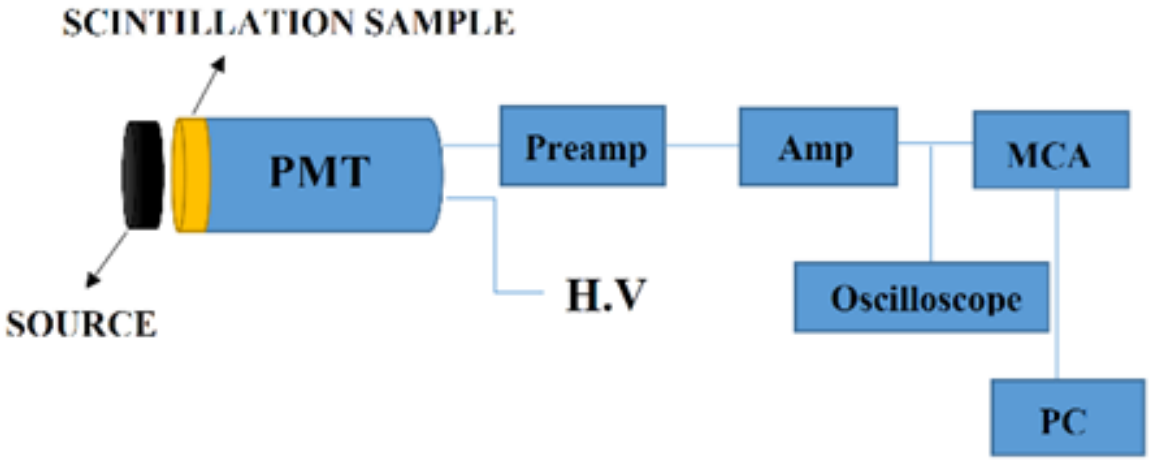

Fig. 2. The experimental set-up for testing the response of $BaMgAl_{10}O_{17}:Eu^{2+}$ with ionizing radiation

Table 1. Properties of radiation source (^{214}Am, ^{230}Th and ^{90}S/^{90}Y).

Nuclide's name	Half-life rad.	Type Energy(Kev)	Intensity (%)
Americium-241	432.2 years	alpha:	
		5388.23	1.60
		5442.80	13.00
		5485.56	84.51
		gamma:	
		26.34	2.40
		59.54	35.90
		x-rays:	
		13.90	42.06
Thorium-230	75380 years	alpha	
		4620.5	23.40
		4687.0	76.30
		x-ray	
		12.30	8.6
Strontium-90	28.74 years	Beta(β-)	
		195.80	100
Yttrium-90	3.19 hours	x-rays	
		14.8829	2.03
		14.9584	3.91
		16.70	1.08
		gamma	
		202.530	97.30
		479.510	90.740
Yttrium-90	64.1 hours	Beta(β-)	
		933.61	100
All nuclear decay data are taken from reference [14]			

Results and Discussion

Fig.3 shows the XRD pattern of the B-E-6% NPs. The XRD pattern has good agreement with the standard JCPDS card 26-0163. As seen; the dopant was not affected by phase structure because of its small amount. The field emission scanning electron microscopy (FE-SEM) images were shown in Figs 4A&D. It is clear that the prepared B-E-6% is nanorods in shape (more like the rice) with diameter ~ 40-60 nm and length 240- 550 nm. Fig. 5 displays the photoluminescence spectrum of B-E-6% and undoped BAM Eu2+ under 365 nm excitation wavelength. As seen, blue emission peak was observed at about 447±2 nm for the B-E-6% %.

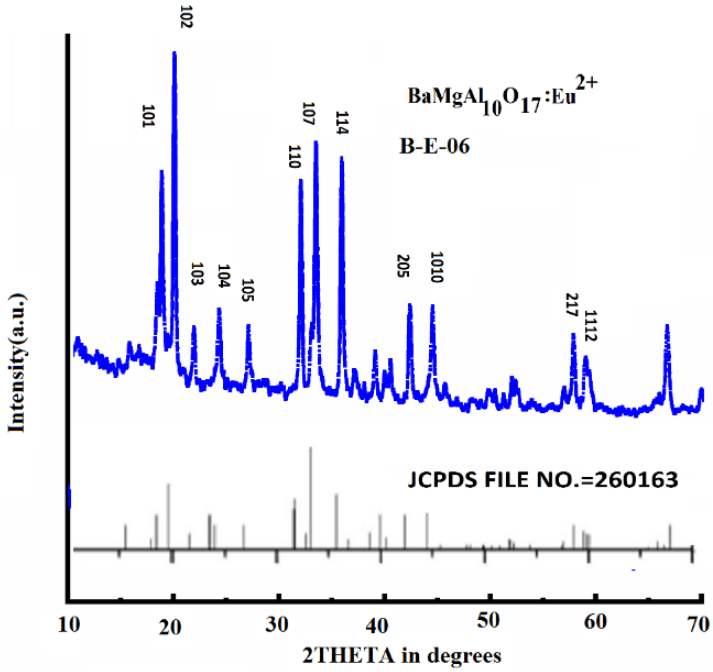

Fig .3. XRD pattern of $BaMgAl_{10}O_{17}:Eu^{2+}$ synthesized by solution combustion method.

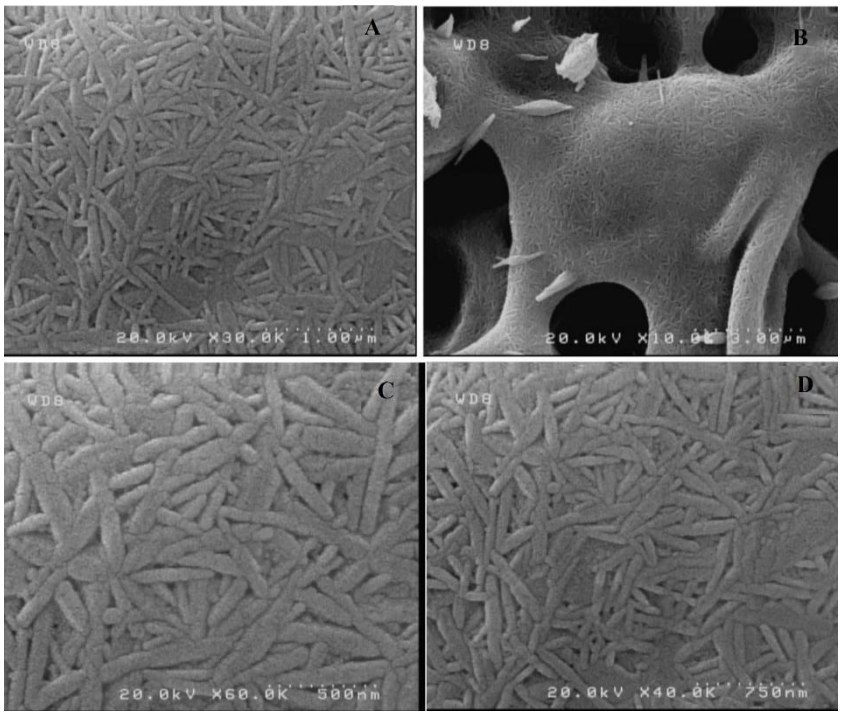

Fig. 4. A&D the typical FE-SEM image of $BaMgAl_{10}O_{17}:Eu^{2+}$ in different magnifications

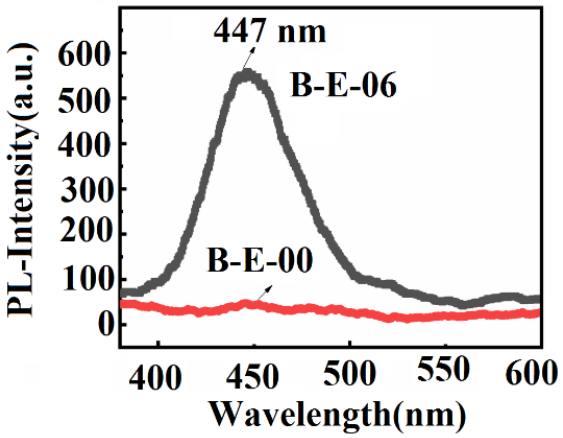

Fig. 5. Photoluminescence spectrum of undoped (B-E-00) and Eu doped $BaMgAl_{10}O_{17}$ (B-E-06)

During the experiment for the study on scintillation properties of sample (B-E-06) at first, the measurements were performed without the scintillation sample under alpha and beta–Ray irradiation and setting of 241Am and 230Th alpha sources directly to the sample (A) in Fig.1. And setting 90S/90Y directly to the sample (B) in Fig 1. In continue, the scintillation pulse height spectra of the B-E-06 (coated on a circular transparent adhesive tape and spread into a PMMA plate), 241Am, 230Th,and 90S/90Y only as well as 241Am, 230Th, 90S/90Y ,and scintillation samples at 300 s under alpha and beta radiation are shown in Figures 6 and 7.

Charge particles hit the BAM: Eu2+ NPs and the produced light reach to the PMT after passing through the coated transparent adhesive tape and produced an electrical pulse. The electrical pulse then is amplified by the preamplifier (Model IAP 3001) and the amplifier (Model IAP 3600) respectively. The pulse height spectrum from the amplified signal was analyzed by MCA (Model IAP 4110) and recorded on a computer [10].

The pulse height spectra of BaMgAl10O17: 6% Eu2+ NPs and a commercial charge particle silicon pixel detector (SPD made in Belgium) under irradiation of 241Am and 230Th alpha sources are shown in Fig. 6.

The wide peak appeared in Fig. 6B, may be attributed to the decays of the 230Th and to their alpha active daughters. A similar results are reported in the literatures for CeF3 Crystal [15], cerium-doped Gd2SiO5 (GSO: 2%Ce) Nano powders [16] and, Ag-doped ZnS [17].

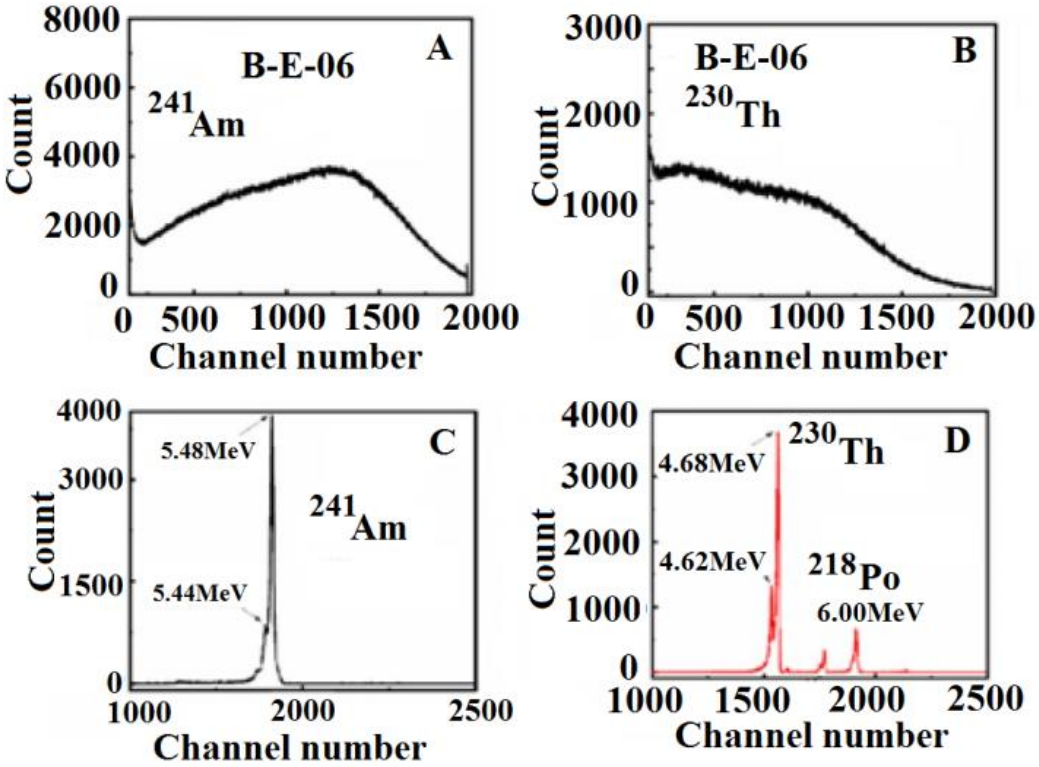

Fig. 6. A&B) the pulse height spectra of BaMgAl10O17: 6% Eu2+ NPs with 241Am and 230Th alpha sources at 300 s. C&D) the pulse height spectra of SPD (commercial charge particle detector, made in Belgium) under same condition

In next step of this study we investigated scintillation property of the BAM: 6% Eu2+, under beta radiation (with sample (B) in Fig.1) Fig.7.A&B. Shows photomultiplier and BAM: Eu NPs backgrounds without radiation source and C&D in Fig.7 are pulse height spectra of background of beta source only and 90S/90Y with transparent PMMA Plate. Fig.7 E&Fshows response of pulse height spectra BAM scintillation to beta radiation and pulse height spectra BAM to beta when a 1.6 mm Aluminum sheet is placed between the beta source and the BAM scintillator respectively.

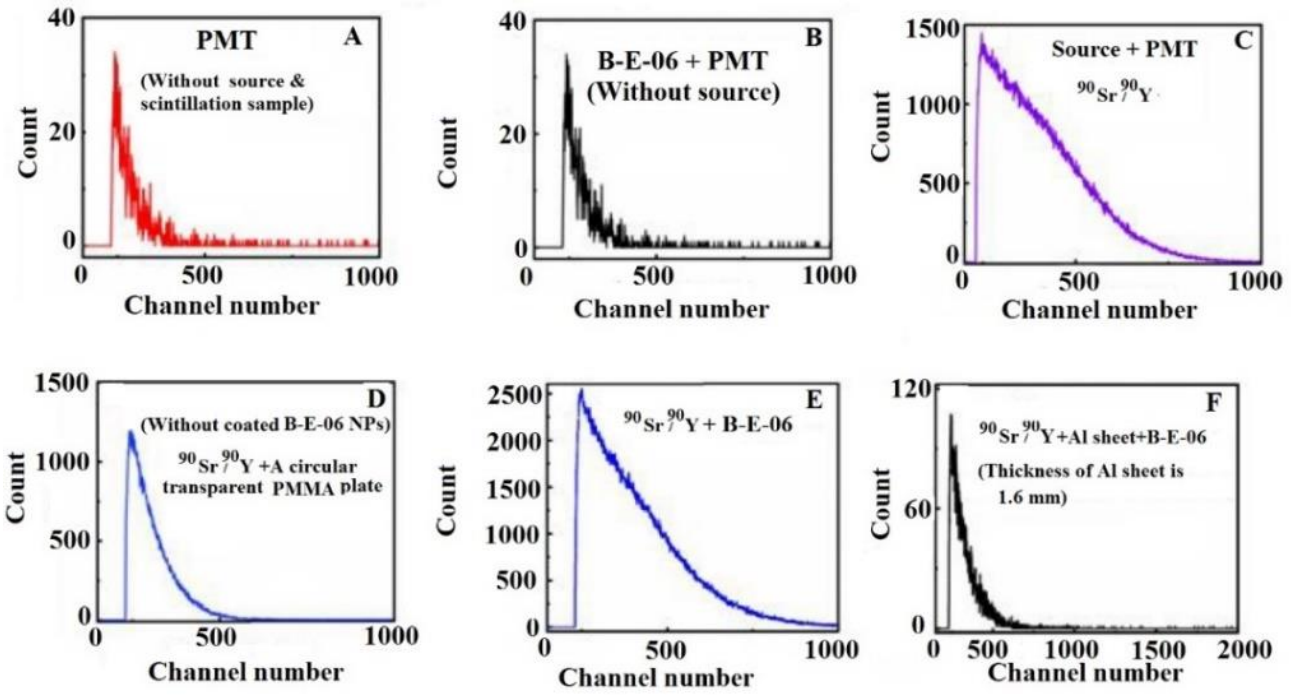

Fig. 7. The scintillation pulse height spectra of the BAM: 6% Eu^{2+}, at 300 s under beta radiation. A) The photomultiplier B) PMT and $BaMgAl_{10}O_{17}$: Eu NPs C) Background of beta source ($^{90}S/^{90}Y$). D) $^{90}S/^{90}Y$ with transparent PMMA Plate. E) $^{90}S/^{90}Y$ and BAM scintillator F) $^{90}S/^{90}Y$ and BAM scintillator and a 1.6 mm Aluminum sheet

Ultimately, we analyzed prepared scintillator sample (Fig. 1A) under 241Am radiation, using a gamma source with a plastic cover and an alpha source without any cover. As seen in Fig. 8A, we observed the pulse height spectrum scintillation sample with a Gamma-ray source, while Fig. 5B showcases the response of BAM: Eu to x-ray with alpha source 241Am. These findings will play a critical role in expanding our understanding of the scintillation properties of BAM: Eu, and will be a valuable addition to the existing body of knowledge.

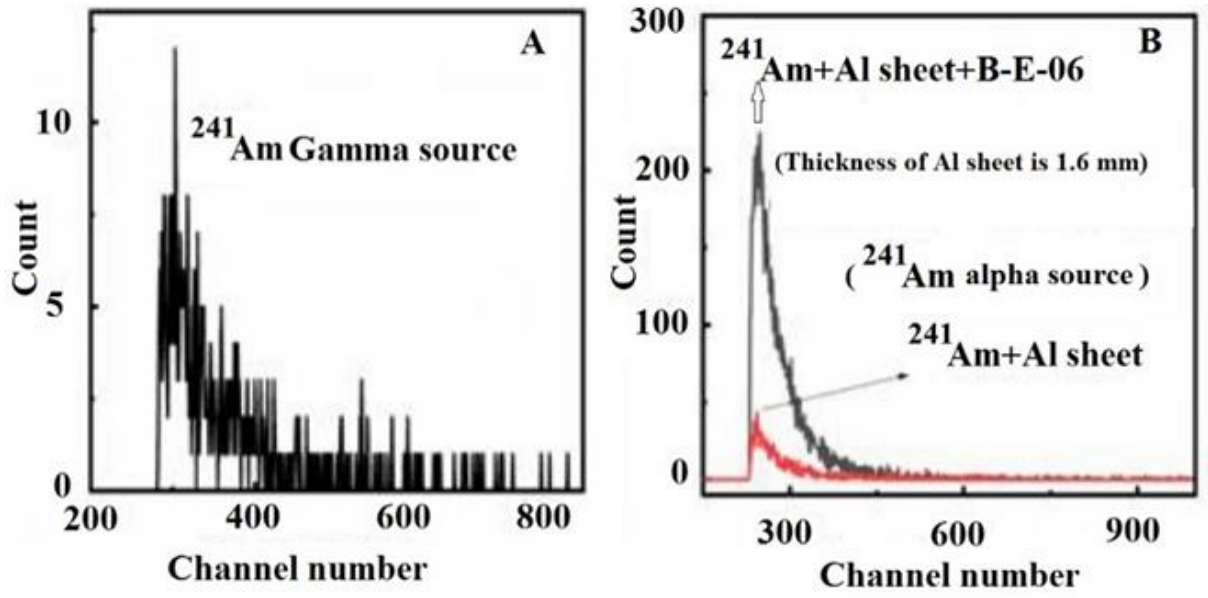

Fig.8. Shows the pulse height spectra of BaMgAl10O17: 6% Eu2+ NPs with A) 241Am Gamma Source B) 241AM with 1.6 mm Aluminum sheet (black spectrum) and source background (red spectrum)

Conclusions

The scintillation properties of BaMgAl10O17: 6% Eu2+ NPs under alpha and beta radiation with 241Am, 230Th and 90S/90Y sources show that BAM: Eu2+ NPs have scintillation properties. The results of the pulse height spectra BaMgAl10O17: 6% Eu2+ NPs can be used for alpha radiation detection as well as the pulse height spectra (Fig.7) show that BaMgAl10O17: 6% Eu can be considered as a Beta charged particle counter. Furthermore results show that scintillation sample with~ 24 µm thicknesses is not sensitive to 241Am gamma source and instead detects low-energy X-rays.

Acknowledgements

This research has been supported by the Imam Hossein University of Tehran and the authors gratefully acknowledge for the financial support.

Data Availability

The data that support the findings of this study are available within the article and its http://doi.org/ [10.1016/j.jlumin.2021.117885].

References

[1] Jaiswal, V.V. Chandar Rao, P. Sreelatha, C. J. Sai Prasad, A.S and Haranath, D. (2021). Luminescence enhancement of high temperature hexagonal phase of Ba0. 99MgAl10O17: Eu0. 01 nanophosphor synthesized at moderately low temperature, Materials Science and Engineering: B 263 114791.

[2] Yang,C. V . Som, S. Das, S. and Lu,C. H. (2017) . Synthesis of Sr 2 Si 5 N 8: Ce 3+ phosphors for white LEDs via efficient chemical vapor deposition, Sci. reports 7, no. 1. 45832.

[3] Terraschke, H. and Wickleder, C.(2015).UV, blue, green, yellow, red, and small: newest developments on Eu2+-doped nanophosphors, Chemical reviews 115, no. 20 . 11352-11378.

[4] Van Eijk, C. W. (2002). Inorganic scintillators in medical imaging. Physics in medicine & biology, 47(8), R85.

[5] Yanagida,T.(2018).Inorganic scintillating materials and scintillation detectors.
Proceedings of the Japan Academy, Series B, 94(2), 75-97.

[6] Belli, P. Bernabei, R. Cerulli, R. Dai, C. J. Danevich, F. A. Incicchitti, A. Kobychev, V. V. Ponkratenko, O. A. Prosperi, D. Tretyak, V. I. and Zdesenko, Y.G. (2003).Performances of a CeF3 crystal scintillator and its application to the search for rare processes, Nuclear Instruments and Methods in Physics Research Section A: Accelerators, Spectrometers, Detectors and Associated Equipment 498(1-3) . 352-361.

[7] Yadav, R.S. Pandey, S. K. and Pandey,A. C. (2010). Blue-shift and enhanced photoluminescence in BaMgAl10O17: Eu2+ nanophosphor under VUV excitation for PDPs application, Materials Sciences and Applications 1(1). 25.

[8] Yokota,K. Zhang,S.X.Kimura,K. and Sakamoto, A. (2001). Eu2+-activated barium magnesium aluminate phosphor for plasma displays–Phase relation and mechanism of thermal degradation, J. luminescence 92 (3) . 223-227.

[9] Do,Y. R. Park,D. H. and Kim, S. (2004). Al2 O 3 Nanoencasulation of BaMgAl10O17: Eu2+ Phosphors for Improved Aging Properties in Plasma Display Panels, J. Electrochemical Society 151 (10) . H210.

[9] Ke,W.C. Lin,C. C. Liu, R.S. and . Kuo, M.C. (2010). Energy transfer and significant improvement moist stability of BaMgAl10O17: Eu2+, Mn2+ as a phosphor for white light-emitting diodes, J. Electrochemical Society 157 (8) . J307.

[10] Alizadeh,V. Hosseinkhani,P. Najafi,M. and Abdolahzadeh,M.(2021). A simple solution combustion synthesis and scintillation studies of undoped and Eu-doped BaMgAl10O17 nanoparticles for radiation detection, J. Luminescence 233 . 117885.

[11] Suda,Y. Kamigaki,Y. and Yamamoto, H. (2018) . Blue emission in photoluminescence spectra of the red phosphor CaAlSiN3: Eu2+ at low Eu2+ concentration, J. Applied Physics 123.16 . 161542.

[12] Liang,L. Mei, L. Liu,H. Wang, C. & Liao, L. (2019). Intense broad-band absorption and blue-emitting Ca9La(PO4)5(SiO4)Cl2:Eu2+ phosphor under near-ultraviolet excitation, J. Luminescence 206 . 154-157.

[13] Uheda,K. Hirosaki,N. Yamamoto,Y. Naito, A. Naito, Nakajima,T. and Yamamoto,H. (2006).Luminescence properties of a red phosphor, CaAlSiN3: Eu2+, for white light-emitting diodes, Electrochemical and Solid State Letters 9 (4) . H22.

[14] Nu Chart, Version 4.0.0, Canberra, July. (1998).

[15] López-Lugo, V.H. Rivera-Medina, M. J. and Alonso-Huitrón, J. C.(2021).Quantitative assessing of crystal field, nephelauxetic, and Stokes shift effects on the blue luminescence of Eu2+ ions incorporated in ZnS films, Materials Research Express 8(3) . 036406.

[16] Mohammadi, H. Abdi, M. R. and Habibi, M. H. (2020).Synthesis and scintillation properties of cerium-doped Gd2SiO5 nanopowders under alpha radiation and the importance of selecting the appropriate calcination temperature, J. Luminescence 219 . 116849.

[17] Lee,S.K. Kang,S. Y. Jang, D. Y. Lee, C. H. and Kang,S. M. (2011).Comparison of new simple methods in fabricating ZnS (Ag) scintillators for detecting alpha particles, Progress in nuclear science and technology 1 .

ICNST 2024
International Conference on Nuclear Science and Technology
6- 8 MAY 2024 | Isfahan, Iran

Construction and assessment of fission chamber neutron detector (Paper ID: 1119)

Ebrahim Teimoory[1,3*], Javad Mokhtari[2] , Mohammad Hosein Choopan Dastjerdi[2*], Mitra Athari Allaf[3]

[1] *Atomic Energy Organization, Shahid Ahmadi Roshan Enrichment Complex - Isfahan - Iran.*

[2] *Reactor and Nuclear Safety Research School, Nuclear Science and Technology Research Institute, AEOI,*

[3] *Science and Research branch, Islamic Azad University, P.O. Box: 14515-775, Tehran, Iran*

[*] *Corresponding authors emails:e.tunivesity@gmail.com , mdastjerdi@aeoi.org.ir*

Abstract

Neutron detectors have many applications for measuring neutron flux in neutron sources, fusion reactors, as well as control and safety of nuclear fission reactors. According to the development of research and power reactors in the country, one of the most important detectors needed in this field is a fission chamber gas detector to measure thermal neutron flux. In this research, a fission chamber detector with a fissile layer of uranium 235 with 60% enrichment has been designed and built for the first time in the country. This detector that is named FC400B consists of two coaxial cylinders called anode and cathode and is made of stainless steel. The outer layer of the anode is covered with a very thin layer of U-235. The detector chamber was sealed with argon-nitrogen gas. This detector has been evaluated in Isfahan MNSR research reactor. Various tests have been performed on the detector, including sensitivity to thermal and fast neutrons using irradiation at the neutron beamline of the MNSR. The results showed that this detector could work in pulsed mode and at a neutron flux range of 102-107 n.cm-2.s-1 and with a sensitivity of 0.1cps/ (1000 n.cm-2.s-1). A spectroscopy software has been also developed, with the help of which the spectroscopy of fission fragments has been also performed, and the results showed that the spectrum of gamma and alpha rays can be easily discriminate from the spectrum of fission fragments.

Keywords: Fission Chamber, Fission Fragments, Thermal Neutron Detector, Heavy Ion Spectroscopy, MNSR Reactor.

Introduction

Due to the neutral electrical charge of neutron particles, their detection by direct ionization method is not possible. In terms of energy, neutrons are usually classified into three categories: thermal, epithermal, and fast. The majority of neutron reactions are with the nucleus of the atom and they have almost no reaction with orbital electrons. The detection of neutrons is done in the form of indirect ionization and by the penetration of this uncharged particle into the nucleus of the atom during the process of nuclear reactions, creating fundamental changes in the nucleus and finally producing ions as a result of this reaction, one of the most important nuclear reactions for thermal neutrons is the nuclear fission reaction of fissile elements. One of the basic instruments in nuclear reactors to detect neutrons is the fission chamber. The neutron detector in nuclear reactors can be used to control the neutron flux in the core of the reactor (In-Core Fission Chamber) and monitor the environment around the reactor (EX-Core Fission Chamber). These detectors can be used in three modes; current, pulse and mean square voltage (MSV) modes. Fission chamber detector is usually made of two coaxial cylindrical electrodes. Usually, the outside of the inner cylinder is coated with a fissile material. The inner cylinder (anode) and outer cylinder (cathode) are kept coaxial and stable with respect to each other by ceramic insulation. The space between these cylinders is filled with a gas such as argon-nitrogen with a pressure of 1-4 Bar. After the collision of thermal neutrons with the fissile material and causing nuclear fission, fission fragments such as barium and krypton, which have a very high ionization ability and have energy of 60 MeV~90 MeV, are created and when they collide with the filling gas molecules between the two electrodes, an ion electron pair is produced. By applying a voltage of approximately 500 volts, an electric field is created between two electrodes, which causes the electron-ion shift. The charges created by the pre-amplifier electronics of the detector are collected, amplified, filtered and displayed and counted as pulses, which the counted pulses are equivalent to the flux of thermal neutrons.

Various researches have been conducted in the field of design, simulation and construction of neutron detectors. Neutron detectors are usually made of 3He, BF3, SPND, fission chamber type [1-6]. Various types of fissile materials such as U-235 and Pu-239 have been used to detect thermal neutrons, or fissionable materials such as U-238 and Pu-242 have been used to detect fast neutrons [18]. The type of filling gas and its amount can affect the sensitivity of the detector. Argon mixed with nitrogen gas is usually used in making these detectors. In the type of detectors inside the core that work at high temperature, pure argon gas is usually used [13]. In order to improve the detector and reduce the manufacturing cost, various software are used to optimize the parameters of the fission chamber detector. For example, in research by Mr. Alfonso, a software was developed to simulate and optimize the various

parameters of the fission chamber detector [10]. The fission chamber detector FC167 made by Centronic company was evaluated using X-Ray and neutron radiography by Mr. Borella and his colleagues, and the mechanical dimensions, thickness of the electrodes and the length of the sensitive area of the detector were obtained. Using the MCNP code to simulate the effect of self- absorption, the effect of the thickness of the fissile layer and the density of the fissile layer were evaluated [11].

In this research, according to the information available in other research and similar activities that have been done on the construction of this type of detectors, a preliminary model was constructed and evaluated. The main difference between this research and other similar researches is in the fissile material, that is, the use of uranium with 60% enrichment instead of using uranium with enrichment above 90%, which is worth mentioning that the reason for this is the national limitation in access and use of Uranium with higher than 60% [1].

Materials and methods for construction of fission chamber detector

As shown in Figure 1, both the inner and outer detector cylinders were made of 316 steel with high precision. The diameter of the outer cylinder of the detector (cathode) was considered to be 25 mm and the thickness was 1 mm, and it is electrically connected to the ground of the electronic circuit. While the diameter of the inner cylinder (anode) is

22.5mm and it is made with the same thickness of 1mm and it is electrically connected to a voltage of 500 volts. The design specifications of the desired detector are in accordance with the FC167 detector of Centronic Company. In fact, the designed detector is an example of reverse engineering of the detector. According to neutron radiography FC167 by Mr. Borella, the desired detector specifications include diameter equal 25.4mm, the distance between the electrodes equal to 1.5mm, gas pressure 4.5atm including the composition of 95% argon and 5% nitrogen, the sensitive length of the detector127mmand with enriched uranium 93%, the material of the electrode is stainless steel. From the mechanical point of view, the built detector (FC400B) is completely the same as the FC167 detector and the only difference is that in the built detector, due to the lack of access to 90% enriched uranium, 60% enriched uranium was used. In this research, the main goal is to achieve the technology of making fission chamber gas detector.

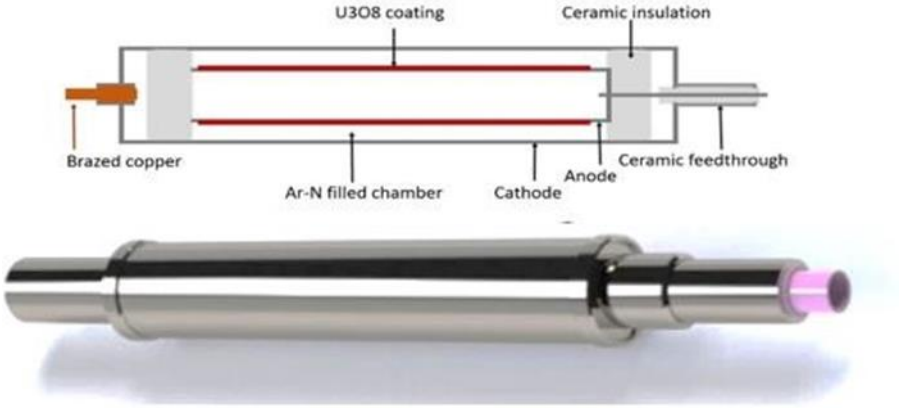

Fig.1. Schematic of the built fission chamber detector FC400B(top) constructed fission chamber detector FC400B (bottom)

There are various methods for uranium coating, one of the simplest methods that has a good control over the uniformity and thickness of the fissile layer is the electrodeposition method. This method includes a plating chamber that consists of a platinum anode, a steel cathode, a solution containing a fissile material with pH = 2.5, and a stepping motor to rotate the desired cathode on which the fissile layer is coated so that the desired material is uniformly coating. The amount of uranium in the solution and the plating time have been done for a layer with an approximate thickness of 1.5 microns. After coating for a specified period of time, the cathode on which the fissile material is coated must be heated for 120 minutes at a temperature of 650 degrees Celsius in the furnace so that all the uranium compounds in the coated layer turn into uranium oxide (U3O8). In the next step, detector parts are assembled and welding of the upper and lower parts of the detector is done. Become One of the interfering molecules in the detector chamber is the oxygen molecule. Because in the process of nuclear fission and the movement of fission fragments, a large number of electron-ion pairs are created, and on the other hand, oxygen molecules are very electrophilic, so the detector must be emptied of all oxygenated molecular compounds, including O2, H2O, CO2. This is done using a high vacuum system according to Figure 2.

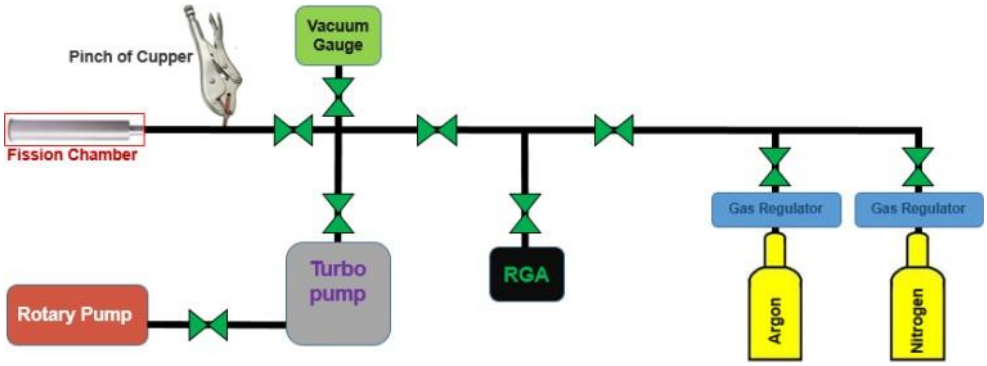

Fig.2. Schematic of the vacuum system and sealing of the detector

According to Figure 2, after emptying and closing the pumps, the detector chamber was sealed with a combination of argon gas (95%) and nitrogen (5%) through a copper tube. After sealing the detector for testing with neutron sources, this detector was transferred to Isfahan Miniature Research Reactor (MNSR). In order to set up and test the desired detector, an electronic system including preamplifier, amplifier, pulse shaping, pulse counter and a fission fragment spectroscopy software was implemented according to Figure 3.

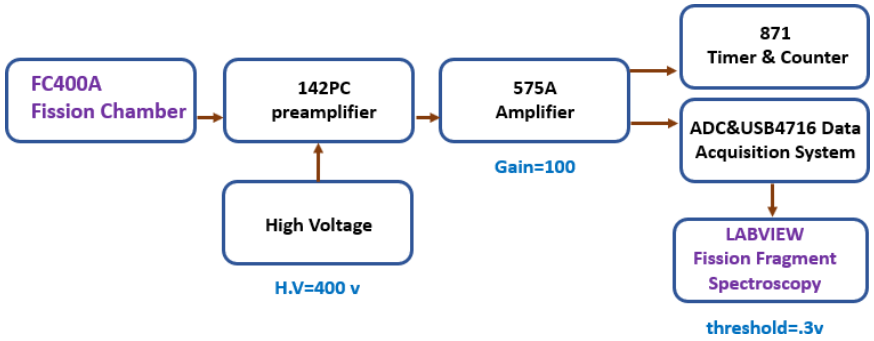

Fig.3. Electronics required to set up the fission chamber detector

Fission fragment spectroscopy software was designed in LabVIEW environment. There are different types of spectroscopies, including x-ray spectroscopy, gamma-ray spectroscopy, alpha particles, and ions. This software was design for spectrometry of heavy ions caused by nuclear fission. The signal processing part of a spectroscopic system includes an analog to digital signal converter to transmit the created pulses and a suitable software for signal analysis. In this design, a USB4716 DAQ card made by Advantech was used. The sampling rate of this card for analog input is 200KS/s and the analog to digital resolution is 16 bits. After selecting the USB4716 card in the LabVIEW program, the pulse input is given to a peak detector module the lower level value is set by the threshold option (Figure 4), then the

peaks detected in the module (general histogram) are grouped and collected in channels and the desired spectrum is drawn. Also, the ability to select the sub-peak level is also included in the software so that the net count can be measured. In addition, in the separator software, the capabilities of the software were added so that the low level of the signal, which includes the alpha spectrum, gamma spectrum and background noise, can be removed.

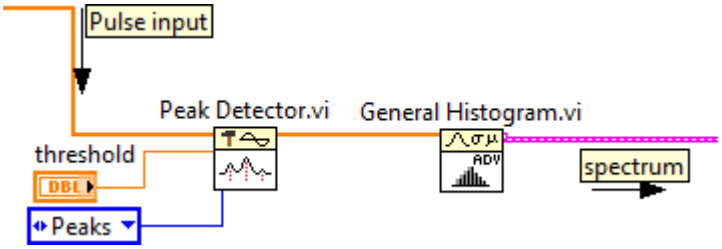

Fig.4.A part of the fission fragment spectroscopy program including the peak detector module (LabVIEW)

Results and Discussion

Evaluation of sensitivity to thermal and fast neutrons in the neutron radiography beamline channel of the MNSR reactor Plotting the plateau curve and obtaining the working voltage of the detector, checking the linearity of the response of the detector to changes in the neutron flux and comparing it with a commercial model were investigated in [1]. The sensitivity of the detector to thermal and fast neutrons was checked at the top of the neutron radiography channel figure.0. The neutron flux at the desired point was changed from 2*102n/cm2.s -2*105n/cm2.s. In the first stage, the detector was placed in a flux of 1*105n/cm2.s, then the voltage of the detector was changed from 50 to 1000 volts, and according to the drawn plateau curve, the working voltage of the detector was considered to be 500 volts[1]. After adjusting the working voltage of the detector and changing the neutron flux, the detector results were recorded. Figure 5 shows the installation location of the detector above the neutron radiographic beamline in the Isfahan MNSR. According to Figure 3, the output of the detector is collected by USB4716 DAQ cards. Figure 6 clearly shows that the amplitude of the pulse produced by fission fragments with an energy of 90 MeV is much higher than the pulses caused by alpha particle with a maximum energy of 5 MeV, which is caused by the spontaneous fission of the fissile layer. Therefore, discriminate the spectrum of particle with 5 MeV energy is easily done using a software discriminator that is implemented in the fission fragment spectroscopy software. The spectrum of fission fragments of a commercial detector with two fission layer by thicknesses 0.02 micron and 0.7 micron was checked and drawn[2]. In figure 6, recorded from the output pulse of detector FC400B, compared to figure 7,

which is the output of a commercial detector, it shows that the thickness of the coated fissile layer of the FC400B detector is over 7 microns.

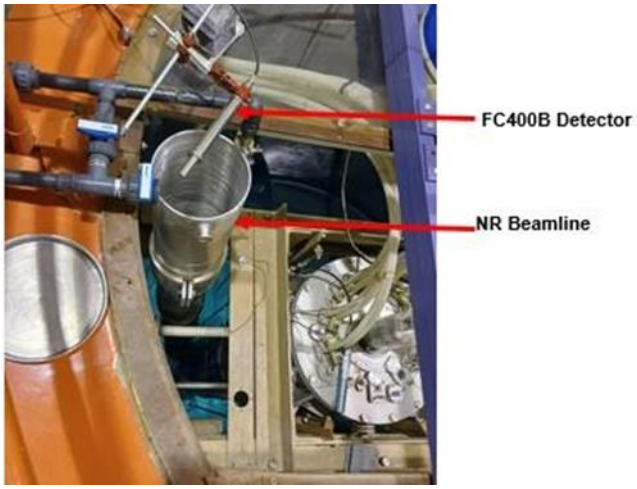

Fig.5. Placement of the FC detector at the outlet of the NR beamline in the Isfahan MNSR

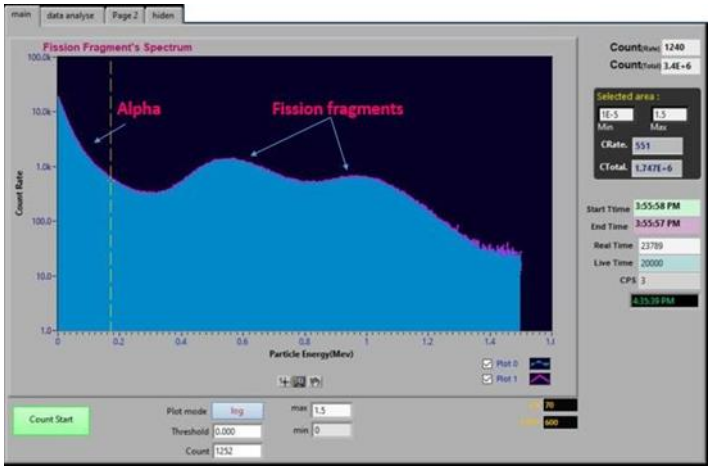

Fig.6. The recorded spectrum of the FC400B detector output at the NR beamline outlet at the maximum power of the reactor

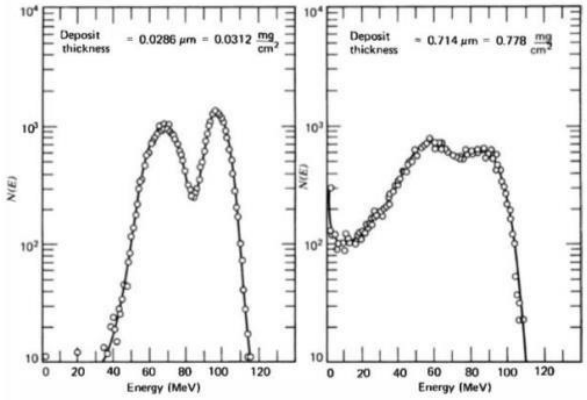

Fig.7. The spectrum of fission fragments of a commercial detector with two fission layer by thicknesses 0.02 micron and 0.7 micron was checked and drawn [2].

After recording the results related to thermal neutrons, according to Figure 8, in order to check the sensitivity of the detector to fast neutrons, a 5 mm thick cadmium sheet was placed between the detector and the NR beamline channel until the thermal neutrons were completely absorbed and only fast neutrons reach the detector. Then the output pulses of the detector are recorded and shown in Figure 9. Compared to Figure 7, almost no pulse with energy higher than 5 MeV is generated. On the other hand, the spectrum recorded in Figure 9 is almost the same as the output spectrum of the detector in the state where no neutrons reach the detector (reactor off) and only the pulses caused by the alpha background related to the fissile layer are created in both states. Therefore, it can be concluded that the built detector has very little sensitivity to fast neutrons.

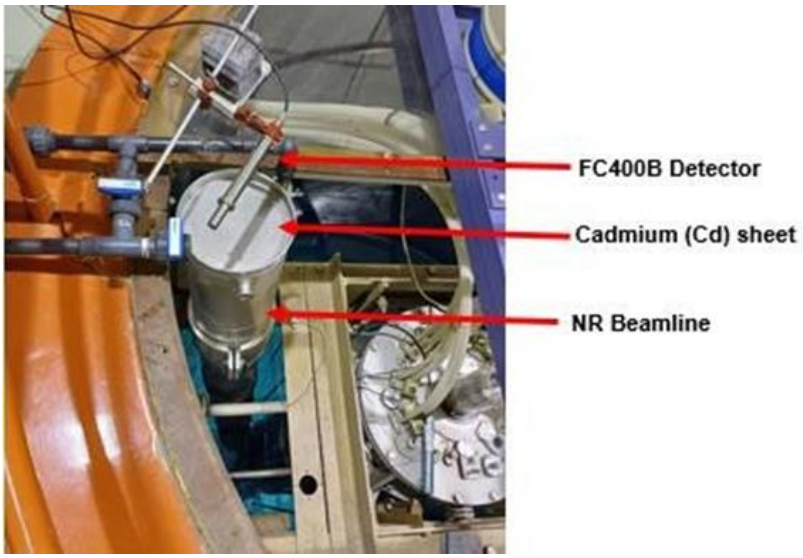

Fig.8. Placement of the FC detector at the outlet of the NR beamline in the Isfahan MNSR and cadmium sheet for absorption thermal neutron.

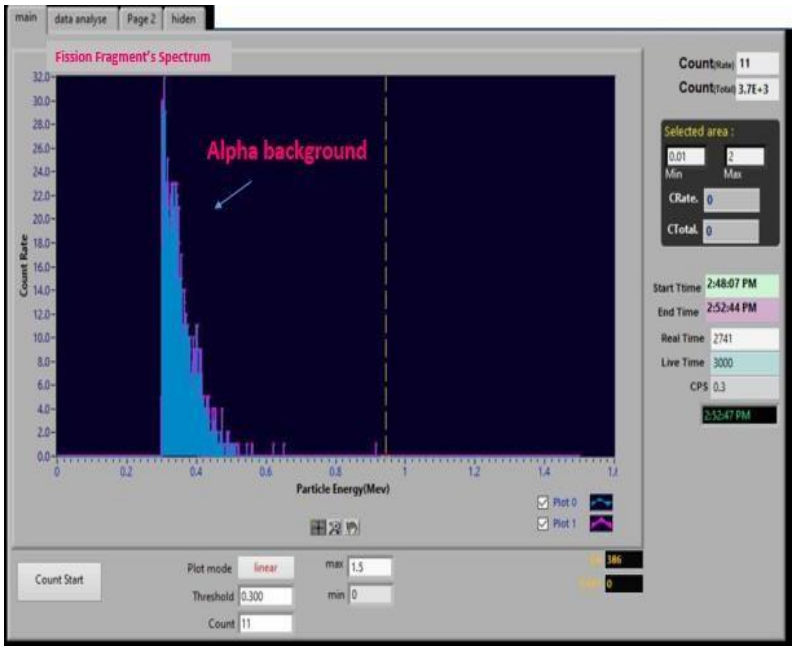

Fig.9. The recorded spectrum of fission fragment related to the fast neutron of the FC400B detector output at the NR beamline outlet at the maximum power of the reactor

Conclusion

In this research, the main goal is to achieve the technology of making fission chamber gas detector which is one of the most important needs of research and power reactors in the country can be solved by localizing and obtaining the technology of construction a fission chamber detector. In the first step, a fission chamber neutron detector was built for the first time in the country, and then sensitivity to thermal neutrons, sensitivity to fast neutrons and range using by MNSR reactor was evaluated. Using the software developed in LabVIEW, the spectroscopy of fission fragments was performed, and the energy spectrum of alpha and gamma can be easily discriminate from the energy spectrum of fission fragments in the software. In the next step and future studies, using simulation and further investigation, in order to improve the sensitivity, various parameters such as filling gas pressure, electrode distance, increasing the length of the sensitive area, reducing the thickness of the fissile layer, increasing the purity of the fissile material from 60% to 90% efficiency and the type of electrodes can be changed in this detector and the design and construction of the next versions can be done in the most optimal way possible.

References

[1] Teimoory, E., et al. "Development and characterization of fission chamber neutron detectors in Isfahan miniature neutron source reactor." Radiation Physics and Chemistry 215 (2024): 111360.
[2] Knoll, G. F. (2010). Radiation detection and measurement. John Wiley & Sons.
[3] Crane, T. W., & Baker, M. P. (1991). Neutron detectors. Passive Nondestructive Assay of Nuclear Materials, (13), 1-28.
[4] Peurrung, A. J. (2000). Recent developments in neutron detection. Nuclear Instruments and Methods in Physics Research Section A: Accelerators, Spectrometers, Detectors and Associated Equipment, 443(2-3), 400-415.
[5] Ahmed, S. N. (2007). Physics and engineering of radiation detection. Academic Press.
[6] Chabod, S., Fioni, G., Letourneau, A., & Marie, F. (2006). Modelling of fission chambers in current mode—analytical approach. Nuclear Instruments and Methods in Physics Research Section A: Accelerators, Spectrometers, Detectors and Associated Equipment, 566(2), 633-653.
[7] Jammes, C., Filliatre, P., Geslot, B., Oriol, L., Berhouet, F., Villard, J. F., & Vermeeren, L. (2010). Research activities in fission chamber modeling in support of the nuclear energy industry. IEEE Transactions on Nuclear Science, 57(6), 3678-3682.
[8] He, Y., QIAN, W., HE, Z., CUI, W., ZHAO, Q., Chen, Z., & Wang, Z. (2017).
[9] Excore Neutron Flux Monitoring Method for an Accelerator Driven Sub-critical System. 原子核物理评论, 34(2).
[10] Miller, J. F. (1999). Fission chambers. Wiley Encyclopedia of Electrical and Electronics Engineering, 1-4.
[11] Antolínez, A., & Rapisarda, D. (2016). Fission chambers designer based on Monte Carlo techniques working in current mode and operated in saturation regime. Nuclear Instruments and Methods in Physics Research Section A: Accelerators, Spectrometers, Detectors and Associated Equipment, 825, 6-16.
[12] Borella, A., Rossa, R., & van Der Meer, K. (2013). Modeling of a highly enriched 235U fission chamber for spent fuel assay. Annals of Nuclear Energy, 62, 224-230.
[13] Taieb, J., Laurent, B., Bélier, G., Sardet, A., & Varignon, C. (2016). A new fission chamber dedicated to prompt fission neutron spectra measurements. Nuclear Instruments and Methods in Physics Research Section A: Accelerators, Spectrometers, Detectors and Associated Equipment, 833, 1-7.
[14] Bell, Z., Harrison, M., Holcomb, D., Britton, C., & Bull, N. (2012). Materials Selection for a High Temperature Fission Chamber. Oak Ridge, TN, USA.
[15] Jammes, C., Filliatre, P., Loiseau, P., & Geslot, B. (2012). On the impact of the fissile coating on the fission chamber signal. Nuclear Instruments and Methods in Physics

Research Section A: Accelerators, Spectrometers, Detectors and Associated Equipment, 681, 101-109.

[16] Poujade, O., & Lebrun, A. (1999). Modeling of the saturation current of a fission chamber taking into account the distorsion of electric field due to space charge effects. Nuclear Instruments and Methods in Physics Research Section A: Accelerators, Spectrometers, Detectors and Associated Equipment, 433(3), 673-682.

[17] Hadad, K., & Hashemi, M. (2009). Analysis and optimization of a fission chamber detector using MCNP4C and SRIM monte carlo codes. Iranian Journal of Science and Technology (Sciences), 33(3), 269-276.

[18] Haddad, G. N. (1983). Drift Velocity of Electrons in Nitrogen? Argon Mixtures. Australian journal of physics, 36(3), 297-304.

[19] Elter, Z. (2016). Neutron monitoring based on the higher order statistics of fission chamber signals. Chalmers Tekniska Hogskola (Sweden).

[20] Mokhtari, J., F. Faghihi, and J. Khorsandi. "Design and optimization of the new LEU MNSR for neutron radiography using thermal column to upgrade thermal flux." Progress in Nuclear Energy 100 (2017): 221-232.

[21] Dastjerdi, M. C., Mokhtari, J., Asgari, A., & Ghahremani, E. (2019). A neutron radiography beamline relying on the Isfahan Miniature Neutron Source Reactor. Nuclear Instruments and Methods in Physics Research Section A: Accelerators, Spectrometers, Detectors and Associated Equipment, 928, 20-25.

[22] Mokhtari, J., & Dastjerdi, M. C. (2023). Development and characterization of a large thermal neutron beam for neutron radiography at Isfahan MNSR. Nuclear Instruments and Methods in Physics Research Section A: Accelerators, Spectrometers, Detectors and Associated Equipment, 1051, 168209.

[23] Moslehi, A., Dastjerdi, M. C., Torkzadeh, F., & Mokhtari, J. (2022). Feasibility study of Isfahan MNSR as a calibration thermal neutron source. Nuclear Instruments and Methods in Physics Research Section A: Accelerators, Spectrometers, Detectors and Associated Equipment, 1024, 166026.

[24] https://www.lndinc.com/products/neutron-detectors/307711/

ICNST 2024
International Conference on Nuclear Science and Technology
6- 8 MAY 2024 | Isfahan, Iran

Investigation of Spark Plasma Sintering on Dosimetric Properties of Calcium Phosphate Samples (Paper ID: 1133)

Mohammad Rafieian[1], Armin Mosayebi[2] ,Hamideh Daneshvar[2*]

[1]Pars Isotope Company, Tehran, Itan

[2]Radiation Application Research School, NSTRI, Tehran, Iran

Abstract

In the range of 10-1000 Gy, there are not many choices to cover the entire range. Considering the equivalence of calcium phosphates with bone minerals, these materials can be used as thermoluminescence dosimeters. The purpose of this article is to convert powder into tablets using the SPS method under different conditions of temperature and pressure, and then dosimetry studies will be performed. The results show that most samples have a linear behavior in the investigated dose range. Also, the temperature range of Tm in the glow curve is in the range of 195-235℃. The weakness of these samples is the fading effects and most samples lose their information within 30 days. According to the obtained results, the conditions of conversion into tablets are the most important factors in improving the dosimetry parameters, and it is not necessarily possible to achieve better dosimetry results than powder with any conditions.

Keywords: calcium phosphate, dosimetry, thermoluminescence, spark plasma sintering

Introduction

The irradiation process has been widely investigated during the last 50 years [1]. In various applications of processing radiation, doses in the range of 10 Gy to 50 kGy are needed to achieve the desired result [2]. Dosimetry provides an independent and effective method for the development and control of many industrial processes. [3]. In the range of 10-1000 Gy, which is the dosimetry range of agricultural products, there are not many choices that cover the entire range. Therefore, the need for a reliable, portable, mechanically strong, inexpensive dosimeter with easy manufacturing capability and a convenient reading system, to use in daily dosimetry of agricultural products, seems necessary [4]. Thermoluminescence (TL) is the light emitted from an insulator or semiconductor when heated after exposure to ionizing radiation. The thermoluminescence method

is a suitable and well-known method for passive dosimetry [5], [6]. Thermoluminescence has a glow curve consisting of one or more peaks. The glow curve is the output of the electric charge in terms of temperature [8]. The temperature peak in the glow curve has the highest intensity and usually has high stability and is not affected by fading effects [9].

Different types of materials have been used to make thermoluminescence dosimeters. Recently, new ideas have been formed based on the use of new materials as thermoluminescence dosimeters. Considering the equivalence of calcium phosphates with bone minerals, these materials can be used as thermoluminescence dosimeters. Calcium phosphates have medical applications as bone replacement ceramics. The dosimetry aspects of the use of these materials are due to the wide use of X-rays in medical applications. Due to the properties of these materials, they have recently been used in retrospective dosimetry [10], [11]. Different methods such as solid-state synthesis, mechanical-chemical, multiple emulsion, hydrothermal, hydrolysis and sol-gel have been developed for the synthesis of this material, and by using these methods, crystals have been produced with dimensions nanometer to micrometer [1], [15], [16].

As it is known, the use of powder will cause non-uniform distribution of the thermoluminescent material on the reader tray. Also, the use of powder causes contamination of the PMT, its filter, and therefore it will cause a background response in the output of the reader. Another disadvantage of using powder is the creation of an unwanted response due to the mechanical stress between the thermoluminescence materials during reading, and therefore it causes an increase in the detection threshold and causes errors in dose determination. Spark plasma sintering (SPS) is a method for sintering of powder materials (conductive and non-conductive). This process is performed by heating the powder materials inside the furnace and below the melting point [18]. The working temperature is (200 to 2400 degrees Celsius), which is usually 200 to 500 degrees Celsius lower than the usual sintering methods, hence SPS is known as a low temperature technology [18], [19]. This method is used in the production of sensitive ceramic parts and nanostructure parts, the production of biological materials and porous materials and thermoelectric semiconductors, and the welding and joining of dissimilar metal and ceramic parts. In this work, SPS method has been used to convert calcium phosphate samples into tablets. Also, the temperature and pressure of the

SPS device have been investigated on the dosimetry response of calcium phosphate samples, both synthesized and purchased.

Research Theories

At first, calcium phosphate samples, including hydroxyapatite and beta-tricalcium phosphate, are synthesized by solid state method. The SPS device in the Materials and Energy Research Institute has been used to convert powder into tablets. In this method, temperature and pressure are applied to the powder at the same time. This work has been performed twice under different conditions. At the first time, the pressure and temperature are 400 MPa and 650 ℃ respectively, and the second time pressure and temperature are 400 MPa and 685 ℃ respectively. To remove the graphite material around the tablet, sanding method should be used. Sandpapers with different hard numbers (800, 1000, 2000) are used. After sanding, felt is used at the end of the work. To cut tablets with a diameter of 1.5 cm and a thickness of 1 mm, the equipment available in Dental Research Institute Tehran University of Medical Sciences is used. The next step is to irradiate powder samples and tablets using a 60 cobalt Gamma cell source available in the dosimetry laboratory located in the Nuclear Science and Technology Research Institute. Finally, the reading is done using the Harshaw device, 4500 model. This work is done at a temperature of 50℃ to 350℃ with a heating rate of 5℃/s.

Experimental Results

In this article, thermoluminescence dosimetry factors for powders and tablets, such as glow curve, dose-response curve, fading and reproducibility, and dosimetry results tables are presented. In these tables, along with the specifications of the samples, the dosimetry linear range, the linear relationship, and the R2 determination coefficient value in this range, the average temperature value of Tm is specified. In Table 1, the notations made for the changes of different quantities are displayed separately.

Table 1: Changes in different quantities of calcium phosphate pellet samples

quantity	Notations
Merck HAP	H(M)
Synthesized HAP	H(S)
Merck β-TCP	B(M)
Synthesized β-TCP	B(S)

XRD analysis

Figure 1 shows the results of XRD analysis related to synthesized and commercial powder samples of HAP and β-TCP. The results of the analysis show the correctness of the synthesis performed for the synthesized samples, by the standards related to XRD analysis, which is specific to calcium phosphate samples.

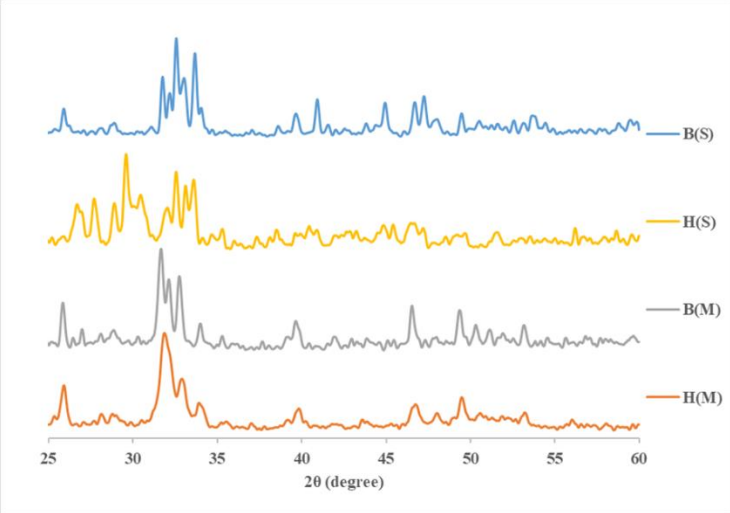

Figure 1- Output results of XRD analysis

Comparison of powders

Figure 2 displays the glow curves of powder samples in radiation with a 400 Gy dose.

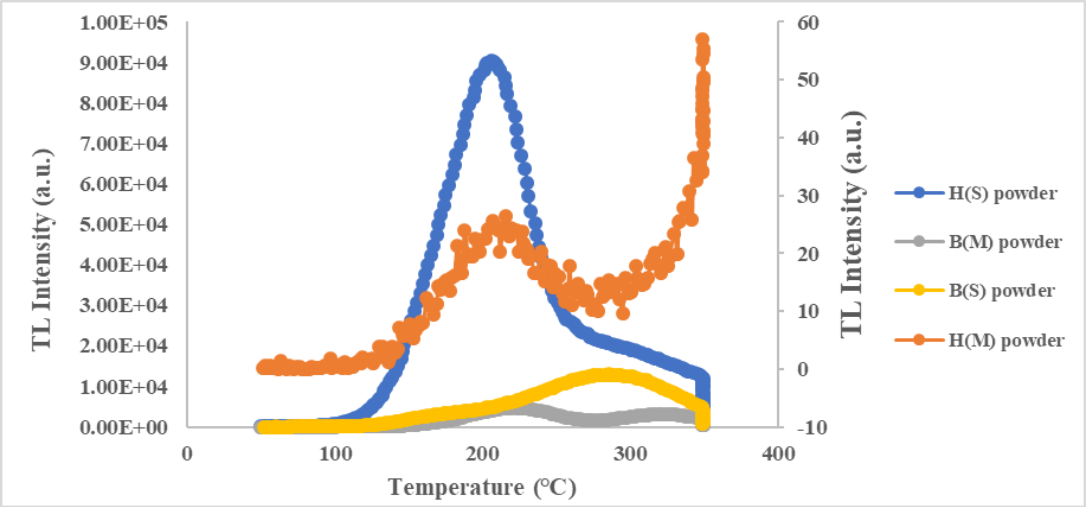

Figure 2- TL glow curve of synthesized powder samples at 400 Gy dose

Due to the large difference in the results, the glow curve of the sample H(M) is displayed in the figure above on the right side

Table 2- Dosimetry response results of powder samples

Sample name H (M)	Linearity Range	Linearity Formula	R^2 in Linearity Formula	Average Temperature	STDEVA in Average Temperature
H (M) powder	20-1000	y = 0.0005x + 0.04	R^2 = 0.9815	215	12.44
B(M) powder	20-1000	y = 0.0346x + 3.1737	R^2 = 0.9785	234.125	21.42386853
H (S) powder	20-800	y = 0.3265x + 17.495	R^2 = 0.9868	231.86	19.07
B (S) powder	20-600	y = 0.0808x + 26.55	R^2 = 0.9812	297.29	27.29

According to the results obtained from Table 2, all the samples except B(s) are linear in the desired range. Also, according to the comparison of the glow curves, it can be concluded that the synthesized hydroxyapatite powder has the most suitable glow curve. According to the standard deviation calculated in Tm, this sample follows the first-order kinetics. Because in first-order kinetics, the position of Tm does not change in different doses.

The peaks of all powders are approximately in the range of 210-230 ℃, but the Tm in B(s) sample is much higher and appears at a temperature of approximately 300 ℃. Figure 3 shows the dose-response curves of the powder samples for the 200-800 Gy irradiation range.

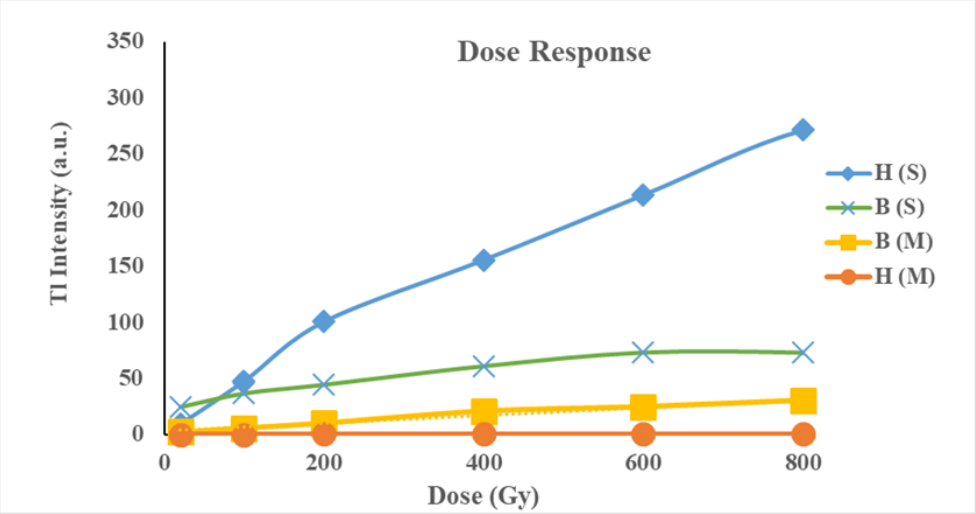

Figure 3 -Dose-response diagram of synthesized powder samples

From the results of the dose-response curve, it is clear that the synthesized powders have a greater response than the purchased powders (MERK). Calcination of HAP powders at 600℃ and BTCP at 900℃ can increase the dosimetric response. These results have been proven in experiments that have already been done by other researchers. To determine the fading effects, the powder samples were irradiated at a dose of 400 Gy and then the reading was done in a period of 28 days. The fading factor is displayed in Figure 4.

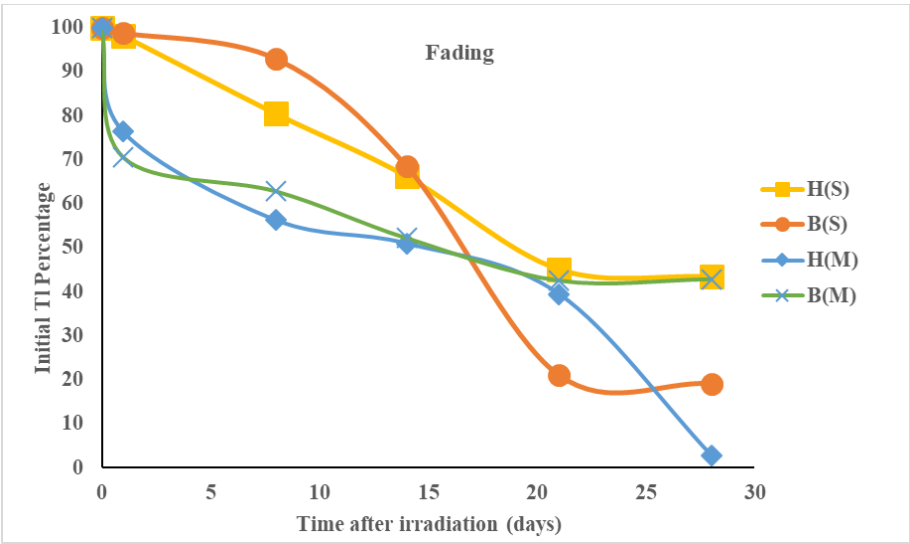

Figure 4: fading effects of powders at 400 Gy and duration of 28 days

If the effects of fading are important, H(S) and B(M) powders have a better performance than the other two powders and have more than 40% of their initial response in a period of 4 weeks (28 days). H(M) powder and B(S) powder lose 98% and 80% of their initial response in this period, respectively. According to these results, in terms of fading effects, H(S) powder has a more favorable condition.To investigate the repeatability factor, the powder samples were tested 5 times continuously at a dose of 400 Gy. For zeroing after each irradiation, the samples are placed at 400℃ for half an hour. (Figure 5)

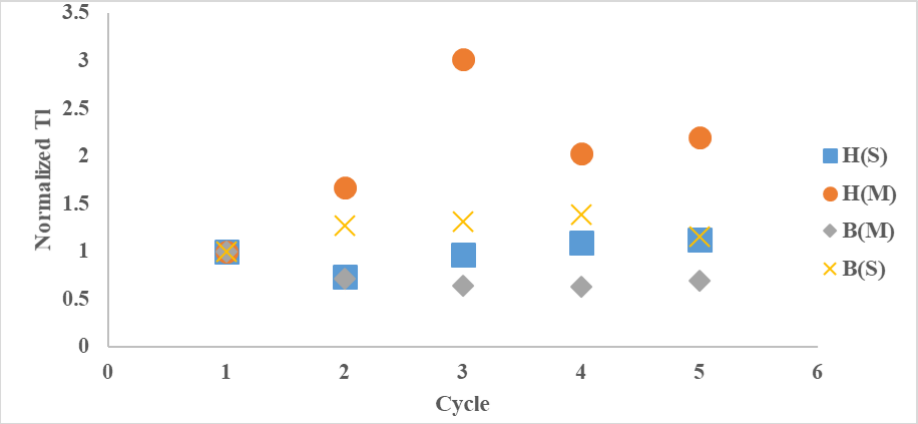

Figure 5: repeatability factor diagram of powders

In this figure, the thermoluminescence intensity is normalized to one and B(S) powder is more suitable for the reproducibility process due to very small changes. H(M) sample has the highest percentage of changes with 37%, and samples H(S) and B(M) have the same change percentage as sample B(S).

Comparison of tablets

The dose response curve of the first time tablets

In the first stage, tablets are made at a temperature of 650 ℃ and a pressure of 400 MPa. As shown in Figure 6, in general, the sensitivity of the dose-response curve of the manufactured tablet samples is higher than that of the powder samples. The sensitivity of B(S) and H(S) tablets are almost 15 and 3 times more than powders respectively. Therefore, at this stage, it shows that better results can be achieved by turning powders into tablets.

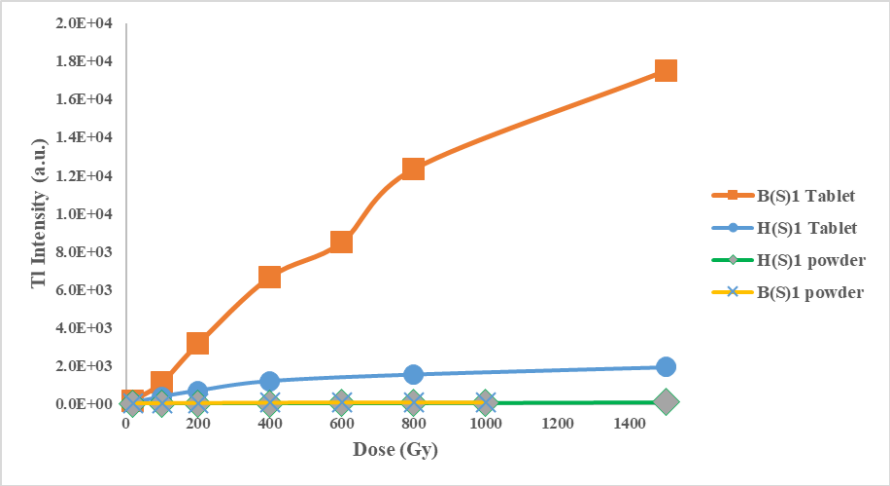

Figure 6: Dose-response diagram of the tablets in the first stage

Table 3- Dosimetry response results of tablet samples at the first-stage

Sample name H (M)	Linearity Range	Linearity Formula	R^2 in Linearity Formula	Average Temperature	STDEVA in Average Temperature
H (S)1 tablet	20-400	y = 2.9352x + 56.885	R^2 = 0.9904	201.00	28.18
B (S)1 tablet	20-800	y = 15.393x - 99.982	R^2 = 0.9916	202.62	8.32
H (S) powder	20-800	y = 0.3265x + 17.495	R^2 = 0.9868	231.86	19.07
B (S) powder	20-600	y = 0.0808x + 26.55	R^2 = 0.9812	297.29	27.29

As it is clear in Table 3, in the first stage by turning into a tablet, the Tm in the glow curve is shifted to lower temperatures. Also, as shown in this table, due to the lower value of the standard deviation of the B(S)1 peak compared to H(S)1, it is more likely that the glow curves obtained from the B (S)1 tablet follow the first oeder kinetics. Therefore, it seems that, in converting B(S) samples into tablets at this stage, in addition to increasing the sensitivity and the linear range, the probability of following the first-order kinetics is also higher. These results show the advantage of turning into tablets to achieve a suitable dosimeter.

The dose-response curve of the second time tablets,

In the second stage, tablets are made at a temperature of 685 ℃ and a pressure of 400 MPa.

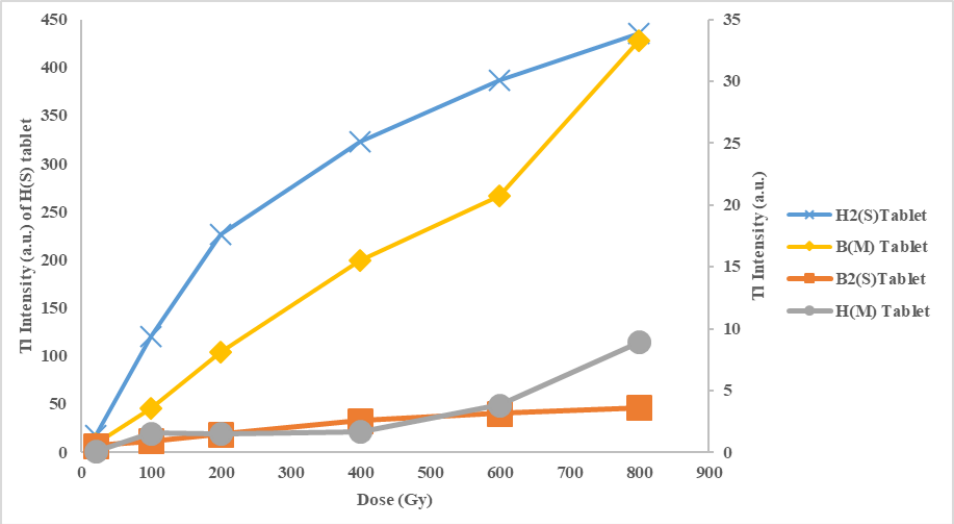

Figure 7: Dose-response diagram of the tablets in the second stage

Table 4- Dosimetry response results of tablet samples at the second-stage

Sample name	Linearity Range	Linearity Formula	R^2 in Linearity Formula	Average Temperature	STDEVA in Average Temperature
H (M) powder	20-1000	y = 0.0005x + 0.04	R^2 = 0.9815	215	12.44
B(M) powder	20-1000	y = 0.0346x + 3.1737	R^2 = 0.9785	234.125	21.42
H (S) powder	20-800	y = 0.3265x + 17.495	R^2 = 0.9868	231.86	19.07
B (S) powder	20-600	y = 0.0808x + 26.55	R^2 = 0.9812	297.29	27.29
H (M) Tablet	-	-	-	235.33	13.32
B(M) Tablet	20-800	y = 0.0397x - 0.393	R^2 = 0.9845	227	23.81
H2(S) Tablet	100-800	y = 0.3448x + 170.51	R^2 = 0.9757	244.87	28.35
B2(S) Tablet	20-800	y = 0.0041x + 0.6079	R^2 = 0.9756	209.5	17.19

As it is clear from Table 4, in the second stage of conversion into tablets, for H(S) and H(M) samples, the Tm shifts towards higher temperatures, but for B(S) and B(M) samples Tm shifts towards lower temperatures. In commercial samples, the probability of following the first-order kinetics changes a little by converting to tablets, but for the H(S) and B(S) sample, the probability decreases and increases respectively. According to the obtained results, H(S) tablets are more sensitive than its powder, although the linear range of dosimetry is decreasing. B(S) tablets are

less sensitive than its powder. And this difference is about 2 orders of magnitude, but the linear range of dosimetry is increasing. H(M) tablets do not have an acceptable linear range for dosimetry, as a result, no meaningful relationship can be found in the range where the sample was tested. In general, it is more sensitive than powder. The linear range of dosimetry decreases with conversion to tablets. The dose-response curves of powder and tablet samples related to B(M) are not significantly different. The dosimetry response range is also linear for both in the range tested From the different results obtained in the second stage for converting to tablets, it can be concluded that converting to tablets does not necessarily improve the dosimetry results and special conditions must be established to convert into tablets.

The fading effects of tablets

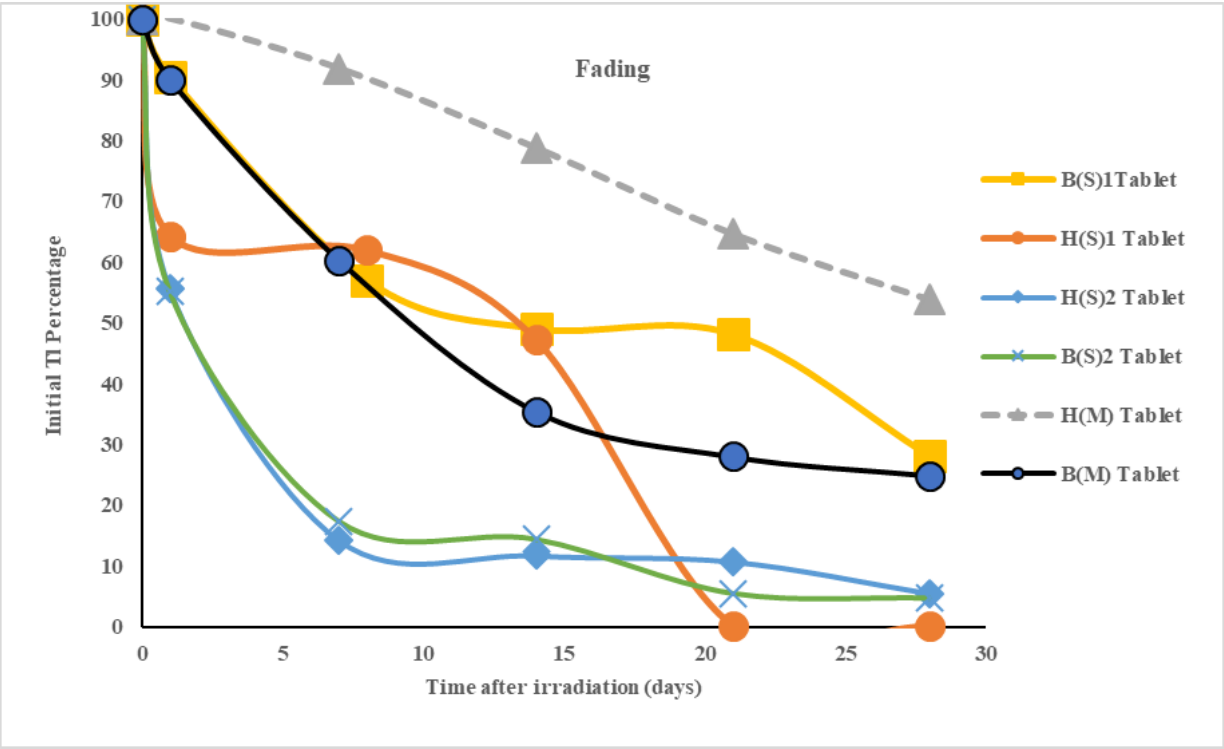

Figure 8: fading effects of tablets at 400 Gy and duration of 28 days

As shown in Figure 8, despite the fact that the sample H(M) does not have a good response in dosimetry, but due to the results of fading effects, it has a favorable condition and after 28 days, it has about 30%. 50% its initial response. B(M) and B(S) have 25% of their initial response in this period. Other samples have lost more than 95% of their initial response in this interval.

repeatability factor of tablets

Among the tablet samples produced, samples B(M) and H(S) produced in the first stage have the best performance from the point of view of reproducibility. The samples of H(S) and B(S) of the second stage do not have a good repeatability percentage. The repeatability curve diagram is shown in Figure 9.

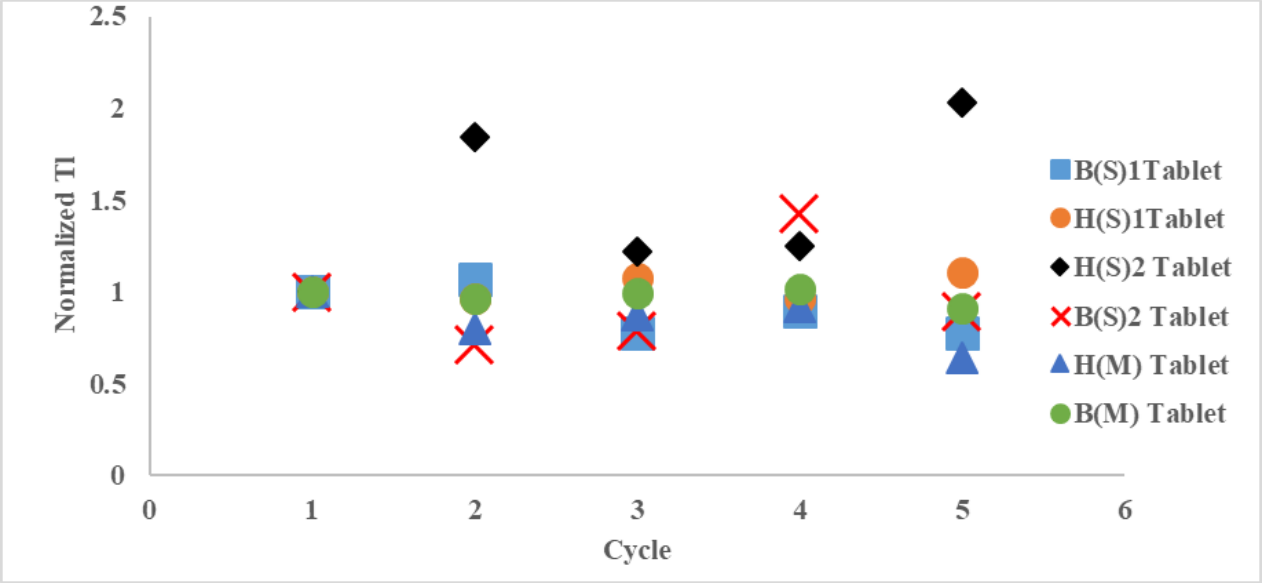

Figure 9: repeatability factor diagram of tablets

Determining the optimal sample

In this research, the dosimetry response by thermoluminescence method of four types of calcium phosphate powders in the form of hydroxyapatite and beta-tricalcium phosphate synthesized and purchased in the form of powder and tablets has been investigated. To determine the optimal samples, the following effects are considered.

1- dosimetry range

2- Sensitivity

3- The average temperature of the peak (Tm)

4- The possibility of following the first-order tradition

5- Fading effects

6- Repeatability

As it is known, each of these parameters has a range, and based on this, the strength and weaknesse of the samples can be divided from the perspective of these parameters. Each of these parameters is divided into 4 categories according to the available data and given points. In

Table **5**, the guide of these parameters is presented according to the points and colors assigned to it. Based on this, the samples are scored and these items can be seen in Table 6.

Table 5: Guide to scoring parameters of optimal tablet samples

Linearity Range	20-800 Gy	4	slope in Linearity Formula	20-1	4	Average Temperature	195-235	4
	20-600 Gy	3		0.9=0.1	3		175-195	3
	20-400 Gy	2		0.09-0.01	2		<175 ,>240	2
	20-200 Gy	1		0.009-0.001	1			

STDEVA in Average Temperature	4-9	4	Fading effects percentage for 30 days	>80	4	Reproducibility	<7.5	4
	9-15	3		50-80	3		7.5-12	3
	15-20	2		30-50	2		18-12	2
	>20	1		<30	1		>18	1

Total	18-20	4
	15-18	3
	15-Dec	2
	<12	1

Table 6: Scoring of optimal samples of calcium phosphate tablets

No.	powder	Tablet sample	Linearity Range	Linearity Formula	Average Temperature	STDEVA in Average Temperature	Fading effects percentage for 30 days	Reproducibility	total
1	B(M)	B(M)1 powder	4	2	4	1			11
2		B(M)2 powder	4	1	4	1	2	1	13
3		B(M) tablet	4	2	4	1	1	4	16
4	H(S)	H(S)1 powder	4	2	4	4			14
5		H(S)2 powder	4	2	4	2	2	2	16
6		H(S)1 tablet	2	4	4	1	1	4	16
7		H(S)2 tablet	3	3	2	1	1	1	11
8	H(M)	H(M) powder	4	0	4	3	1	1	13
9		H(M) tablet			4	3	1	1	9
10	B(S)	B(S)2 powder	3	2	2	1	1	3	12

11		B(S)1 tablet	4	4	4	4	2	2	20
12		B(S)2tablet	4	1	4	2	1	1	13

As it is known, most of the samples are linear in the tested range. The temperature range of the samples is in a suitable range for dosimetry and most of the samples are in the peaks between 195-235.℃. The weakness points of these samples are the effects of fading; most samples lose their information within 30 days.

The only samples that are suitable in terms of repeatability are the tablet samples B(M) made in the second step and the H(S) sample in the first step. As it is known, among all the samples, both powder and tablets, B(S) has the highest score in the first stage, This sample has all the advantages related to dosimetry, including sensitivity, temperature peak formation, following the first-order kinetics and a favorable condition in terms of repeatability and fading. Therefore, among other samples, this sample is considered the best dosimetry sample. After that, the B(M) and H(S) tablets made in the first stage are the best. In general, it can be concluded that the conditions of vovesion into tablets are the most important factor in improving the dosimetry parameters, and it is not necessarily possible to achieve better dosimetry results than powder with any conditions.

Conclusions

According to the conformity of the pattern created from the results of XRD analysis with the relevant standards, the correctness of the synthesis can be understood. The synthesized hydroxyapatite powder has the most suitable shape of the glow curve and follows the first-order kinetics. Temperature changes in peak formation for powder samples are less than for tablet samples. Due to the calcination of the synthesized powders, these samples have a higher response than the purchased powders (MERK). Obviously, most of the samples are linear in the tested range. From the point of view of fading effects, H(S) powder has a more favorable condition than the rest of the powder samples. The only samples that are suitable for repeatability are the B(M) tablets made in the second step and the H(S) sample is in the first step. As it is known, among all the samples, both powder and tablets, B(S) has the highest score in the first stage and therefore, among other samples, this sample is considered the best dosimetry sample. After that, B(M) and H(S)

tablets made in the first stage are the best. Therefore, in general, it can be concluded that the most important factor in optimizing dosimetry parameters is an investigation of the conditions for conversion into tablets, and therefore, no better dosimetry results can be achieved than powder under any conditions.

References

[1] M. T. Munir a/ac M. Federighi, 'Control of foodborne biological hazards by ionizing radiations', Foods, rhif. 9, rhif. 7, t. 878, 2020, doi: 10.3390/foods9070878.

[2] G. G. Eichholz, 'Dosimetry for Food Irradiation', yn Health Physics, rhif. 84, rhif. 5, 2003, t. 665.

[3] T. Kojima, S. Kashiwazaki, a/ac Y. Zhang, 'Alanine-polystyrene dosimeters prepared by injection moulding', Appl. Radiat. Isot., rhif. 48, rhif. 7, tt. 965–968, 1997, doi: 10.1016/S0969-8043(97)00010-9.

[4] M. Adachi, T. Bredow, a/ac K. Jug, 'What is the origin of color on metal complex dyes? Theoretical analysis of a Ni-coordinate azo dye', Dye. Pigment., rhif. 63, rhif. 3, tt. 225–230, 2004, doi: 10.1016/j.dyepig.2004.02.013.

[5] M. Shafaei, F. Ziaie, a/ac N. Hajiloo, 'Thermoluminescence properties of micro and nano structure hydroxyapatite after gamma irradiation', Kerntechnik, rhif. 81, rhif. 6, tt. 651–654, 2016, doi: 10.3139/124.110579.

[6] R. Alvarez, T. Rivera, J. Guzman, M. C. Piña-Barba, a/ac J. Azorin, 'Thermoluminescent characteristics of synthetic hydroxyapatite (SHAp)', Appl. Radiat. Isot., rhif. 83, tt. 192–195, 2014, doi: 10.1016/j.apradiso.2013.04.011.

[7] Y. Sun a/ac A. G. Chmielewski, Applications of ionizing radiation in materials processing. Institute of Nuclear Chemistry and Technology, 2017.

[8] R. V. Tauxe, 'Food safety and irradiation: Protecting the public from foodborne infections', Emerg. Infect. Dis., rhif. 7, rhif. 3, tt. 516–521, 2001, doi: 10.3201/eid0707.017706.

[9] R. Chen a/ac S. W. S. McKeever, Theory of Thermoluminescence and Related Phenomena. World Scientific, 1997.

[10] V. S. M. Barros, W. M. Azevedo, H. J. Khoury, a/ac C. Filho, 'ASSOCIAÇÃO BRASILEIRA DE ENERGIA NUCLEAR-ABEN Rare earth doped aluminum oxide dosimeter prepared by combustion synthesis', tt. 7–10, 2007, [Arlein]. Ar gael: https://pdfs.semanticscholar.org/60f1/ef510c6517a2642b273a81aadff6e9f8ac33.pdf.

[11]M. Shafaei, F. Ziaie, D. Sardari, a/ac M. M. Larijani, 'Study on carbonated hydroxyapatite as a thermoluminescence dosimeter', Kerntechnik, rhif. 80, rhif. 1, tt. 66–69, 2015, doi: 10.3139/124.110484.

[12]K. Nakashima, M. Takami, M. Ohta, T. Yasue, a/ac J. Yamauchi, 'Thermoluminescence mechanism of dysprosium-doped β-tricalcium phosphate phosphor', J. Lumin., rhif. 111, rhif. 1–2, tt. 113–120, 2005, doi: 10.1016/j.jlumin.2004.07.002.

[13]M. A. V. de Alencar, "The TL and OSL study of hydroxyapatites for dosimetric applications".

[14]Lewis, R.J., Sr (Ed.). Hawley's Condensed Chemical Dictionary. 12th ed. New York, NY: Van Nostrand Rheinhold Co., 1993, p. 206

[15] A. Khanafari, T. Akbari, and M. R. Sohrabi, "Comparison of nano-hydroxyapatite productivity by Pseudomonas aeruginosa and Serratia marcescense through encapsulation method," Nanomedicine Journal, vol. 1, pp. 276-284, 2014

[16] M. Shafaei, F. Ziaie, D. Sardari, and M. Larijani, "Study on carbonated hydroxyapatite as a thermoluminescence dosimeter," Kerntechnik, vol. 80, pp. 66-69, 2015

[17] C. Murru, 'Research about pressureless sintering of milled powder zrb2 based ceramic with carbon', UNIVERSITÀ DEGLI STUDI DI PADOVA, 2012.

[18] U. Anselmi-Tamburini, 'Spark Plasma Sintering', M. B. T.-E. of M. T. C. and G. Pomeroy, Gol. Oxford: Elsevier, 2021, tt. 294–310.

[19] No Title', J. Iran. Ceram. Soc., rhif. 15, rhif. 2, 2019, [Arlein]. Ar gael: http://jicers.ir/article-1-276-fa.html.

Investigating the use of the time-of-flight method for high resolution alpha-particle spectrometry (Paper ID: 1134)

M. Azizi[1], O. Kakuee[2], B. Ghasemi[1*], A. Biganeh[2], M. Esmaeili Noje Dehi[2]

[1] Nuclear engineering school, Shahid Beheshti University, Tehran, Iran.

[2]Physics & Accelerators Research School, Nuclear Science and Technology Research Institute, P. O. Box 14395-836, Tehran, Iran.

Abstract

The concept of time-of-flight measurement has played an important role in nuclear physics experiments. This method establishes a correlation between the flight time of a particle and its energy and it has become an important technique in ion-related applications. This study focuses on investigating the use of the time-of-flight method for high-resolution alpha-particle spectroscopy. The main components of the device, including the start and stop detectors, as well as the required electronics setup are described. Main considerations in the construction of an alpha time-of-flight spectrometer such as designing the vacuum chambers (source chamber and flight tube) for housing the source and detectors, flight length, geometrical efficiency, and achievable energy resolution are presented. According to the obtained results, to improve the spectrometer performance in the measurement of alpha-emitter sources, it is necessary to employ different flight lengths, long counting times, and high-timing-resolution nuclear electronics. Considering the presented details, an energy resolution of less than 7 keV is anticipated.

Keywords: Alpha-particle energy, Time-of-flight spectrometer, Energy resolution, Multi-channel plates, Carbon foil.

Introduction

Alpha-particle spectroscopy performs for various purposes including the determination of the activity and the record of decay data such as the probability of alpha-particle emission and branching factors [1]. Numerous instruments have been developed for alpha-particle spectrometry. In a traditional arrangement, the detector and the source are aligned face-to-face in a vacuum

chamber. This technique commonly performs using ion-implanted silicon detectors. Despite its advantages, this method also presents disadvantages, with the primary drawback being the limited energy resolution of the detector. This limitation in some cases results in unresolved alpha energy peaks due to low-energy tailing [2]. To determine the main alpha-particle emission probabilities in the decay of alpha-emitters, it is essential to utilize instruments that offer high-energy resolution. To improve energy resolution, various alternative methods have been developed and employed, including magnetic spectrometers [3], cryogenic detectors [4], and Time-Of-Flight (TOF) devices [5, 6]. These alternative methods provide enhanced detection capabilities.

The concept of TOF measurement has played an important role in nuclear physics experiments. This method establishes a correlation between the flight time of a particle and its energy. TOF measurement has found widespread applications in various scientific and technological domains, including energy and mass spectrometers [5-7], Elastic Recoil Detection [8], Rutherford Backscattering [9], and Neutron depth profiling for near-surface analysis [10]. It has increasingly become an important technique in ion-related applications. This article discusses the use of the TOF method for measuring the energy of alpha particles. A conceptual design of a TOF device for this purpose has been presented by García-Toraño [6]. Recent studies have shown that significant improvements in energy resolution can be achieved by measuring the TOF of particles over a flight length of several meters. For instance, Frolov et al [5] developed a TOF spectrometer for measuring alpha-particle energies at VNIIM. This spectrometer was used to measure the energies of a few radionuclides. The main performance characteristics of the spectrometer include a 3.5m flight path, an energy resolution of 5.2 keV at the energy of 5804 keV of Cm-244 source, and a reported time resolution of 99 ps. However, the detection efficiency of the spectrometer was low (about $0.4 \times 10{-}6$). The Joint Research Centre (JRC) is constructing a TOF spectrometer to achieve superior energy resolution and linearity in measuring the energy of alpha particles emitted in radioactive decays. Their goal is to provide accurate nuclear decay data for alpha emitters [2].

In this article, the alpha TOF spectrometer, which is being constructed at the physics and accelerator research school of the Nuclear Science and Technology Research Institute (NSTRI), has been introduced. The main components of the spectrometer, including the start and stop detectors, as well as the required electronics setup, have been described. The key considerations

in the design process such as determining flight length and designing the vacuum chambers for housing the source and detectors are discussed. Furthermore, an energy resolution that could be obtained has been estimated.

Principles of the A-TOF spectrometer

The Alpha Time-Of-Flight (A-TOF) is measured by two-timing detectors. The start detector is typically a transmission detector based on a Multi-Channel Plate (MCP). On the other hand, for the stop detector, other options such as fast scintillators and semiconductor detectors have been utilized. The advantage of using a transmission detector as a stop detector is that a third detector can be applied to conduct further measurements or lower the background [6]. The transmission detector has four main parts: (1) a conversion foil (usually made of carbon) that produces Secondary Electrons (SEs) from the incident particles, (2) an acceleration grid that speeds up the SEs, (3) an electrostatic mirror that consists of two parallel grids at a 45° angle to the acceleration grid and deflects the SEs toward the MCP, and (4) an MCP detector that detects the SE and generates a signal. MCP detectors exhibit remarkable timing properties and detection efficiencies for the electrons being examined [6]. The diagram of a TOF set-up for the determination of the energy of alpha particles is presented in Figure 1. The device consists of two MCP-based transmission detectors as the start and stop units, and the desired electronic setup to obtain the timing signals from them.

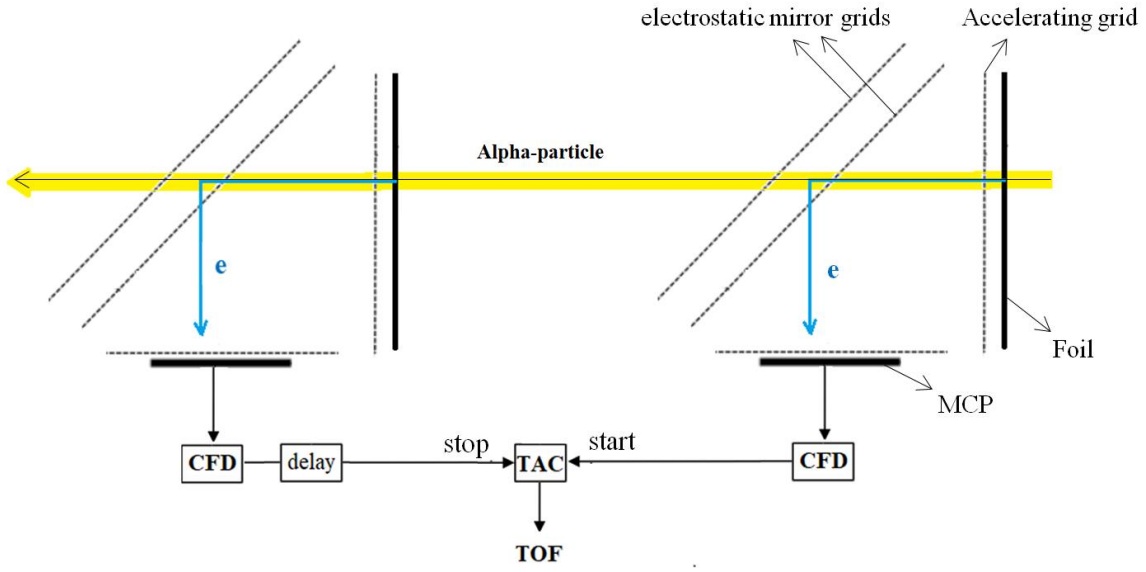

Fig. 1. Schematic of an alpha TOF spectrometer based on MCP detectors.

As alpha particles pass through the foil of the start and stop units. They produce Secondary Electrons (SEs). The typical energy of these SEs is a few eV [7]. The secondary electrons drift through the field-free region and are subsequently deflected by 90◦ toward MCP to produce the start signal. One of the two branches is delayed by a fixed amount of time. The two triggers arrive at a Time-to-Amplitude Converted (TAC), device that produces an output pulse with an amplitude proportional to the time interval between input start and stop pulses. Finally, a Multi-Channel Analyzer (MCA) provides a differential amplitude distribution, also called the TOF spectrum. The obtained time spectrum can be converted to the energy spectrum.

Structure of designed A-TOF spectrometer at NSTRI

The structure of the A-TOF spectrometer, which is being constructed at the Nuclear Science and Technology Research Institute, is depicted in Figure 2. The device comprises two chambers (source chamber and flight tube). The design of the device facilitates the separation of the flight tube by closing the valve when replacing the source, eliminating the need to interrupt the vacuum and supply the detectors.

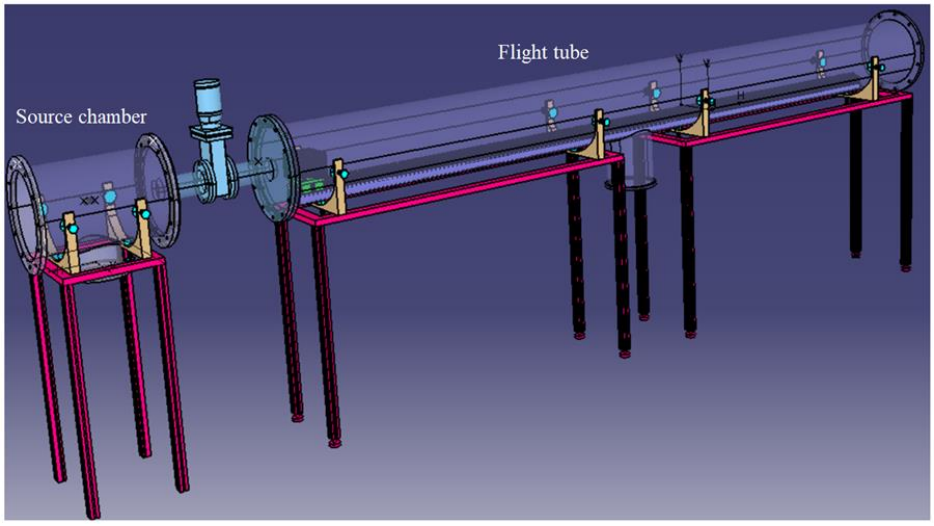

Fig. 2. Structure of the A-TOF spectrometer under construction at the Nuclear Science and Technology Research Institute.

The start and stop detectors, along with the linear displacement system used to move the stop detector, are located within the flight tube. In practical applications, measurements will be conducted with a variable flight path, the length of which is varied by moving the position of the stop detector to a range of approximately 3 meters.

Main considerations in the use of A-TOF spectrometer

Flight length of the spectrometer

The energy of the alpha-particle and its arrival time are correlated by:

$$E = \frac{1}{2} m_{Alpha} V^2 = \frac{1}{2} m_{Alpha} \left(\frac{L}{t}\right)^2 \quad (1)$$

Where E indicates the calculated energy of the alpha-particle, mAlpha is the mass of the alpha-particle, L is the flight length, and t is the measured TOF. The conversion from time to energy is not a linear transformation. Each point on the time spectrum has a distinct value in the energy space. For instance, Figure 3 illustrates the uncertainty in determining energy as a function of flight time (varying flight lengths) for alpha-particles of 5.5 MeV, assuming a timing uncertainty of 42 ps.

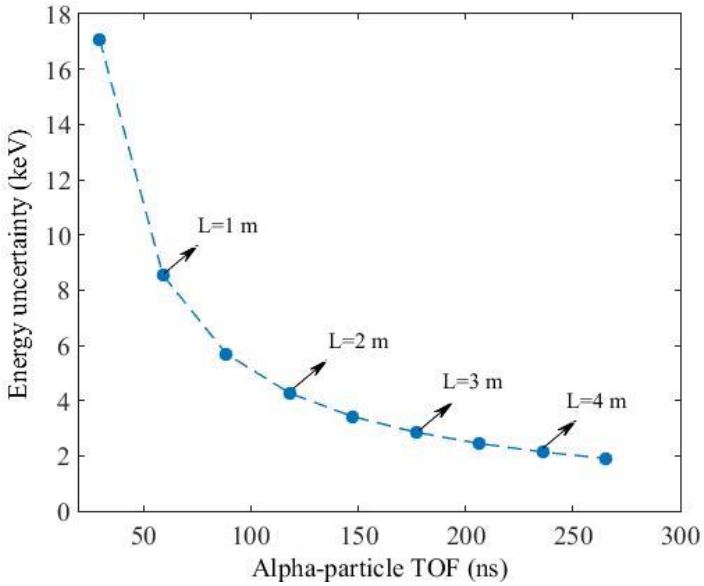

Fig. 3. Energy uncertainty as a function of the peak location on the time spectrum

As depicted in the figure, the conversion is more susceptible to time variations at lower flight times (or shorter flight lengths) within the spectrum. This observation stems directly from the quadratic relationship between the particle's flight time and its energy. To achieve a smaller energy uncertainty, the flight length of the alpha particle must be extended to several meters. This prolongs the alpha particle's flight time and shifts it to less sensitive areas on the time spectrum.

Considering that alpha particles with different energies have different flight times over the same flight length, and that the TOF contributes to the uncertainty of achievable energy, it becomes necessary to use different flight lengths to achieve a specific energy uncertainty. As indicated in Figure 4, achieving an uncertainty of 3 keV requires a larger flight length for alpha particles with higher energy compared to those with lower energy. Consequently, to accommodate different flight distances in the measurements, the stop detector must be movable.

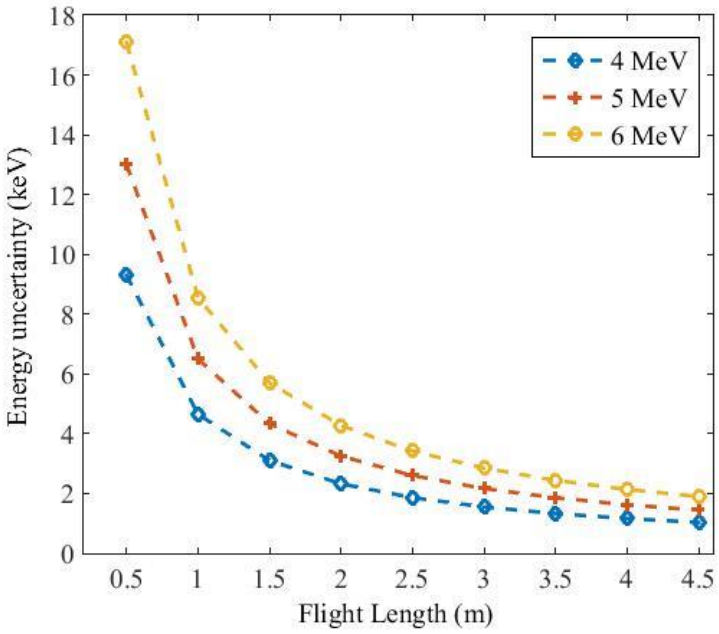

Fig. 4. Energy uncertainty as a function of flight length for alpha-particles with different energies.

Geometrical efficiency

The use of long flight lengths to achieve small energy uncertainty suggests that the solid angle subtended by the source and the final unit (stop detector) is very small, necessitating extended counting times to achieve the desired statistical in the counting. The geometrical efficiency of the

TOF spectrometer, or in other words, the solid angle of the measurement in the system, is presented in Table 1.

Table 1. The solid angle of the TOF spectrometer as a function of flight length (assuming a source radius of 8 mm and final unit radius of 20 mm).

Flight Length (m)	Solid angle of the measurement (mSr)
1	1.25
2	0.31
3	0.13

As indicated in the table, the solid angle of the measurement is quite small. Consequently, for the measurement of TOF alpha particles, especially those alpha-emitters with long half-lives, a long measurement time is required.

Energy resolution

There are some factors that can affect the device's performance and cause the spread of the obtained energy. The main contributions to the resolution of a TOF spectrometer are the following form [11]:

$$\Delta E = \left\{ \Delta E_{loss}^2 + \left(\frac{2E}{L}\,\Delta L\right)^2 + \left(\frac{(2E)^{3/2}}{L m_{Alpha}{}^{1/2}}\,\Delta t\right)^2 + \left(\overline{\Delta q}.V_{foil}\right)^2 \right\}^{1/2} \quad (2)$$

Where ΔE_{loss}^2 is energy straggling, ΔL is uncertainty in determining the distance between the start and stop detectors, Δt is the time resolution, $\overline{\Delta q}$ is the average change in the charge state of the alpha-particles as they pass through the foil, and Vfoil is the high voltage potential applied to the foil. The first term represents energy straggling in the foil of the transmission detector, the second term is related to the variation in flight length, and the third and fourth terms are the effects related to the time resolution of the system and the tandem effect, respectively. To estimate the achievable energy resolution, it is essential to calculate the contribution of each term. The SRIM program was used to calculate the energy straggling of the alpha particles in the 10 nm carbon foil. Also, to estimate the effects associated with the second and third terms, it was assumed that ΔL is about 0.2 mm and Δt is 100 ps. The tandem effect pertains to the alteration in a particle's charge state as it traverses the foil, leading to a subsequent change in its acceleration or deceleration [6]. A

comprehensive study on the equilibrium charge state of helium ions in carbon was conducted by Armstrong et al [12]. Their findings indicate that for the alpha particle energies pertinent to this study, the ratio of He+ to He2+ ions is around 1%. Therefore, this effect can be considered negligible. The energy resolution of the spectrometer for alpha particles with different energies over a 2 m flight length, as predicted by Equation (2), is depicted in Figure 5.

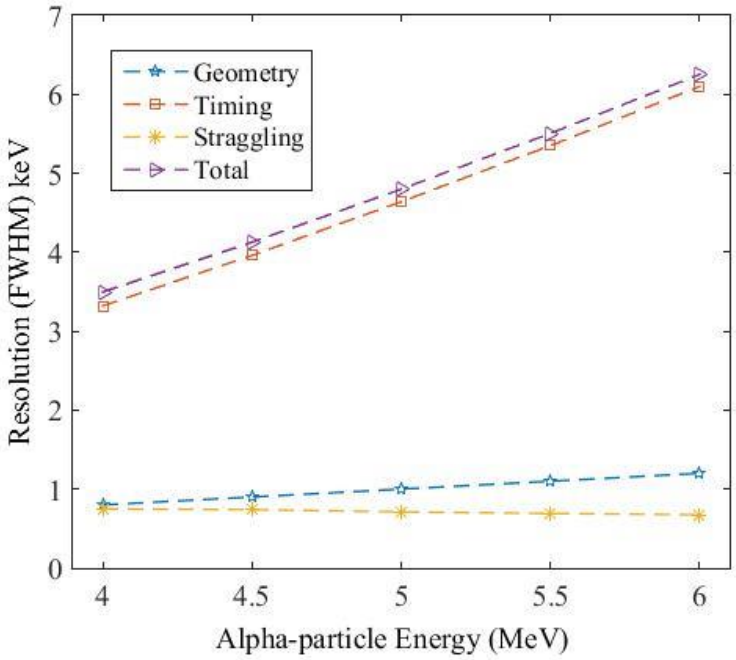

Fig. 5. Energy resolution of the spectrometer for alpha-particles over a 2 m flight length

As depicted in Figure 5, the effect related to the third term, which is the time resolution of the system, plays an important role in the achievable energy resolution of the spectrometer. Therefore, in practical measurements, the use of pulse-processing electronics with improved time resolution in the range of picoseconds is essential. The results also demonstrate that a high resolution has been achieved for low-energy alpha particles over a flight length of 2 meters. However, as the energy of alpha particles increases, the resolution drops, thus requiring longer flight lengths to measure high-energy alpha particles with a good resolution.

Conclusions

This article explores the principles of the TOF technique used for measuring the energy of alpha particles with high energy resolution. The results suggest that different flight lengths are required to achieve a high energy resolution in the measurement of alpha particles with varying energies. Additionally, due to the small solid angle of the measurement, a long measurement time is necessary to achieve good statistical counting. The main contributions to the energy resolution of a TOF spectrometer indicate that the time resolution of the system plays a significant role in the achievable energy resolution of the spectrometer. Hence, it is essential to use pulse-processing electronics with improved time resolution in the picosecond range.

References

1. Pommé, S., Typical uncertainties in alpha-particle spectrometry. Metrologia, 2015. 52(3): p. S146.
2. Pommé, S., Radionuclide metrology: confidence in radioactivity measurements. Journal of Radioanalytical and Nuclear Chemistry, 2022. 331(12): p. 4771-4798.
3. Yoon, W., et al., Development of a high resolution alpha spectrometer using a magnetic calorimeter. Nuclear Instruments and Methods in Physics Research Section A: Accelerators, Spectrometers, Detectors and Associated Equipment, 2015. 784: p. 143-146.
4. Leblanc, E., et al., High-energy resolution alpha spectrometry using cryogenic detectors. Applied radiation and isotopes, 2006. 64(10-11): p. 1281-1286.
5. Frolov, E., A precision facility for measuring alpha-particle energies and flux density. Applied Radiation and Isotopes, 1992. 43(1-2): p. 211-222.
6. García-Toraño, E., Concept design of a time-of-flight spectrometer for the measurement of the energy of alpha particles. Applied Radiation and Isotopes, 2018. 134: p. 219-224.
7. Arnold, C., et al., Development of position-sensitive time-of-flight spectrometer for fission fragment research. Nuclear Instruments and Methods in Physics Research Section A: Accelerators, Spectrometers, Detectors and Associated Equipment, 2014. 764: p. 53-58.
8. Yasuda, K., et al., Depth resolution of TOF-ERDA using a He beam. Nuclear Instruments and Methods in Physics Research Section B: Beam Interactions with Materials and Atoms, 2011. 269(9): p. 1019-1022.

9. Giangrandi, S., et al., Time-of-flight telescope for heavy-ion RBS. Nuclear Instruments and Methods in Physics Research Section B: Beam Interactions with Materials and Atoms, 2007. 261(1-2): p. 529-533.

10. Cetiner, M.S., Development of an ion time-of-flight spectrometer for neutron depth profiling. 2008: The Pennsylvania State University.

11. Döbeli, M., et al., Time-of-flight spectrometry applied to 2 MeV He RBS. Nuclear Instruments and Methods in Physics Research Section B: Beam Interactions with Materials and Atoms, 1998. 142(3): p. 417-424.

12. Armstrong, J., et al., Equilibrium charge-state fractions of 0.2 to 6.5 MeV helium ions in carbon. Proceedings of the Physical Society, 1965. 86(6): p. 1283.

ICNST 2024
International Conference on Nuclear Science and Technology
6- 8 MAY 2024 | Isfahan, Iran

Development of a Fricke gel dosimeter for use for dosimetry of X and gamma rays Fields (Paper ID: 1149)

Saeedi Sini S.A.[1*], Sina S.[2,1], Rakeb Z.[1], Sadeghi M.H.[1]
[1]*Department of Nuclear Engineering, School of Mechanical Engineering, Shiraz University, Shiraz, Iran*
[2]*Radiation Research Center, Shiraz University, Shiraz, Iran*

Abstract

The measurement of absorbed dose in various radiation applications, including medical and industrial applications such as radiography, CT scans, and food irradiation, is one of the most important goals of radiation protection. Dosimeters are currently used as a means of quality control in medicine and industry. Radiochromic chemical dosimeters are widely used in radiotherapy, because they often have a linear response at high doses, are low in manufacturing cost, and are easy to read. This study aimed to develop a chemical dosimeter for use at low doses by changing the proportion and composition of the Fricke-Xylenol gel.

The result was the construction of a Fricke gel dosimeter for use in low-dose and intermediate-dose measurements, using various materials, such as gelatin, distilled water, ammonium ferrous sulfate, sulfuric acid, benzoic acid, and xylenol orange. The calibration curves, fading, sensitivity to the environmental temperature, and repeatability of the dosimeter responses were investigated. According to the results of this study, the manufactured gel dosimeter has a linear response in the dose range of 0.05 to 5 Gy. The Fricke gel dosimeter prepared in this study can be used effectively in low-dose measurements in industrial and medical applications of radiation.

Keywords: Dosimetry, Dose-response, Chemical dosimeter, Fricke dosimeter, Radiochromic

Introduction

In recent years, technological advances in radiation therapy have been significant, and as a result, the quality of radiotherapy has greatly increased. Fundamental progress with the development of external beam techniques, especially intensity-modulated radiotherapy (IMRT), has allowed the clinical implementation of highly non-convex dose distributions. This provides consistency, as shown in [1, 2]. In radiation therapy, controlling and measuring doses, along with associated parameters, is essential to ensure that the target treatment volume receives the prescribed dose. A dosimeter, such as an adequate ionization chamber, is usually used for measurements, although

other types of dosimeters can also be used [3-7]. In general, gel dosimetry using optical scanners for measuring induced attenuation has the highest rank among all dosimeters [8-10]. Ideally, commissioning and routine quality assurance of these complex therapeutic techniques (IMRT) require a dosimeter that can accurately and conveniently measure the dose distribution in three dimensions [1, 2].

There are several classes of gel dosimeters, such as radio-chromic dosimeters and polymer gels [9-13]. Gel dosimeters are unique in that they can measure the dose distribution in three dimensions and their ability to specify other characteristics such as radiation direction, energy and dose rate independence, and soft tissue equivalent. One of the disadvantages of gel dosimeters is the high uncertainty in measuring low doses, especially at doses lower than 25 cGy. Therefore, to avoid this uncertainty in the treatment evaluation, a higher dose was prescribed. For example, if the prescribed dose was 2 Gy per fraction, a dose of approximately 10 Gy was given to the gel dosimeter to evaluate the treatment, especially in the surrounding tissues that received lower doses than the target. As a result, it can be said that the effective and useful life of the linear accelerator and the time devoted to the treatment of patients will be reduced due to the delivery of a large number of monitor units (MU). As a result, it can be said that, for the reasons presented above, obtaining a gel dosimeter that is sensitive to low dose levels has a high value [14-18].

It can be said that these dosimeters rely on the oxidation caused by the radiation of Fe^{2+} ions to Fe^{3+} ions, which are dispersed in a tissue-equivalent gel matrix. Usually, these dosimeters are made of gelatin, agarose, or polyvinyl alcohol., which is connected to glutaraldehyde (PVA-GTA) as a gel matrix. Usually, to make these dosimeters, dye materials such as xylenol, nitrotetrazolium chloride, and Methylthymol blue, and activating elements such as silver nitrate, and ammonium ferros sulfate are needed [19-23]. The gel dosimeters are usually used for high-dose measurements in radiotherapy, or in blood irradiation. [24] . The purpose of this study is to develop a gel Fricke gel dosimeter for use in low- dose measurement.

Material and Methods:

In this experiment, 80 samples of gel dosimeter with different chemical compounds were made to measure low doses, and finally, we succeeded in making a Fricke gel dosimeter sensitive to low

doses. The chemical materials used in the gel dosimeter structure are as follows: Gelatin (or Polyvinyl alcohol) as the gelling agent, Ferrous ammonium sulfate as the activator, Xylenol orange as the chemical dye. Water, and sulfuric acid as the solvent.

A summary of how to make gel dosimeters is:

The chemicals were inserted in 4 glasses, the first glass contained a gelling agent (gelatin or PVA) and water. The second glass contained orange xylenol, water, and sulfuric acid. The third glass contained benzoic acid and water, and the fourth glass contained ammonium ferrous ammonium sulfate and water.

The first glass was heated on a heater- stirrer. For gelatin, heating continued until the temperature reached 45 degrees Celsius. For PVA, for uniform heating, the beaker was not placed directly on the heater, it was placed in a container containing oil and water, and the heating was continued until the temperature reached 85 °C to heat the PVA solution homogeneously. When the temperature of the solution reached the desired value, it was removed from the heater, and when the temperature reached about 35 degrees Celsius, the glass containing the gelatin was placed in water to cool. The contents of the second beaker were added to the first beaker whose temperature had reached ambient temperature to obtain a clear and homogeneous solution with a bright orange color. The contents of the fourth glass were added to the first glass and mixed well. The contents of the third beaker were added to the first beaker, and the final solution was mixed well. Finally, the solution was inserted into cuvettes measuring 1 x 1 x 4.5 cubic centimeters, and kept in the refrigerator until the next day.

To optimize and reach the target gel dosimeters, more than 70 dosimeters were made, and with various compositions. Finally, a gelatin-based gel dosimeter was found to have significant sensitivity to the dose in the low ranges. After preparing the dosimeters, they were kept in the refrigerator at a temperature of 5 degrees Celsius for 12 hours. Gel dosimeters were irradiated using a Cs-137 source calibrated by a standard dosimetry laboratory. The samples were placed at a distance of 60 cm from the source, where the dose rate was 2 Gy/h and the size of the irradiated field was 10 x 10 cm2. After the irradiation, the dosimeters were placed in front of a negatoscope, and a photo was taken with a camera. The average values of red and green pixels in the images, L (1/cm), were used to obtain changes in optical absorption. In this experiment, the linearity, and the

fading of the dosimeter response, energy dependence, and repeatability of the dosimeter were investigated.

Results and discussion

As previously mentioned, one of the gelatin-based dosimeters was efficient in low-dose measurement. Table 1 shows the composition of this low-dose gel dosimeter.

Table 1: Composition of the gel dosimeter for low-dose measurement

Material	Gelatin-base dosimeter
Gelatin	124 mM
Water	100 ml
Xylenol orange	0.0416 mM
Sulfuric acid	90 mM
Ferrous ammonium sulfate	1.000 mM
Benzoic Acid	6.60 mM

The different characteristics of the dosimeter are presented in the next section.

Calibration curve of the gel dosimeter

The calibration curve of a Fricke gel dosimeter was plotted and it was observed that the response of this dosimeter is linear. This curve can be seen in Figure 1. Based on the obtained results, it was observed that the lower detection limit for this gelatin is approximately 50 mGy. The minimum detectable limit of the detector is obtained by the reading (color) of the background dosimeter. The dosimeter does not change color when exposed to a dose lower than 50mGy.

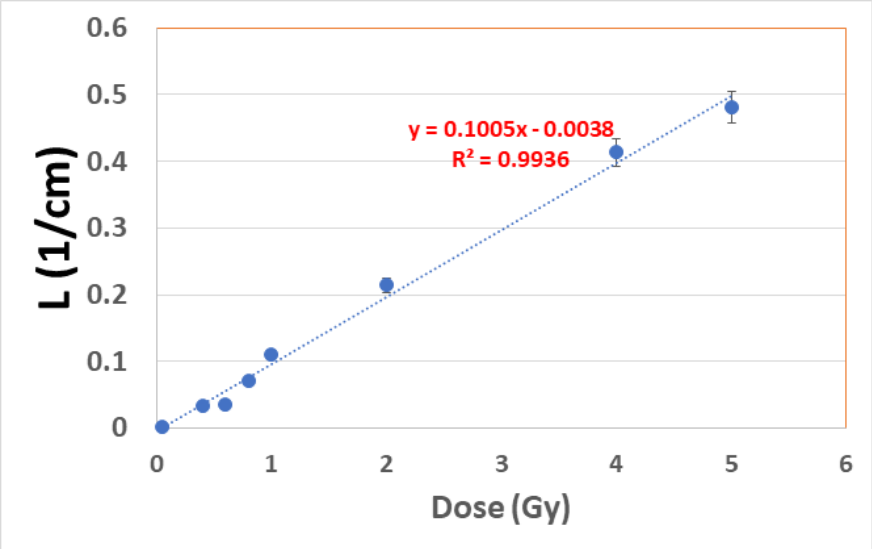

Fig. 1. Calibration curve of a gel dosimeter sample

Temperature dependency, and fading of the dosimeter response

To investigate the effect of the environmental temperature on the dosimeter response, the gelatin-based dosimeter response was obtained at room temperature, and in the refrigerator. Comparing the results shows that the responses of the gelatin-based dosimeters are temperature dependent and the stability of the samples increases by keeping the dosimeters in the refrigerator. The results show that the response of the dosimeter kept at room temperature, undergoes a 40% variation after 100 hours. However, less variation is observed in the response of the dosimeter when kept in the refrigerator.

A decrease in stability over time was observed even when the dosimeters were stored in the refrigerator. Figure 2 shows the stability of the dosimeter when exposed to doses and stored in a refrigerator. The change in gelatin-based dosimeter response was less than 0.5% at 120 hours after irradiation.

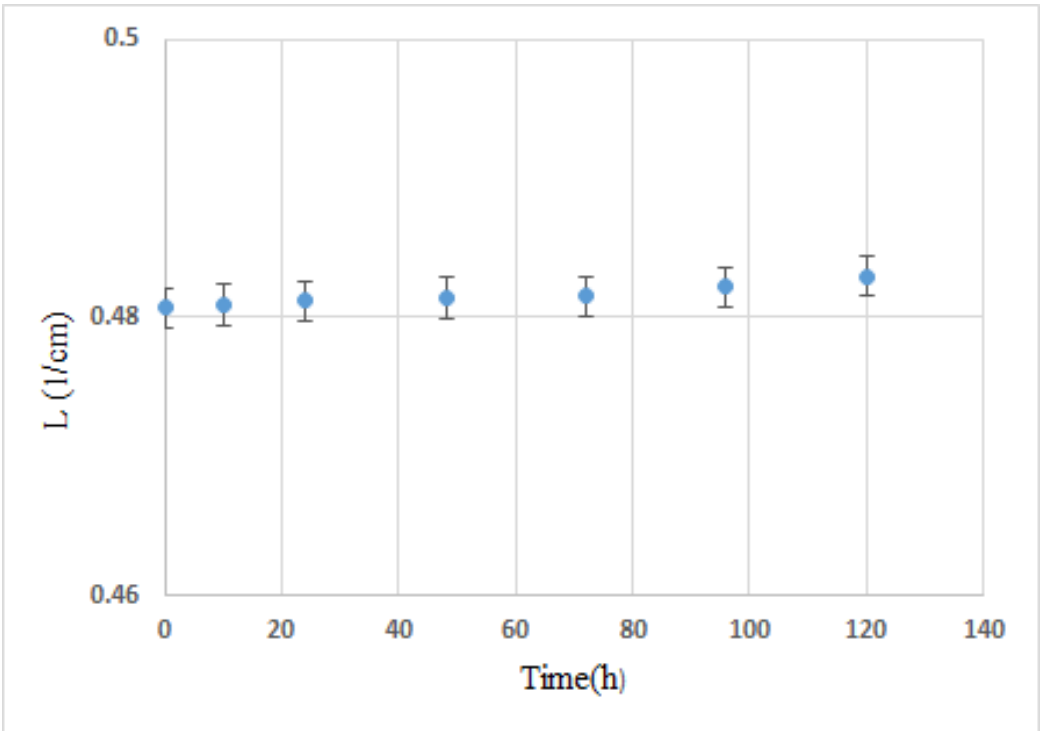

Fig. 2. Percentage changes in dosimeter response stability with time elapsed after exposure when stored at 5°C.

Repeatability of the dosimeter response

The dosimeter was prepared again, and irradiated for calibration. Figure 3 shows the reproducibility of the gel.

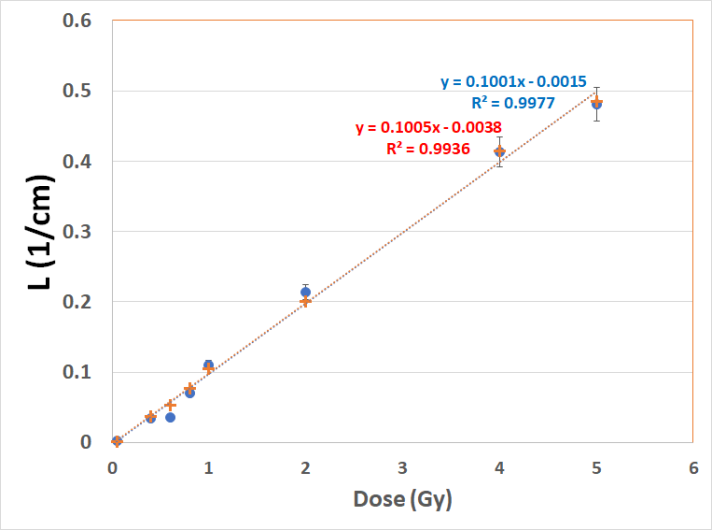

Fig. 3. Repeatability of the gelatin-based gel dosimeter sample

Energy dependency of the gel dosimeter

The dosimeter was exposed to a dose of 2Gy in 662keV gamma rays, and 70kVp X-rays. As shown in Figure 4, the obtained results show that the response of the dosimeters does not depend on the energy of the radiation rays, for the energies of 70kVp, and 662keV.

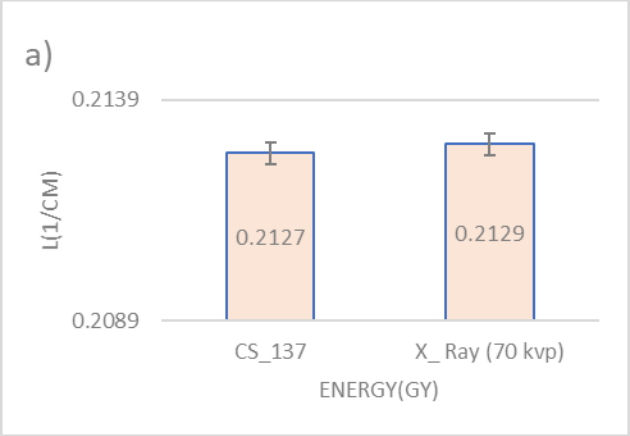

Fig. 4. Response of a gel dosimeter sample to the same dose of gamma and X

Conclusions

When a new dosimeter is established, its characteristics such as linearity of the response, repeatability, energy dependence, etc., must be investigated. In the case of gel dosimeters, when a compound with high enough sensitivity is made, further studies should be performed to investigate the linearity, stability, repeatability, and energy dependence. In this study, it was shown that a long storage time between gel preparation and irradiation may cause a noticeable decrease in dosimeter sensitivity and darkening of dosimeters, which can be seen even with the naked eye. Gel dosimeters are often used to calculate high doses, but in this study, we managed to make a Fricke gel dosimeter to measure the dose in the mGy range. It was shown that the dosimeter introduced here has a linear response in the range of 50 to 5000 mGy. The developed gelatin-based dosimeters are a promising tool for radiation detection and are potentially applicable for industrial and medical dosimetry.

Acknowledgements

We extend our gratitude to the Radiation Research Center of Shiraz University for their invaluable support.

References

[1] McAuley, K. B., & Nasr, A. T. (2013, June). Fundamentals of gel dosimeters. In Journal of Physics: Conference Series (Vol. 444, No. 1, p. 012001). IOP Publishing.

[2] Mayles, P., Nahum, A., & Rosenwald, J. C. (2007). Handbook of radiotherapy physics: theory and practice. CRC Press.

[3] Baskar, R., Lee, K. A., Yeo, R., & Yeoh, K. W. (2012). Cancer and radiation therapy: current advances and future directions. International journal of medical sciences, 9(3), 193.

[4] Attix, F. H. (2008). Introduction to radiological physics and radiation dosimetry. John Wiley & Sons.

[5] F.M. Khan, "The physics of radiation therapy,"William and Wilkins, Maryland (2003).

[6] Mizukami, S., Watanabe, Y., Mizoguchi, T., Gomi, T., Hara, H., Takei, H., ... & Maeyama, T. (2021). Whole three-dimensional dosimetry of carbon ion beams with an MRI-based nanocomposite Fricke gel dosimeter using rapid T1 mapping method. Gels, 7(4), 233.

[7] Webb, S. (2001). Concepts for shuttling multileaf collimators for intensitymodulated radiation therapy. Physics in Medicine & Biology, 46(3), 637.

[8] Baldock, C., De Deene, Y., Doran, S., Ibbott, G., Jirasek, A., Lepage, M., ... & Schreiner, L. (2010). Polymer gel dosimetry. Physics in Medicine & Biology, 55(5), R1.

[9] Rabaeh, K. A., Eyadeh, M. M., Hailat, T. F., Aldweri, F. M., Alheet, S. M., & Eid, R. M. (2018). Characterization of ferrous-methylthymol blue-polyvinyl alcohol gel dosimeters using nuclear magnetic resonance and optical techniques. Radiation Physics and Chemistry, 148, 25-32.

[10] Maryanski, M. J., Gore, J. C., Kennan, R. P., & Schulz, R. J. (1993). NMR relaxation enhancement in gels polymerized and cross-linked by ionizing radiation: a new approach to 3D dosimetry by MRI. Magnetic resonance imaging, 11(2), 253-258.

[11] Noushin Bani Rezaieh, Hassan Ali Nadai, Ali Reza Shirazi, Ali Reza Zirak and Sudeh Sadat Sajjadi (2014). An overview of three-dimensional dosimeters. Razi Journal of Medical Sciences.

[12] De Deene, Y., De Wagter, C., Van Duyse, B., Derycke, S., Mersseman, B., De Gersem, W., ... & De Neve, W. (2000). Validation of MR-based polymer gel dosimetry as a preclinical three-dimensional verification tool in conformal radiotherapy. Magnetic Resonance in Medicine: An Official Journal of the International Society for Magnetic Resonance in Medicine, 43(1), 116-125.

[13] Ibbott G S. (2006). Clinical Applications of Gel Dosimeters. J Phys Conf Ser, 56:108-131.

[14] Alashrah, S., El-Ghoul, Y., & Omer, M. A. A. (2021). Synthesis and characterization of a new nanocomposite film based on polyvinyl alcohol polymer and nitro blue tetrazolium dye as a low radiation dosimeter in medical diagnostics application. Polymers, 13(11), 1815.

[15] Ranjbar, A. H., & Randle, K. (2008). Hyper pure quartz as a promising material for retrospective and radiation processing dosimetry using ESR technique. Applied Radiation and Isotopes, 66(9), 1240-1244.

[16] Kozicki, M., Berg, A., Maras, P., Jaszczak, M., & Dudek, M. (2020). Clinical radiotherapy application of N-vinylpyrrolidone-containing 3D polymer gel dosimeters with remote external MR-reading. Physica Medica, 69, 134-146.

[17] Matrosic, C. K., Culberson, W., Shepard, A., Jupitz, S., & Bednarz, B. (2021). 3D dosimetric validation of ultrasound-guided radiotherapy with a dynamically deformable abdominal phantom. Physica Medica, 84, 159-167.

[18] Babic, S., Battista, J., & Jordan, K. (2008). Three-dimensional dose verification for intensity-modulated radiation therapy in the radiological physics centre headand-neck phantom using optical computed tomography scans of ferrous xylenol– orange gel dosimeters. International Journal of Radiation Oncology Biology Physics, 70(4), 1281-1291.

[19] LJ, S. (2004). Review of Fricke gel dosimeters.

[20] Schreiner, L. J. (2015, January). True 3D chemical dosimetry (gels, plastics): Development and clinical role. In Journal of Physics: Conference Series (Vol. 573, No. 1, p. 012003). IOP Publishing.

[21] Tippayamontri, T., Guérin, B., Ouellet, R., Sarrhini, O., Rousseau, J., Lecomte, 82 R., ... & Sanche, L. (2019). Intratumoral 18F-FLT infusion in metabolic targeted radiotherapy. EJNMMI research, 9(1), 1-13.

[22] Schulz, R. J., DeGuzman, A. F., Nguyen, D. B., & Gore, J. C. (1990). Doseresponse curves for Fricke-infused agarose gels as obtained by nuclear magnetic resonance. Physics in Medicine & Biology, 35(12), 1611.

[23] Rabaeh, K. A., Eyadeh, M. M., Hailat, T. F., Aldweri, F. M., Alheet, S. M., & Eid, R. M. (2018). Characterization of ferrous-methylthymol blue-polyvinyl alcohol gel dosimeters using nuclear magnetic resonance and optical techniques. Radiation Physics and Chemistry, 148, 25-32.

[24] Farajzadeh, E., and Sina, S. (2022). Development of radiochromic dosimeter for dosimetry in blood irradiation chambers. Radiation Physics and Chemistry, 188, 109637.

Determination of the optimal thickness of a hot cell for cobalt source and the feasibility of using it for spent fuel source (Paper ID: 1188)

Ehsan Boustani*, Mostafa Hassanzadeh

Reactor and nuclear safety school, Nuclear Science and Technology Research Institute (NSTRI), Tehran, Iran

Abstract

To design a hot cell, it is necessary to consider all safety requirements and radiation protection acceptance criteria. In this research, the design of a hot cell with specific geometric dimensions and materials was simulated using MCNP6 code. Then, the gamma dose rate was calculated for a 60Co source with 1.85E13 Bq activity and a silicide spent fuel plate with 90% burnup with a cooling time of 30 days to determine the appropriate shielding thickness. In these calculations, the source intensity and the gamma spectrum of the spent silicide fuel plate were obtained using the ORIGEN code.

According to the references, the gamma dose rate criterion of 10 μSv/h was considered to determine the thickness of the hot cell wall, which is made of barite concrete with a density of 3.35 gcm-3 and a combination of concrete and paraffin, in different directions. The results show that for the corridor as the worst case, the maximum concrete thicknesses without compromising the gamma dose rate criterion are 76 and 86 cm for 60Co and silicide fuel plate respectively.

Keywords: Hot cell, Shielding calculations, 60Co source, Fuel burnup, Optimal thickness, MCNP6 and ORIGEN codes.

Introduction

Many shielding design safety requirements and acceptance criteria in nuclear facilities such as hot cells are in line with the radiation protection safety requirements and acceptance criteria. It is worth mentioning that good design, high-quality construction and proper operation will create safety through radiation protection [i]. The determined occupational dose ranges in the safety standards of the IAEA are defined as a maximum effective dose of 20 mSv/h with an average of 5 consecutive years [ii]. The hot cell laboratory can consist of several hot cells, which are considered as protection for highly radioactive materials. The dose rate for expected radioactive materials is defined based on working hours. The working time of personnel for the hot cell is 2000 hours per

year, therefore, the dose rate criterion is 10 μSv/h for this facility. The hot cell laboratory has various applications, for example, in some countries such as Malaysia, there is a semi-permanent hot cell for the production of radioisotopes such as 99mTc and 131I. Also, this type of hot cell for research works used lead as biological shielding. Further, other hot cells are used to manage radioactive sources with high activity such as radiation and teletherapy. This type of hot cell is used for research activities such as spent fuel inspection, Post-Irradiation Evaluation (PIE) and fuel fabrication. The main goal for the development of the hot cell is to prepare a condition for research on the behavior of the fuel [iii].

In the design of shielding, the used material and its thickness are the basic principles in which the shield thickness depends highly on the energy and the type of the source. Lead or concrete materials are usually used for shielding gamma sources as in most cases, concrete shielding is used because of its cheapness, lightness, and availability. Of course, it is worth mentioning that for situations where space is limited, it is better to use materials with high atomic number and density such as lead. Otherwise, concrete may be used, whose effective density can be increased by using special materials and additives.

The design of one hot cell shielding is done regarding different materials and thicknesses using MCNP code. Gamma and neutron dose rate are calculated for a spent fuel source according to proposed criteria [iv]. The shielding calculations for activated first wall transferring of ITER using MCNP code is done in another research work [v]. Also, the shielding structure of hot cell shielding door is introduced for one nuclear power plant where the neutron shielding performance is studied by experimental and simulation methods. Finally, the material and its thickness for hot cell shielding door is provided [vi].

In this research, the optimal thickness of a hot cell for a 60Co source with 1.85E13 Bq activity was calculated using MCNP6 code [vii] and the feasibility of using it for silicide spent fuel plate was investigated which is the first time in our country and an innovation in comparison to the other research works. In this feasibility study, a silicide fuel plate with 90% burnup with a cooling time of 30 days is considered as the most pessimistic mode of the gamma source where calculations are done using ORIGEN code [viii]. Finally, the results of the gamma dose rate for this mode have

been calculated and the optimal thickness values have been determined with the preset value of 10 μSv/h in different parts of the outer of the hot cell.

Materials and methods

In order to calculate the gamma dose rate to determine the thickness of the shield in a hot cell, a 60Co point-source having 1.85E13 Bq activity and 1.17 MeV and 1.33 MeV energies and a silicide fuel plate have been simulated, separately. The sources are considered homogeneous in all directions. Then, the values of the gamma dose rate in different places outside the concrete shield of the hot cell have been calculated without compromising the preset criterion of 10 μSv/h [ix, x]. Figure 10 shows the dispersion of 60Co gamma sources (right) and gamma tracks (left) in the hot cell simulated by MCNP6 code.

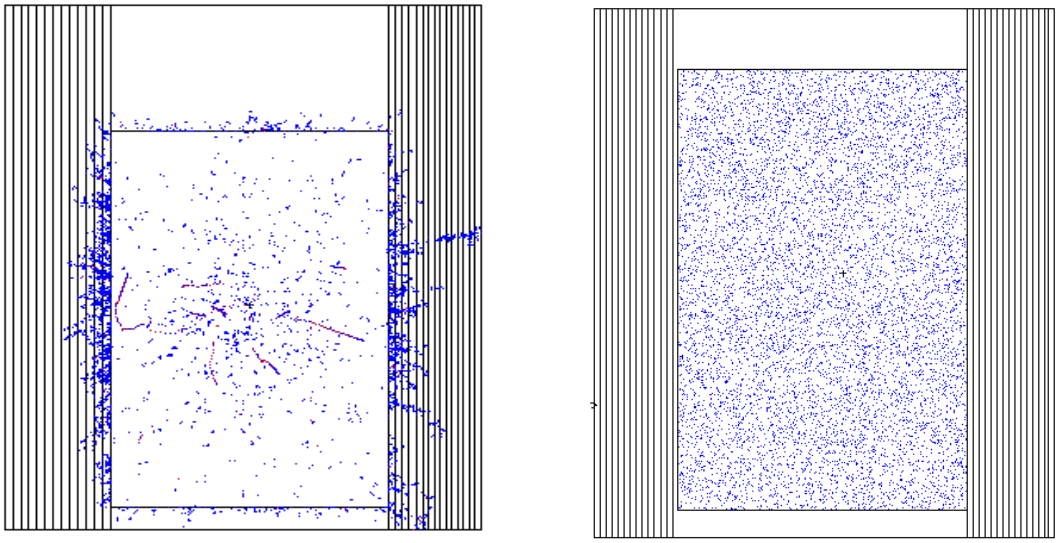

Figure 10. Dispersion of gamma sources (right) and gamma tracks (left).

Figure 2 shows the characteristics of the components and dimensions of the systems and the materials used in the hot cell.

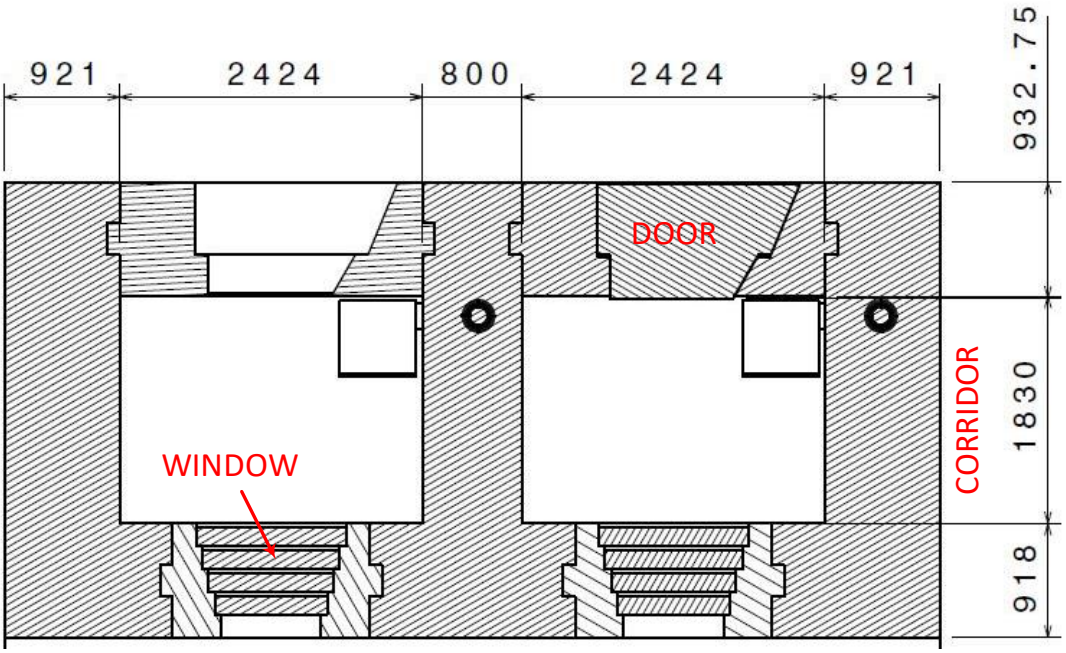

Figure 11. Characteristics of the components and dimensions (mm).

Figure 12 shows two different views of the hot cell simulated using MCNP6 code.

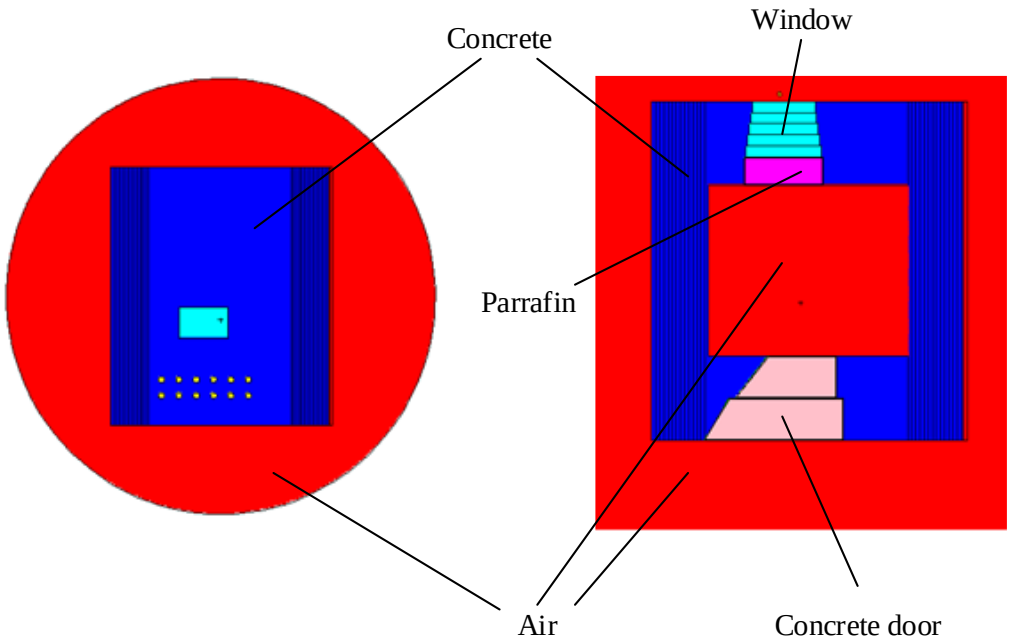

Figure 12. Upper (right) and side view (left) of the simulated hot cell.

The concrete enclosure is made of barite concrete in which two rows of six holes are intended for the passage of special equipment. The fillers of the holes are made of 45.5 centimeters long lead parts. The window is composed of lead glass with 6.22 gcm-3 density. Compositions and weight

percentages of all materials mentioned in this report for the MCNP6 input were based on validated references [xi].

Gamma dose rate calculations are done using F5 Tally of MCNP6 code. This tally use from response function for point wise dose rate calculations from flux through IC and IU cards. MCNP code using ENDF/B-VI cross section library for dose rate calculations.

Results and discussion

Dose rate calculations

The gamma dose rate in the hot cell was calculated for 90% burned silicide fuel plate with 30 days cooling time and for a 1.85E13 Bq 60Co point-source using F5 point tally in the MCNP6 code. In this research, the variance reduction method based on statistical population control was used based on multiplication methods and Russian Roulette with spatial meshing as well as energy cutting methods to reduce results errors and execution times. The average error of the calculations in all results is less than 10%.

It is worth mentioning that the intensity of the source is 1.60E+14 Bq. One silicide fuel plate dimension is 7.7×0.15×61.5 cm3 with 4.8 gcm-3 U3Si2 meat in an Al clad. The spent silicide fuel gamma spectrum is obtained using the ORIGEN code and given in Figure 13.

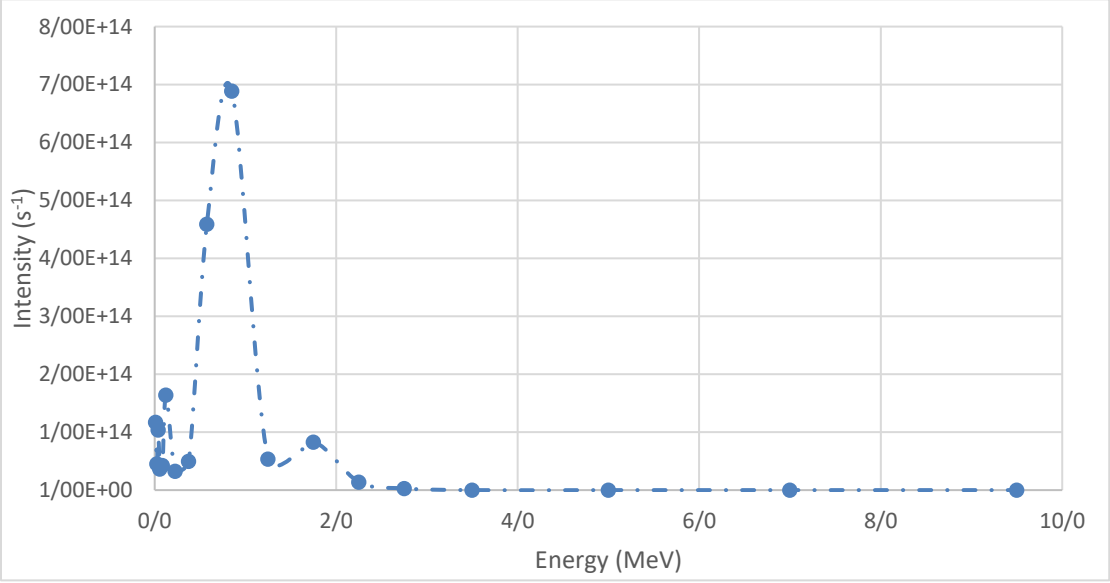

Figure 13. Gamma spectrum of a silicide spent fuel.

In these calculations, the gamma dose rate was obtained for three different situations including the corridor behind of the concrete wall, behind the window and behind the door of the hot cell are shown in Figure 14, Figure 15 and Figure 16.

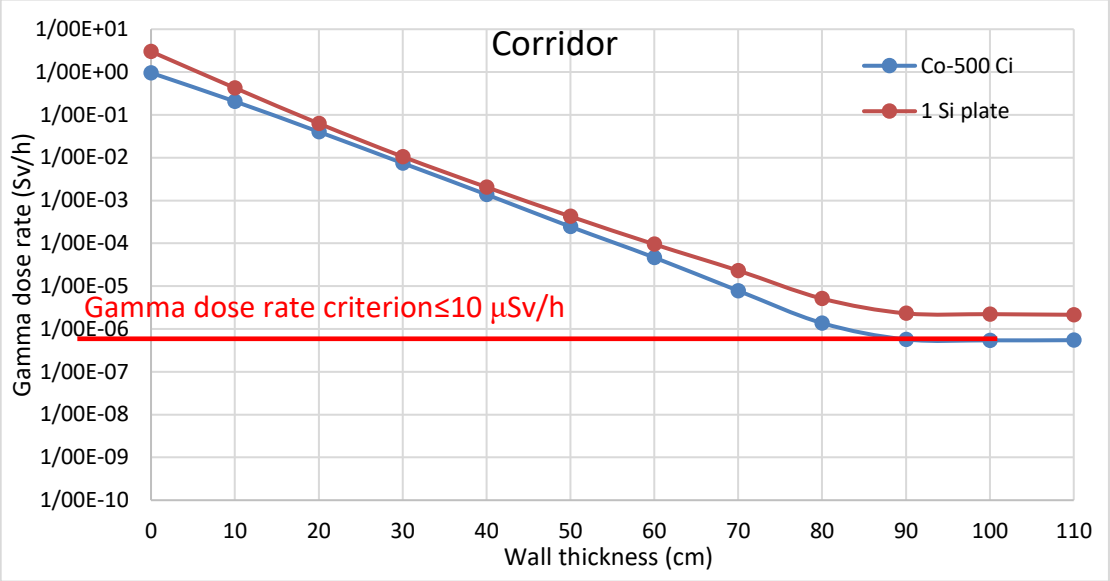

Figure 14. Gamma dose rate for concrete wall in the side of corridor.

As Figure 14 shows, based on the defined criterion of less than 10 µSv/h, the optimum thickness of the corridor wall for having less than the preset dose rate values are 70 and 78 cm for for 60Co and spent fuel plate, respectively.

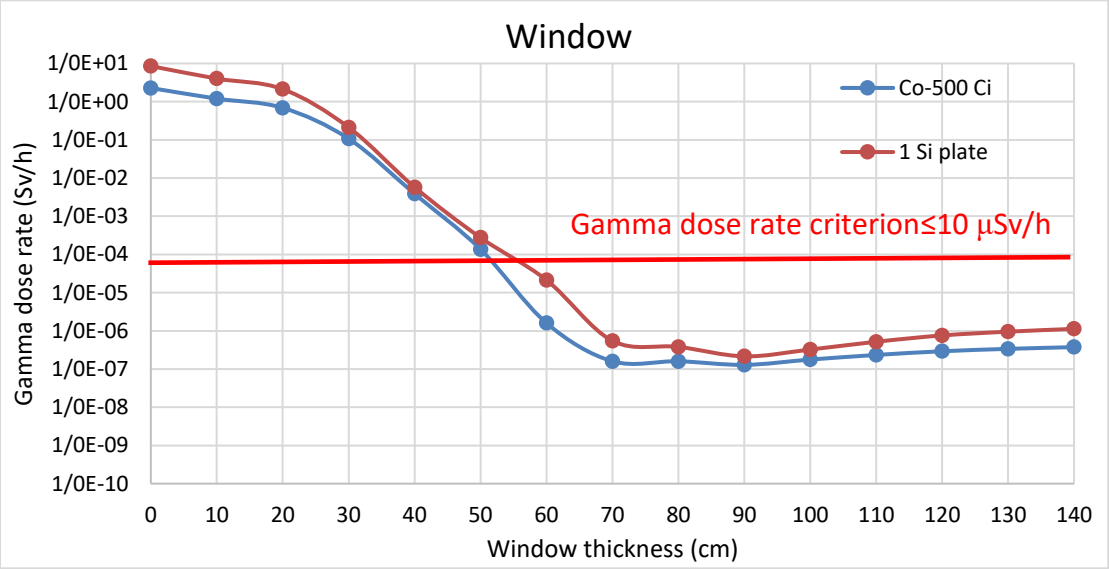

Figure 15. Gamma dose rate for inside and outside of window

As could be seen from Figure 15, the optimal thickness of window for silicide fuel plate and cobalt source are 67 and 60 cm with dose rate values of 5.7 and 1.6 µSv/h, respectively.

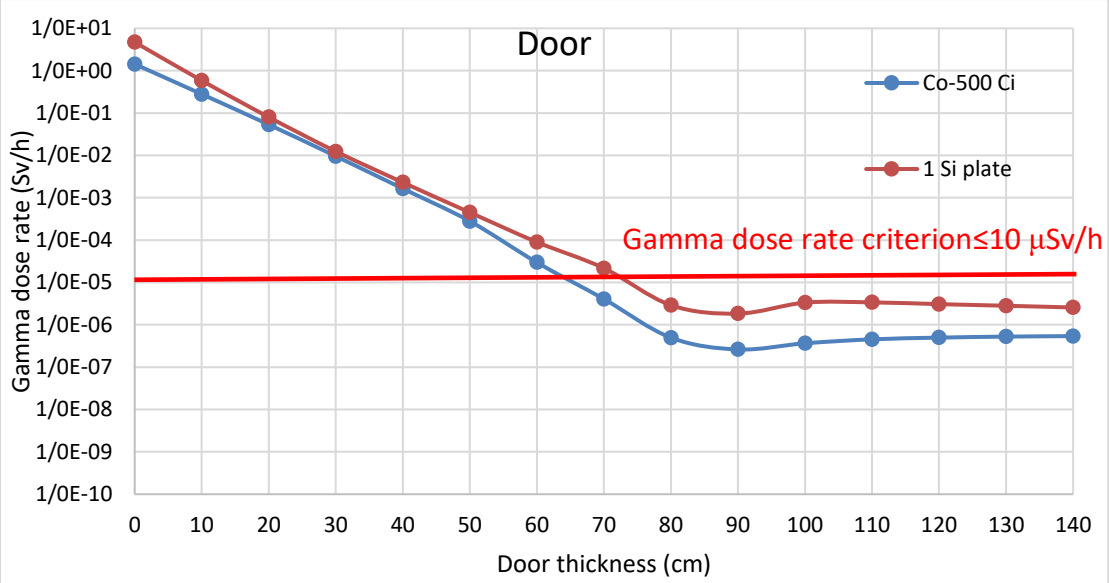

Figure 16. Gamma dose rate for inside and outside of the door

As could be seen from Figure 16, the optimal thickness of concrete door for silicide fuel plate and cobalt source are about 80 and 70 cm with dose rate values of 2.9 and 4.1 µSv/h, respectively.

As could be seen form the given results, the gamma dose rate out of the hot cell is lower that the preset criterion where the silicide spent fuel plate has bigger dose rate values in comparison to the 60Co in all of investigated cases.

Conclusions

In this research, the gamma dose rate for a 60Co point-source with 1.85E13 Bq activity and a silicide fuel plate with 90% burnup after 30 days cooling as the most conservative cases were calculated using MCNP6 code to determination of the optimum thickness of the shielding of hot cell.

The source intensity and gamma spectrum of the silicide fuel plate was done using ORIGEN code. It should be mentioned that the criterion of 10 µSv/h was used to determine the optimum thickness of the hot cell wall in different directions. Finally, the results of this article show that the gamma dose rate of silicide fuel plate is slightly higher than the cobalt source. Also, the maximum concrete

thickness for having less than dose rate criterion is in the corridor with 86 and 76 cm concrete shielding for silicide fuel plate and cobalt sources, respectively.

References

[1] IAEA (2016), Safety of Nuclear Power Plants: Design, IAEA Safety Standards, Specific Safety Requirement NO. SSR-2/1.

[2] IAEA (2008), Radiation. Radioactive Waste Management in the Design and Operation of Research Reactors, IAEA Safety Standard Series No. NS-G-4.6.

[3] M. Hannan Bahrin, etc. (2019), The design of a Hot Cell with interlocking concrete wall, IOP Conf. Series: Materials Science and Engineering 555.

[4] Cho IJ, You GS, Choung WM, Ku JH, Kook DH, Hwang YH, Lee EP, Park SW (2004). Evaluation on the radiation shielding for the design of a hot cell facility. Journal of Nuclear Science and Technology; 41(sup4):97-100.

[5] Yu S, Yang Q, Chen C, Hu L, Wu Y, (2015). Loughlin M. Shielding design for activated first wall transferring in ITER hot cell building. Journal of Fusion Energy.34:887-94.

[6] Zhang S, Wang Z, Li C, Zhao Y, Feng C, Dai M. (2022), Study on neutron shielding performance of hot cell shielding door for nuclear power plant. Annals of Nuclear Energy.1;166:108752.

[7] B. P. Denise (2013), Mcnp6 User's Manual Version 1.0.

[8] Crofft AG (2000). A User's Manual for the ORIGEN 2.1 Computer Code. Rep. ORNL/TM-7175Oak Ridge National Laboratory.

[9] M. R. Akbar and T. J. Van Rooyen (2013), Modelling and Comparison of Hot Cell Shielding Capabilities During a Criticality Excursion South African Nuclear Energy Corporation (NECSA), P.O. Box 582, Pretoria.

[10] A. B. Chilton, K. Shultis, J. Faw, E. Richard (1984), Principles of Radiation Shielding, Prentice-Hall, Inc., Englewood, New jersey.

[11] R. J. McConn Jr, C. J. Gesh, R. T. Pagh, R. A. Rucker, RG Williams (2011), III Compendium of Material Composition Data for Radiation Transport Modeling, Prepared for the U.S. Department of Homeland Security, PNNL-15870 Rev. 1.

ICNST 2024
International Conference on Nuclear Science and Technology
6- 8 MAY 2024 | Isfahan, Iran

Digital discrimination of alpha particles and gamma-rays in phoswich detector using charge comparison method (Paper ID: 1228)

Panahi. R.[1], Feghhi SAH[1*], Rajabi Moghadam. S[2], Zamzamian. SM[1]
[1]Department of Radiation Application, Shahid Beheshti University, Tehran, Iran
[2]Department of Medical Radiation Engeneering, Central Tehran Branch, Islamic Azad University, Tehran, Iran.

Abstract

Analysis of most environmental samples demands precise detection of their emitted radiation, which in many cases includes both alpha particles and gamma-rays. Simultaneous detection of these radiations enhances the identification and distinguishes potentially unknown components. Phoswich detectors are a reliable and low-cost solution for the simultaneous detection of different types of radiation. In phoswich detectors, identification of radiation types is based on pulse shape differences among the scintillators which can be performed by analog or digital methods. In the current study, a two-layer phoswich detector consisting of BC-400/CsI(Tl) is used for the simultaneous detection of alpha particles and gamma rays emitted from common radionuclides. The digital charge comparison method is employed for alpha/gamma discrimination using the phoswich detector. This method resulted in a figure of merit (FOM) of 2.7. The misclassification of gamma-rays is less than 5% by this method.

Keywords: phoswich detector, scintillator, radiation discrimination, charge comparison method, figure of merit (FOM)

Introduction

Analysis of most environmental samples demands spectroscopy of their emitted radiations which in many cases (such as actinide elements) are alpha particles and gamma rays [1]. The difference in the output pulses from the scintillator detector can be used to identify the type of radiation interaction with the detector. It can be performed either by using a single crystal that has several decay times for the different types of radiations or by two different optically coupled scintillators where each scintillator responds to a particular type of radiation [2].

The combination of two dissimilar scintillators optically coupled to a single PMT is often called a phoswich detector [3]. The scintillators have different decay times so the shape of the output pulse

from the PMT is dependent on the relative contribution of light from the two scintillators [4]. By analyzing the specific pulse shape, it is possible to determine the radiation type. This is commonly referred to as the Pulse Shape Discrimination (PSD) method. PSD methods can be performed using analog [5] or digital methods [6]. The digital systems have several advantages such as digital pulse charge integration, elimination of distorted pulses, pulse shape discrimination capability, and effective baseline correction, accompanied by post-trigging of the data pulse. The Rise Time Discrimination (RTD) and Charge Comparison (CC) methods are the most popular techniques to discriminate among pulses from a phoswich detector. The time it takes for the pulse to rise from the lower fraction to the upper fraction is known as the rise time. In the RTD method, the radiation discrimination is caried out based on analyzing the rise time interval [7]. On the other hand, the CC method is based on a comparison of the integrals of the pulses for two different time intervals [8]. In this paper, digital charge comparison method is used for Simultaneous α/γ discrimination in phoswich detector.

Research Theories

The CC method is based on a comparison of the integrals of a pulse, over two different time intervals. These integrals are often referred to as the long integral and the short integral [8]. The former corresponds to the large area of the pulse, while the latter includes only a short part of the pulse [9, 10]. In this method, the charge ratio is used for pulse-type identification. As illustrated in Fig. 1, the charge ratio (CR) is the ratio of the short integral (S_1) to the long integral (S_2). Using mixed alpha and gamma sources, we obtained two separate charge ratios for received pulses. A charge ratio interval was considered for gamma rays (called CR_g) and another one was considered for alpha particles (called CR_a). If the pulse is identified in each of these intervals, it is then known as the corresponding radiation type. If the pulse was not within these intervals, it was rejected.

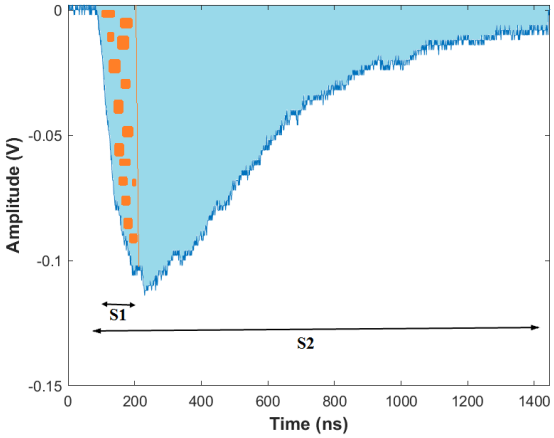

Fig. 1. Charge comparison method description

Experimental

The phoswich detector consisted of BC-400 (with a thickness of 50 µm) and CsI(Tl) (with a thickness of 3 mm) for detecting alpha particles and gamma rays, respectively. The most common alpha-emitter radionuclides have alpha particles with energy about 4-6 MeV. Alpha particles with this amount of energy stop completely in 50 µm of BC-400 scintillator [1]. These scintillators were assembled and optically coupled to a PHOTONIS XP3132 photomultiplier (PMT) tube. The experimental setup is shown in Fig. 2. Using a digital oscilloscope (Tektronix TDS2024), anode pulses were directly digitized and then transferred to a personal computer for analysis. In all of the experiments, to avoid disturbance by ambient light, the phoswich detector and the PMT were placed in a black box. Also, to reduce background radiation, the complete configuration was placed in the lead shield.

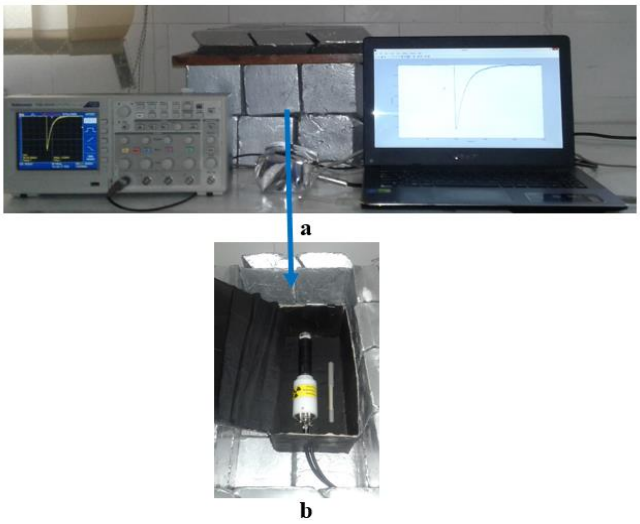

Fig. 2. a) experimental configuration and b) phoswich detector inside a black box.

Results and Discussion

A phoswich detector was exposed to mixed radiation emitted from a 241Am source. 241Am emits alpha particles and gamma rays coincidentally. Fig. 3 (a) and (b) show the 2-D scatter plot and the abundance of charge ratio for the 241Am source. Herein, the long integral corresponds to the total area of the pulse, whereas the short integral was taken from the beginning of the pulse to 160 ns afterward. In the CC method, CR_g is between 0.25 and 0.41 for gamma rays, and CR_a is between 0.45 and 0.6 for alpha particles. The performance of PSD methods has traditionally been qualified by the figure of merit (FOM), which measures the width and locations of peaks in a histogram of pulse shape data and is defined by:

$$FOM = \frac{s}{w_1 + w_2}$$

Where, s is the separation between Gaussian centroids, w_1 and w_2 are the FWHM of them. According to the Fig. 3 (b), FOM of the CC method is 2.7 which provides reasonable discrimination quality.

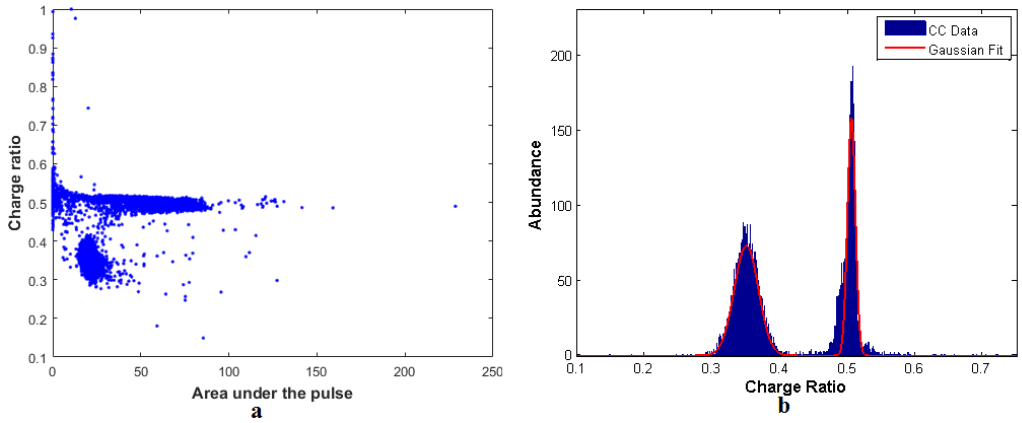

Fig. 3. a) Scatter plot, b) abundance of charge ratio

Another method of quantification of PSD performance involves measuring the percentage of radiation pulses of a particular type misclassified as the other type e.g. the spillover of gamma radiation signal into the alpha region of interest. To investigate the performance of the CC method in separating alpha and gamma events, more than 10,000 pulses were recorded when the detector was exposed to 137Cs source and 241Am source shielded by a thin sheet of aluminum. The results of the measurements are given in Table 1. The misclasification of gamma-ray is less than 5% by the CC method.

Table 1. The fraction of event types from ^{137}Cs and alpha-shielded ^{241}Am

sources	Radiation type	CC
^{137}Cs	Pulses recorded as alpha particles (error rate in gamma classification)	1.22%
	Pulses recorded as gamma rays	98.28%
	Rejected pulse	0.5%
^{241}Am	Pulses recorded as alpha particles (error rate in gamma classification)	4.21%
	Pulses recorded as gamma rays	95.69%
	Rejected pulse	0.1%

Conclusions

In this paper, the digital charge comparison (CC) method was employed to discriminate between alpha particles and gamma rays emitted from the most common radioisotopes, utilizing a BC-400/CsI(Tl) phoswich detector. The signal from the anode of the PMT was directly digitized and then transferred to a personal computer for analysis. The performance of the CC method is

quantified based on the FOM and misclassification of the radiation types. The CC method resulted in a FOM of 2.7. The misclassification of gamma rays is less than 5%, so the alpha/gamma discrimination system has reasonable discrimination quality.

References

1. Moghadam, S.R., S. Feghhi, and M. Safari, A phoswich detector for simultaneous alpha–gamma spectroscopy. Nuclear Instruments and Methods in Physics Research Section A: Accelerators, Spectrometers, Detectors and Associated Equipment, 2015. 799: p. 59-63.
2. Chandrikamohan, P. and T.A. DeVol, Comparison of pulse shape discrimination methods for phoswich and CsI: Tl detectors. IEEE Transactions on Nuclear Science, 2007. 54(2): p. 398-403.
3. Farsoni, A. and D. Hamby, MCNP analysis of a multilayer phoswich detector for β-particle dosimetry and spectroscopy. Nuclear Instruments and Methods in Physics Research Section A: Accelerators, Spectrometers, Detectors and Associated Equipment, 2005. 555(1-2): p. 225-230.
4. Knoll, G.F., Radiation detection and measurement. 2010: John Wiley & Sons.
5. Wang, C.-F., J.-H. Lee, and H.-J. Chiou, Rapid determination of Sr-89/Sr-90 in radwaste by low-level background beta counting system. Applied radiation and isotopes, 1994. 45(2): p. 251-256.
6. Farsoni, A. and D. Hamby, A system for simultaneous beta and gamma spectroscopy. Nuclear Instruments and Methods in Physics Research Section A: Accelerators, Spectrometers, Detectors and Associated Equipment, 2007. 578(3): p. 528-536.
7. Panahi, R., et al., Simultaneous alpha and gamma discrimination with a phoswich detector using a rise time method and an artificial neural network method. Applied Radiation and Isotopes, 2019. 154: p. 108881.
8. Gamage, K., M. Joyce, and N. Hawkes, A comparison of four different digital algorithms for pulse-shape discrimination in fast scintillators. Nuclear Instruments and Methods in Physics Research Section A: Accelerators, Spectrometers, Detectors and Associated Equipment, 2011. 642(1): p. 78-83.
9. Alharbi, T., Simple algorithms for digital pulse-shape discrimination with liquid scintillation detectors. Radiation Physics and Chemistry, 2015. 106: p. 50-55.
10. Nakhostin, M., A technique for the reduction of pulse pile-up effect in pulse-shape discrimination of organic scintillation detectors. Nuclear Engineering and Technology, 2020. 52(2): p. 360-365.

ICNST 2024
International Conference on Nuclear Science and Technology
6- 8 MAY 2024 | Isfahan, Iran

Experimental measurement of dosimetry tests on a nanocomposite dosimeter (Paper ID: 1235)

A. Mosayebi*, S. Malekie and H. Daneshvar
Radiation Processing and Dosimetry Research Group, Radiation Application Research Institute, Nuclear Science and Technology Research Institute, Tehran, IRAN.

Abstract

Polystyrene-multi-wall carbon nanotube have many applications in various fields, especially sensors and radiation dosimeters. Carbon nanotubes (CNTs) due to their unique properties such as high length-to-diameter ratio and high electrical conductivity, through addition to polymer substrates, lead to the formation of three-dimensional conductive networks in these materials. When the volume or weight fraction of CNTs in the polymer substrate exceeds a critical limit, the polymer undergoes a phase change, and its electrical conductivity increases. In this experimental work, angle dependence, field size, energy and reproducibility of Polystyrene-multi-wall carbon nanotube nanocomposite dosimeter response under gamma irradiation in the radiation field of the National Secondary Standard Dosimetry Laboratory (SSDL) were performed. In order to measure these characteristics on the response of PS-MWCNT nanocomposite dosimeter, the distance of the dosimeter from the source was 80 cm and the fixed dose rate was 75 mGy/min. The results showed that the response of this dosimeter in the range of ±40 degree, the angle difference was 3.9% and the repeatability changes were equal to 0.48%.

Key words: nanocomposite dosimeter, gamma radiation, dosimetry tests, constant dose rate.

Introduction

In order to make an active dosimeter based on polymer nanocomposites, it is necessary to investigate the effect of gamma radiation on the physical properties of the mentioned materials. Nanocomposite dosimeters consist of two phases: soft (polymer) and hard (carbon nanotubes). Polymer nanocomposite-carbon nanotube has been proposed as a radiation dosimeter in previous studies by the present authors from simulation and experimental aspects [1-9]. In this dosimeter, the radiation current created by the beam is designed as voltage changes at the output of the electronic system and is shown digitally. In this experimental work, the dosimetry characteristics

of PS-MWCNT nanocomposite under gamma irradiation related to Cobalt-60 source in the radiation field of the National Secondary Standard Dosimetry Laboratory (SSDL) were performed.

Experimental

In this experimental research, polystyrene (PS) grade 1540 and density 1.05 g/cm3 was prepared in the form of powder from Tabriz Petrochemical. Multi-walled carbon nanotubes (MWCNT) with a purity of more than 99% were purchased from US-Nano. The physical characteristics of the prepared multi-walled carbon nanotubes are: outer diameter 5-15 nm, inner diameter 3-5 nm, length 50 µm, density 1/2 g/cm3, SSA greater than 233 m2/g and electrical conductivity S /m 107-105; Finally, chemical solvents with high purity were obtained from Merck. In order to prepare the materials, first, multi-walled carbon nanotubes were added to a specific volume of dichloromethane (DCM) solvent and ultrasonicated in a UP200H probed ultrasonic device with a power of 200 W and a working frequency of 24 kHz for 20 minutes. At the same time, polystyrene was placed in another container containing toluene solvent at a temperature of 135°C for 30 minutes on a magnetic stirrer until the polymer was completely dissolved in it. It is worth mentioning that at this stage, in order to prevent the evaporation of the solvent at high temperature, the container was covered with aluminum foil. Finally, these two solutions were combined and sonicated again for one hour. Due to the difference in the boiling point of dichloromethane (boiling point 39.6 °C) and toluene (boiling point 111 °C), when the two solutions were mixed together, cavities or bubbles were observed, which probably led to the breaking of nanotube clumps. carbon nanotubes and finally a better and more uniform distribution of carbon nanotubes inside the polymer substrate. Then, in order to make the said nanocomposite, according to Figure 1, the desired designs were made. In the manufactured sample, the electrodes are made of silver (silver paste). According to Figure 1, multi-walled carbon nanotubes are depicted in the polystyrene substrate.

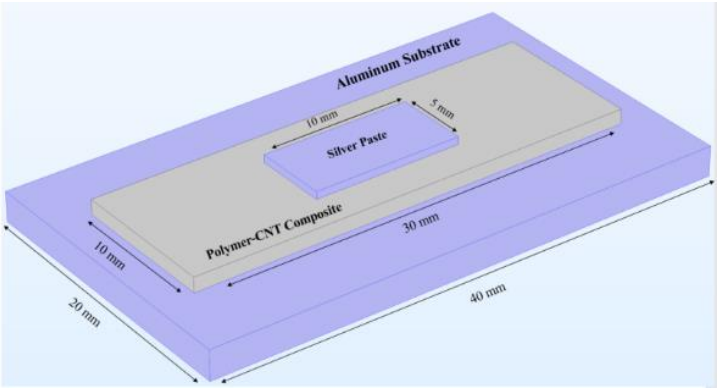

Fig. 1. Design of polymer-carbon nanotube nanocomposite and presentation of electrodes made of silver paste

According to Figure 2, in the irradiation stage of the nanocomposite dosimeter, the 60Co source of the Picker-V9 model located in the secondary standard dosimetry laboratory of the Atomic Energy Organization, Karaj was used. In order to measure the current resulting from radiation, an electronic system has been used that shows the generated current in terms of voltage changes at the output.

Fig. 2. Gamma irradiation system (Picker V9) used in this research

After making the PS/MWCNT nanocomposite, in order to ensure proper and uniform dispersion and distribution of nanoparticles in the polymer substrate, according to Figure 3, FESEM test was used.

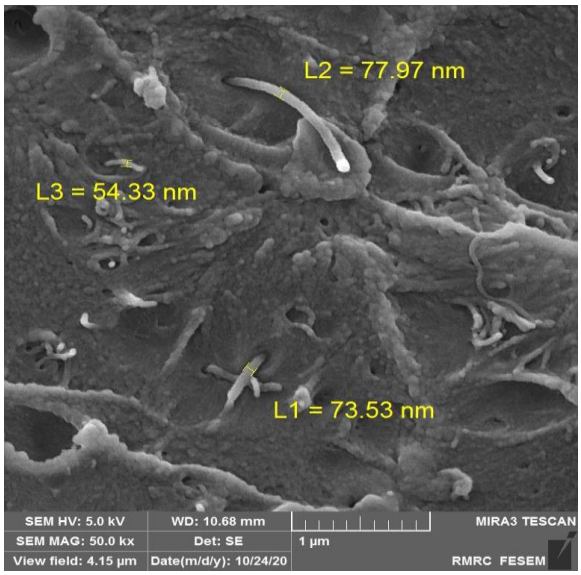

Fig. 3. FESEM image of PS/MWCNT nanocomposite

Results and Discussion

In this experimental work, after making the PS/MWCNT nanocomposite and ensuring the homogeneous distribution of carbon nanotubes in the polymer substrate, the irradiation process was carried out. The dose rate used in this experimental work to investigate the dosimetry characteristics of nanocomposite under irradiation is 75 mGy/min. The nanocomposite dosimeter was exposed to radiation with a 60Co source, model Picker-V9. According to Figure 4, the flow related to radiation in the range of 47-157 mGy/min has increased completely linearly. According to the linear fit of these points from the least squares approximation R2=0.9996, it can be said that the response of the mentioned nanocomposite in the dose range of 47-157 mGy/min is linear with very good accuracy and in this range it can be as The radiation dosimeter used the mentioned nanocomposite.

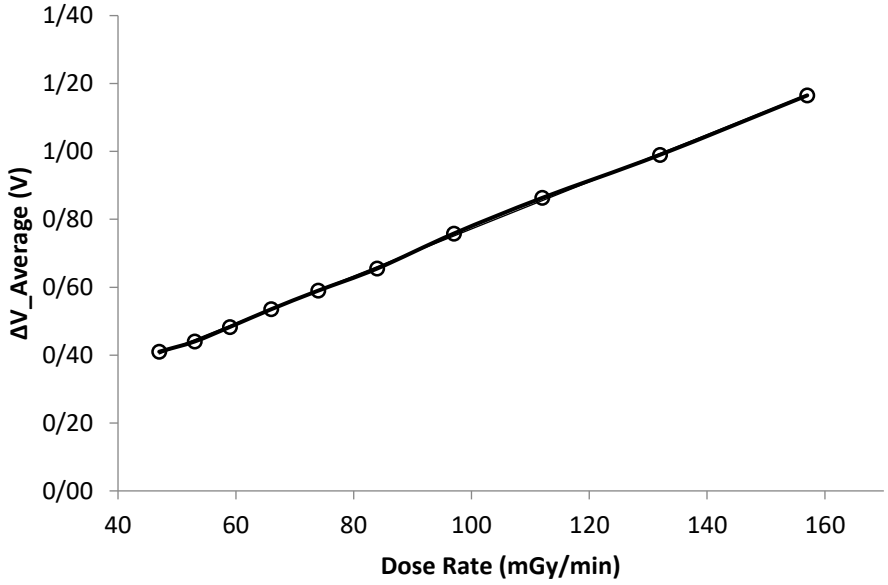

Fig. 4. Average radiation current at different doses for nanocomposite dosimeter under irradiation with Picker-V9 ^{60}Co source

Fig. 5 shows the angular dependence of PS-MWCNT nanocomposite sample that was irradiated at 75 mGy/min. The orientation of the normal line on the sample page with the incident gamma-ray was assumed as the measurement angle and set at $\theta = \pm 40°$ and the average ΔV were measured. The results show a change of 4.5% of the voltage in comparison to the response obtained at θ = zero.

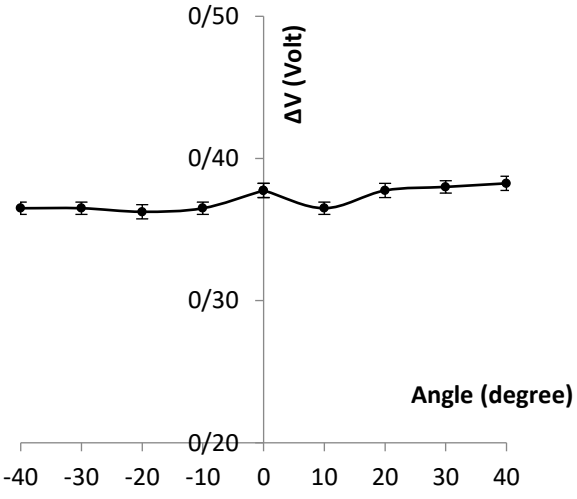

Fig. 5. Variation of ΔV of the PS-MWCNT nanocomposite sample in different gamma-ray incident angles

The reproducibility of the prepared nanocomposite sample as a realtime dosimeter at the same dose-rate of 75 mGy/min, SSD = 80 cm, a bias voltage of 800 V, and field size of 10 × 10 cm2 was investigated as well. In this regard one sample was irradiated under 60Co gamma-ray and the photocurrent was measured for 15 s. This procedure was repeated for 10 times in each independent measurement and its variations are demonstrated in Fig. 6. The result shows the ΔV repeatability equal to 0.48%.

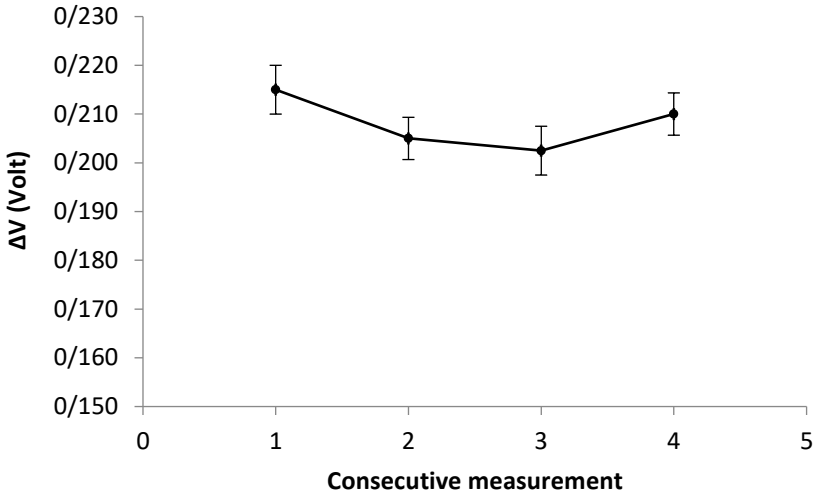

Fig. 6. Repeatability investigation for PS-MWCNT nanocomposite sample at the same dose-rate of 75 mGy/min.

Conclusions

In this experimental work, angle dependence, field size, energy and reproducibility of Polystyrene-multi-wall carbon nanotube nanocomposite dosimeter response under gamma irradiation in the radiation field of the National Secondary Standard Dosimetry Laboratory (SSDL) were performed. In order to measure these characteristics on the response of PS-MWCNT nanocomposite dosimeter, the distance of the dosimeter from the source was 80 cm and the fixed dose rate was 75 mGy/min. The results showed that the response of this dosimeter in the range of ±40 degree, the angle difference was 3.9% and the repeatability changes were equal to 0.48%.

References

[1] Mosayebi, A., et al. (2017). "A feasibility study of polystyrene/CNT nano-composite as a dosimeter for diagnostic and therapeutic purposes," Journal of Instrumentation, 12: P05012.

[2] Malekie, S., et al. (2016). "Study on dosimetry characteristics of polymer–CNT nanocomposites: Effect of polymer matrix," Nuclear Instruments and Methods in Physics Research Section A: Accelerators, Spectrometers, Detectors and Associated Equipment, 816: 101-105.
[3] Malekie S., et al. (2015). "Study on a novel dosimeter based on polyethylene–carbon nanotube composite," Nuclear Instruments and Methods in Physics Research Section A: Accelerators, Spectrometers, Detectors and Associated Equipment, 791: 1-5.
[4] Mosayebi, A., et al. (2019). "Experimental investigation of dosimetry response of nanocomposite of polystyrene-multiwall carbon nanotube in gamma radiation field. Iranian Journal of Radiation Safety and Measurement," 7: 21-26.
[5] Maleki, S., et al. (2017). "Simulation of a novel dosimeter based on electrical characteristics of polymethyl Methacrylate-Carbon nanotube composite," Nuclear Science and Technology, 79: 53-62.
[6] Malekie, S. (2016). "A Dissertation entitled the Study of Electrical Conductivity Variation of Polymer-Carbon Nanotube Composite for Radiation Dosimetry Utilization," PhD, Nuclear Science & Technology Research Institute, Tehran, Iran.
[7] Malekie S., et al. (2017). "Comparative Study of Micro and Nano Size WO3/E44 Epoxy Composite as Gamma Radiation Shielding Using MCNP and Experiment," Chinese Physics Letter, 34: p. 108102.
[8] Malekie, S., et al. (2018). "Experimental comparison of dosimetry and detection response of micro/ nano WO3-PVA composite to gamma and neutron beams," Iranian Journal of Radiation Safety and Measurement, 6: p. 9-16.
[9] Mosayebi, A., et al. (2019). "Experimental study on polystyrene-MWCNT nanocomposite as a radiation dosimeter," Radiation Physics and Chemistry: p. 108362.

ICNST 2024 International Conference on Nuclear Science and Technology
6- 8 MAY 2024 | Isfahan, Iran

Assessment of plastic scintillation detectors for use in vehicle gamma-ray portal monitors (Paper ID: 1270)

E. Javadi[1], A. Ghalehasadi[1], M. Monshizadeh[1], M. Khosravani[1], R. Roozehdar Mogaddam[1], A. Taheri[1,2*] and S.P. Shirmardi[1,2]

[1]Iran Radiation Application Development Company (IRAD Co.) – Atomic Energy Organization of Iran, Tehran – I.R. of Iran, PO Box: 14395-836.

[2]Radiation Application Research School, Nuclear Science and Technology Research Institute, Tehran, Iran, Postal code: 14395-836.

Abstract

Iran Radiation Application Development Company (IRAD Co.) has undertaken the design and construction of gamma-ray portal monitors specifically designed for detecting radioactive materials and contamination. These monitors have been developed for various applications such as controlling the transportation of radioactive materials and inspecting and identifying radioactive materials in customs. A particular focus has been placed on monitoring the inner space of vehicles and truckloads. The system consisted of electronic circuits, mechanical holders, and four plastic scintillation detectors, which collectively serve as the monitoring system. The precise design of the dimensions and spacing between the plastic scintillation detectors significantly influences the performance and effectiveness of the developed portal monitor. The accuracy of the system was demonstrated through functional tests using a 137Cs source. These tests revealed that the monitoring system was capable of detecting a source inside a car, with at a minimum activity level of 3 µCi, when positioned at a distance of 100 cm. This outcome underscores the precise and reliable performance of the monitors' design.

Keywords: Portal monitors, Plastic scintillator, Moving radioactive sources, Minimum Detectable Activity, Gamma-ray.

Introduction

Radiation Portal Monitors (RPMs) are critical components in national and international security for the detection of radioactive materials. With the rise of nuclear technology, both for power generation and medicinal purposes, as well as the threat of nuclear terrorism, the importance of

effective RPMs has never been greater [1]. These monitors are non-intrusive and are used to screen vehicles, containers, and other conveyances for special nuclear materials [2]. Plastic scintillation detectors have gained attention for their potential use in radiation portal monitors due to their characteristics. Studies have shown that plastic scintillation detectors exhibit nearly energy-independent behavior over a range of energies from 0.5 to 20 MeV, making them suitable for radiation detection applications [3]. Furthermore, plastic scintillation detectors have been deployed in radiation portal monitor systems for the interdiction of nuclear material at borders, highlighting their practical application in security measures [4]. Moreover, the development of integrated and portable probes based on functional plastic scintillators for the detection of radioactive cesium demonstrates the versatility and applicability of plastic scintillation detectors in radiation detection scenarios [5]. The evaluation of source identification methods using plastic scintillators in portal monitoring systems further emphasizes their role in detecting illicit trafficking of radioactive sources in cargo containers [6]. These findings collectively underscore the significance of plastic scintillation detectors in radiation portal monitoring, demonstrating their potential for use in detecting radioactive materials and enhancing security measures at border crossings and ports.

In this study, taking into account the important quantities of the radiation portal monitor, how to choose and the exact type of detector specifications for making a car radiation portal monitor has been investigated. Then, by Monte Carlo simulation, the optimal dimensions and distance between the large-sized plastic scintillation detectors of the gated monitor have been designed. Also, experimental tests have been done for evaluation of the minimum detectable activity.

Design Simulation

In the design phase of the radiation monitoring system, Monte Carlo simulation of MCNPX code was used. The dimensions and the distance between two detectors in the detector are important parameters for the design and construction of the detector system, and therefore the simulation was carried out based on the Monte Carlo method for the transmission of gamma rays with the aim of measuring the detector gate counting speed with different detector dimensions and also the distance between the detectors. For this purpose, two flickering plastic screens on one side with different widths of 25, 50 and 100 cm and 100 cm long on each side of the monitor were

considered. Each of these scintillation plates are placed on one side in the code input file for separation distances of 0, 30, 60, 90 and 120 cm.

Counting rate values were obtained by all 4 scintillation plates for three widely used industrial sources of radioactive gamma 137Cs, 60Co, and 241Am in the space between the gate and at 3 positions 20, 225, and 450 cm from the ground. Various simulation scenarios are presented below.

Scenario 1: In this scenario, we consider the changes in the total count rate of 4 detection plates for the triple heights of 20, 225, and 450 cm and the placement of the radioactive gamma source 137Cs, 60Co, and 241Am in the space between the two plates and the separation distances of the double plates above and the bottom on both sides for different dimensions of 100 x 25 cm2, 100 x 50 cm2 and 100 x 100 cm2 detector.

Scenario 2: In this scenario, the percentage changes of the total detection plate count rate with triple energies of 60, 662 and 1250 keV related to the radioactive sources of gamma 241Am, 137Cs and 60Co with different separation distances of the upper and lower double plates, were considered.

Scenario 3: Given that the two most important parameters in determining the optimal separation distance of scintillation plates on both sides of the detector gate and on the one hand high sensitivity in reading and tracing the passing source (large counting rate values) and on the other hand less changes in the dynamic range of rate changes of the total count is (more smooth dynamic range), so equation (1) can be presented as follows:

$$C = \frac{cpp_{max} \times 100}{\text{dynamic range}(\%)} \quad (1)$$

The optimal condition is when we face the maximum of the numerator and the minimum of the denominator, and in other words, the parameter C has a maximum value.

Design and construction

Normally, plastic scintillation detectors are used in RPMs because they have the characteristics of fast response time, sensitive to nearly all types of radiation, affordable cost, high and varied manufacturing, low radiation damage, etc. and therefore it is mostly used in most personal and car gate monitors. In the production monitoring system, due to these characteristics, four PVT plastic scintillation detectors and four PMTs have been used. To obtain the dimensions and distance

between the detectors, the Monte Carlo simulation of MCNPX nuclear code has been used, as mentioned in previous section. The electronic boards were placed in the space between the two detectors. By choosing 5 mm iron metal with 6 mm lead shielding for the back plate and 2 mm thick aluminum metal for the front plates, the devices were made to house the detectors, PMTs and system electronics. The image of the constructed radiation portal monitor is given in figure (1).

Fig. 1. Radiation portal monitor system

Determining minimum detectable activity

For a source to be detectable, the difference between the average source count and the average background count must be greater than the product of the confidence level in the sum of the standard deviation of the source count and the standard deviation of the background count. At the minimum detectable activity of the device, 137Cs with an activity of 3μCi were placed at a distance of 100cm from each panel, and the count rate was read 30 times in a two-second period, and the average and standard deviation of the readings with the average and the standard deviation of the context has been compared and it is reported in different standard deviations. These tests revealed that the monitoring system successfully detected a source inside a car at a distance of 100 cm with a minimum activity level of 3 μCi.

Results and Discussion

As discussed in scenario 1, in Figure (2), the changes in the total count rate of 4 detection plates for the triple heights of 20, 225, and 450 cm and the placement of the radioactive gamma source

137Cs, 60Co, and 241Am in the space between the two plates and the separation distances of the double plates above and the bottom on both sides is given for different dimensions of 100 x 25 cm2, 100 x 50 cm2 and 100 x 100 cm2 detector. What can be inferred from Figure (2), we are faced with the highest value of the total count rate in the middle position (distance of 225 cm from the ground). By increasing the distance between the two detector plates on each side of the RPM, the amount of the total counting rate at the source position in the middle decreases as much as possible and the total counting rate increases as much as possible at the bottom and top of the source (distances 20 and 450 cm from the ground).

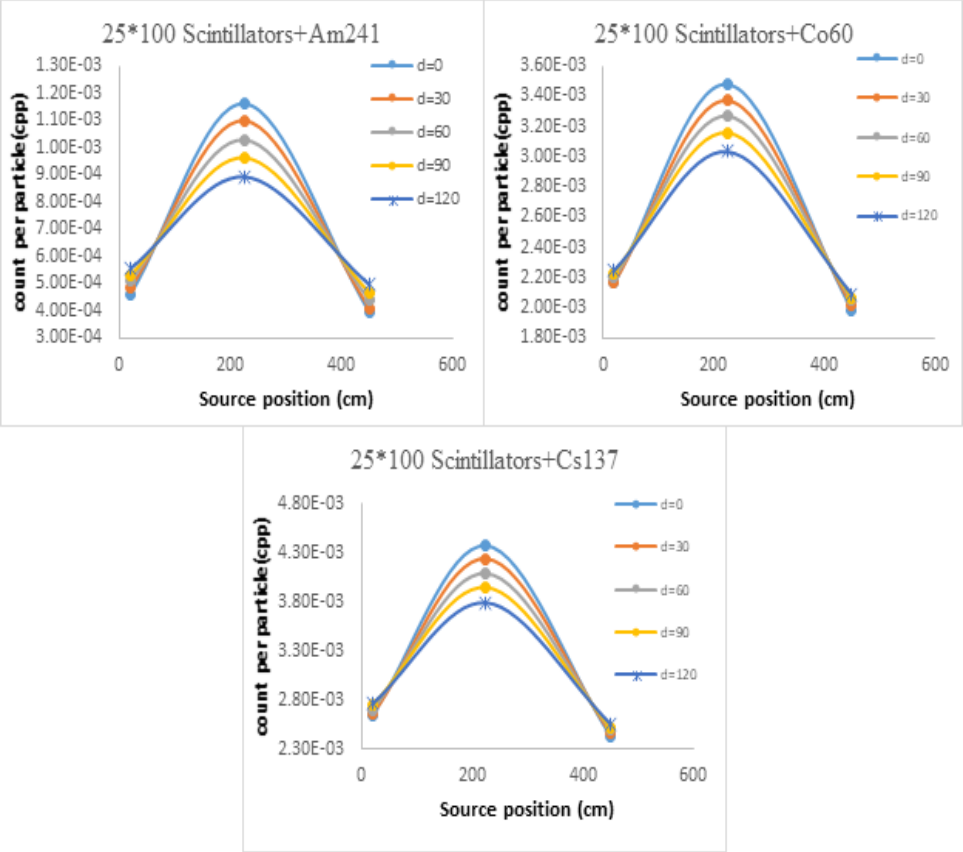

Fig. 2. The graph of changes of the total count rate of 4 detection plates with dimensions of 25 x 100 cm^2 for three heights of 20, 225, and 450 cm for ^{137}Cs, ^{60}Co, and ^{241}Am sources.

What can be inferred from figures (2) to (4) is that the process of changes in the total counting rate is the same as the previous case. By changing the dimensions of the detectors and increasing these dimensions, it is evident from the comparison of the above diagrams that the values of the total

counting rate will increase in proportion to this increase in the dimensions of the detection plates. For example, with the increase in the width of the plates from 25 to 50 cm, the corresponding values of the counting intensity have doubled. Other trends that govern the changes in the intensity of the counting distance, the change in the distance between the two screens located on each side of the gate, and the change in the location of the fountain remain the same as before.

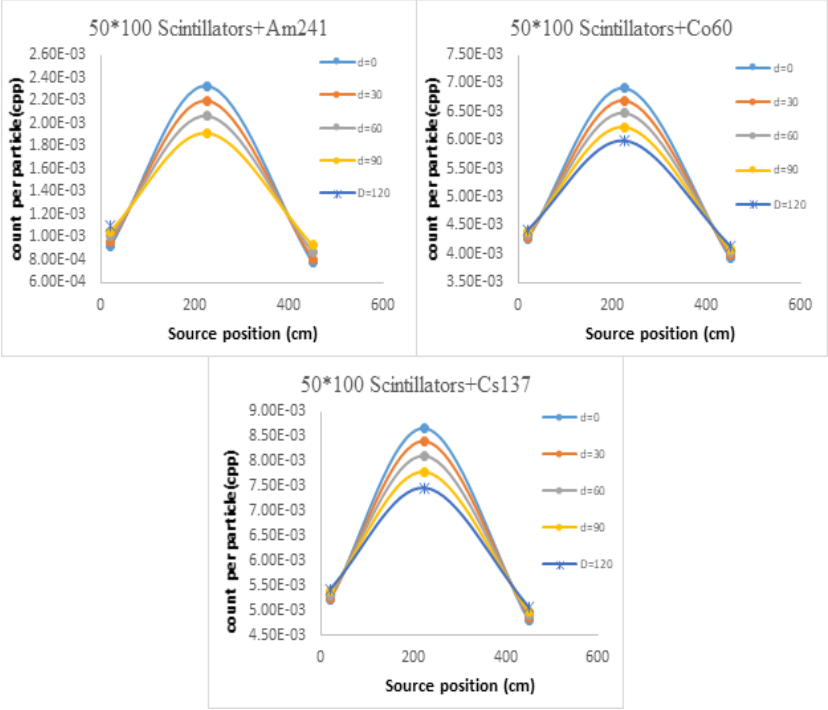

Fig. 3. The graph of changes of the total count rate of 4 detection plates with dimensions of 50 x 100 cm^2 for the three heights of 20, 225, and 450 cm for ^{137}Cs, ^{60}Co, and ^{241}Am sources.

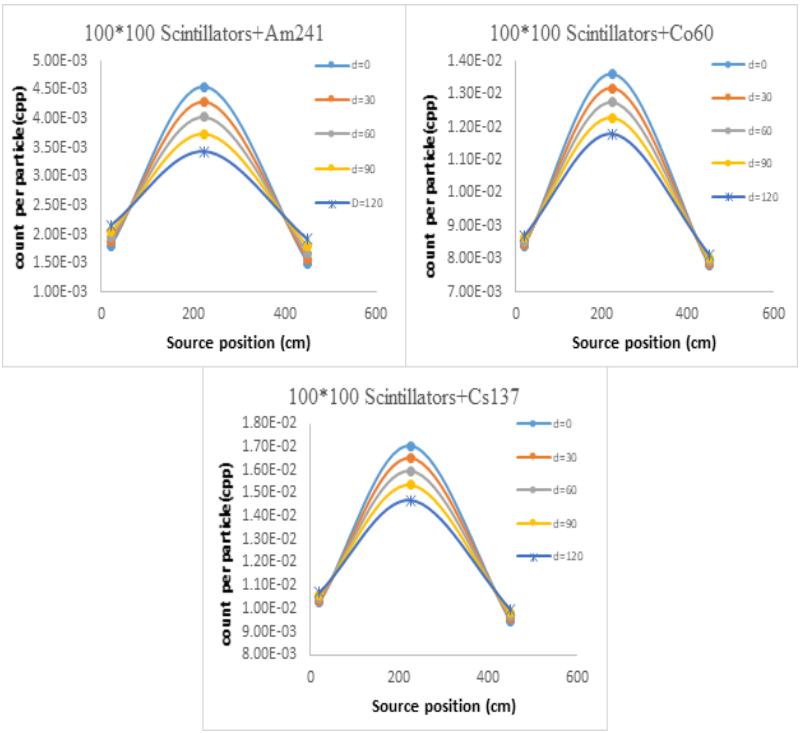

Fig. 4. The graph of changes of the total count rate of 4 detection plates with dimensions of 100 x 100 cm^2 square for the three heights of 20, 225, and 450 cm for ^{137}Cs, ^{60}Co, and ^{241}Am sources.

By increasing the width of the plates up to 100 cm, it does not lead to a change in the observed trends of the simulation with the previous geometry. The process of changing the total counting rate is the same as before. By changing the dimensions of the detectors and increasing these dimensions, it is evident from the comparison of the above diagrams that the values of the total counting rate will increase in proportion to this increase in the dimensions of the detection plates. For example, by increasing the width of the pages from 25 to 100, the corresponding values of the counting intensity have been increased by almost 4 times. Other trends that govern the changes in the intensity of the counting distance, the change in the distance between the two plates located on each side of the RPM, and the change in the location of the source remain the same as before.

In the case of scenario 2, as can be seen from Figure (5), the maximum percentage changes of the total detection plate count rate with triple energies of 60, 662 and 1250 keV related to the radioactive sources of gamma 241Am, 137Cs and 60Co with different separation distances of the upper and lower double plates.

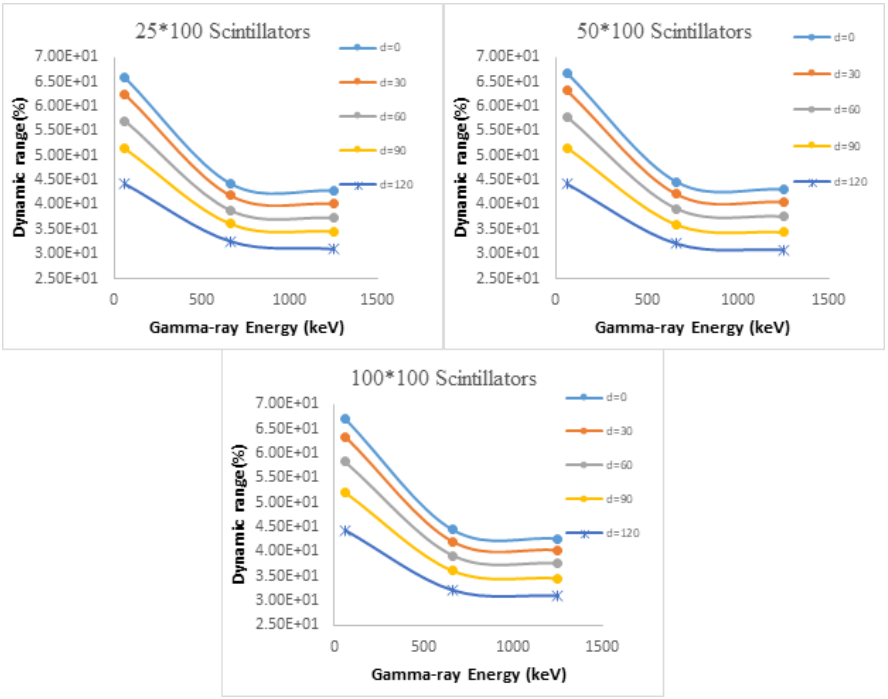

Fig. 5. The graph of the changes of the total detection plate count rate for different distances for ^{137}Cs, ^{60}Co and ^{241}Am sources.

In the case of third scenario, by drawing the graph of changes of C in terms of energy with different separation distances of scintillation plates on both sides, it is possible to see the optimal position clearly, which is shown in figure (6).

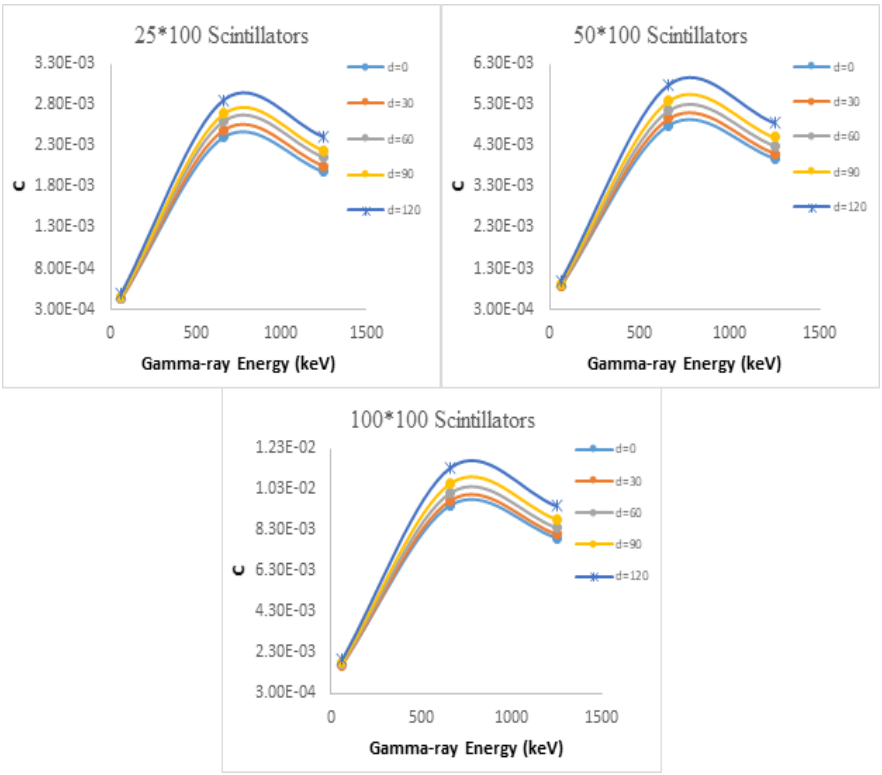

Fig. 6. Plotting the changes of C changes in terms of energy with different scintillation plate separation distances.

With the increase in the energy of the gamma source passing through the monitor gate, we face an increase and then a decrease in the value of the parameter C. The larger the separation of the scintillation plates on both sides, the greater the value of C, which is at most 14% and occurs between the two states of separation of the plates of 0 and 120 cm.

Finally, Monte-Carlo simulation has been done in the design of the radiation portal monitor detection system, and the selection and exact type of detection specifications for the construction of a vehicle radiation portal monitor have been obtained. Regarding the result of the simulation scenarios, considering the simultaneous importance of parameter C (Figure 6), the sensitivity in counting and the finished price of the product, the separation value of the scintillation plates of 60 cm along with the scintillation dimensions of 50 x 100 cm were selected for the final construction of the RPM. Finally, in order to obtain the minimum detectable activity of the device, using the results of the detection system, this monitor has the ability to detect the source of 137Cs with an activity of 3 µCi at 100 cm.

Conclusions

Radiation portal monitors (RPMs) play a crucial role in global security efforts against nuclear terrorism and the proliferation of nuclear weapons. These monitors are deployed at security checkpoints, borders, and secure facilities to detect nuclear and other radioactive materials. The design of an RPM system with plastic scintillation detectors was done with the help of Monte-Carlo simulation to get the proper dimensions and layout. The simulation results indicated that the most optimal dimensions of the usable detector are 50x100 cm2. Finally, the radiation portal monitor system was constructed according to simulation results. Also, with experimental tests, the minimum detectable activity was determined by 137Cs radioactive source. This system has the ability to detect at least 3 of μCi activity inside the car at a maximum speed of 1 m/s. It is obvious that the higher the activity of the source or the lower the speed of the source, the easier it is to identify the radioactive source, and in other words, the minimum detectable activity of the device decreases.

References

[1] Kouzes R T (2005). Detecting illicit nuclear materials: The installation of radiological monitoring equipment in the united states and overseas is helping thwart nuclear terrorism Am Sci 93 422–7

[2] Burr T and Hamada M S (2013). Moving Neutron Source Detection in Radiation Portal Monitoring Technometrics 55 296–308

[3] Beddar A S, Briere T M, Mourtada F A, Vassiliev O N, Liu H H and Mohan R (2005). Monte Carlo calculations of the absorbed dose and energy dependence of plastic scintillators Med Phys 32 1265–9

[4] Kouzes R T, Siciliano E R, Ely J H, Keller P E and McConn R J (2008). Passive neutron detection for interdiction of nuclear material at borders Nucl Instrum Methods Phys Res A 584 383–400

[5] Min S, Kang H, Seo B, Roh C, Hong S and Cheong J (2021). Integrated and Portable Probe Based on Functional Plastic Scintillator for Detection of Radioactive Cesium Applied Sciences 11 5210

[6] Lee H C, Koo B T, Choi C Il, Park C S, Kwon J, Kim H-S, Chung H and Min C H (2020). Evaluation of Source Identification Method Based on Energy-Weighting Level with Portal Monitoring System Using Plastic Scintillator Journal of Radiation Protection and Research 45 117–29

ICNST 2024
International Conference on Nuclear Science and Technology
6- 8 MAY 2024 | Isfahan, Iran

Investigation of dosimetry characteristics on MOSFET transistors (Paper ID: 1303)

A. Mosayebi[1*], H. Jafari[2], P. Hosseini[2] and S. Boorboor[2]
1- Radiation Processing and Dosimetry Research Group, Radiation Application Research Institute, Nuclear Science and Technology Research Institute, Tehran, IRAN.
2- Radiation Application Department, Shahid Beheshti University, Tehran, IRAN.

Abstract

The use of MOSFET transistors to measure the dose of ionizing radiation is widely used as a dosimeter. MOSFET dosimeters provide rapid dose reading. In addition, information is permanently stored in the MOSFET. In this experimental work, the response of P type MOSFET transistors (SMD) under gamma irradiation in the radiation field of the National Secondary Standard Dosimetry Laboratory (SSDL) was performed to measure their sensitivity as a dosimeter. The electric current and voltage of the transistor bases were recorded and analyzed with high accuracy in a wide range of the gate sweep before and after irradiation. The difference in threshold voltage value before and after irradiation indicates the amount of radiation current in the MOSFET transistor. MOSFET irradiation was done to check the dosimetry characteristics at a fixed dose. In the results section, it is shown that P-type MOSFET transistors have angle changes of ±60 degree and the field size is equal to 0.5% and 3.53%, respectively. In the following, the results of the energy dependence of the dosimeter response of MOSFET transistors with Cobalt-60 sources with an average energy of 1.25 MeV and Cesium-137 with an energy of 662 keV irradiation and their results are analyzed and reported.

Key words: MOSFET transistor, gamma radiation, threshold voltage, energy dependence.

Introduction

Radiation dosimetry has many applications, one of the important areas of its application is medical dosimetry, in which the absorbed dose required for treatment and any side absorbed dose are controlled; In other words, in radiation therapy, it evaluates the planned and delivered dose to ensure the accuracy of the dose delivered to the tumor [1]. Various dosimeters are used to accurately measure the amount of dose [1]. One of these cases is the use of semiconductor parts of MOSFET transistors as dosimeters. The use of MOSFET transistor as a tool for measuring ionizing radiation was proposed many years ago [1]. MOSFET dosimeters provide rapid dose readout. In

addition, information is permanently stored in the MOSFET [1]. Therefore, a measure of the total accumulated dose during the treatment period can be obtained. Their small size makes them very useful for measurements in areas with high dose gradients (eg, in brachytherapy). It also allows them to easily enter the body cavities without causing too much discomfort to the patient [2]. They do not need to be connected to the reader during the radiation time, thus eliminating the need for cables that run throughout the treatment room. In recent years, the use of MOSFET dosimeters is increasing strongly in radiation therapy and is of great importance in surgeries and brachytherapy. These parts have the possibility of real-time readout, simple instrumentation and high strength. In addition, MOSFET dual voltage dosimeters are independent of temperature, which is an advantage in clinical dosimetry [3]. These dosimeters have better performance than other dosimeters due to their simplicity and high reading speed in cases where the dose is required outside the body [4,5]. In Figure (1), the process of particle collision with the oxide layer of the transistor, creation of charges and transfer of charges is presented. When the ionizing rays collide with the oxide layer of the transistor, electron-hole pairs are created in this layer. After creating charges, some of them are combined with each other, and the number of combined charges depends on the type of falling particle, electric field, temperature, etc. Under the influence of the electric field, the remaining charges start to move. Also, the mobility of electrons in the oxide layer is thousands of times higher than the mobility of holes. Therefore, within a few picoseconds, the electrons leave the oxide layer, but the holes remain in the traps in the oxide layer for a very long time. In addition, there is a possibility of releasing a hydrogen atom and creating a proton when the particles collide with the oxide layer. The movement of these protons in the direction of the electric field can destroy and shift the energy levels at the interface between the oxide and silicon layers [6].

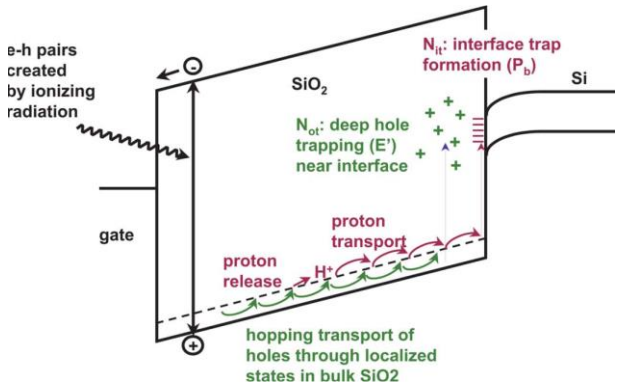

Fig. 1. The process of collision of particles with the MOSFET oxide layer, creation and transport of charges [7]

The displacement factor of the potential distribution in this layer is the accumulation of positive charges in the oxide layer, and on the other hand, according to equation (1), the amount of charges accumulated in the oxide layer shifts the flat band voltage of the transistor.

$$\boldsymbol{V_{fb}} = \emptyset_{\boldsymbol{ms}} - \frac{\boldsymbol{Q_{ss}}}{\boldsymbol{C_{ox}}} \quad (1)$$

In relation (1), $\emptyset_{\boldsymbol{ms}}$, $\emptyset_{\boldsymbol{ms}}$ and $\boldsymbol{C_{ox}}$ are the work function difference between the gate metal and the transistor substrate semiconductor, the amount of trapped charges in the oxide layer, and the capacitance of the oxide layer, respectively. As can be seen in this regard, with the increase in the amount of trapped charges in the oxide layer, the flat band voltage of the transistor changes more [7]. This flat strip voltage parameter is directly related to the threshold voltage value of the transistor. An important quantity in dosimetry by MOSFETs is the amount of changes in the threshold voltage of the transistor. It has been shown in various experiments that changes in the threshold voltage of the MOSFET transistor have an almost linear relationship with the amount of radiation applied to the transistor. In the simplest form, this relationship can be expressed by equation (2) [7].

$$\Delta\mathbf{V_T} = \boldsymbol{A} \times \boldsymbol{D^n} \quad (2)$$

In equation (1), $\Delta\mathbf{V_T}$, $\boldsymbol{D}$, $\boldsymbol{n}$ and $\boldsymbol{A}$ Threshold voltage changes, dose amount in the transistor gate insulation layer, degree of linearity and constant coefficient are respectively. Factors such as MOSFET construction quality, oxide layer thickness, electric field and to some extent total dose have an effect on the degree of linearity of the relationship. Ideally, these factors are linear and the value of parameter n should be close to one. There are several methods for extracting the threshold voltage value, and also various extractor circuits are provided for automatic measurement of this parameter. A large part of the existing methods for determining the threshold voltage include the static measurement of the transition drain current in terms of the gate voltage (ID-Vg characteristic) of a transistor.

Methode and Device

In this work, P type MOSFET transistors CD4007 with SMD structure was selected and investigated as a dosimeter. The voltage-current curve was measured in the saturation working area of the transistor. To measure the threshold voltage of MOSFET transistors, in order to measure the dose of gamma rays, the current-voltage curve plotting device made in Shahid Beheshti Nuclear Engineering Faculty was used [7]. The appearance of the device is shown in Figure 2.

Fig. 2. The appearance of the current-voltage curve drawing device of MOSFET transistors made in Shahid Beheshti University [7]

According to Figure (2), to connect the part under test to the device, connectors are installed on it. Through these connectors, protection, main signal and feedback signal for gate, drain and source terminals are connected to the test board. Also, a separate connector is provided on the device to connect to the temperature sensor in the test board compartment. This system has already been calibrated by a radiation test at the Secondary Standard Dosimetry Laboratory (SSDL) in Karaj [7]. Irradiation of MOSFETs in this work was done in the secondary standard dosimetry laboratory of Karaj in doses of 1-100 Gy. In order to test the stability and determine the accuracy, 3 CD4007 types were irradiated and the I-V curve reading of each of them was done three times. The average of all these data was calculated along with the deviation from the standard observed in each dose. Figure (3) shows the irradiation system of Karaj secondary standard dosimetry laboratory along with the placement of different samples (range including MOSFET) in each irradiation time. Irradiation of parts is done without bias.

Fig. 3. Irradiation system of secondary standard dosimetry laboratory of Karaj and placement board of MOSFET parts.

Results and Discussion

In table (1) according to figure (4) the measured changes of threshold voltage displacement of CD4007 transistors in different doses up to 100 Gy are shown. The results show that the displacement of the threshold voltage for this transistor is linear in all the desired doses. This transistor has a sensitivity of 4.39 mV/Gy in this dose range.

Table 1. Threshold voltage changes of CD4007 transistor in different doses up to 100 Gy

	CD4007 P-type
Dose (Gy)	ΔVth _Ave(mV)
10	53.80
20	106.01
40	202.53
60	276.90
80	384.49
100	444.62

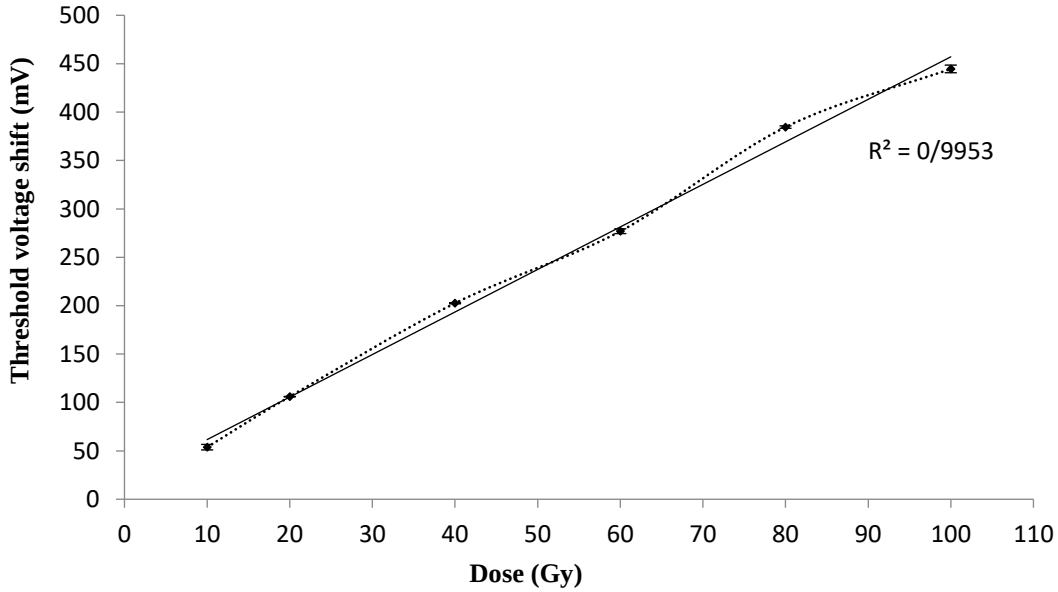

Fig. 4. The Threshold voltage changes of CD4007 transistor in different doses up to 100 Gy

Fig. 5. shows the angular dependence of CD4007 transistor that was irradiated at dose of 5 Gy. The orientation of the normal line on the sample page with the incident gamma-ray was assumed as the measurement angle and set at θ = ± 60° and the average photocurrents were measured. The results show a change of 0.5% of the photocurrent in comparison to the response obtained at θ = zero.

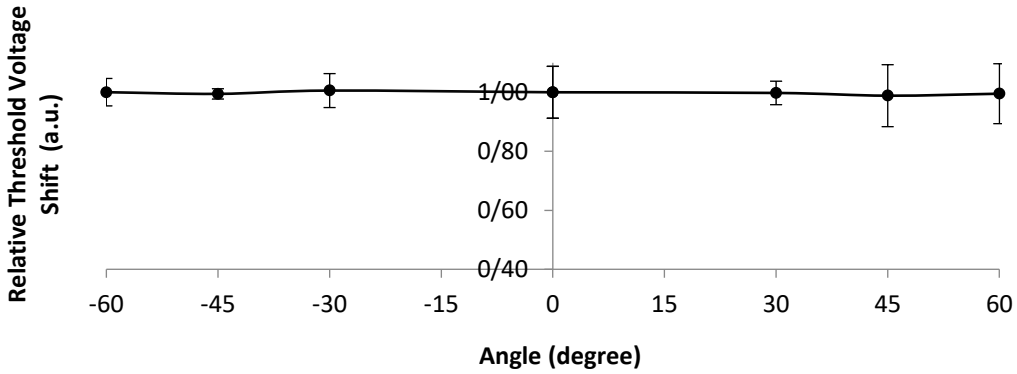

Fig. 5. Variation of relative threshold voltage shift of the CD4007 transistor in different gamma-ray incident angles

Fig. 6 shows the radiation field size dependence of the CD4007 transistor. The most changes field size in the range of 5 × 5 cm2 up to 25 × 25 cm2 were shown by 3.53%.

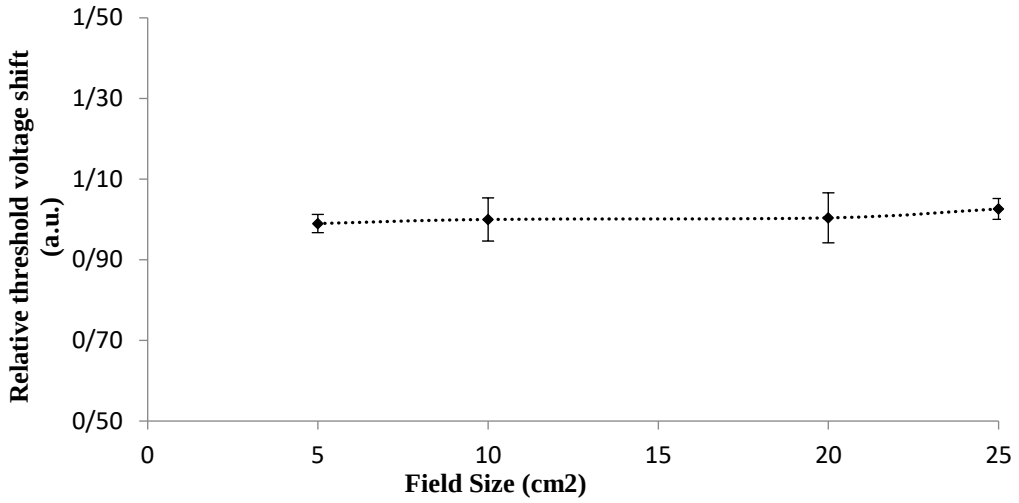

Fig. 6. Variation of relative photocurrent threshold voltage shift vs field size for the CD4007 transistor

Fig. 7 shows the radiation energy dependence of the CD4007 transistor. Energy changes with two sources of cobalt-60 and cesium-137 were shown equal to 6.58%.

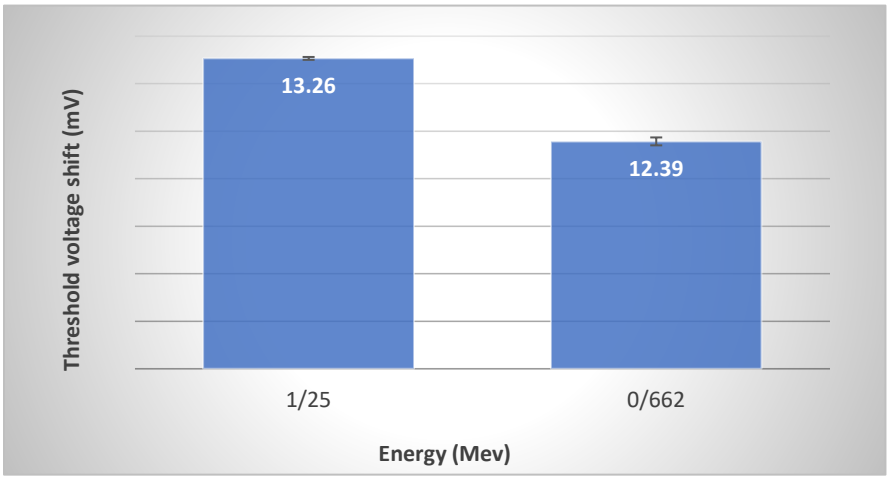

Fig. 7. Variation of threshold voltage shift vs energy for **the** CD4007 transistor

Conclusions

In this experimental work, the response of P type MOSFET transistors (SMD) under gamma irradiation in the radiation field of the National Secondary Standard Dosimetry Laboratory (SSDL) was performed to measure their sensitivity as a dosimeter. The electric current and voltage of the transistor bases were recorded and analyzed with high accuracy in a wide range of the gate sweep before and after irradiation. The difference in threshold voltage value before and after irradiation indicates the amount of radiation current in the MOSFET transistor. MOSFET irradiation was done to check the dosimetry characteristics at a fixed dose. In the results section, it is shown that P-type MOSFET transistors have angle changes of ±60 degree and the field size is equal to 0.5% and 3.53%, respectively. In the following, the results of the energy dependence of the dosimeter response of MOSFET transistors with Cobalt-60 sources with an average energy of 1.25 MeV and Cesium-137 with an energy of 662 keV irradiation and their results are analyzed and reported.

References

[1] Chuang, C. F., Verhey, L. J., & Xia, P. (2002). Investigation of the use of MOSFET for clinical IMRT dosimetric verification. Medical physics, 29(6), 1109-1115.

[2] Cheung, T., Butson, M. J., & Peter, K. N. (2004). Effects of temperature variation on MOSFET dosimetry. Physics in Medicine & Biology, 49(13), N191.

[3] L. Frohlich. (2013). "DOSFET-L02: An advanced online dosimetry system for radfet sensors," presented at the IBIC, UK.

[4] ramaseshan, R., Kohli, K. S., Zhang, T. J., Lam, T., Norlinger, B., Hallil, A., & Islam, M. (2004). Performance characteristics of a microMOSFET as an in vivo dosimeter in radiation therapy. Physics in Medicine & Biology, 49(17), 4031.

[5] World health organization. (2008). radiotherapy risk profile, Who press, Geneva.

[6] T. R. Oldham and F. B. McLean. (2003). "Total ionizing dose effects in MOS oxides and devices," Nuclear Science, IEEE Transactions on, vol. 50, pp. 483-499.

[7] Boorboor, S., Jafari, H. (2022). 'Design and construction of dose-measuring device using MOSFET transistors based on threshold voltage shift', Radiation Safety and Measurement, 9(1), pp. 55-64. doi: 10.22052/9.1.55.

ICNST 2024
International Conference on Nuclear Science and Technology
6- 8 MAY 2024 | Isfahan, Iran

Physical and gamma radiation shielding effects of pure zinc cobaltite and graphene added nanoparticles (Paper ID: 1323)

Khoshhal A.R.[1], Tirehdast Z.[2], Bagheri Khatibani A.[2]*, Nirouei M.[3]
[1] *Department of Nuclear Engineering, Graduate University of Advanced Technology, Kerman, Iran*
[2] *Nano Research Lab, Lahijan Branch, Islamic Azad University, Lahijan, Iran*
[3] *Faculty of Engineering, Lahijan Branch, Islamic Azad University, Lahijan, Iran*

Abstract

Pristine zinc cobaltite (ZnCo2O4) and graphene zinc cobaltite nanoparticles (NPs) have been successfully synthesized by hydrothermal method. The physical properties of both structures were studied using X-ray diffraction (XRD), field emission scanning electron microscopy (FESEM), and energy dispersive X-ray spectroscopy (EDX). XRD results indicated a formation of spinel structure. The lattice parameters and some other physical properties of them have been calculated. The elemental composition of the samples has been determined through EDX analysis. From morphological investigation, nano-sized quasi-spherical grains, and the agglomeration of grains were observed. Nuclear radiation shielding investigation for gamma-ray has been studied for both samples. Since mass and linear attenuation coefficients are two basic parameters in the matter of shielding, they were estimated and obtained as 3.95/4 and 0.659/0.643 for ZnCo2O4/ZnCo2O4: graphene, respectively. Other significant shielding properties were also evaluated. Half value layer, mean free path and tenth value layer of pure ZnCo2O4 and ZnCo2O4/graphene were calculated as follows: 0.175/0.175, 0.253/0.250, 0.58/0.57, respectively. The results show that the presence of graphene has affected all the protection parameters. The ultimate results from these calculations can be beneficial to understand the radiation shielding effect of zinc cobaltite based samples.

Keywords: Zinc cobaltite, gamma shielding, structural properties, hydrothermal method

Introduction

Zinc cobaltite (ZnCo2O4) as a usual spinel structure, has received considerable attention due to its potential applications in super-capacitors, lithium-ion batteries, sensors, electro-catalysts, photo-voltaics and so on. The nature of the p-type semiconductor ZnCo2O4 affects the electrical conductivity of the material. The spinel structure of ZnCo2O4 consists of a close-packed cubic array of oxide ions, where divalent Zn occupies the tetrahedral site and trivalent Co occupies the

octahedral site. Different synthesis processes for ZnCo2O4 include hydrothermal, solvothermal, pulse laser deposition, co-precipitation reaction and solid state reaction [1].

Gamma rays have been used as a valuable tool in medicine, agriculture and scientific research. While such applications are very beneficial for human life, undesirable exposures like scattering gamma-rays and cosmic ray are dangerous to human and their environment with different impacts. Exposure to high doses of gamma may cause direct harmful effects such as radiation sickness and an increased risk of cancer. Therefore, shielding materials are used to prevent radiation from various sources [2]. Radiation shields are materials that are placed between the radiation source and the human body and are specifically designed to absorb the maximum number of photons for that particular application. Ideal radiation shields should be lightweight, effective at absorbing a wide range of photons, thin, inexpensive, easy to fabricate, and so on. They vary from simple lead aprons to glasses, composites, polymers, alloys, etc. These materials are often reinforced using various micro and nanoparticles, which are suitable for the intended application [3].

Currently, the dynamically developing and specifically understood nanotechnology comes with a solution. In general, additive nanoparticles (including metals, non-metals, metal oxides, and many others) have been investigated for many applications. Their outstanding properties including high, surface-to-volume ratio and enhanced absorption play a significant role. It is also noteworthy that nanocomposites, i.e. a composite, which includes the main component and nano or micro-material of a certain mass fraction, have found a wide application, including in radiation protection (radiation shielding) [4].

Despite many searches, no report on the protective use of zinc cobaltite based samples has been found. It may be possible to state with a little boldness that there are no articles dealing with the gamma shielding property of zinc cobaltite and for this reason, the topic of the article has its own attractiveness and novelty. Even though, similar reports exist. In the article of M.I. Sayyed et al. (2022) the radiation shielding properties of mortar samples with Fe2O3 nanoparticles were investigated for radiation shielding applications. The results of radiation protection parameters showed that new mortars can be developed for radiation protection applications by introducing higher concentrations of Fe2O3 nanoparticles [3]. Also in the article of M. Rashad et al. (2020) the radiation shielding features of magnesium oxide (MgO) and zinc oxide (ZnO) nanoparticles

(NPs) were investigated. The results showed that zinc oxide (ZnO) nanoparticles with the smallest diameter of 50 nm have a satisfactory capacity in nuclear radiation shielding [5].

In this research, ZnCo2O4 and ZnCo2O4/graphene were synthesized by sol-gel method and then they were prepared in the form of tablets. The structural and morphological properties of these nanoparticles were investigated using some analytical tools (XRD- FESEM-EDX). Also, the radiation shielding features of these samples were evaluated by calculating the radiation shielding parameters such as linear attenuation coefficient (LAC), mass attenuation coefficient (MAC), mean free path (MFP), half-value layer (HVL) and tenth value layer (TVL).

Experimental

Description of the Materials and Methods used in the research

The amount of 0.9 grams of zinc chloride is mixed with 50 ml of distilled water, placed on the stirrer and stirred for 15 minutes. After that, we added 1.9 grams of cobalt chloride to the solution and let the stirring process continue for another 15 minutes. Then 0.72 grams of urea were inserted and stirring continued for 30 minutes. The content of the solution is poured into a Teflon container and placed in the reactor in the furnace for 12 hours at a temperature of 140 ℃. We poured the pink sediment with distilled water into the two test tubes and put it in a centrifuge at 3000 rpm for 3 minutes, and then we washed it twice with distilled water and twice with ethanol. The material obtained was poured into a porcelain container and heated for 6 hours at a temperature of 70 ℃, after which it is placed in the furnace at a temperature of 450 ℃ for 3 hours, and as the last step, the resultant transferred into a mortar and turned into finer grains and pressed at a pressure of 1.2 MPa to acquire some pellets of~1 mm thickness and ~10 mm diameter .The first sample was obtained with the abbreviation name as ZCO. To produce the second material after addition of urea, 20 mg of graphene is added to it and finally ZCG material is obtained. (Fig. 1.)

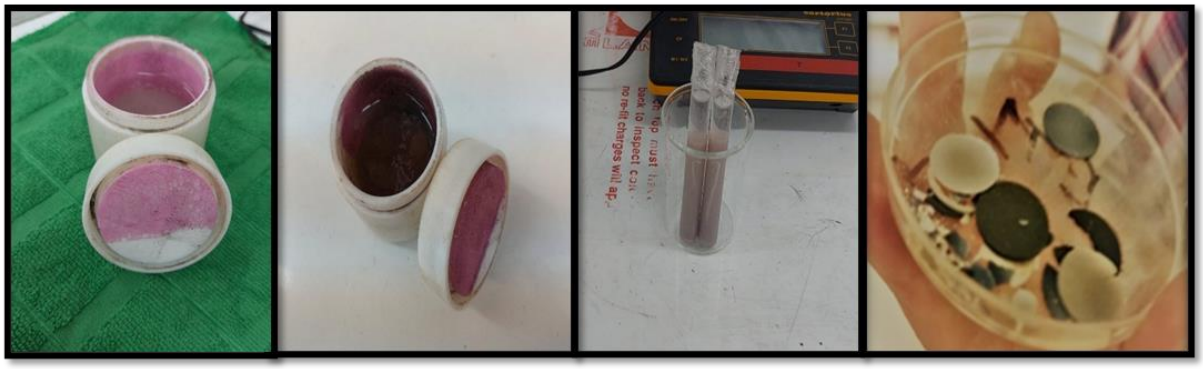

Fig. 1. Images of Protective production steps

For radiation investigation, the desired samples were placed in the medical radiation laboratory to check their radiation protection properties between the cesium 137 point source and a Geiger-Muller type gas detector (Fig. 2). According to the count values obtained from the Geiger-Muller detector, radiation protection parameters of samples including LAC, MAC, HVL, TVL, and MFP have been determined.

Fig. 2. Image of radiation protection experiment for ZCO and ZCG

Definition of Radiation shielding parameters

The LAC (μ, linear attenuation coefficient) measures an attenuator's shielding performance for gamma irradiation. The LAC is computed through the Beer–Lambert law [6]:

$$\mu = \ln \left({}^{I_0}/_{I} \right) \Big/ _{x}$$

The MAC (μρ, cm2/g, mass attenuation coefficient) characterizes the absorbing material and is obtained from the ratio of LAC divided by absorber density. In this research, the MAC values calculated with the following formula [6]:

$$\mu_m = \sum_i w_i(\mu/\rho)_i$$

The thickness required to attenuate the radiation beam to half the value before passing through the absorbing material is known as the half value layer (HVL). Thus, this can be determined by the following formula [6]:

$$HLV = \ln 2/\mu$$

Whereas the tenth value layer known as the thickness of a shielding material that required to reduce the incident intensity of gamma-ray photons to its tenth value at given energy [6]:

$$TVL = \ln 10/\mu$$

The mean free path (MFP) is the average distance an electron travels in a given sample environment before interacting with matter [6].

$$\boldsymbol{MFP = {}^{1}/_{\mu}} \quad (\boldsymbol{cm})$$

Results and Discussion

XRD results

Fig. 3 shows the XRD data of the hydrothermal prepared pure zinc cobaltite and graphene added samples which was taken in the 2θ region from 10◦ to 80◦. The miller indices (hkl) of the diffraction planes are also marked. A very good match between our prepared samples and the standard zinc cobaltite sample is observed. A standard cubic spinel ZnCo2O4 with the code of 23-1390 was selected. Due to the small amount of graphene, the related graphitic diffraction planes did not observe. Comparing the two graphs demonstrated that the attendance of graphene decreased the intensity of the diffraction peaks relatively, and caused some diffraction lines to disappear.

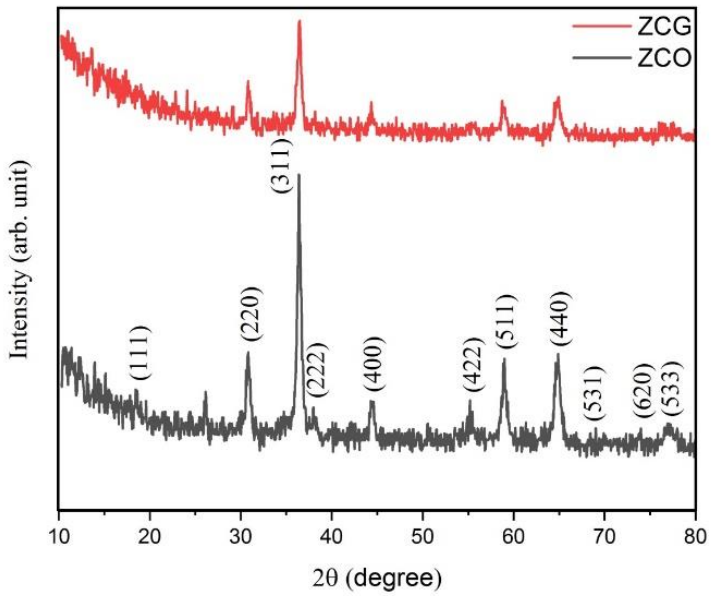

Fig. 3. The XRD Rusults of $ZnCo_2O_4$ and (b) $ZnO/ZnCo_2O_4$

Lattice parameters of the main peak (311) for both samples were calculated and compared with standard values (Table 1). They were decreased due to the addition of graphene and it seems the lattice parameters become closer to the standard values. It may be legitimate due to Vegard's law. Negligible deviation from the standard values is observed, for example, in the case of unit cell volums, that can be the result of iconicity and instability of the lattice. Other reasons probably play a role in this deviation such as variation of bond angle, bond length, and twisting of the main structure. It is known that various defects inside the main structure cause to band edge variation process [7].

Table 1. The calculated and standard values of the lattice parameters for the main reflection peaks (i.e. (100), (002), (101)) and other relevant parameters.

Sample	Miller indices	$\boldsymbol{d}$ (Å)		$\boldsymbol{a}$ (Å)		Volume of unit cell $(Å)^3$	
		Cal.	Sta.	Cal.	Sta.	Cal.	Sta.
ZCO	311	2.4677	2.4400	8.1846	8.0946	548.261	530.38

ZCG	311	2.4371	2.4400	8.0829	8.0946	528.091	530.38

FESEM and EDX results

Fig. 4 shows the FESEM micrographs of the ZnCo2O4 and ZnCo2O4/Graphene nanoparticles with specific magnification. Generally, all of the micrographs show grains with nano-scale amounts, and the aggregation of grains is clear in all samples. For ZC0, semi-spherical grains can be observed ranging from 75 to 175 nm. The ZCG sample also consists of semi-spherical nanoparticles with diameters of 75 to 180 nm. The particle sizes of pure ZnCo2O4 and ZnCo2O4/Graphene are almost the same. Both samples are quasi-spherical in shape.

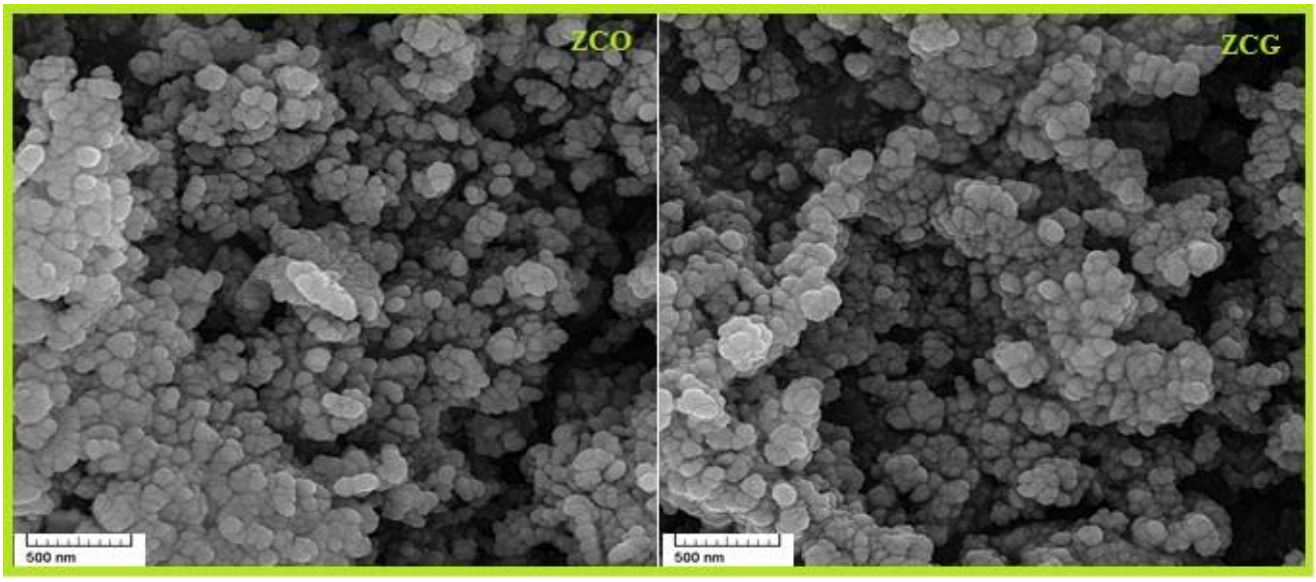

Fig. 4. FESEM images of ZnCo2O4 (ZCO) and ZnCo2O4/Graphene(ZCG)

In order to study the elemental composition of prepared nano-materials, the EDX analysis has been applied. The EDX spectrum of the ZnCo2O4 and ZnCo2O4/Graphene nanoparticles is shown in Fig.5. The characteristic EDX are displayed in Fig.1. According to the results, the traces of impurities and other elements are not observed. In the spectrum of ZC0, four peaks are observed, which are identified as zinc and copper.

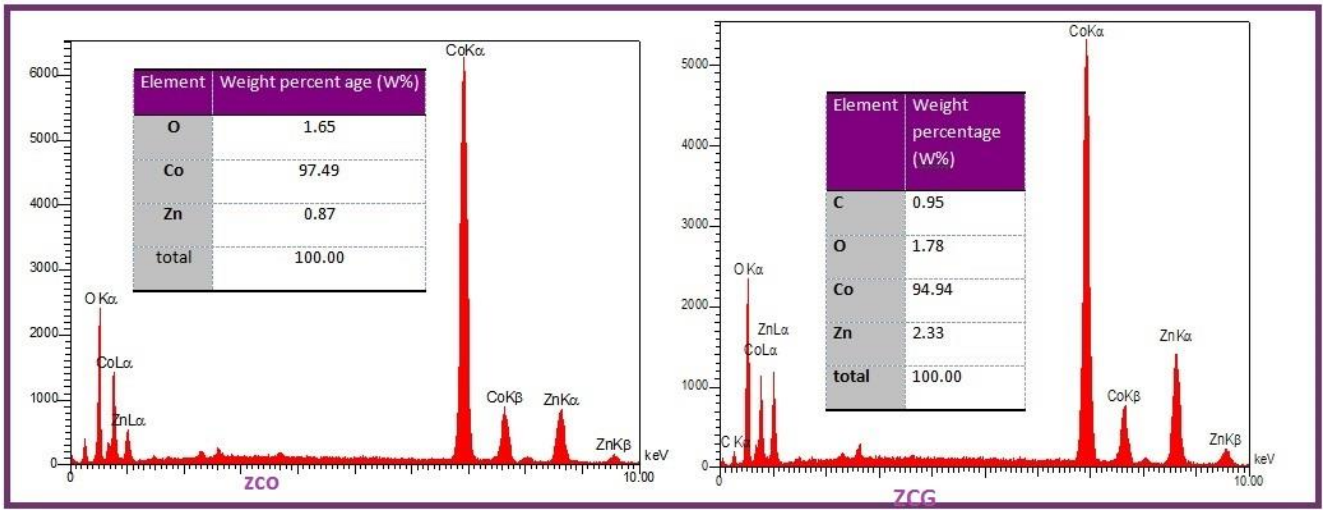

Fig. 5. EDS images of $ZnCo_2O_4$ (ZCO) and $ZnCo_2O_4$/Graphene(ZCG)

Radiation Shielding Parameters

The linear attenuation amount provide noteworthy data about radiation shielding parameters of ZCO and ZCG nanoparticles. All the mentioned nanoparticles were prepared in the form of tablets. All the samples were exposed to the gamma source of cesium 137 with an activity of 8.7 μCi and a gamma energy peak of 0.662 MeV. The duration of placing the samples between the source and detector was 4 minutes. The obtained results of mean free path (MFP), one-tenth value layer (TVL), half value layer (HVL), mass attenuation coefficient (μρ) and linear attenuation (μ) of ZCO and ZCG nanoparticles have been shown in Table 2. The highest value of linear attenuation coefficient has been obtained for ZCG (4 cm-1) and lowest value has been obtained for ZCO nanoparticles (3.95cm-1). The lowest value of mass attenuation coefficient of ZCO and ZCG that have been shown in Table 2 are 0.643 cm2/g 0.659 cm2/g respectively. The one-tenth values layer (TVL), half-value layer (HVL) and mean free path (MFP) of ZCO and ZCG have been shown in Table 2. The HVL value have changed from 0.175 cm to 0.17 cm, which depends on the persence of graphene in ZnCo2O4. Also, the one-tenth layer value has changed from 0.58 cm to 0.57cm. Lastly, The mean free path of ZCO and ZCG have changed from 0.253 cm to 0.250 cm. It can be seen that the attendance of graphene cause to decraes the MFP. In addition to this study, in future

researches, different experimental setups can be prepared and various nanoparticles can be synthesized in different methods to investigate the radiation protection characteristics.

Table 2. Results of radiation protection parameters for ZCO and ZCG

Sample	LAC(cm^{-1})	MAC(cm^2/g)	MFP(cm)	HVL(cm)	TVL(cm)
ZCO	3.95	0.659	0.253	0.175	0.58
ZCG	4	0.643	0.25	0.17	0.57

Conclusion

The powder of ZnCo2O4 and ZnCo2O4/Graphene were prepared by hydrothermal method. Their structural and morphological properties were investigated. According to the XRD data, the formation of zinc cobaltite in cubic spinel structure is approved. However, the signs of the presence of graphene are not appeared in our sample. According to FE-SEM micrographs, all samples had similar microstructures and all of them consisted of nanosized quasi-spherical grains. The radiation shielding properties of the samples (LAC, MAC, MFP, HVL, and TVL) were also calculated. The results showed that ZnCo2O4/Graphene is considered a suitable competitor for ZnCo2O4 as a shielding protector.

References

[1]. Lobo, L.S. and Kumar, A.R., 2019. Structural and electrical properties of ZnCo2O4 spinel synthesized by sol-gel combustion method. Journal of Non-Crystalline Solids, 505, pp.301-309.

[2]. Ali, A.M., Issa, S.A., Ahmed, M.R., Saddeek, Y.B., Zaid, M.H.M., Sayed, M., Somaily, H.H., Tekin, H.O., Matori, K.A. and Zakaly, H.M., 2020. Promising applicable heterometallic Al2O3/PbO2 nanoparticles in shielding properties. Journal of Materials Research and Technology, 9(6), pp.13956-13962.

[3]. Sayyed, M.I., Almousa, N. and Elsafi, M., 2022. Preparation of Mortar with Fe2O3 nanoparticles for radiation shielding application. Coatings, 12(9), p.1329.

[4]. Sobczak, J. and Żyła, G., 2024. Nano and microcomposites as gamma and X-ray ionizing radiation shielding materials—A review. Energy, p.130210.

[5]. Rashad, M., Tekin, H.O., Zakaly, H.M., Pyshkina, M., Issa, S.A. and Susoy, G., 2020. Physical and nuclear shielding properties of newly synthesized magnesium oxide and zinc oxide nanoparticles. Nuclear Engineering and Technology, 52(9), pp.2078-2084.

[6] Eskalen, H., Kavun, Y., Kerli, S. and Eken, S., 2020. An investigation of radiation shielding properties of boron doped ZnO thin films. Optical Materials, 105, p. 109871.

[7] Bagheri Khatibani, A., Shabankhah, A., 2021. Fabrication and ethanol sensing of sol–gel grown zinc oxide powder: the effect of cobalt and copper doping, Appl. Phys. A, 127, pp. 308.

ICNST 2024
International Conference on Nuclear Science and Technology
6- 8 MAY 2024 | Isfahan, Iran

Structural, morphological, and gamma shielding properties of hydrothermally prepared CuCo2O4/graphene sample for radiation shielding application (Paper ID: 1327)

Khoshhal A.R.[1], Rezapour A.[2], Bagheri Khatibani A.[2*], Nirouei M.[3]
[1]*Department of Nuclear Engineering, Graduate University of Advanced Technology, Kerman, Iran*
[2] *Nano Research Lab, Lahijan Branch, Islamic Azad University, Lahijan, Iran*
[3] *Faculty of Engineering, Lahijan Branch, Islamic Azad University, Lahijan, Iran*

Abstract

Nowadays, using of alternative materials instead of lead in the environmentally sensitive and nontoxic material research in radiation shielding has attracted a lot of attention. In this study, pure spinel copper cobaltite (CuCo2O4) and graphene added were synthesized by hydrothermal method. The structural, morphological, and gamma shielding properties of the prepared samples were investigated through X-ray diffraction (XRD), field emission scanning electron microscopy (FESEM), and energy dispersive X-ray spectroscopy (EDX). The cubic spinel structure of pure CuCo2O4 was verified and the presence of graphene did not change the main structure. Spherical particles as well as irregular geometrical particles are observed in both samples, obtained from morphological analyze. The factors related to radiation shielding such as mass and linear attenuation coefficients, half value layer, mean free path and tenth value layer of the samples were calculated. The obtained results from these measurements can be useful to understand the radiation shielding performance of copper cobaltite based samples.

Keywords: copper cobaltite, hydrothermal method, structural properties, gamma shielding

Introduction

A promising electrode material for hybrid super capacitors, electric catalysts and lithium-ion batteries due to its electronic properties, low cost and excellent electrochemical performance is CuCo2O4 with the general formula CuxCo2xO4, which is one of the spinel oxide materials. [1,2] Also, the optical gap of this material is close to the ideal value for photo electrochemical needs. [1,3] Cobaltite can be crystallized as an inverted or normal spinel structure. [1,4] Unfortunately, the use of cobaltite as a potential electrode material for energy storage applications is limited due to the toxicity of one of the cobalt ions present in the composition [1,5]. It is possible to reduce this toxicity by combining one of the cobalt ions with other environmentally compatible metal ions such as nickel, copper and zinc. Also, considering that the presence of two intermediary metals in

one compound may increase the electrochemical performance and other properties compared to a substance that has only one transfer ion. [1,6] As an example, copper cobaltite and nickel cobaltite can be used in cancer treatment as well as anti-tumor research. [7,8]

Radiation can be defined as energy emitted from the nucleus in the form of particles or waves. Subject to radiation, they are divided into two categories: natural and artificial, where natural sources include cosmic rays and natural radioactive series found in the earth's crust, and artificial sources include industrial radionuclides that have various uses in medicine and industry. [9]

The short wavelengths of gamma rays make gamma rays have good energy and more power than other electromagnetic waves. One of the uses of gamma is in the treatment of cancer. Due to this, gamma rays destroy not only cancer cells but also healthy cells known as organs at risk. Protection against radiation is very important to prevent the destruction of healthy cells in a patient exposed to radiation. [10]

There are some basic principles for radiation protection (such as shielding). Shielding is intrinsically safe, while distance, time under radiation, the activity of the radiation source, the amount of the allowed dose should be taken into consideration. A shield is effective when it weakens the rays with high energies and also the effects of the radiation on its optical and mechanical properties are very small. [11]

In this research, CuCo2O4 and CuCo2O4/graphene were prepared by hydrothermal synthesis and then in tablet form and the structural and morphological characteristics of these nanoparticles were investigated using some analytical tools (XRD-FESEM-EDX). Also, by calculating radiation shielding parameters such as mass attenuation coefficient (MAC), mean free path (MFP), half value layer (HVL), tenth value layer (TVL) and linear attenuation coefficient (LAC), the radiation shielding characteristics of these samples were evaluated.

It should be noted that very little research has been done regarding the radiation protection characteristics of the mentioned samples, and for this reason, the topic of this article has its own special attraction and novelty.

Experimental

Description of the Materials and Methods used in the research

The amount of 0.686 g of copper was dissolved in 50 ml of distilled water and placed on the stirrer with a magnet and heater at a temperature of 55 degrees Celsius for 10 minutes. After adding 1.901 g of cobalt to the solution, it was again placed on the stirrer and heater for another 10 minutes. After this step, 0.72 g of urea was added to the solution and stirring process continued for another 30 minutes until a uniform solution was formed. The obtained solution was transferred to a Teflon container and then it was placed in a stainless steel autoclave and placed in an oven at a temperature of 140 degrees Celsius for 12 hours. An equal amount of sediment and water was placed in two test tubes in a centrifuge with 3000 revolutions in 3 times. After that, the material was washed twice with water and the last time with ethanol. In the next step, for annealing, the obtained material is placed in the furnace for 3 hours and remains in the furnace for drying for 2 hours. The resultant powder fully pulverized in a porcelain mortar and pressed at a pressure of 1.2 MPa within 10 min to acquire some pellets of ~1 mm thickness and ~10 mm diameter. The first sample was obtained with the abbreviation CuCo2O4 (CCO). To make the second sample with the abbreviation CuCo2O4 /Graphene (CCG), the above steps were repeated; with the difference that after adding urea, 0.01 g of graphene was added to it and the sample solution was colored black. The color of the tableted samples was not different from each other. (Fig. 1)

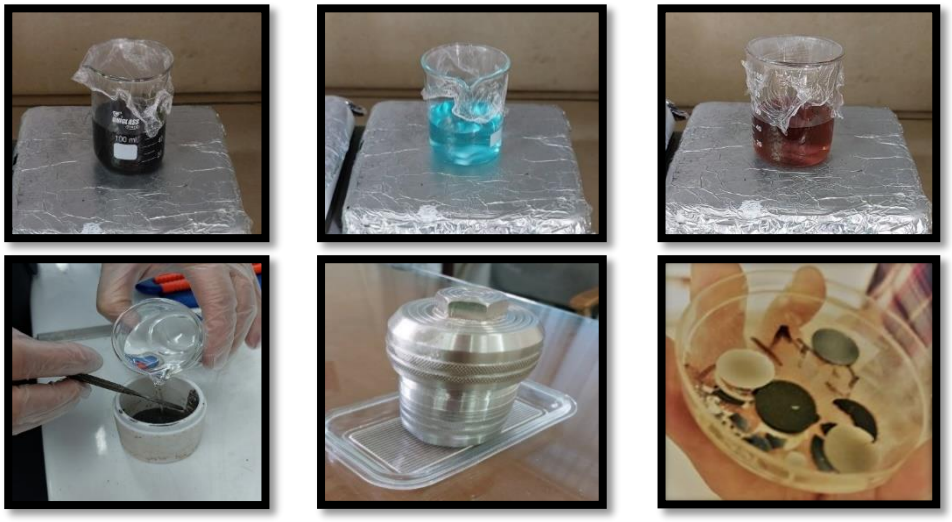

Fig. 1. Images of Protective production steps

For radiation protection testing, the desired samples were placed in the medical radiation laboratory to check their radiation protection properties between the cesium 137 point source and a Geiger-Muller type gas detector (Fig. 2). According to the count values obtained from the Geiger-Muller detector, radiation protection parameters of samples including LAC, MAC, HVL, TVL, and MFP have been determined.

Fig. 2. Image of radiation protection experiment for CCO and CCG

Also, in this research, the structural and morphological characteristics of pure zinc oxide nanoparticles and zinc oxide doped with 10% and 20% copper were also investigated by performing XRD, EDX and FESEM analyses.

Definition of Radiation shielding parameters

The LAC (μ, linear attenuation coefficient) measures an attenuator's shielding performance for gamma irradiation. The LAC is computed through the Beer–Lambert law [6]:

$$\mu = \ln \left({}^{I_0}/_{I} \right) \Big/ _{x}$$

The MAC (μρ, cm2/g, Mass Attenuation Coefficient) characterizes the absorbing material and is obtained from the ratio of LAC divided by and absorber density. In this research, the MAC values calculated with the following formula [6]:

$$\mu_m = \sum_i w_i (\mu/\rho)_i$$

The thickness required to attenuate the radiation beam to half the value before passing through the absorbing material is known as the half value layer (HVL). Thus, this can be determined by the following formula [9]:

$$HLV = \ln 2/\mu$$

Whereas the tenth value layer known as the thickness of a shielding material that required to reduce the incident intensity of gamma-ray photons to its tenth value at given energy [9]:

$$TVL = \ln 10/\mu$$

The mean free path (MFP) is the average distance an electron travels in a given sample environment before interacting with matter [2].

$$\boldsymbol{MFP = {}^{1}/_{\mu}} \quad (\boldsymbol{cm})$$

Results and discussion

Radiation shielding parameters

The linear attenuation values provide noteworthy data about Radiation shielding performance of CCO nanoparticles and CCG . All the mentioned nanoparticles were prepared in the form of tablets. All the samples were exposed for 4 minutes to the gamma source of Cesium 137 with an activity of 8.7 μCi and a gamma energy peak of 0.662 MeV. The obtained results of TVL, HVL, LAC, MFP and MAC CCO nanoparticles and CCG have been showed in Table 1. The highest value of linear attenuation coefficient has been obtained for CCG (3.4cm-1) and lowest value has been obtained for CCO nanoparticles (2.35cm-1). The lowest value of MAC is 0.38 cm2/g for CCO. This value increases when the graphene comes to structure. The MAC value has highest value as 0.55 cm2/g for CCG. The mean free path (MFP), half-value layer (HVL) and one-tenth values (TVL) of CCO and CCG have been shown in Table1. The HVL value have changed from 0.29 cm to 0.2 cm, which depends on the percentage of Graphene in CuCo2O4. Also, the TVL has changed from 1.97 cm to 0.67cm. Lastly, the mean free path of CCO and CCG has changed from 0.42 cm to 0.29 cm, these values have been seen to decrease when graphene is present. In addition to this study, different experimental setups can be prepared in future researches and nanoparticles can be synthesized in different ways to investigate the radiation protection characteristics.

Table 1. Results of radiation protection parameters for CCO and CCG XRD results

Sample	LAC(cm^{-1})	MAC(cm^2/g)	MFP(cm)	HVL(cm)	TVL(cm)
CCO	2.35	0.38	0.42	0.29	1.97
CCG	3.4	0.55	0.29	0.2	0.67

Fig. 3 shows the XRD data of the hydrothermal prepared pure copper cobaltite and graphene added samples which was taken in the 2θ region from 10◦ to 80◦. The miller indices (hkl) of the diffraction planes are also marked. A very good match between our prepared samples and the standard copper cobaltite sample is observed. A standard cubic spinel CuCo2O4 with the code of 78-2172 was selected. Due to the small amount of graphene, the related graphitic diffraction planes did not observe. Comparing the two graphs demonstrated that the attendance of graphene decreased the intensity of the diffraction peaks relatively, and caused some diffraction lines to disappear.

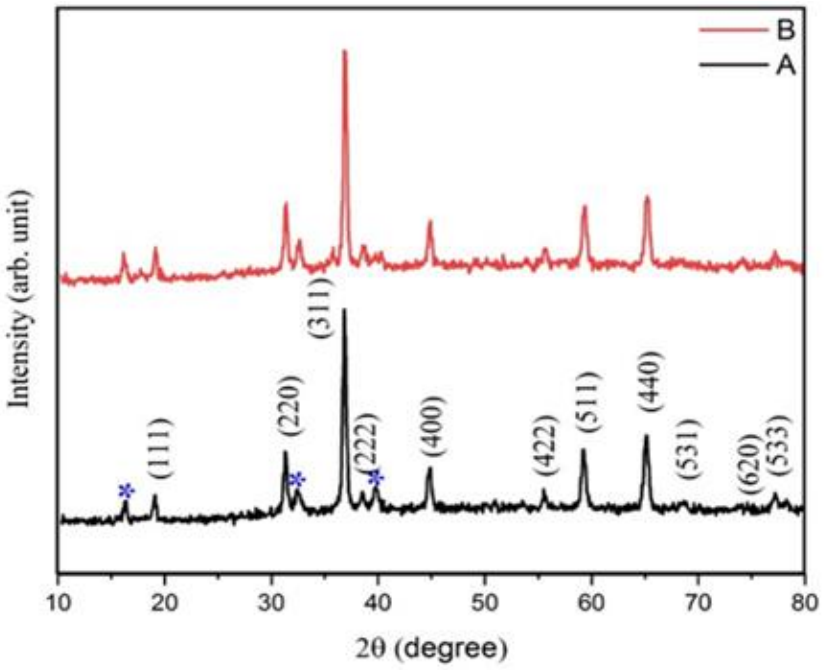

Fig. 3. The XRD results of $CuCo_2O_4$ and $CuCo_2O_4$/Graphene

Lattice parameters of the main peak (311) for both samples were calculated and compared with standard values (Table 2). They were decreased due to addition of graphene and it seems the lattice parameters become closer to the standard values. It may be legitimate due to Vegard's law. Negligible deviation from the standard values is observed, for example, in the case of unit cell volumes, that can be the result of iconicity and instability of the lattice. Other reasons probably play a role in this deviation such as variation of bond angle, bond length, and twisting of the main structure. It is known that various defects inside the main structure cause to band edge variation process [12].

Table 2. The calculated and standard values of the lattice parameters for the main reflection peaks (i.e. (100), (002), (101)) and other relevant parameters.

Miller indices	d (Å)		a (Å)		Volume of unit cell (Å)^3	
	Cal.	Sta.	Cal.	Sta.	Cal.	Sta.
311	2.4368	2.4374	8.0819	8.0840	527.896	528.300
311	2.4371	2.4374	8.0829	8.0840	528.091	528.300

FESEM and EDX results

Morphology and composition could be understood by employing field-emission scanning electron microscope (FESEM) images, as shown in Figure 4. the surface of CuCo2O4 with irregular nanoparticles. The CuCo2O4/Graphene has also irregular nanostructure but more compactness is observed between its structure, which means the reduction of grain boundaries. The CCG microporous nanostructure has a variety of shapes, which makes more surface available and strengthens the reactive points, which increases the electrochemical efficiency. The presence of four elements copper, cobalt, oxygen and carbon was confirmed in EDX analysis and no additional peak indicating the presence of pollutants was seen.

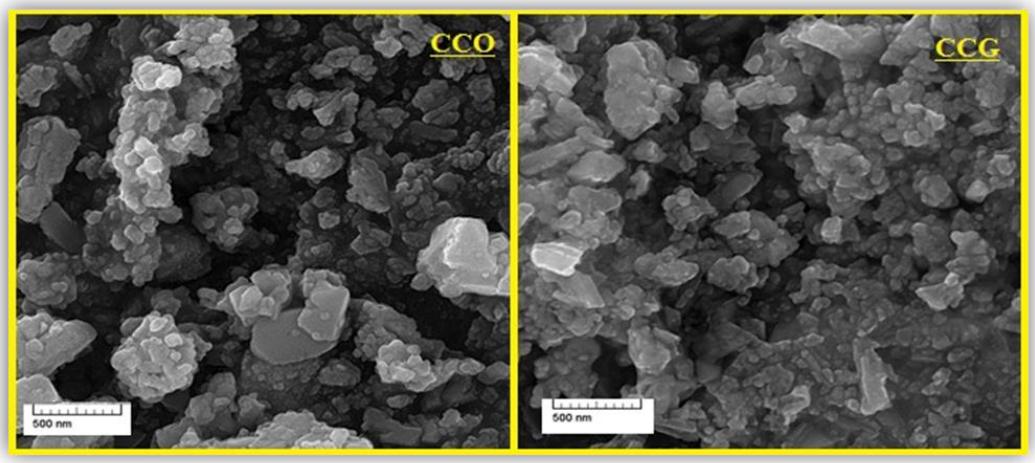

Fig. 4. FESEM images of $CuCo_2O_4$ (CCO) and $CuCo_2O_4$/Graphene (CCG)

The constituent elements analyzed by EDS (Figure 5) confirm the homogeneous distribution of elements copper, cobalt and oxygen. Because EDS in the most cases shows the concentration of heavy elements whose characteristic X-ray energy and efficiency are high and does not take into

account the opposite principle. As shown in Figure 5, there is no contaminants in the synthesized product because no extra peak is observed. So it can be concluded that this fact confirms the purity of the sample and the substance is correctly combined.The presence of carbon in EDS indicates the presence of graphite in the second sample (CCG).

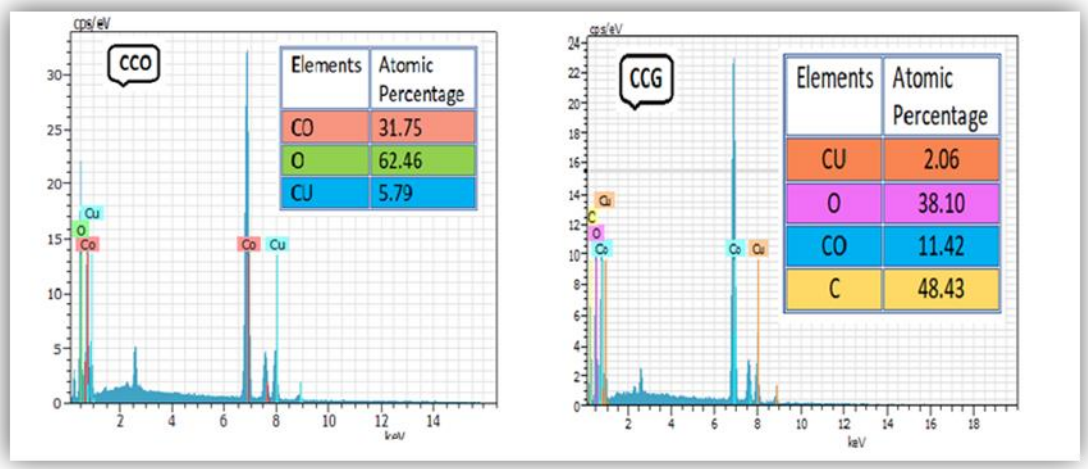

Fig. 5. EDS images of $CuCo_2O_4$ (CCO) and $CuCo_2O_4$/Graphene (CCG)

Conclusions

The powder of CuCo2O4 and CuCo2O4/Graphene were prepared by hydrothermal method. Their structural and morphological properties were investigated. According to the XRD data, the formation of cobaltite in wurtzite structure is approved. However, the signs of the presence of copper oxide are appeared in the main structure. According to FESEM micrographs, all samples had similar microstructures and all of them consisted of nanosized irregular grains. However, by the addition of graphen into the main structure, the connection of nanoparticles increased. The radiation shielding properties of the samples (LAC, MAC, MFP, HVL, and TVL) were also calculated. The results showed that both samples are suitable to be used as a gamma shielding material.

References

[1] Farag, N.M., Deyab, M.A., El-Naggar, A.M., Aldhafiri, A.M., Mohamed, M.B. and Heiba, Z.K., 2021. Exploring the functional properties of CuCo2O4/CuS nanocomposite as improved

material for supercapacitor electrode. Journal of Materials Research and Technology, 10, pp.1415-1426.

[2] Wang, Q., Chen, D. and Zhang, D., 2015. Electrospun porous CuCo 2 O 4 nanowire network electrode for asymmetric supercapacitors. RSC advances, 5(117), pp.96448-96454.

[3] Bagtache, R., Zahra, S., Abdi, A. and Trari, M., 2020. Characterization of CuCo2O4 prepared by nitrate route: application to Ni2+ reduction under visible light. Journal of Photochemistry and Photobiology A: Chemistry, 400, p.112728.

[4] Asl, H.Z. and Rozati, S.M., 2020. Spray deposition of n-type cobalt-doped CuO thin films: influence of cobalt doping on structural, morphological, electrical, and optical properties. Journal of Electronic Materials, 49(2), pp.1534-1540.

[5] Gu, S., Lou, Z., Ma, X. and Shen, G., 2015. CuCo2O4 nanowires grown on a Ni wire for high-performance, flexible fiber supercapacitors. ChemElectroChem, 2(7), pp.1042-1047.

[6] Bhagwan, J., Nagaraju, G., Ramulu, B. and Yu, J.S., 2019. Promotive effect of MWCNT on ZnCo2O4 hexagonal plates and their application in aqueous asymmetric supercapacitor. Journal of The Electrochemical Society, 166(2), p.A217.

[7] Goudarzi, M., Salavati-Niasari, M. and Amiri, M., 2019. Effective induction of death in breast cancer cells with magnetite NiCo2O4/NiO nanocomposite. Composites Part B: Engineering, 166, pp.457-463.

[8] Goudarzi, M., Salavati-Niasari, M., Yazdian, F. and Amiri, M., 2019. Sonochemical assisted thermal decomposition method for green synthesis of CuCo2O4/CuO ceramic nanocomposite using Dactylopius Coccus for anti-tumor investigations. Journal of Alloys and Compounds, 788, pp.944-953.

[9] Bawazeer, O., Makkawi, K., Aga, Z.B., Albakri, H., Assiri, N., Althagafy, K. and Ajlouni, A.W., 2023. A review on using nanocomposites as shielding materials against ionizing radiation. Journal of Umm Al-Qura University for Applied Sciences, pp.1-16.

[10] El-Khatib, A.M., Abbas, M.I., Hammoury, S.I., Gouda, M.M., Zard, K. and Elsafi, M., 2022. Effect of PbO-nanoparticles on dimethyl polysiloxane for use in radiation shielding applications. Scientific Reports, 12(1), p.15722.

[11] Erdem, M., Baykara, O., Doğru, M. and Kuluöztürk, F., 2010. A novel shielding material prepared from solid waste containing lead for gamma ray. Radiation Physics and Chemistry, 79(9), pp.917-922.

[12] Bagheri Khatibani, A., Shabankhah, A., 2021. Fabrication and ethanol sensing of sol–gel grown zinc oxide powder: the effect of cobalt and copper doping, Appl. Phys. A, 127, pp. 308.

ICNST 2024
International Conference on Nuclear Science and Technology
6- 8 MAY 2024 | Isfahan, Iran

Comparative study of dosimetry response of gamma-rays for PC/Bi2O3 and HDPE/Bi2O3 nanocomposites (Paper ID: 1348)

Veiskarami A. [1*], Malekie S. [2], Kashian S. [2]. Veiskarami A[1]

[1] *Department of Medical Radiation Engineering, Science and Research Branch, Islamic Azad University, Tehran, Iran*

[2] *Radiation Application Research School, Nuclear Science and Technology Research Institute, P.O. Box 31485-498, Karaj, Iran*

Abstract

Recently polymer-heavy metal oxide nanocomposites have recently attracted a large amount of attention due to the remarkable advantages as the radiation sensor, detector and dosimeters for gamma-rays, X-rays and charged particles. Several factors can affect the sensitivity including the amount of sensitive volume, concentration of the heavy metal oxide nanoparticles, applied bias voltage, and crystallinity of the polymer matrix. It has been demonstrated that a high degree of polymer crystallinity can impede the uniform distribution of nanoparticles. This study employed two different polymer matrices, namely high-density polyethylene (HDPE) as a semi-crystalline polymer and polycarbonate (PC) as an amorphous polymer, in a nanocomposite containing bismuth oxide nanoparticles up to 60 wt%. Results showed that PC demonstrated a better dispersion state up to 60 wt%, while HDPE was agglomerated at 40 wt%. Therefore, PC as an amorphous polymer containing 50 wt% Bi2O3 can be considered as a suitable candidate in a heavy metal oxide-nanocomposite for dosimetry purposes.

Keywords: Dosimetry, Gamma-rays, polymer- heavy metal oxide nanocomposite, Crystallinity.

Introduction

Recently, polymer nanocomposites have attracted significant attention from scientists for use as radiation protection, sensors, detectors, and dosimeters [1-10]. These materials have many advantages due to their lightness, flexibility, ease of processing, being tissue equivalent, and relatively low cost. Polymer-nanocomposites exhibit low sensitivity to gamma-rays due to their low densities. Therefore, to overcome this problem, bismuth oxide (Bi2O3) nanoparticles with a density of 8.9 g/cm3 (with atomic number Z=83 for Bi) are added to the polymer matrix. This can increase the sensitivity of radiation detection and dosimetry by increasing the probability of the photoelectric effect. Several investigations were carried out on the polymer-heavy metal oxide

composites with radiation detection and dosimetry. For example Intaniwet et al. investigated the addition of Bi2O3 nanoparticles in a semiconductor polymer to improve the detector sensitivity against the 17.5 keV X-rays [8].

The dispersion of nanoparticles in polymer matrices can be challenging, particularly at higher volume fractions, due to the aggregation effects of the inclusions [11]. It has been demonstrated that high levels of the polymer crystallinity can hinder the homogenous dispersion of the nanoparticles [12]. In this research, Polycarbonate (PC), a thermoset polymer with an amorphous structure and repeat units of -CH2-CH (C6H5) is a superior candidate for making homogenous nanocomposites [3]. PC exhibits a suitable radiation hardness and superior breakdown voltage with regard to the aromatic structure [13-15]. PC is expected to have more suitable bonds with Bi2O3 nanoparticles. PC contains end groups including conjugated double bonds [16], C=O (carbonyl), C-H, Phenyl, and C-O-C bands [17]. Also, HDPE with a repeat unit of –[C2H4]– as a thermoplastic polymer exhibiting a semi-crystalline structure was selected as a polymer matrix.

In this work, a comparative study of the dosimetry response of two nanocomposites namely PC/Bi2O3 and HDPE/Bi2O3 were carried out. The novelty of this work is investigating the effect of polymer matrix on the dosimetry response of the polymer- Bi2O3 nanocomposite dosimeter.

Research Theories

Efficiency of detection and dosimetry is improved when radiation interacts with matter having a higher attenuation coefficient at a given energy. Quantum efficiency (QE) is often defined as [8]:

$$QE = \left(1 - e^{-(\frac{\mu}{\rho})\rho x}\right) 100\% \quad (1)$$

where μ/ρ is the mass attenuation coefficient obtained from the photon cross-section database [18], ρ and x are the composite density and thickness, accordingly. So, μ/ρ was obtained for the two composites of PC/Bi2O3 and HDPE/Bi2O3 through online access and definition of the mentioned compounds using XCOM [18].

Experimental

In this experimental work, PC, and HDPE granules were supplied from Iranian-Khuzestan petrochemical company with a density of 1.2 g/cm3, and 0.93 g/cm3 respectively. Bi2O3 nanopowders with a density of 8.9 g/cm3 and average particle sizes between 90-210 nm were prepared from Sigma-Aldrich. In a summary, the polymers were dissolved in the suitable solvents using a hotplate magnetic stirrer, and then the Bi2O3 nanoparticles were added to the polymer solution and dispersed with an ultrasonic probe. Finally the samples were conducted to hot press to make the fixed thickness of 1 mm, and size 4×4 cm2 at various concentrations. As can be seen in Fig. 1a, copper plates with thickness of 100 μm were adhered to the samples using the silver paste in order to fabricate electrodes on both surfaces of the dosimeters. The details of fabrication process can be found in our earlier studies [1, 3, 19].

Thus, PC/Bi2O3 nanocomposites at concentrations of 0, 5, 20, 40, and 50 Bi2O3 wt% and HDPE/Bi2O3 nanocomposites at loadings of 0, 20, 40, and 60 Bi2O3 wt% were fabricated via a solution method. Afterward, the samples were irradiated by gamma-rays of 60Co related to Picker V-9 at the Secondary Standard Dosimetry Laboratory (SSDL) of Iran-Karaj, in various source to surface distances (SSDs). The change in electrical current pass through the samples was considered as the dosimetry response, which was measured by an electrometer model SuperMax Standard Imaging at 400 V.

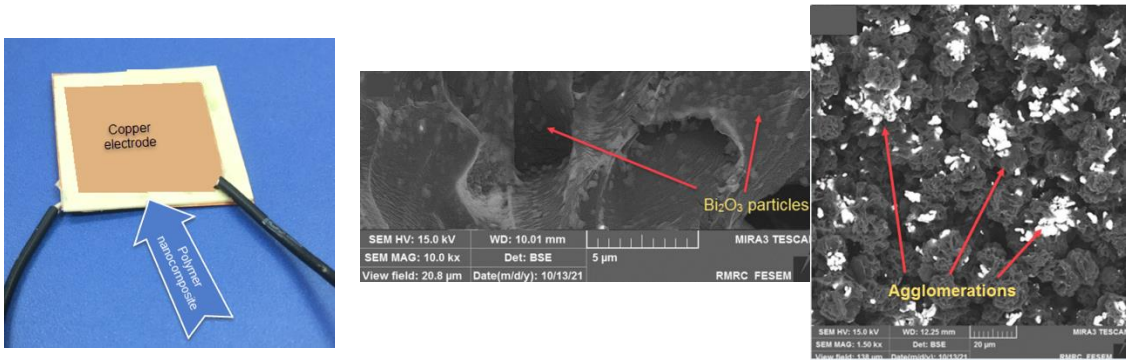

(a) (b) (c)

(a) Preparation of the nanocomposite dosimeter, and FESEM for (b) PC/Bi_2O_3, and (c) HDPE/Bi_2O_3 nanocomposites.

Results and Discussion

Fig.2 displays the predicted quantum efficiencies of a 1 mm thickness for the two composites namely PC/Bi2O3, and and HDPE/Bi2O3 at 1250 keV with various concentrations of the inclusioins using the XCOM program [18]. For both composites, as the Bi2O3 concentration increases, the QA enhances consequentntly. Also, PC due to higher density (1.2 g/cm3) in comparision with the HDPE (0.93 g/cm3) exhibits the higher QE.

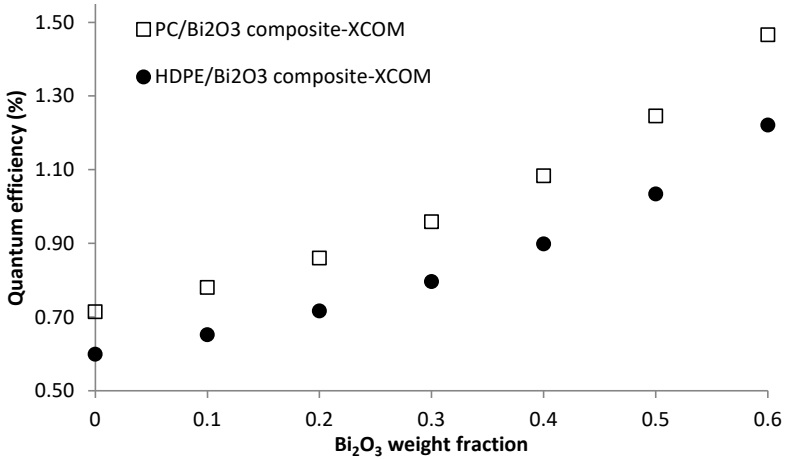

Quantum efficiency for PC/Bi_2O_3, and HDPE/ Bi_2O_3 composites, thickness of 1 mm at 1250 keV for various inclusions up to 60 wt% using the XCOM.

Fig.1 (1b, 1c) shows the FESEM images of PC/Bi2O3 and HDPE/Bi2O3 nanocomposites. As can be seen from Fig. 1b, the Bi2O3 nanoparticles were dispersed uniformly in the PC matrix. But, as shown in Fig. 1c, the nanoparticles were agglomerated, which exhibited a non-uniform dispersion in the HDPE matrix. Thus, PC exhibits a better dispersion state of the inclusions in comparison with HDPE. To interpret this effect, it can be mentioned that HDPE as a semi-crystalline polymer impede the uniform distribution of the nanoparticles due to presence of the crystallites.

Fig. 3 exhibits the average photocurrent vs. SSD for various samples for PC/Bi2O3, and HDPE/Bi2O3 nanocomposites. As the Bi2O3 wt% increases, the dosimeter response enhances subsequently. As shown in Fig. 3b, for HDPE/Bi2O3 nanocomposite, this trend is valid up to 40 wt%; but for 60 wt% sample, the dosimeter response decreases by 20-30% in comparison with the 40 wt% sample. To justify this phenomenon, it can be mentioned that due to the semi-crystalline nature of the HDPE matrix, the agglomeration occurs at the higher reinforcement loadings namely 60 wt% leading to decrease of the dosimeter response subsequently.

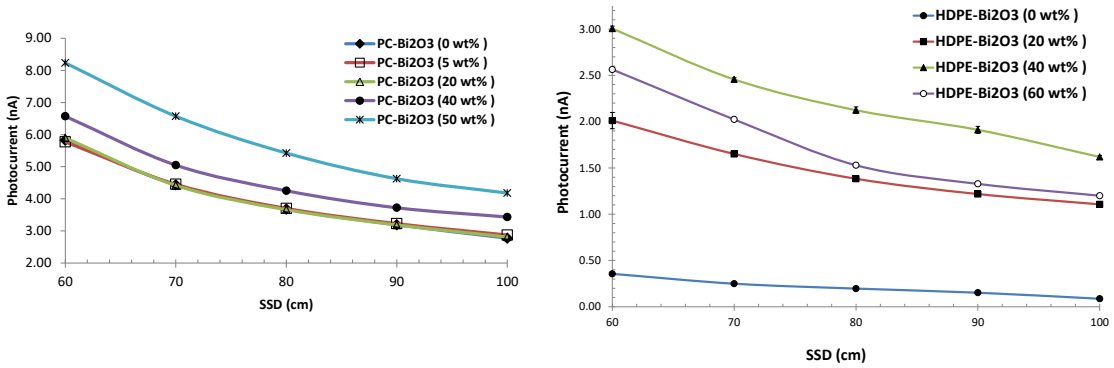

(a) (b)

Average photocurrent vs. SSD for (a) PC/Bi_2O_3, and (b) HDPE/ Bi_2O_3 nanocomposites.

The dosimetry response of PC/Bi2O3 and HDPE/Bi2O3 nanocomposites for various Bi2O3 wt% at the fixed SSD=80 cm which is equal to dose rate of 42.67 mGy/min is depicted in Fig. 4. As can be seen from Fig. 4a, the dosimetry response for PC/Bi2O3 nanocomposite is linear between 20-50 wt%. But, as shown for in Fig. 4b, for HDPE it was increases linearly up to 40 wt%, then decreases 25% at 60 wt%. This is due to agglomeration of the inclusions in the semi-crystalline polymer of HDPE.

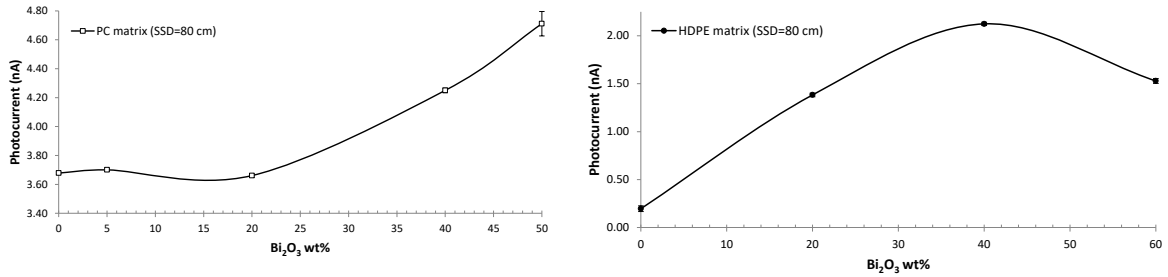

(a) (b)

Dosimetry response at a fixed SSD=80 cm for a) PC/Bi_2O_3, and b) HDPE/Bi_2O_3nanocomposites.

Conclusions

In this research, effect of polymer matrix on the sensitivity of a novel radiation dosimeter based on polymer-heavy metal oxide nanocomposites was investigated. For this purpose, two composites namely PC/Bi2O3 and HDPE/Bi2O3 were considered with different crystallinity degree of the polymer matrices. Quantum efficiency was evaluated for both composites using the XCOM. It was

concluded that PC with higher density exhibited higher efficiency at various concentrations in comparison with the HDPE. FESEM images demonstrated that agglomeration happened at the composites containing HDPE as a semi-crystalline polymer matrix. This is due to the fact that crystallinity can hinder the homogenous dispersion of the nanoparticles. So, PC/Bi2O3 has potential application to be used as a real-time dosimeter for therapeutic dose level.

Acknowledgements

We would like to express our gratitude to all those who assisted us in carrying out this research, especially the NSTRI staff, whose contributions greatly contributed to the success of this study.

References

[1] Safdari, S. M., Malekie, S., Kashian, S., & Akbari, M. (2022). Introducing a novel beta-ray sensor based on polycarbonate/bismuth oxide nanocomposite. Scientific Reports, 12(1), 2496.
[2] Hosseini, M. A., Malekie, S., & Kazemi, F. (2022). Experimental evaluation of gamma radiation shielding characteristics of Polyvinyl Alcohol/Tungsten oxide composite: A comparison study of micro and nano sizes of the fillers. Nuclear Instruments and Methods in Physics Research Section A: Accelerators, Spectrometers, Detectors and Associated Equipment, 1026, 166214.
[3] Mehrara, R., Malekie, S., Saleh Kotahi, S. M., & Kashian, S. (2021). Introducing a novel low energy gamma ray shield utilizing Polycarbonate Bismuth Oxide composite. Scientific Reports, 11(1), 10614.
[4] Malekie, S., & Ziaie, F. (2015). Study on a novel dosimeter based on polyethylene–carbon nanotube composite. Nuclear Instruments and Methods in Physics Research Section A: Accelerators, Spectrometers, Detectors and Associated Equipment, 791, 1-5.
[5] Malekie, S., Ziaie, F., & Esmaeli, A. (2016). Study on dosimetry characteristics of polymer–CNT nanocomposites: Effect of polymer matrix. Nuclear Instruments and Methods in Physics Research Section A: Accelerators, Spectrometers, Detectors and Associated Equipment, 816, 101-105.
[6] Malekie, S., Ziaie, F., Feizi, S., & Esmaeli, A. (2016). Dosimetry characteristics of HDPE-SWCNT nanocomposite for real time application. Nuclear Instruments and Methods in Physics Research Section A: Accelerators, Spectrometers, Detectors and Associated Equipment, 833, 127-133.
[7] Mosayebi, A., Malekie, S., & Ziaie, F. (2017). A feasibility study of polystyrene/CNT nano-composite as a dosimeter for diagnostic and therapeutic purposes. Journal of Instrumentation, 12(05), P05012.

[8] Intaniwet, A., Mills, C. A., Shkunov, M., Sellin, P. J., & Keddie, J. L. (2012). Heavy metallic oxide nanoparticles for enhanced sensitivity in semiconducting polymer x-ray detectors. Nanotechnology, 23, 235502.
[9] Mosayebi, A., Malekie, S., Rahimi, A., & Ziaie, F. (2019). Experimental study on polystyrene-MWCNT nanocomposite as a radiation dosimeter. Radiation Physics and Chemistry, 164, 108362.
[10] Kyatsandra, S., & Wilkins, R. (2015). Total Ionizing Dose X-ray Radiation Effects on MWCNT/PMMA Thin Film Composites. Nanotechnology, IEEE Transactions on, 14(1), 152-158.
[11] Kim, J., Seo, D., Lee, B. C., Seo, Y. S., & Miller, W. H. (2014). Nano-W Dispersed Gamma Radiation Shielding Materials. Advanced engineering materials, 16(9), 1083-1089.
[12] Kaur, J., Lee, J. H., & Shofner, M. L. (2011). Influence of polymer matrix crystallinity on nanocomposite morphology and properties. Polymer, 52(19), 4337-4344.
[13] Chen, J., Huang, X., Jiang, P., & Wang, G. (2009). Protection of SEBS/PS blends against gamma radiation by aromatic compounds. Journal of applied polymer science, 112(2), 1076-1081.
[14] Gurkalenko, Y. A., Eliseev, D., Zhmurin, P., Pereymak, V., & Svidlo, O. (2017). The plastic scintillator activated with fluorinated hydroxyflavone. Functional materials, 24(2), 244-249.
[15] Mark, J. E. (2007). Physical properties of polymers handbook (Vol. 1076): Springer.
[16] Stix, W., Bottenbruch, L., & Neuray, D. (1985). Polycarbonates having terminal groups which contain conjugated double bonds. In: Google Patents.
[17] Yadav, R., Naebe, M., Wang, X., & Kandasubramanian, B. (2017). Structural and thermal stability of polycarbonate decorated fumed silica nanocomposite via thermomechanical analysis and in-situ temperature assisted SAXS. Scientific Reports 7(1), 1-11.
[18] Berger M J, Hubbell J H, Seltzer S M, Chang J, Coursey J S, Sukumar R and Zucker D S 2011 XCOM: Photon Cross Sections Database, National Institute of Standards and Technology, USA, http://physics.nist.gov/PhysRefData/Xcom/Text/XCOM.html.
[19] Veiskarami, A., Sardari, D., Malekie, S., Mofrad, F. B., & Kashian, S. (2022). Evaluation of dosimetric characteristics of a ternary nanocomposite based on High Density Polyethylene/Bismuth Oxide/Graphene Oxide for gamma-rays. Scientific Reports, 12(1), 1-17.

ICNST 2024
International Conference on Nuclear Science and Technology
6- 8 MAY 2024 | Isfahan, Iran

Displacement Damage Study in Tungsten by Molecular Dynamics Simulation (Paper ID: 1378)

Shafiei S [1*]

[1] *Radiation Applications Research School, Nuclear Science and Technology Research Institute, AEOI, Tehran, Iran*

Abstract

In the present study, a series of displacement cascade simulations were carried out to explore the irradiation behavior in tungsten while cosidering the effects of temperature and the primary knock-on atom (PKA) directions. The irradiation process was simulated in the temperature range of 300 to 700 K, with a PKA energy of 1 keV along three different lattice directions. The number of Frenkel pairs, the type of defect and the size distributions for the defect clusters were all determined. As the temperature increased, the thermal spike stage and the peak defect count also increased, while the effect of temperature on the surviving defect number was negligible. The stable vacancies in the [01$\bar{1}$]/(001) direction could cause the collapse of the lattice due to their lamella-like shape. Clusters with a size of two were found in the quenching stage.

Keywords: Displacement cascade; Tungsten; Defects; Molecular dynamics

Introduction

Tungsten and its alloys are currently the most promising candidates for the first wall in DEMO and future fusion reactors. It is also foreseen as a diverter plasma-facing material in the activated phase of ITER [1]. Tungsten has the advantage of the highest melting point (3680 K), excellent thermal conductivity, and low or negligible sputtering at low plasma temperatures[2]. Materials in the fusion reactor will be irradiated by high-energy neutrons. In addition, they have to tolerate high temperatures and pressures. Energetic neutrons produce high-energy recoils, known as primary knock-on atoms (PKA). PKA initiate displacement cascades that lead to the production of interstitials and vacancies, both known as Frenkel pairs (FPs), which can further aggregate to form clusters and voids. At the time of initiation of the damage cascade, a large number of Frenkel pairs are formed, but during the relaxation of the collision cascade, most of the displaced atoms tend to return to equilibrium crystal lattice positions. This effect results in the recombination of interstitials and vacancies and stable point defects remain at the end of the damage process. These stable

defects degrade the structural material properties, limiting the lifetime and operation of nuclear power systems[3]. As a result, it is essential to understand the materials' behavior in radiation damage environments for the design and maintenance of advanced structural materials for nuclear reactor power applications. However, it is not easy to obtain knowledge about the temporal development of the defect structures by experiments. Thus, computer simulations are needed to gain a better understanding of the spatial and temporal development of the cascade, the number of various point defect types, and the size distribution of their clusters. Molecular dynamics (MD)-based atomistic modeling methods, whose length and time scales are compatible with displacement cascades, are well-known tools for modeling and analyzing irradiation-induced microstructural changes. Many papers have taken the advantage of MD simulation and studied the process of irradiation-induced defects, the influence of interatomic potentials, the irradiation temperature, PKA energy, and grain boundaries on the tungsten irradiation results.

A.E. Sand et al. compared the effect of various interatomic potentials on defect generation in tungsten in cascades with PKA energies ranging from 1 keV to 200 keV [4, 5]. D.R. Mason et al. presented an empirical interatomic potential for tungsten, particularly well-suited for simulations of vacancy-type defects[6].

Mohammad Bany Salman et al. investigated the effect of strain on the formation of primary defects and the probability of interstitial dislocation loops (IDLs) formation in tungsten (W) during a collision cascade event with PKA energies of 1, 6, 10, and 14 keV, applied on a deformed W structure [7]. The coupling effect of strain field and displacement cascade in tungsten at different temperatures was also studied by D.Wang et. al [8].

Jun Fu and his co-worker simulated high-energy collision cascades with energies up to 300 keV for PKA along the <135> direction in W and W-Re alloys containing 5 or 10 at.% Re atoms. They analyzed the effects of PKA energy and Re concentration on defect production, defect clustering, and states of dislocation loops[9]. A comprehensive database of surviving defects due to displacement cascades with PKA energies ranging from 100 eV to 100 keV in bulk tungsten has been generated by W.Setyawan et al. [10]. Mayank Rajput et al. carried out MD simulations of self-recoils of with damage energies ranging from 5 keV to 200 keV to predict the number of Frenkel pairs in iron and tungsten [11]. Recently cascade damage databases with different PKA

energies ranging from 1 keV to 300 keV in directions <135>, <235>, <111>, <110>, <100>, <122> and <133> at 300 K, 363 K and 600 K have been compiled [12].

Although the displacement cascade behaviors of tungsten with high and low PKA energy have been investigated in the literature, most of them considered random PKA direction. Moreover, the illustration of results for collision cascade with a PKA energy of 1 keV was ignored in comparison to those with high-energy PKA. Consequently, this work mainly focuses on the defects generated by a PKA with an energy of 1 keV along $[00\bar{1}]/(001)$, $[01\bar{1}]/(001)$, and $[11\bar{1}]/(001)$ directions of W with temperatures ranging from 300 K to 700 K. The results based on MD simulation were presented in more detail. Contrary to other literature our output data from the MD simulation doesn't need to be analyzed because a compute and dump style presented by K.D. Hammond for LAMMPS was used in simulations[13].

Research Theories

In this studt, MD simulations were conducted using the Large-scale Atomic/Molecular Massively Parallel Simulator (LAMMPS) code developed by Sandia National Laboratory[14]. To characterize the interatomic interactions among tungsten atoms, an Embedded Atom Method (EAM) potential was utilized. [15]. The Ziegler-Biersacl-Littmark (ZBL) function was applied to correct the potential for irradiation simulation in the short range[16]. Body-centered cubic supercells were generated for the W with size of 30 a × 30 a × 30 a, where a is the lattice constant, which is 3.17Å. The atomic number in the supercell was 54000 atoms. Periodic boundary conditions were imposed in all three directions. The simulation system was equilibrated for 10 ps in the canonical ensemble (NVT) using a Nose-Hoover thermostat at temperature of 300K, 500K and 700 K. Cascades were initiated by providing the kinetic energy of 1 keV in the form of velocity to an atom in the top layer along the $[00\bar{1}]/(001)$, $[01\bar{1}]/(001)$ and $[11\bar{1}]/(001)$ directions. During the displacement cascade process, simulations were carried out under the microcanonical NVE ensemble for the inner atoms, while the outer lattice atomic layers were maintained under the NVT ensemble with the Nose-Hoover thermostat. The simulation box for MD cascade simulations and PKA directions is illustrated in Fig. 1. An automatically adaptive time step method was employed during the simulation by limiting the maximum atomic displacement to 0.005a Å per step.

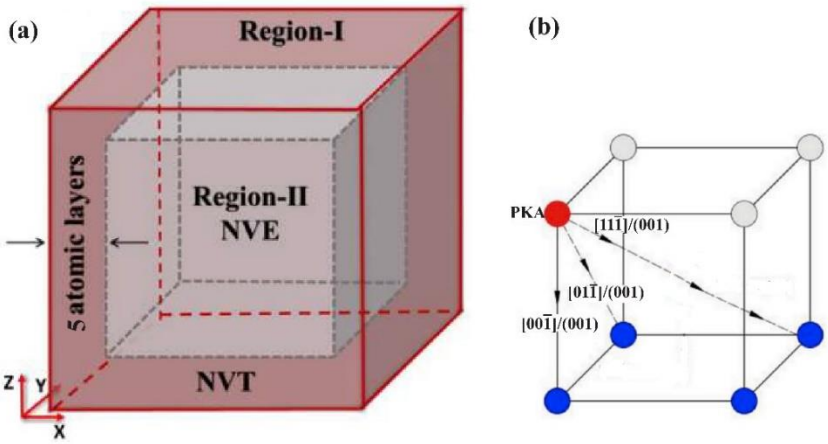

Fig. 1. (a) The simulation box for MD cascade simulations. (b) The incidence directions of PKA.

All defect identification, analysis and output relevant to cascade damage simulations were completed without the need for post-processing by utilizing a compute and dump style presented by K.D. Hammond for LAMMPS [13]. The visualization file of point defects and the clusters was opened using the OVITO software package.

Results and discussion

The typical evolution of the number of point defects (self-interstitial atoms or vacancies) during displacement cascades for each direction is presented in Fig.2. These results exhibit good consistency with those presented for the crystal structure of bcc [17]. A complete cascade collision process involves three stages: the collision stage, thermal spike, and quenching stage. In the collision stage defects were created and their numbers increased over time. Then the dislocation peak appeared in the thermal spike stage. The duration time for the first two stages is less than 0.4 ps. Finally, in the quenching stage annihilation of defects occured. In this stage the temperature in the cascade region was high due to the collision, resulting in self-interstitial atoms (SIAs) vibrating in a range and SIA-vacancy recombination. Therefore, the number of defects dropped, and only the stable defects survived. It was observed that the difference of FPs in various PKA directions was small which is in good agreement with previous work in W cascades[12].

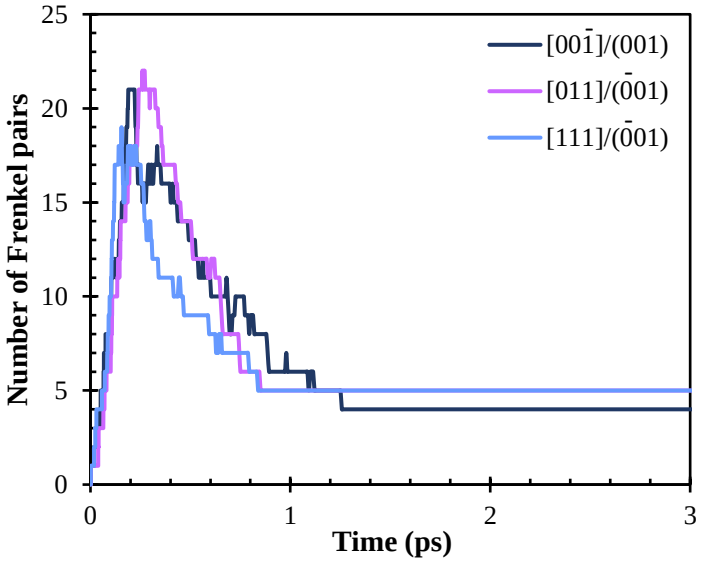

Fig. 2. Defect productions evoked by PKAs with 1 keV energy in three incidence directions.

The creation, thermal spike and annihilation process of defects in the [00$\bar{\mathbf{1}}$]/(001) direction are displayed in Fig. 3. It can be seen that the number of point defects rapidly increased over time, reaching a peak value at about 0.2 ps (ballistic phase). As time elapsed, the cascade region quickly disappeared due to high rate of SIAs-vacancies recombination (recovery phase).

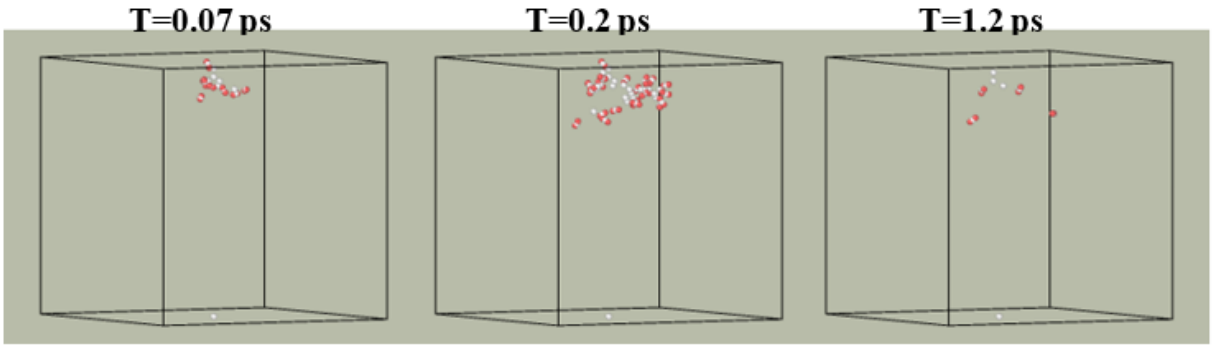

Fig. 3. The creation and annihilation process of point defects in [00$\bar{1}$]/(001) direction.

The configuration of the surviving point defects in all three directions is shown in Fig.4. This figure illustrate that after the annihilation recombination of interstitials and vacancies, the shape of vacancies in the [00$\bar{1}$]/(001) and [11$\bar{1}$]/(001) directions was three-dimensional. The stable vacancies accumulated around the location where the cascade initiated. However, the distribution of vacancies in the [01$\bar{1}$]/(001) direction was lamella-like in shape. additionally, the stable

vacancies in this direction were distributed farther from the location where the cascade initiated. It was observed that the vacancy cluster in Fe along the $[01\bar{1}]/(001)$ direction had a lamella-like shape in both the collision stage and thermal spike stage [18]. This configuration of defects is important because it leads to the collapse of the lattice.

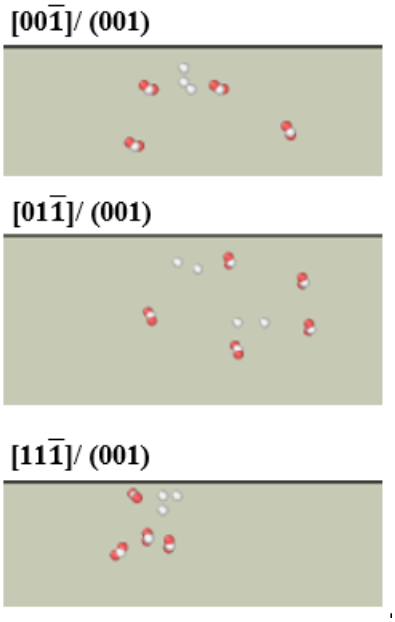

Fig. 4. The defect configuration diagram after the annihilation recombine of interstitials (red ball) and vacancies (white ball) in different directions.

The temporal evolution of the average number of Frenkel pairs during displacement cascades at three different temperatures was studied. The peak and surviving number of Frenkel pairs in the $[00\bar{1}]/(001)$ direction at different temperatures are shown in Fig.5. The graph illustrates that the peak defect count increased with the increment of temperature, emphasizing the role of temperature in increasing defect production during the thermal spike phase. However, the differences in final defect production, as indicated by the error bars, suggest that the influence of temperature on final defect production is not significant. This trend may become more prounounced at higher PKA energy and temperature levels.

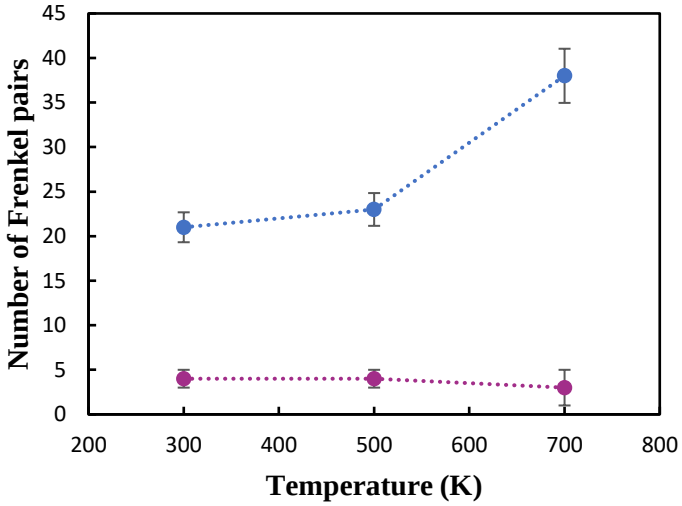

Fig. 5. Peak (blue dots) and surviving (purple dots) lnumber of Frenkel pairs at different temperatures in $[00\bar{1}]/(001)$ direction.

To gather detailed information about the surviving defects, a cluster of these defects was identified. The cutoff distance for vacancy and interstitial clusters was considered to be 1.1a and 1.42a respectively. It was obserevd that the size of vacancy clusters increased by the time. The vacancy clusters reached a maximum size of six and five during the thermal spike, then decreased in all three directions. In the quenching state, only vacancy clusters with a size less than three were found. The maximum size of the interstitial cluster observed during the thermal spike was three. In the quenching state only interstitial clusters with a size of two survived.

Conclusions

This research discusses the primary damage in tungsten caused by displacement cascades with a PKA energy of 1 keV in three different directions at 300, 500 and 700 K . The point defects and clusters were searched for and counted according to a compute and dump style presented by K.D. Hammond. The time evolution of defects produced during displacement cascades showed that defect formation and thermal spike stages in tungsten irradiation occurred rapidly. The number of stable defects produced by a PKA with an energy of 1 keV did not depend on the PKA direction. It was oserved that in the quenching stage when the PKA direction was along $[00\bar{1}]/(001)$ and $[11\bar{1}]/(001)$ directions, vacancies were distributed in three dimensions around the region where the

cascade initiated. When the PKA initiated along the $[01\bar{1}]/(001)$ direction the surviving vacancy clusters were distributed in planes near and far from the region where the cascade initiated. The lamella-like shape of vacancies in the $[01\bar{1}]/(001)$ direction could cause the lattice to collapse. The effect of temperature on the peak and the surviving number of Frenkel pairs was investigated. Although defect production increased with temperature, the number of surviving defects declined insignificantly. It was found that in the quenching stage, only clusters with a size of two survived.

References

[1] Linsmeier C, Unterberg B, Coenen J, Doerner R, Greuner H, Kreter A, et al. Material testing facilities and programs for plasma-facing component testing. Nuclear Fusion. 2017;57:092012.

[2] Bolt H, Barabash V, Krauss W, Linke J, Neu R, Suzuki S, et al. Materials for the plasma-facing components of fusion reactors. Journal of nuclear materials. 2004;329:66-73.

[3] Was G, Andresen P. Radiation damage to structural alloys in nuclear power plants: mechanisms and remediation. Structural Alloys for Power Plants: Elsevier; 2014. p. 355-420.

[4] Sand AE, Dequeker J, Becquart C, Domain C, Nordlund K. Non-equilibrium properties of interatomic potentials in cascade simulations in tungsten. Journal of Nuclear Materials. 2016;470:119-27.

[5] Sand AE, Nordlund K, Dudarev S. Radiation damage production in massive cascades initiated by fusion neutrons in tungsten. Journal of Nuclear Materials. 2014;455:207-11.

[6] Mason DR, Nguyen-Manh D, Becquart CS. An empirical potential for simulating vacancy clusters in tungsten. Journal of Physics: Condensed Matter. 2017;29:505501.

[7] Bany Salman M, Park M, Banisalman MJ. A Molecular Dynamics Study of Tungsten's Interstitial Dislocation Loops Formation Induced by Irradiation under Local Strain. Solids. 2022;3:219-30.

[8] Wang D, Gao N, Wang Z, Gao X, He W, Cui M, et al. Effect of strain field on displacement cascade in tungsten studied by molecular dynamics simulation. Nuclear Instruments and Methods in Physics Research section B: Beam Interactions with Materials and Atoms. 2016;384:68-75.

[9] Fu J, Chen Y, Fang J, Gao N, Hu W, Jiang C, et al. Molecular dynamics simulations of high-energy radiation damage in W and W–Re alloys. Journal of Nuclear Materials. 2019;524:9-20.

[10] Setyawan W, Nandipati G, Roche KJ, Heinisch HL, Wirth BD, Kurtz RJ. Displacement cascades and defects annealing in tungsten, Part I: Defect database from molecular dynamics simulations. Journal of Nuclear Materials. 2015;462:329-37.

[11] Rajput M, Subhash P, Srinivasan R. Displacement damage study in tungsten and iron for fusion neutron irradiation. Fusion Engineering and Design. 2020;150:111370.

[12] Liu L, Qiu R, Chen Y, Jiang M, Gao N, Huang B, et al. Displacement cascades database from molecular dynamics simulations in tungsten. Journal of Nuclear Materials. 2023;580:154415.

[13] Hammond KD. Parallel point defect identification in molecular dynamics simulations without post-processing: a compute and dump style for LAMMPS. Computer Physics Communications. 2020;247:106862.

[14] Plimpton S. Fast parallel algorithms for short-range molecular dynamics. Journal of computational physics. 1995;117:1-19.

[15] Ackland GJ, Huang X, Rabe KM. First-principles thermodynamics of transition metals: W, NiAl, and PdTi. Physical Review B. 2003;68:214104.

[16] Ziegler JF, Biersack JP. The stopping and range of ions in matter. Treatise on Heavy-Ion Science: Volume 6: Astrophysics, Chemistry, and Condensed Matter: Springer; 1985. p. 93-129.

[17] Guo X, Li H, Wang J, Liu C, Xu J, Xi Y, et al. Molecular dynamics simulations of irradiated defect clusters evolution in different crystal structures. Physica Scripta. 2022;98:015003.

[18] Zhang M, Peng W, Zhang H, Wu B, Sun K, Fang L. The effect of PKA directions on the primary radiation damage in the alpha iron nanowires. Materials Chemistry and Physics. 2019;232:16-22.

ICNST 2024
International Conference on Nuclear Science and Technology
6- 8 MAY 2024 | Isfahan, Iran

Measuring Glass resistivity for Resistive Plate Chambers (Paper ID: 1388)

Ahmadpouri M.*, Pezeshkian Y.
Department of Physics, Sahand University of Technology, Sahand, Iran

Abstract

The resistive plate chambers are widespread gaseous detectors in physics experiments. Depending on the application, these detectors are made of plates with resistivity at the range of 10^8 to 10^{14} ohm.m. The glass plates are one of the candidates for manufacturing these detectors. In this study, we constructed an experimental setup to measure the resistivity of a 2 mm thick glass plate. The glass plate is serried in a voltage dividing circuit and the current is recorded over the time by an ADC. The current in the circuit varies by time right after applying the voltage and eventually reaches a stable value. The measurement is repeated at eight different voltages between 0.5 to 4 kV. The value of the current in the stable phase was obtained offline by a Python code for each voltage. By having the current as a function of the voltage, we find the resistivity of the sample $1.29 \pm 0.04 \times 10^{10}$ Ohm.m.

Keywords: Resistive plate chambers, Resistivity measurement, Gaseous detectors, Glass resistivity

Introduction

Resistive plate chambers (RPC) are gaseous detectors made of resistive materials with a volume resistivity at the range of 10^{10} to 10^{14} Ohm.m. In addition to resistivity, surface smoothness and stability of properties in long-term applications are also important in selecting the material. Commonly, bakelite and glass are the two materials used in resistive plate chambers. For improving the surface roughness in bakelite plates, special oils such as linseed oil are used. Using oil causes a reduction in the lifetime of manufactured detectors [1]. Therefore, many researchers are looking to use other materials in manufacturing insulated plates. In addition to glass and bakelite, efforts have been made to use ceramic materials to improve the properties of resistive plates [2].

The surface smoothness, availability, ability to manufacture in plate form and electrical properties of glass have attracted attentions toward itself. Also, in recent years, with the advancement of technology and the possibility of improving glass properties, more people have turned to using

glass as a resistive plate in RPC manufacturing [3]. However, working with glass also has disadvantages such as the inability to machine and weak mechanical strength. As we are developing glass RPCs at Sahand University of Technology [4,5], the ability to measure the electric properties of the glass plates has crucial importance to us. In this paper, the resistivity measuring setup and experimental details will be discussed.

Electrical Conductivity of Glass

Glass is considered a resistive material. Since the resistive materials have a slight electrical conductivity, we do not have an ideal insulator. The process of conductivity inside glass is related to the drift movement of positive and negative ions. Glasses usually contain 60 to 65 percent silica. Other compounds such as sodium carbonate, lime, feldspar and sulfate are added during glass production. Colored glasses are also produced by adding iron oxide, cobalt oxide, chromium, cobalt and manganese. Typical float glasses contain SiO2, Na2O, MgO, Al2O3 and CaO [6]. A tiny percentage of sodium, potassium and other atoms in the form of positive ions and a small percentage of oxygen atoms in the form of negative ions can move freely inside the glass which is also temperature dependent. In other words, these are cations and anions that are charge carriers.

The resistivity of glass usually depends on the composition and concentration of ions. For resistivities in the range of glass, measurement of resistivity for high resistive materials like glass, conventional methods can't be applied. Suppose the resistance is of the order of 10^{12} ohms, the current intensity will also be of the order of 10^{-9} amperes (for a potential difference of a few kV) very low to be measured by conventional ammeters.

Some advanced tools such as GUILDLINE 6530 or Vitrek 955I can be used to measure the conductivity or resistance of glass, but they are costly. A simple and less costly way is to use a voltage divider circuit, i.e., a known significant resistance will be serried with a glass sample, and measure the potential difference between the two ends of the known resistance. This known resistance is connected in series with the resistive material (glass). The general circuit diagram resembles Fig. 17, in which a glass sheet is placed between two electrodes and connected in series to the power supply and a resistance R.

Considering Fig. 17 and using Kirchhoff's laws, the following equation can be written:

$$V - IR - IR_s = 0 \xrightarrow{IR=\Delta V} R_s = \frac{V - \Delta V}{\frac{\Delta V}{R}}$$

Where R_s is the sample (glass) resistance, V is the voltage of the high-voltage power supply and ΔV is the potential difference between the two ends of the known resistance (R). Although the order of magnitude of the electric current intensity remains 10^{-9} amperes, by placing a resistance about 10^6 Ohm, the potential difference between the two ends of the series resistance (ΔV) will be $\sim 10^{-3}$ Volts, which can be measured easily.

$$V \approx 10^{-9}(A) \times 10^{6}(\Omega) \approx 10^{-3}(V)$$

The conduction process in glass seems very simple at first glance, but as we will see in the following sections, it has specific complexities. After connecting the power supply, an electric field is created between the electrode plates and inside the glass sheet. Positive and negative ions inside the glass move towards the electrodes due to the force of the electric field. Negative ions (usually oxygen) lose their electrons in proximity to the positive electrode and positive ions (such as sodium ions) absorb electrons and neutralize in proximity to the negative electrode. The current in the circuit is proportional to the neutralization rate of the ions.

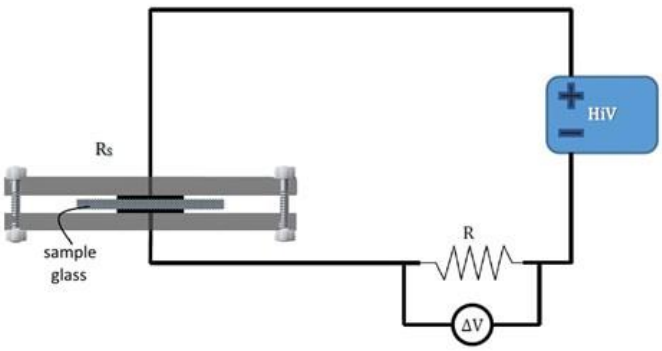

Fig. 17. Schematic of glass resistivity measurement setup

Experimental Setup of Resistivity Measuring

In this experiment, we want to measure the resistivity of a 2 mm thick glass sheet. According to the follow-ups, glass factories in Iran do not produce sheets with a thickness of less than 3 mm, and thin samples are mainly imported from Turkey. A piece of 70×70 mm2 was cut from a glass

sheet whose exact thickness was 2.07 mm for measuring resistance. To pass current through the sheet, it was sandwiched between two copper electrodes measuring 22×22 mm2 in cross-section. The electrodes were firmly attached to the glass using resistive sheets made of plexiglass (Fig. 17 and upper right image in Fig. 18). This structure reduces the possibility of leakage of current from the sides of that. The glass sample was connected in series with a 20 MΩ resistance. The resulting assembly was connected to a high-voltage power supply (PHYWE-10kV Power Supply). We used a simple voltmeter to measure the potential difference across the R (see Fig. 18).

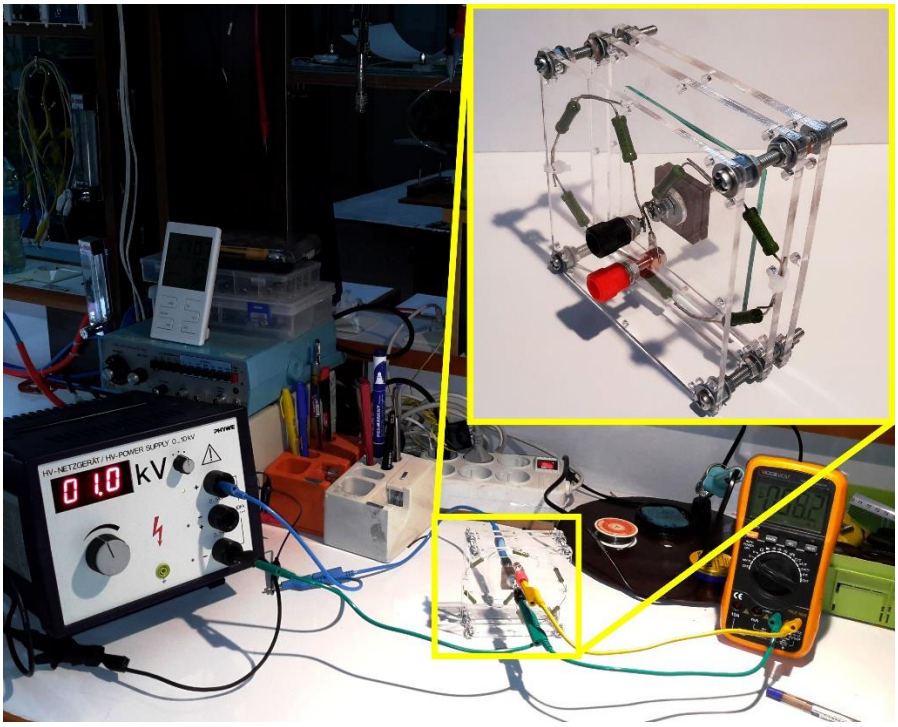

Fig. 18. Measurement setup for the resistivity of glass

After applying the power supply, the voltage across the R rapidly increases to a higher value. Then it decreases gradually over time (several tens of seconds) and eventually reaches a steady value with minor fluctuations. This initial transient or unstable state is considered the transition phase. To accurately record the changes in voltage across the resistance (which is proportional to the circuit current) over time and to repeat the experiment for different voltages, we need a circuit with data logging capabilities and higher measurement precision.

The method used to measure the volume resistivity of glass is based on the technique described in [7], with the addition of an ADC to record voltage values as a function of time. We need a current-

to-voltage converter to amplify and convert the small current into a voltage. This is done by considering the resistance R as negative feedback in an operational amplifier (TL082) circuit. The schematic of the circuit and the constructed board are shown in Fig. 19.

The experiment is repeated at eight different voltages between 0.5 to 4 kV (in 0.5 kV steps). The resistance values are then calculated using Ohm's law. The volume resistivity is finally computed using the sample dimensions and resistance values. This method allows the recording of transient changes during the initial phase and steady-state measurements with reasonable precision and accuracy. Multiple voltage levels can also be tested to study the effect of electric field intensity on conduction inside the glass sample.

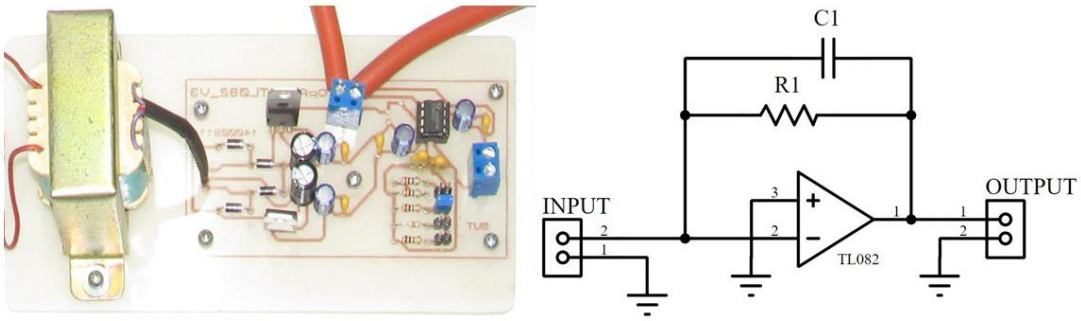

Fig. 19. The circuit for measuring current using an amplifier

Due to the small electric current values, switching power supplies will likely cause noise issues. In this circuit, a 220V to 12V symmetric transformer (positive and negative 12V) is used to power the Op-Amp. In noisy environments, it is better to use a battery. Appropriate filters must also be considered in the DC paths for ADC and Op-Amp power supply. Using ferrite beads, 100nF and 100uF capacitors can significantly reduce noise.

We have configured the ADC to measure for 10 minutes with a sampling frequency of 2 samples per second. Therefore, we can obtain the current-time curve from the moment the electric field is applied to the material under test, which is glass. The effect of electric field intensity on conduction inside the glass can be studied by repeating the measurements at different voltages. Fig. 20 shows the curves of measuring the electric current passing through the glass sample at several potential

differences. The initial higher current gradually decreases and stabilizes after some tens of seconds, showing the transition phase.

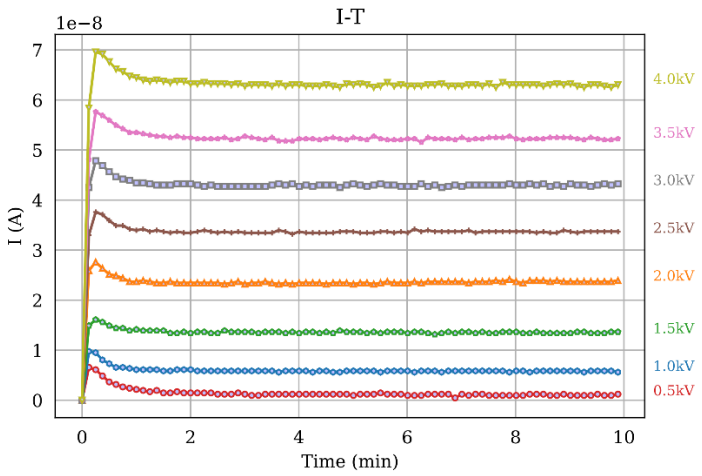

Fig. 20. Electric current as a function of time at eight different voltages

Results and discussion

Considering the transient behavior of the glass sample, we use the data from the last minute of data collection (120 final data points) to more accurately calculate the resistance and resistivity. As shown in Fig. 21, the resistance of glass exhibits nearly ohmic behavior, with the electric current increasing linearly with increasing potential difference. The resistance is obtained from the inverse of the slope of this curve, which is on the order of 10^{10} ohms for the glass sample measured.

By considering the electrode cross-sectional area (22×22 cm2) and glass thickness (2.07 mm), the volume resistivity can also be determined. The resistivity of the glass sample is $1.29 \pm 0.04 \times 10^{10}$ Ohm.m.

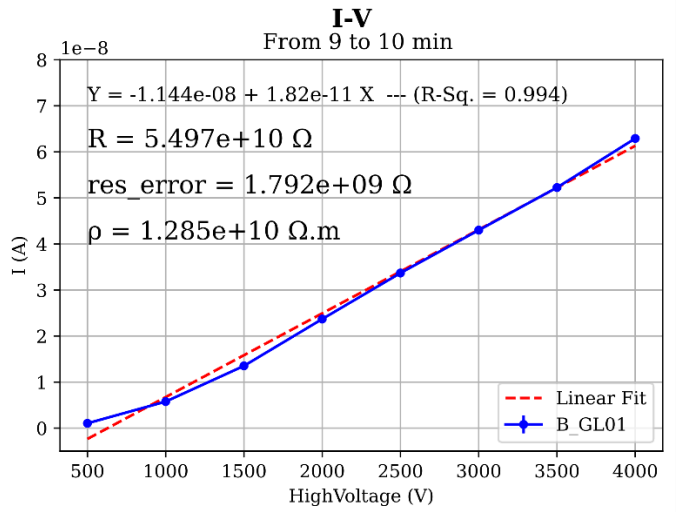

Fig. 21. The amount of resistance and resistivity of glass

Current decreases exponentially and tends to an asymptotic final value after a few tens of seconds. There is also a fluctuation in the current value. To find the asymptotic value of the current, we have to average the current value from a specific time and for a specific duration. Suppose we average the value of the current from t_1 to $t_2 = t_1 + \Delta t$, t_1 and Δt can be chosen wisely to minimize the error due to fluctuation and transient phase of the current.

For this purpose, the changes in error related to the resistance value were plotted for one-minute time intervals. Fig. 22 shows the curve of these changes. Therefore, based on the error analysis, the data can be reliably used for resistance calculation after a few minutes of applying the electric field. This analysis determines the transition or initial phase duration for the glass sample. The resistance value calculated after stabilization can be considered as the actual resistance of the glass.

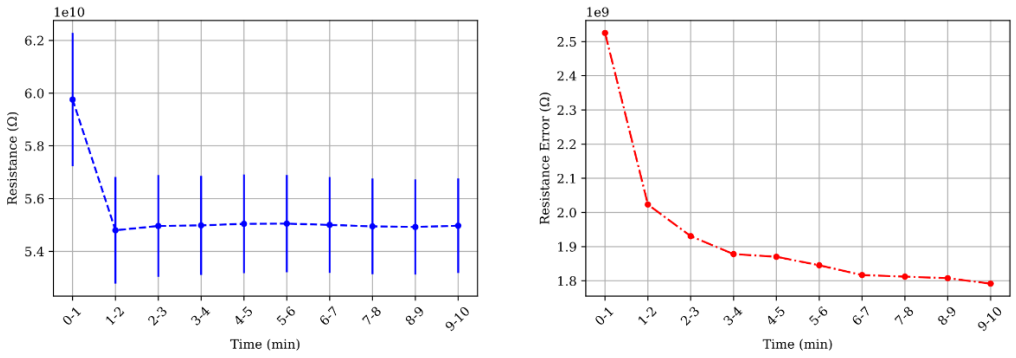

Fig. 22. Changes in the measurement error of the resistance of the glass according to the time of

application of the electric field

Conclusions

An experimental setup was designed and implemented to measure the resistivity of the glass. A transient behavior in the resistivity of glass was recorded. We observed an initial fast decreasing resistivity which tends to an asymptotic value. The obtained resistance and volume resistivity values can be used in detector design calculations and simulations. This experimental method can be extended to characterize other resistive materials.

References

[1] Abbrescia, M. Peskov, V. and Fonte P. (2018). Resistive Gaseous Detectors. Weinheim, Germany: Wiley. 53(9).

[2] Naumann, L. Kotte, R. Stach, D. and Wüstenfeld, J. (2010). Ceramics high rate timing RPC. Nucl. Instruments Methods Phys. 628(1):138–141.

[3] Liu, Z. et al. (2020). Novel low resistivity glass: MRPC detectors for ultra high rate applications. Nucl. Instruments Methods Phys. 959:163483.

[4] Pezeshkian, Y. and Ahmadpouri, M. (2021). Research Paper: Evaluating the Performance of a Resistive Plate Chamber by Measurement of the Detector's Count Rate. J. Appl. Phys. 11(4):38–56.

[5] Pezeshkian, Y. Kiyoumarsioskouei, A. Ahmadpouri, M. and Ghorbani, G. (2021). The gas flow pattern through small size Resistive Plate Chambers with 2 mm gap. J. Instrum., 16(11):11022.

[6] Raveendrababu, K. Behera, P. K. and Satyanarayana, B. (2016). Effect of electrical properties of glass electrodes on the performance of RPC detectors for the INO-ICAL experiment. J. Instrum. 11(08):P08024–P08024.

[7] Meghna, K. K. et al. (2012). Measurement of electrical properties of electrode materials for the bakelite Resistive Plate Chambers. J. Instrum. 7(10):P10003–P10003.

ICNST 2024
International Conference on Nuclear Science and Technology
6- 8 MAY 2024 | Isfahan, Iran

The Feasibility Evaluation of Backscattered Muons for Subsurface Imaging: A Monte Carlo Study (Paper ID: 1390)

Imani Z., Mohammadi N. * , Pezeshkian Y. *
Department of Physics, Sahand University of Technology, Sahand, Iran

Abstract

Cosmic muons are generated due to the interaction of cosmic rays and molecules of the atmosphere. They are the most penetrable charge particles owing to their low cross-section. Considering the budgetary and safety issues, muons have garnered significant attention for potential imaging applications. Recently, a variety of emerging applications for muography have been identified, with most falling into the categories of geoscience, civil engineering, archaeology, nuclear safety and security. In some studies, muons are proposed to be utilized for imaging the interior of geological underground structures by locating muon detectors below the structure using boreholes or tunnels. In this study, the possibility of using backscattered muons for subsurface imaging was evaluated. For this purpose, the mono energy muons of 1, and 3GeV were simulated using MCNPX code and transported through the soil thicknesses of 1m, and 100m. The results showed that up to 99% of incident high energy muons passed the soil. It seems that the rate of backscattered muons is not applicable for muon imaging of underground structures.

Keywords: Cosmic muons, Backscattered muons, MCNPX code, Imaging applications, Monte Carlo

Introduction

Muons, as charged particles, were discovered in 1936 at Caltech when Carl Anderson and Seth Neddermeyer were investigating cosmic rays [1]. They are fundamental particles similar to electrons, but are about 207 times heavier, because of their high average energy (on the order of a few gigaelectron volts at sea level, i.e. 10,000 times more than the energy of a normal X-ray) and low cross-section, they are so penetrating that they can pass hundreds of meters of rock. The source of muons is cosmic rays, which are a natural source, so there is no cost or energy required to produce them, and these particles are available indefinitely in terms of time. On the other hand, muons are considered safe according to health and safety regulations.

The proposed features of muons have drawn much attention to their use in imaging applications. In such a way that this technology has developed rapidly in the last two decades and is currently expanding to different fields. Most of the applications of muography can be classified in the categories of geological sciences, civil engineering, archeology, nuclear safety and security. In the field of archeology, for the first time in the 1960s, Luis Alvarez used muons to search for hidden chambers in the pyramid of Khufu in Egypt [2]. Even today, many studies are conducted to better understand the pyramids in Egypt using this technique, in this regard, we can refer to the study conducted in 2017 by Morishima and his colleagues [3]. Another application of muography is nuclear safety and security. Because nuclear materials and waste are safely stored in containers that are resistant to nuclear radiation, the same radiation cannot be used to image their contents. Therefore, the use of muon imaging in this field can be very beneficial. For the first time in 2009, the Department of Nuclear Physics at the University of Glasgow together with the British National Nuclear Laboratory (NNL) conducted studies related to the identification of protected nuclear waste containers using muon imaging [4]. Regarding the application in geological science, we can mention the imaging of the inside of volcanoes [5], [6], mine exploration and imaging of underground structures and monitoring of carbon or fuel storage underground [7]–[12]. Monitoring of underground carbon or fuel storage using muography often requires drilling a borehole to send the muon detector to the depths of the earth for imaging, which requires a lot of time and money. In the present study, the feasibility of using backscattered muons for imaging subsurface structures has been done through simulation.

Research Theories

Muons are relatively unstable particles that have a lifetime of 2.2 μs [13]. There are two types of charged muons with opposite charge (μ+, μ-) which decay into electron or positron and two neutrinos due to weak interaction [14].

$$\mu^+ \rightarrow e^+ \nu_e \bar{\nu}_\mu$$

$$\mu^- \rightarrow e^- \bar{\nu}_e \nu_\mu$$

Since muons are charged particles, before decaying, they lose about 2 MeV of energy by interacting with matter's atoms per gram per square centimeter through the processes of ionization,

bremsstrahlung, pair production, and inelastic interactions with the nucleus. At relatively low energies, ionization is the dominant process, while at high energies, ionization can be neglected, since in this case the decisive contribution to the energy loss is due to pair production and bremsstrahlung radiation [15], [16]

Materials and Methods

In this study, the simulation of the muons transport has been carried out using the Monte Carlo code of MCNPX 2.6. Since the mean energy of muons at the sea level is around 3 - 4 GeV [17], the mono energy muons of 1, and 3GeV were simulated as for this simulation muons of single energy a surface source with dimensions of 500 m × 500 m which entering the soil thicknesses of 1, and 100 m (d), (see Fig. 1). The soil density was set 1.74 g/cm3 and its composition used in MCNP input as

Table 7. The number of 2e9 muons were transported and the flux of passed muons was calculated using F1 tally.

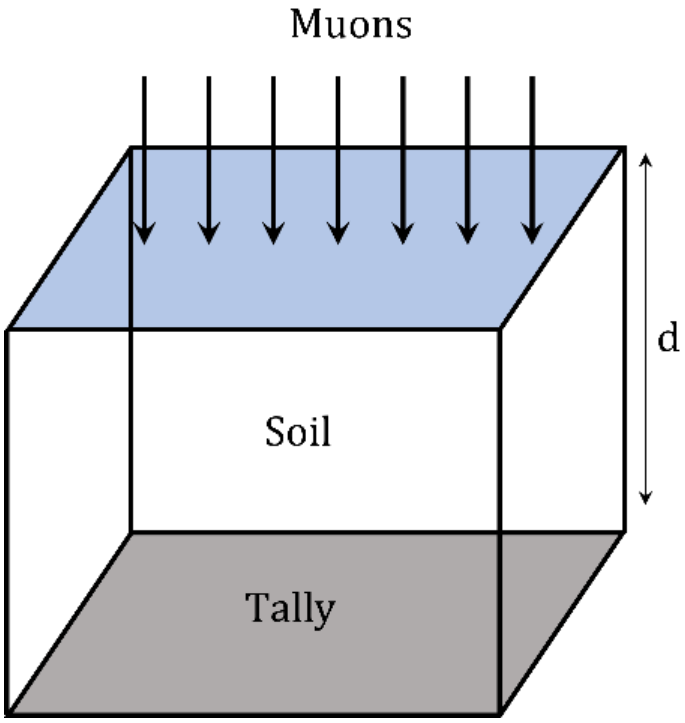

Fig. 1. Geometry of the performed simulation

Table 7. Soil constituent elements.

Element	Mass percentage (%)
O	53.6153
C	0.3360
H	0.7833
Si	36.5067
Al	3.4401
Fe	1.3289
K	1.1622
Ca	1.1212
Na	1.7063

Results and Discussion

According to the results of different inputs that were runned separately for energies of 1, and 3 GeV with thicknesses of 1, and 100 m of soil, the percentage of muons that escaped the soil, decayed, and interacted was calculated. The obtained results showed that for 1 GeV energy, with the increase in soil thickness, the number of muons that managed to escape from the soil decreased from 95.95% to 0.5% (see Fig. 2) while the number of decayed muons increased by 84.95% (see Fig. 3) and the inelastic interactions of muons in the soil decreased by 10.51% (see Fig. 4). Increasing the thickness of the soil has weakened the muon flux due to increased interactions with matter, resulting in a high proportion of muons decaying and some escaping from the soil. Similar results were observed for 3 GeV energy, as well. On the other hand, by increasing the energy from 1, to 3 GeV, the number of muons escaping from the soil has decreased from 0.5% to 0.23%, which can be attributed to an increase in interactions from 10.51% to 10.54% and an increase in the number of decayed muons from 89% to 89.23%. The value of F1 tally in Table 2 indicated that as soil thickness increases, the muon flux passing through the material per incident muon decreases, resulting in higher errors at 100 m thickness. To reduce this error, a larger number of muons must be simulated, which requires a significant amount of time. Therefore, utilizing passing muons is advisable for applications without time constraints for imaging.

In this investigation no backscattered muons were observed and the output of backscattered muons was zero, which is consistent with muon simulation results using the MUSIC code presented by Antonioli et al. Using this code, they investigated the propagation spectrum containing 100,000 muons with a minimum muon energy of 900 GeV through 3 km.w.e. In this investigation, results obtained for the angular distribution of the muon spectrum indicated that the number of muons scattered under high angles is close to zero [18]. According to these results, backscattered muons are unsuitable for subsurface imaging applications, while muons passing through matter can be utilized. However, some researchers such as Bonal have proposed and investigated this possibility for backscattered muons [19].

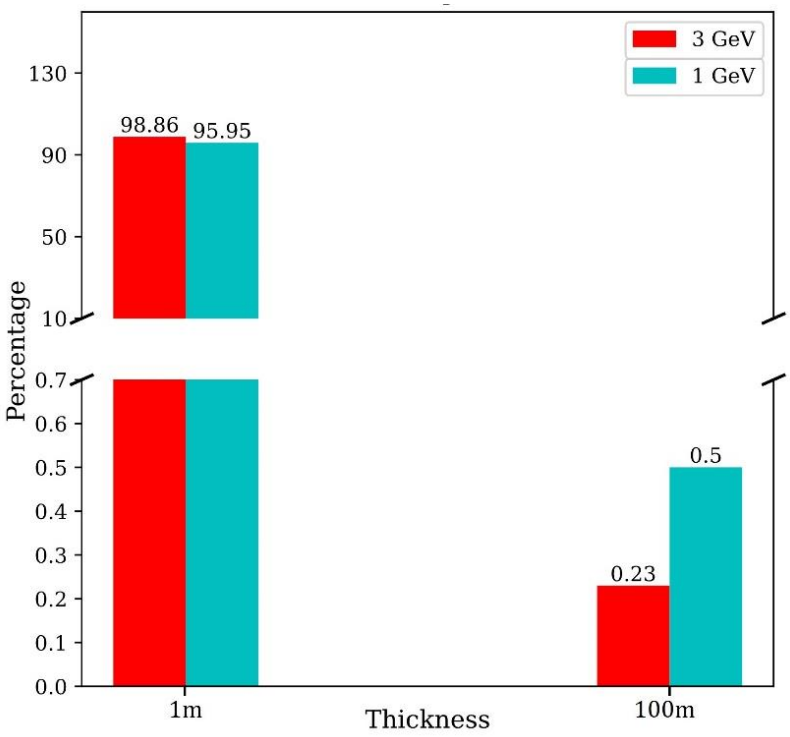

Fig. 2. Percentage of escaped muons from soil

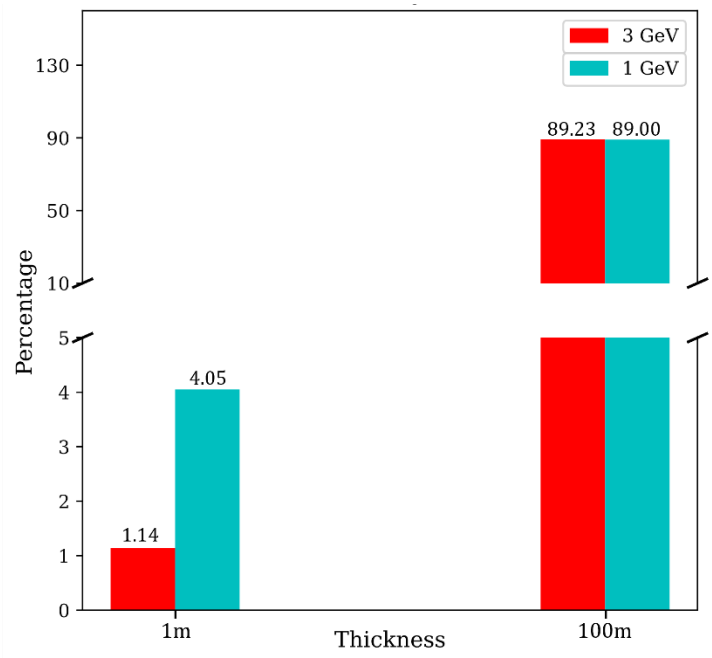

Fig. 3. Percentage of decayed muons in the soil.

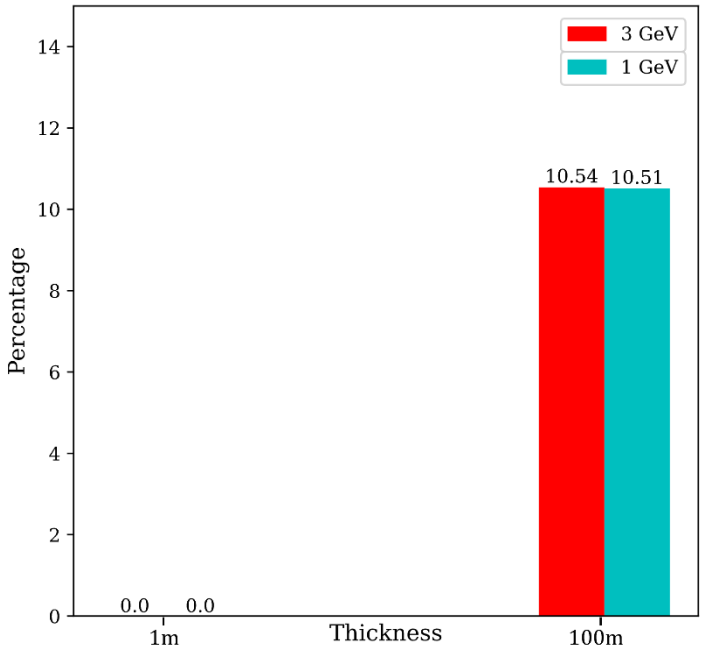

Fig. 4. Percentage of inelastic interaction of muons.

Table 8. Muon flux passed the soil.

Soil thickness (m)	Muon energy (GeV)	F1(muon/cm^2/incident muon	Relative error (%)
1	1	99.94×10^{-2}	10^{-5}
100	1	15.76×10^{-8}	15
1	3	99.98×10^{-2}	10^{-5}
100	3	85.76×10^{-9}	23

Conclusions

In this study, we used the MCNPX 2.6 code to simulate the passage of 1, and 3 GeV muons through soil with a density of 1.74 g/cm3 at thicknesses of 1, and 100 m. The results indicated that the escaped muon flux decreases with increasing soil thickness, from 95.95% to 0.23% for 1 GeV muons and from 98.86% to 0.5% for 3 GeV muons. Given the obtained results using of backscattered muons, are not reasonable for imaging subsurface targets. Furthermore, due to the muon flux reduction at higher thicknesses, utilizing passing muons for subsurface imaging will be

time-consuming. However, newer codes that use Monte Carlo may take into account more details of muon interactions and have more accurate simulations. Therefore, it is recommended to use other codes to verify the behavior of muons.

References

[1] R. Kaiser, "Muography: overview and future directions," Philos. Trans. R. Soc. A Math. Phys. Eng. Sci., vol. 377, no. 2137, p. 20180049, Jan. 2019, doi: 10.1098/rsta.2018.0049.
[2] L. W. Alvarez et al., "Search for Hidden Chambers in the Pyramids," Science (80-.)., vol. 167, no. 3919, pp. 832–839, Feb. 1970, doi: 10.1126/science.167.3919.832.
[3] K. Morishima et al., "Discovery of a big void in Khufu's Pyramid by observation of cosmic-ray muons," Nature, vol. 552, no. 7685, pp. 386–390, 2017, doi: 10.1038/nature24647.
[4] D. Mahon et al., "First-of-a-kind muography for nuclear waste characterization," Philos. Trans. R. Soc. A Math. Phys. Eng. Sci., vol. 377, no. 2137, p. 20180048, Jan. 2019, doi: 10.1098/rsta.2018.0048.
[5] H. K. M. Tanaka, "Japanese volcanoes visualized with muography," Philos. Trans. R. Soc. A Math. Phys. Eng. Sci., vol. 377, no. 2137, p. 20180142, Jan. 2019, doi: 10.1098/rsta.2018.0142.
[6] R. D'Alessandro et al., "Volcanoes in Italy and the role of muon radiography," Philos. Trans. R. Soc. A Math. Phys. Eng. Sci., vol. 377, no. 2137, p. 20180050, Jan. 2019, doi: 10.1098/rsta.2018.0050.
[7] D. Schouten, "Muon geotomography: selected case studies," Philos. Trans. R. Soc. A Math. Phys. Eng. Sci., vol. 377, no. 2137, p. 20180061, Jan. 2019, doi: 10.1098/rsta.2018.0061.
[8] A. Bonneville et al., "Borehole muography of subsurface reservoirs," Philos. Trans. R. Soc. A Math. Phys. Eng. Sci., vol. 377, no. 2137, p. 20180060, Jan. 2019, doi: 10.1098/rsta.2018.0060.
[9] D. Schouten, D. Furseth, and J. van Nieuwkoop, "Muon tomography for underground resources," in Muography: Exploring Earth's Subsurface with Elementary Particles, 2022, pp. 221–235. doi: 10.1002/9781119722748.ch16.
[10] J. Flygare, A. Bonneville, R. Kouzes, J. Yamaoka, and A. Lintereur, "Muon borehole detector design for use in 4-D density overburden monitoring," IEEE Trans. Nucl. Sci., vol. 65, no. 10, pp. 2724–2731, Oct. 2018, doi: 10.1109/TNS.2018.2869196.
[11] L. Cimmino, F. Ambrosino, M. D'Errico, V. Masone, L. Roscilli, and G. Saracino, "A novel cylindrical detector for borehole muon radiography.," J. Phys. Conf. Ser., vol. 2374, no. 1, p. 012189, Nov. 2022, doi: 10.1088/1742-6596/2374/1/012189.
[12] S. Pal et al., "Muon tomography for carbon storage and monitoring," in Springer Proceedings in Physics, B. Bhuyan, Ed., in Springer Proceedings in Physics, vol. 174. Cham: Springer International Publishing, 2016, pp. 479–485. doi: 10.1007/978-3-319-25619-1_73.
[13] M. G. Schmidt, F. E. Wietfeldt, and G. L. Greene, "n MASS (atomic mass units u)," vol. 010001, no. 2014, pp. 1–17, 2012.

[14] A. M. SACHS and A. SIRLIN, “Muon Decay,” Muon Phys., pp. 49–81, 1975, doi: 10.1016/b978-0-12-360602-0.50008-7.
[15] D. Chirkin and W. Rhode, “Muon Monte Carlo: A High-precision tool for muon propagation through matter,” 2004.
[16] F. Scheck, “Muon physics,” Phys. Rep., vol. 44, no. 4, pp. 187–248, 1978, doi: 10.1016/0370-1573(78)90014-5.
[17] R. M. Barnett et al., “Review of Particle Physics,” Phys. Rev. D, vol. 54, no. 1, pp. 1–708, Jul. 1996, doi: 10.1103/PhysRevD.54.1.
[18] P. Antonioli, C. Ghetti, E. V. Korolkova, V. A. Kudryavtsev, and G. Sartorelli, “A three-dimensional code for muon propagation through the rock: MUSIC,” Astropart. Phys., vol. 7, no. 4, pp. 357–368, Oct. 1997, doi: 10.1016/S0927-6505(97)00035-2.
[19] N. Bonal and L. A. Preston, “Feasibility of using backscattered muons for archeological imaging,” in AGU Fall Meeting Abstracts, 2013, pp. NS43B-07.

ICNST 2024
International Conference on Nuclear Science and Technology
6- 8 MAY 2024 | Isfahan, Iran

Calculating the received dose in the body organs due to the use of radiopharmaceuticals using the Geant4 tools (Paper ID: 1404)

Hosseini Sarteshnizi H., Zaki Dizaji H.*, Eshghi M., Hajiali E.
Department of Physics, Imam Hossein University, Tehran, Iran
Email: kpzaki@ihu.ac.ir

Abstract

Radioactive substances enter the human body in various ways, intentionally and unintentionally. The distribution of radioactive substances in the body depends on factors such as the way they enter the body, the amount of the infiltrated substance, its physical shape and size, and the type of chemical and biological relationship it has with the body.

The movement of radiopharmaceuticals in the body creates a dose in the adjacent organs and tissues. When radios are ingested, important organs are treated with radioactive material. Depending on the specific activity of the radiopharmaceutical and its duration in each organ, the amount of the created dose is also different. In the ICRP reports, there are many specifications of radiopharmaceuticals along with how long they remain in some organs of the body. In this article, using Monte Carlo tool Geant4 the forced dose created on body organs has been calculated. In the Monte Carlo method, taking into account the movement of the radioactive drug, the results have been extracted in more detail.

Keywords: Geant4, Monte Carlo, Dosimetry, Human Phantom, Radiopharmaceutical

Introduction

Internal contamination is the accumulation of radioactive materials in the body. The most important ways of penetration of radioactive materials into the body are inhalation, ingestion and penetration through wound beds into blood vessels [1]. Radioactive substances enter the body intentionally and in the form of nuclear medicine drugs and pills, or enter the body unintentionally as a result of being in environments contaminated with radioactive substances. The distribution of radioactive substances in the body depends on factors such as the way they enter the body, the amount of the infiltrated substance, its physical shape and size, and the type of chemical and biological relationship it has with the body [2]. When radioactive materials are ingested, a fraction of them will be absorbed and the rest will be excreted through feces. For chemicals that contain

tritium, iodine or cesium, the amount of absorption in the body is high, but for substances that contain plutonium and uranium, the absorption rate is low and they stay in the body for a shorter period of time [3, 4]. Due to their chemical structure, radioactive substances may accumulate in an organ of the body and emit nuclear radiation [5].

Nuclear radiation of radioactive substances inside the body causes a dose inside the body and its organs. Therefore, it is necessary to calculate the dose created in the internal organs of the body. Considering the danger of nuclear radiation and performing practical tests related to it, simulation and calculation methods, including the Monte Carlo method, are a safe and low-cost science in the field of internal dosimetry[6,7,8].

In this article, the Geant4 Monte Carlo tool was used to calculate the dose created in the gastrointestinal organs and some body organs by the radiopharmaceutical pills that were ingested.

Materials and Methods

Two radiopharmaceuticals ^{131}I and ^{67}Ga have been selected for investigation, which have energy spectra. ^{67}Ga is a gamma emitter, while ^{131}I is a beta emitter. However, ^{131}I decays to excited $^{131}Xe^{*}$ by beta emission, and excited $^{131}Xe^{*}$ decays to its ground state by gamma emission. The half-life of ^{131}I is 8.019 days, and the half-life of gallium-67 is 78.3 hours. In the simulation with Geant4 tool, the radiopharmaceuticals are listed as pills containing isotopes, whose geometric shape is cylindrical with a radius of 2.5 mm and a height of 10 mm. Now, in order to simulate the movement of the pill in the body and calculate the resulting dose, a human geometry including the human head and upper body has been simulated and is shown in Figure 1. The dimensions, weight, volume, Elemental compounds and density of each organ have been simulated using ICRP data . Also, in figure 1, the simulated mouth, esophagus, stomach, small intestine and large intestine are shown in which the pill containing the radiopharmaceutical moves linearly [9].

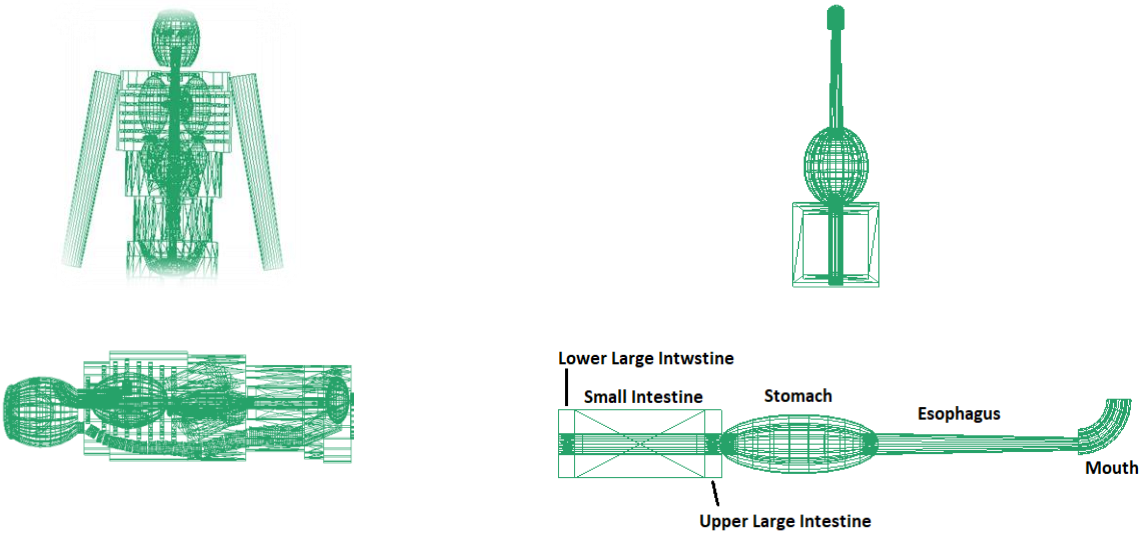

Fig. 1. Left, images of human geometry and Right, images related to the gastrointestinal system.

The shelf life of the tablet in each organ of the gastrointestinal system is shown in Table 1.

Table 1. The time the pill spends in each of the gastrointestinal organs[10].

Section of gastrointestinal tract	Mean residence time (h)
Stomach	1
Small intestine	4
Upper large intestine	13
Lower large intestine	24

Also, the mechanism of tablet movement in the gastrointestinal tract is shown in figure 2.

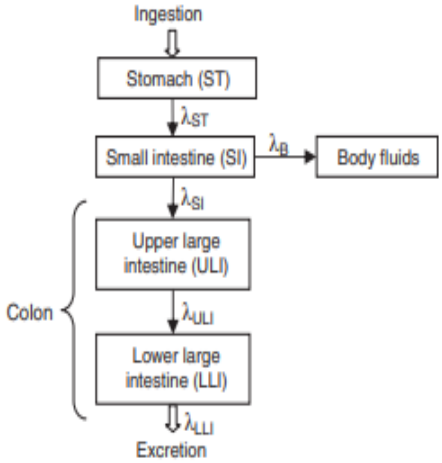

Fig. 2. The mechanism of tablet movement in the gastrointestinal tract[10]

According to the shelf life of the tablet in each of the digestive organs and the activity of the radioisotope and considering the half-life of the isotopes, the number of radioactive particles in each organ of the digestive system was calculated and entered as an input in the Geant4 tool. The pre-compiled reference FTFP_BERT library, encompassing a vast array of nuclear interactions, was employed for physics interactions.

Finally, the dose created by two radiopharmaceuticals ^{131}I and ^{67}Ga in digestive organs and some body organs has been calculated.

Results and Discussion

The activity of isotopes ^{131}I and ^{67}Ga is considered to be $0.1\ \mu Ci$ and the amount of dose created was calculated using the Geant4 tool and its results are shown in Table 2.

Table 2. Dose generated in body organs in Gy

Organs	^{67}Ga		^{131}I	
	Empty	Full of water	Empty	Full of water
Bladder	5.6355e-04	5.5847e-04	1.83820e-03	1.7376e-04
Brain	2.5e-07	1.3e-07	2.45e-06	6.5e-07
Esophagus	1.293e-05	8.75e-06	7.314e-05	2.637e-05
Head	1.9e-07	1.3e-07	1.80e-06	6.1e-07
Heart	3.48e-06	3.7e-06	2.492e-05	1.25e-05
Large Intestine	3.9139e-04	5.4591e-04	1.72591e-03	1.65414e-03
Left Adrenal	8.33e-06	1.309e-05	2.96e-06	3.95e-06
Left Kidney	1.556e-05	1.54e-05	1.218e-05	8.892e-05
Left Lung	3.72e-06	4.55e-06	4.73e-06	1.498e-05
Left Teste	1.2583e-04	1.2394e-04	4.2143e-04	3.8962e-04
Pancreas	2.329e-05	5.395e-05	1.7130e-04	3.7059e-04
Pelvis	2.9283e-04	3.1971e-04	6.4978e-04	6.3562e-04
Right Adrenal	8.39e-06	8.31e-06	2.95e-06	3.96e-06
Right Kidney	1.558e-05	1.416e-05	1.321e-05	8.878e-05
Right Lung	3.74e-06	4.55e-06	4.62e-06	1.523e-05
Right Teste	1.2585e-04	1.2299e-04	4.2139e-04	3.8954e-04
Ribcage	2.802e-05	2.788e-05	6.014e-05	6.313e-05
Spine's Bone	7.122e-05	6.88e-05	3.0667e-04	2.9164e-04
Small Intestine	4.7575e-04	7.0734e-04	2.70853e-03	2.09959e-03
Spleen	3.477e-05	1.1797e-04	3.4109e-04	3.275e-04
Stomach	1.5288e-04	1.2265e-04	4.3566e-04	3.4245e-04
Thyroid	1.5e-07	1.05e-06	9.32e-06	3.94e-06

Thymus	2.15e-06	2.15e-06	1.623e-05	7.01e-06
Trachea	1.5e-07	1.0e-07	1.36e-06	5.2e-07
Trunk	3.691e-05	5.296e-05	4.8807e-04	1.5879e-04

For each isotope, we have calculated the received dose in body organs twice. Once when the digestive tract, including the esophagus, stomach, small intestine, and large intestine, is empty, and once when the digestive tract is full of water.

As can be seen from the results, when the digestive system is full of water, the dose created in the organs is usually lower. This is especially true for isotope ^{131}I, because most of the beta rays are emitted from the isotope^{131}I They are stopped in the water or their energy is reduced. But in the case of isotope ^{67}Ga, because gamma rays are long-range, these changes are less.

The results show that the organs that were in the vicinity of the radio drug received a higher dose than the distant organs. In addition to the distance, the amount of time the radiopharmaceutical stays in any part of the body have an effect on the dose received in the surrounding organs. For example, the dose received in the lower organs of the body, such as the intestines, bladder and pelvis, is much higher than in the upper organs of the body, which is the reason for the high retention time of radiopharmaceuticals in the intestines.

As mentioned, the place of passage of the radiopharmaceutical has a direct effect on the amount of absorbed dose in the surrounding tissues. In figure 3, the absorbed dose in some organs of the body, in different locations of the radiopharmaceutical in the stomach, has been investigated.

Here, the stomach is in the form of an oval wall, the inner diameter of which is 9.6 cm. The dose created in the stomach and kidneys, and in cases where the radiopharmaceutical is located in different places in the stomach, i.e. from -4.8cm to +4.8cm from the center of the stomach, has been calculated. Then, the amount of dose created at each point is divided by the amount of dose created at the border point of the stomach wall, i.e. the point of ±4.8 cm, and the relative dose is calculated .Since the simulation sites are from the left side to the right side of the stomach, for this purpose, the relative dose produced in the kidneys, which are located on the left and right side of the stomach, has been calculated and is shown in figure 3 on the right side.

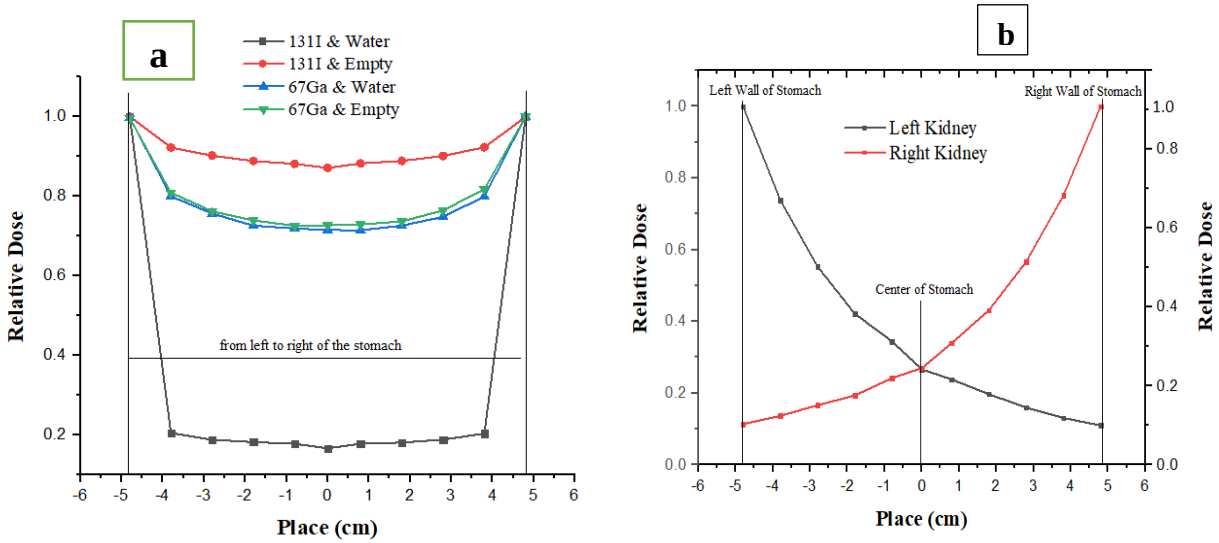

Fig. 3. a) Relative dose in the stomach and **b)** relative dose in kidneys According to the location of the radiopharmaceutical in the stomach

From figure 3, we can conclude that the amount of absorbed dose in the stomach decreases with the distance of the radiopharmaceutical from the stomach wall. And when the stomach is considered full of water, a lower dose is created in the stomach than when it is empty. In the case of radioisotope ^{131}I and when the stomach is full, by taking a distance from the stomach wall, the created dose is noticeably reduced, because the range of Beta particles is short and they are absorbed in water. But in the case of radioisotope ^{67}Ga, this is less common. Also, the relative dose created in the kidneys due to radiation of radioisotope ^{67}Ga across the stomach is shown in figure3 on the right. When the radiopharmaceutical is close to a right (left) kidney, the dose created in it increases (decreases) and vice versa. It seems that these increases and decreases are exponential.

Conclusions

Geant4 tool has high flexibility in the field of simulation. By applying more accurate conditions and making the simulations closer to reality, such as considering the movement of radiopharmaceuticals, more accurate and closer to reality results can be extracted.

According to the data in Table 2, it can be seen that the small intestine received the highest dose and the Trachea received the lowest dose. Of course, the threshold of radiation damage is different for each organ and tissue, and the risk of radiation damage and the expected consequences of

receiving a radiation dose, especially the possibility of possible and definitive effects of radiation can be determined.

References

[1] IAEA (2018). Medical management of persons internally contaminated with radionuclides in a nuclear or radiological emergency IAEA, Vienna, 2018

[2] IAEA (2004). Methods for assessing occupational radiation doses due to intakes of radionuclides. Vienna: International Atomic Energy Agency, 2004.

[3] ICRP 2006 Human alimentary tract model for radiological protection ICRP Publication 100; Ann. ICRP 36.

[4] Paquet F, Etherington G, Bailey MR, Leggett RW, Lipsztein J, Bolch W, Eckerman KF, Harrison JD; ICRP. ICRP Publication 130: Occupational Intakes of Radionuclides: Part 1. Ann ICRP. 2015 Sep;44(2):5-188

[5] Harrison J, Day P, Radiation doses and risks from internal emitters. J Radiol Prot. 2008 Jun;28(2):137-59.

[6] Lee Y, Hugot F, Current Status of TRIPOLI-4® Monte Carlo Radiation Transport Code on Adult and Pediatric Computational Phantoms for Radiation Dosimetry Study, Nuclear Science and Engineering, 2024, 198:2, 274-286.

[7] Massera R T, Tomal A, Thomson R M, Multiscale Monte Carlo simulations for dosimetry in x-ray breast imaging: Part II - Microscopic scales, Med Phys, 2024, 51:1117–1126.

[8]Kosaka T, Takatsu J, Inou T, Iijima K, Suzuki M, Murakami N, Shikama N, Dosimetric evaluation in Helical TomoTherapy for lung SBRT using Monte Carlo-based independent dose verification software, J Appl Clin Med Phys, 2024; 1-9

[9] ICRP. ICRP Publication ١١٠:Adult Reference Computational Phantoms. Ann ICRP. Volume 39 No. 2 2009.

[10] ICRP. ICRP Publication 128: Radiation Dose to Patients from Radiopharmaceuticals: A Compendium of Current Information Related to Frequently Used Substances. Ann ICRP. Volume 44 No. 2S 2015.

preliminary results of a proper sample for alpha time-of-flight measurement (Paper ID: 1423)

M. Azizi[1], M.R. Einian[1], B. Ghasemi[1]*, Z. Akbari[2]
[1] Nuclear engineering school, Shahid Beheshti University, Tehran, Iran.
[2]Physics & Accelerators Research School, Nuclear Science and Technology Research Institute, P. O. Box 14395-836, Tehran, Iran.

Abstract

Alpha-particles time-of-flight measurement is a method for spectrometry of alpha-particles with high energy resolution. To achieve high energy resolution in the measurement of the energy of alpha-particles, alpha sources should be prepared with good-quality. The requirements for good-quality sources include having a thin and homogeneous deposition with a smooth surface. Electrodeposition is one of the most common methods for preparing good-quality alpha sources. In this method, alpha-emitting nuclides are electrochemically plated with high yield from an electrolyte solution onto a metal backing. This paper describes a typical procedure for preparing a uranium source from a uranyl nitrate solution using the electrodeposition method. The procedure used is based on the ASTM standard practice C1284-05. After the alpha source was prepared, its characteristics were analyzed using digital alpha spectrometry by an ion-implanted Si detector. The obtained procedure will be used for the optimization of the required source for the-under construction Alpha Time-Of-Flight (A-TOF) spectrometer in Iran.

Keywords: Alpha time-of-flight, Alpha sources, Electrodeposition, Alpha spectrometry.

Introduction

The time-of-flight measurement of alpha particles is a method used for alpha particle spectrometry with high energy resolution. In order to achieve high energy resolution in the measurement of alpha particle energy, alpha sources should be prepared with good-quality. Several techniques have been developed to prepare alpha sources. These techniques include evaporation, microcoprecipitation, and electrodeposition [1]. Among these methods, electrodeposition is the most commonly utilized method for the preparation of good-quality sources, and it is widely employed in laboratories [2].

In the electrodeposition method, alpha-emitting nuclide, specifically actinide elements, is electrochemically plated onto a polished metal backing from either an organic or an aqueous electrolyte solution. The conventional setup for the electrodeposition typically involves a cylindrical cell, which is commonly made of materials such as Teflon, polyethylene, or plastic vials. Within the cell, a planar metallic cathode with a diameter of approximately 20-30 mm is positioned at the bottom, along with an anode [3]. The electrodeposition process is often carried out at a constant current density of 0.5 A.cm2 and a low voltage of less than 10 V, typically for a duration ranging from half an hour to two hours [1]. The aim of this study is to produce an alpha uranium source with good-quality using the electrodeposition technique. The electrodeposition process is affected by multiple factors, such as the material and surface quality of the cathode, and anode, the current density, the pH of the sample solution, and the deposition time. Jobba´gy et al. [4] provide a comprehensive analysis of the parameters that influence the electrodeposition. Hence, in this study, we used ASTM standard practice C1284-05 [5] and findings from previous research [3, 4] that proposed these parameters.

Experimental procedure

The steps involved in the electrodeposition method are depicted in Figure 1 and are explained in this section.

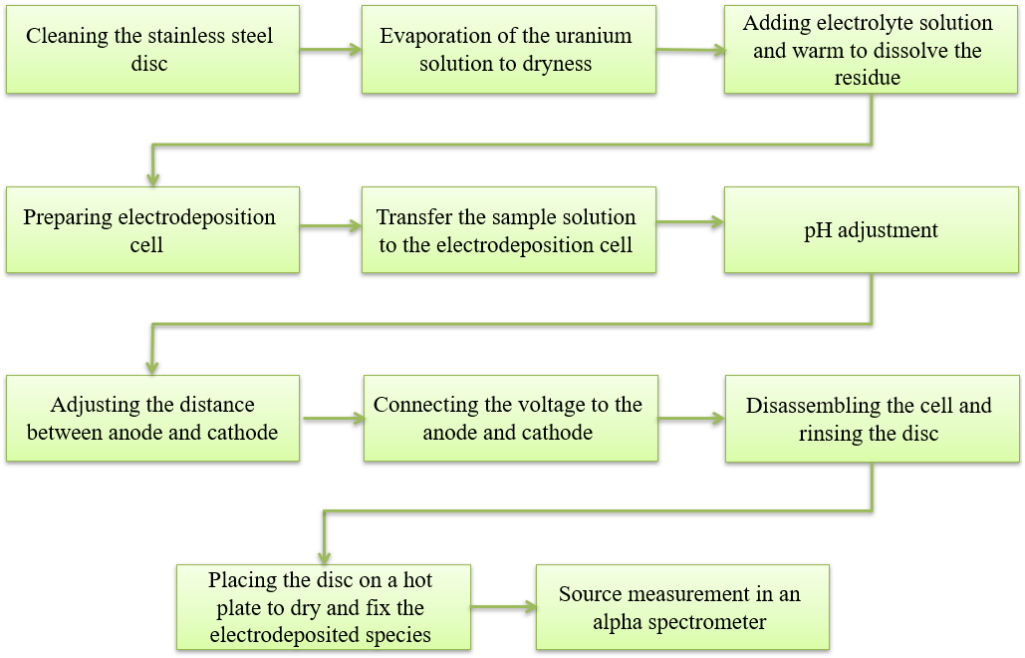

Fig. 1. A flow chart showing the steps of electrodeposition

2.1. Preparation of the backing and setup of electrodeposition cell

In this study, a stainless steel disc was utilized as the backing material. The importance of the glossy surface in deposition quality, including source thickness and homogeneity, has been emphasized in previous studies as well [3]. Consequently, the preparation of the backing involved several steps. Initially, the protective plastic tape was removed from the surface of the disc. Subsequently, diamond polishing paste was used to polish it. The surface of the backing was then rinsed with acetone and cleaned with deionized water to eliminate any remnants of grease. Figure 2 depicts an image of a thoroughly cleaned and polished stainless steel disc.

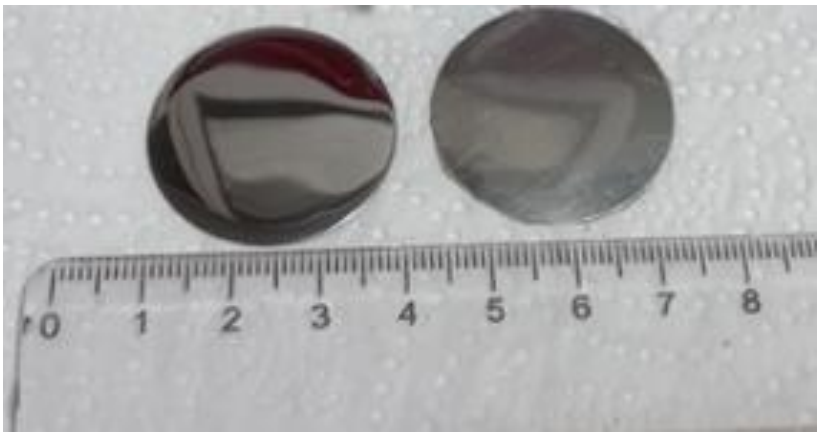

Fig. 2. Stainless steel disc used as source support (right: before polishing and left: After polishing).

The anode material also affects the electrodeposition process. Usually, a platinum (Pt) anode is employed for electrodeposition. In this study, a platinum wire measuring 1.5 mm in diameter and 100 mm in length was utilized as the anode. The cathode is positioned within an electrodeposition cell, which is a plastic vial. The cell was visually inspected for any leaks by filling it with deionized water. Figure 3 shows the assembled electrodeposition cell.

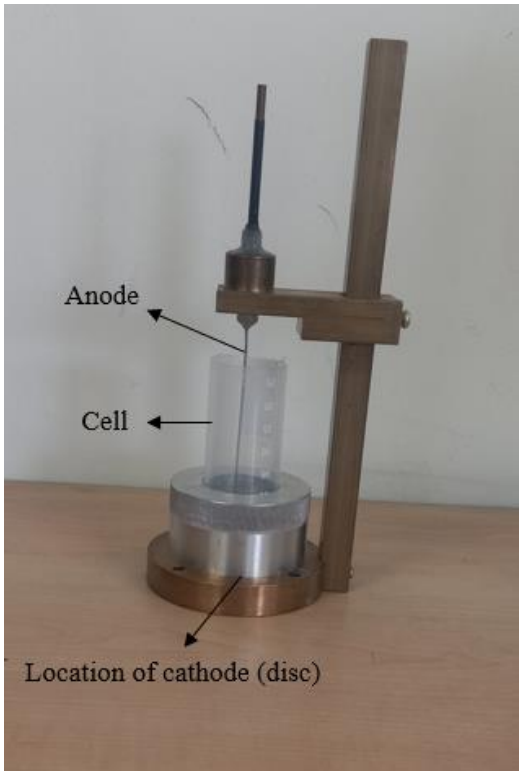

Fig. 3. The setup of the electrodeposition cell.

2.2. Preparation of the sample solution and the electrodeposition process

An aliquot of the Uranyl nitrate solution (1 ml) was transferred into a glass beaker and placed on a hot plate. The solution was evaporated to dryness. Then, 2 ml of concentrated HNO_3 and 0.5 ml of concentrated H_2SO_4 were added to the beaker. The beaker was returned to the hot plate, and the solution was evaporated until only a few drops remained but not baked. The beaker was then removed from the heat and allowed to cool slightly. Following that, 2-3 drops of an aqueous reagent containing Thymol blue were introduced into the beaker. The inner wall of the beaker was rinsed with 3 ml of distilled water. While stirring the solution, a small amount of concentrated NH_4OH solution was gradually added to adjust the pH of the solution to approximately 4. It is important to note that all the chemicals used, such as HNO_3, NH_4OH, and H_2SO_4, were of analytical grade.

The sample solution was transferred into the electrodeposition cell. The beaker was rinsed three times, each time with 2 ml of 1:99 H_2SO_4, and the rinsings were added to the electrodeposition cell. During this step, the pH of the solution was measured using a digital pH meter. If the pH was

below 2, it was gradually adjusted within the range of 2-2.4 by adding NH_4OH solution slowly (Figure 4). It is important to note that the pH of the electrolyte greatly affects the electrodeposition yield, as mentioned in [6] reference. At a low pH (pH < 2), the deposited uranium layer can be redissolved into the electrolyte. On the other hand, at higher pH values (pH > 4), it forms hydroxide complexes with varying stoichiometry, impeding its deposition [4].

(a) (b)

Fig. 4. Calibration of pH-meter using the buffer solution (a) and pH adjustment of the sample solution in the range of 2-2.4 (b)

The platinum anode was inserted in the solution. The distance between the anode and the stainless steel backing cathode was set to 1 cm. The experimental arrangement used for the electrodeposition process is shown in Figure 5. The anode is inserted into the solution. The distance between the anode and the stainless steel backing cathode was adjusted to 1 cm. The cathode and anode electrodes were connected to the base of the electrodeposition cell and the platinum anode, respectively. To achieve an approximate current density of 0.5 A.cm-2 over the disc area, the electric current was adjusted to 0.96 A.

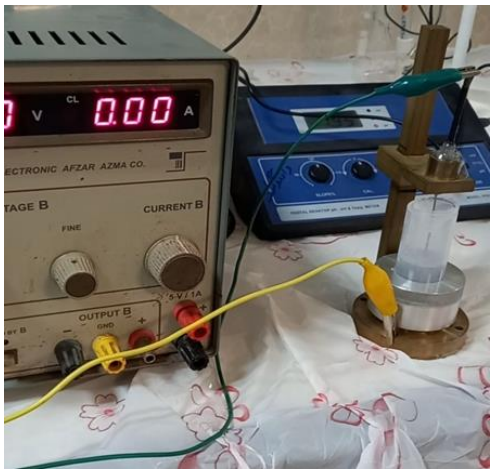

Fig. 5. Experimental setup of the electrodeposition cell

Electrodeposition was carried out at a constant current for 60 minutes. Then, 1 ml of concentrated NH_4OH was introduced into the cell, and electrodeposition continued for an additional 1 minute. The addition of concentrated NH_4OH results in an alkali shift in pH, preventing uranium re-dissolution from the deposit [4]. The settings applied for the electrodeposition are listed in Table 1.

Table 1. Settings applied for the electrodeposition.

Parameters	Optimized value
Deposition time (min)	60
Current (A)	0.97
Voltage (V)	<10
Source diameter (mm)	30
Deposition diameter (mm)	16
Cathode to anode distance (mm)	10
Backing material	Stainless steel

After the anode was removed and the current was turned off, the solution was discharged. Subsequently, the electrodeposition cell was disassembled, and the disc was rinsed with distilled water. Following this, the disc was placed on a hot plate set at 200°C to stabilize and dry the species deposited through the process of electrodeposition.

Results and Discussion

Figure 6 shows the sources prepared using this method. The deposited species have been well stabilized on the backing surface. To measure the source, a vacuum chamber with an ion-implanted Si detector was utilized. The detector had an active area of 100 mm2. The measurement setup involved a preamplifier and a digitizer (CAEN DT5724). The digitizer directly samples the output of the preamplifier of the detector. The MC2 software records the energy of each detected event in a text file. Figure 7 presents the setup of the alpha spectrometry setup.

Fig. 6. Sources prepared using electrodeposition method

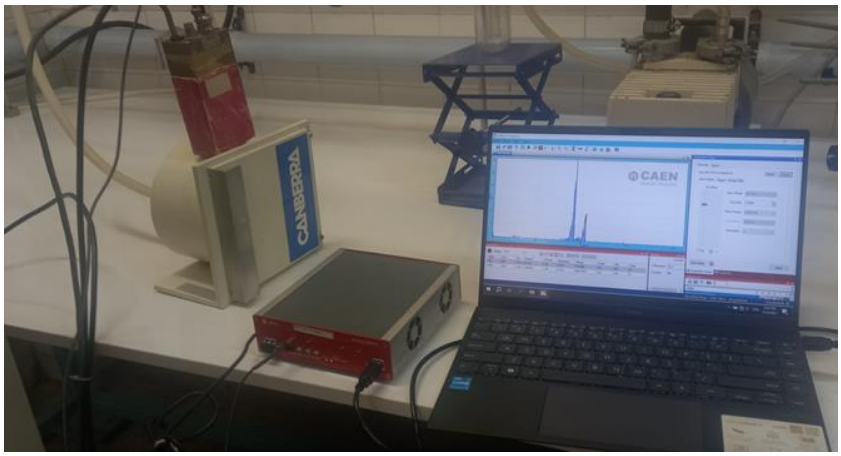

Fig. 7. Alpha spectrometry setup using digital pulse processing.

A mixed nuclide source containing Pu-239, Am-241, and Cm-244 was utilized for the energy calibration of the spectrometer. The energy spectrum of the mixed nuclide energy calibration source obtained with the ion-implanted Si detector is shown in Figure 8. Subsequently, the

prepared source was positioned within the vacuum chamber, and data collection was carried out for 10 hours. The measured spectrum is shown in Figure 9.

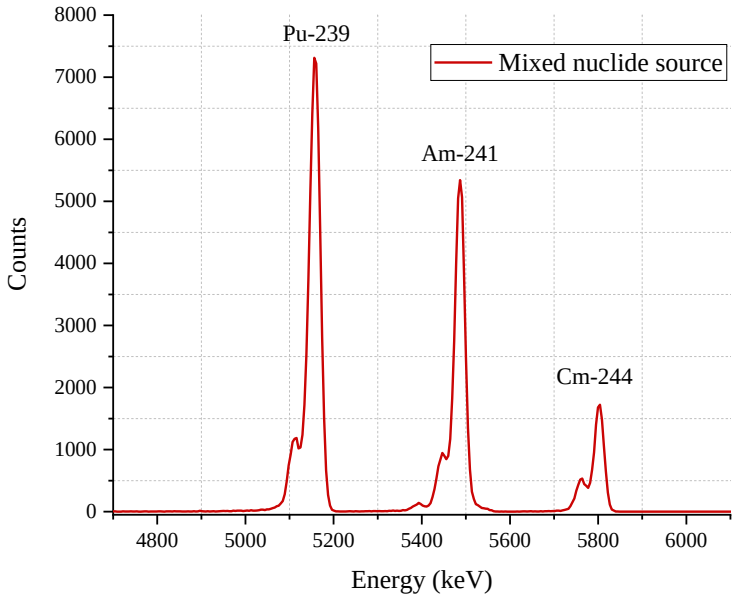

Fig. 8. Energy spectrum of the mixed nuclide energy calibration source obtained with the ion-implanted Si detector

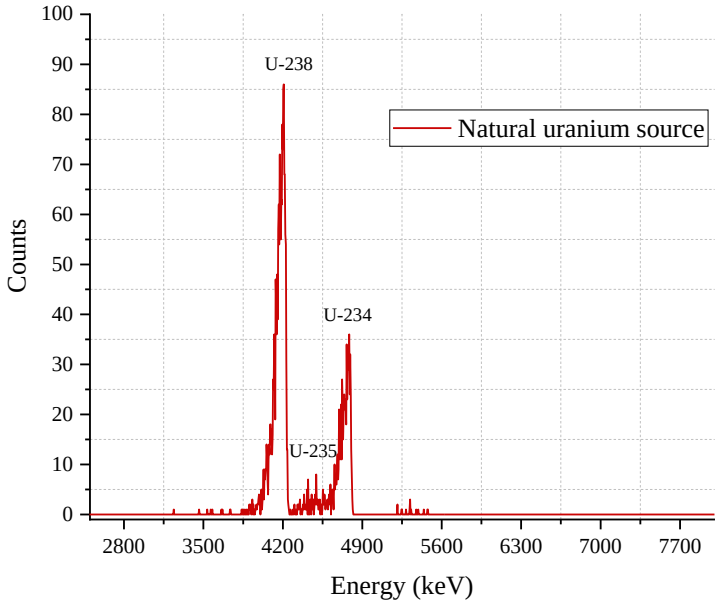

Fig. 9. Energy spectrum of uranium source obtained with ion-implanted Si detector

Figure 9 clearly shows the distinct peaks corresponding to the isotopes U-238, U-235, and U-234 at 4198, 4395, and 4774 keV energy line respectively. To obtain the required statistics in the counting, a longer measurement time is essential.

Conclusions

In this work, a typical procedure for preparing an alpha uranium source for the characteristics optimization of the-under construction alpha time-of-flight spectrometer was used. Considering that many parameters affect the efficiency of electrodeposition, we incorporated the findings of other researchers to produce a good-quality alpha source. Following the preparation of the source, alpha spectrometry was employed for its characterization. In future studies, we aim to use additional analysis such as Rutherford Backscattering Spectrometry (RBS) to gather information on the composition and surface properties of the electrodeposited alpha sources.

References

1. Vajda, N., et al., Alpha spectrometry, in Handbook of radioactivity analysis. 2020, Elsevier. p. 493-573.
2. Da Cruz, P. and R. Poledna, Alpha-source preparation by electrodeposition. Nuclear Instruments and Methods in Physics Research Section A: Accelerators, Spectrometers, Detectors and Associated Equipment, 1990. 286(3): p. 453-456.
3. Crespo, M., A review of electrodeposition methods for the preparation of alpha-radiation sources. Applied Radiation and Isotopes, 2012. 70(1): p. 210-215.
4. Jobbágy, V., et al., Preparation of high-resolution 238 U α-sources by electrodeposition: a comprehensive study. Journal of Radioanalytical and Nuclear Chemistry, 2013. 298: p. 345-352.
5. Standard Practice for Electrodeposition of the Actinides for Alpha Spectrometry. ASTM C1284-05, 2005.
6. Maya, L., et al., Electrodeposition of uranium dioxide films. Journal of radioanalytical and nuclear chemistry, 2004. 261(3): p. 605-607.

ICNST 2024
International Conference on Nuclear Science and Technology
6- 8 MAY 2024 | Isfahan, Iran

Investigating dispersion of Cesium 137 released from the Bushehr nuclear reactor in a hypothetical accident (Paper ID: 1427)

Nemati K. [1*], Shaiste S. [1]

[1] *Department of Physics, Faculty of Basic Sciences, Imam Hossein University, P.O.BOX: 1698715461, Tehran, Iran*

Abstract

Usually, the focus of programs and actions in various incidents is on implementing measures to combat leakage and the release of radioactive materials. The consequences of radiation incidents lead to the release of radiation and radioactive substances in the environment, leaving their effects on the environment and living organisms in different ways. Forecasting, estimating, and performing calculations related to the consequences of incidents, the amount of radioactive material released, the level of radiation generated, the dose absorbed by humans, etc., are among the actions that take place in the field of modeling the consequences of radiation incidents. These calculations can be carried out manually using existing relationships or by utilizing software developed in this field.

Consequence modeling can be conducted before, during, and after the incident to extract the required information. In this study, it was assumed that an incident occurred at a specific time in the Bushehr nuclear reactor, and all radioactive Cs-137 present in the reactor core entered the atmosphere within the first hour. The atmospheric distribution of this isotope was then examined using meteorological data relevant to the moment of the incident for up to 12 hours. Subsequently, the effective cumulative total dose, cumulative total thyroid dose, inhalation committed effective dose (CEDE), open window external dose rate, and closed window external dose rate were calculated, and a graph depicting their changes at a distance of 80 kilometers from the incident site was plotted.

Keywords: Bushehr Nuclear Reactor, RASCAL Code, Dose, Radionuclide, Cs-137

Introduction

The safety standards defined for nuclear reactors are consistently set at the highest levels, and they are rigorously enforced by official international organizations such as the International Atomic

Energy Agency. As a result, the likelihood of all radioactive isotopes in the reactor core entering the atmosphere due to a technical accident or human error is very low [1].

Typically, the focus of programs and actions in various incidents is on implementing measures to combat leakage and the release of radioactive materials. The consequences of radiation incidents lead to the release of radiation and radioactive substances into the environment, leaving their effects on the environment and living organisms in different ways. Forecasting, estimating, and performing calculations related to the consequences of incidents, including the quantity of radioactive material released, the level of radiation generated, the dose absorbed by humans, etc., are among the actions that take place in the field of modeling the consequences of radiation incidents. These calculations can be carried out manually using existing relationships or by utilizing software developed in this field.

Consequence modeling can be conducted before, during, and after the incident to extract the required information.

Nuclear reactors, alongside their important capabilities, can have detrimental effects on human health, other living organisms, and the environment in the event of accidents and insufficient safety measures. Among the most notable radiation incidents, the Three Mile Island power plant [2], Chernobyl power plant [3], and Fukushima power plant [4] can be mentioned. Following the occurrence of these nuclear accidents, various types of radioisotopes present in the damaged reactors core of these power plants have spread to the surrounding environment and have spread to very large areas through weather currents. Various researches have been conducted to investigate the amount and manner of distribution of these radioisotopes [5]. Mr. Junjikai and his colleagues evaluated the distribution of released radionuclides and dose in an area of the Great China Bay by simulating a nuclear accident [6]. In another research activity, Oleg Skrynik and his colleagues used HYSPLIT software to investigate the atmospheric release of Cs-137 caused by the Chernobyl nuclear power plant accident [7]. By Mr. Ahmad Pirouzmand and his colleagues, the atmospheric dispersion of radioactive materials caused by the hypothetical incident of the Bushehr nuclear power plant was carried out using the HYSPLIT code [8].

Introducing RASCAL software

RASCAL, short for Radiological Assessment System for Consequence Analysis, is a software developed by the US Nuclear Regulatory Commission (NRC) Emergency Operations Center to assess the release of radioactive materials in emergency conditions and during incidents. The software calculations are based on current and accurate equations and are designed to consider the worst-case scenario. As a fundamental goal, the software aims to minimize human exposure to radioactive materials to the lowest achievable level. RASCAL software includes two main tools: Source-Term to Dose (STD) and Field Measurement to Dose model (FMD) [9].

This software is designed to be applicable in various scenarios within nuclear facilities, demonstrating acceptable generality and efficiency in modeling the consequences of radiation incidents. Pressurized water and boiling water nuclear reactors, enrichment and processing facilities, as well as fuel manufacturing and spent fuel storage centers, are among the facilities for which this software is specifically designed to model accident consequences. The calculation error in the results of the RASCAL software is less than 3% [5].

Familiarity with Bushehr nuclear reactor:

The Bushehr reactor is a Russian VVER-1000 model, and its specifications are detailed in Table 1. The reactor's fuel consists of uranium oxide with enrichments of 2.4%, 1.6%, and 3.6%. Control of this reactor is achieved through the movement mechanism of the control rods, water-soluble chemicals, boric acid with a specific concentration, and poisons with defined percentages. The reactor is equipped with various groups of control rods, each with different reactivity values. During start-up, only 10% of the control rods, equivalent to 35 cm of its active length, enter the core, distributed across 6 fuel assemblies within the core [10] [11].

Table 1. Specifications of Bushehr Reactor (VVER[4]-1000 Reactor)[12]

Title	Value
Reactor Nominal Thermal Power	3000 MWth
Electric power	1000 MWe
Number of FA in the core, pcs.	163
Type of fuel complex	Hexagonal
The number of fuel rods in each complex	311
Cooling flow rate	84800 m^3/h

[4] **Voda Voda Energo Reactor**

In table 2, all the fission fragments in the Bushehr reactor core along with their activity and half-life values are mentioned.

Table2. The isotopes in the Russian reactor core [VVER] or PWR of Type the 1000Mwe[13]

				Radioactivity	
		Nuclide	Half-life (days)	(Bq*10^{18})	(MCi)
Noble Gases	Krypton	^{85}Kr	3950	2.072	56
		^{85m}Kr	0.183	0.888	4
		^{87}Kr	0.0528	1.739	47
		^{88}Kr	0.117	2.516	68
	Xenon	^{130}Xe	5.28	6.29	170
		^{13}Xe	0.384	1.258	34
	Iodine	^{131}I	8.05	3.145	85
		^{132}I	0.0958	4.44	120
		^{133}I	0.875	6.29	170
		^{134}I	0.0366	7.03	190
		^{135}I	0.28	5.55	150
caesium & Rubidium	caesium	^{134}Cs	750	0.2775	7.5
		^{136}Cs	13	0.111	3
		^{137}Cs	11000	0.1739	4.7
	Rubidium	^{86}Rb	18.7	0.00096	0.026
Tellurium & Antimony	Tellurium	^{127}Te	0.391	0.2183	5.9
		^{127m}Te	109	0.0407	1.1
		^{129}Te	0.048	1.147	31
		^{129m}Te	0.34	0.1961	5.3
		^{131m}Te	1.25	0.481	13
		^{132}Te	3.25	4.44	120
	Antimony	^{127}Sb	3.88	0.2257	6.1
		^{129}Sb	0.179	1.221	33
Alkaline Earths	Strontium	^{89}Sr	52.1	3.478	94
		^{90}Sr	11030	0.1369	3.7
		^{91}Sr	0.403	4.07	110
	Barium	^{140}Ba	12.8	5.92	160
Volatile Oxides	Cobalt	^{58}Co	71	0.02886	0.78
		^{60}Co	1920	0.01073	0.29
	Molybdenum	^{99}Mo	2.8	5.92	160
	Technetium	^{99m}Tc	0.25	5.18	140
	Ruthenium	^{103}Ru	39.5	4.07	110
		^{105}Ru	0.185	2.664	72
		^{106}Ru	366	0.925	25
		^{107}Ru	1.5	1.813	49
Non-volatile Oxides	Yttrium	^{90}Y	2.67	0.1443	3.9
		^{91}Y	59	4.44	120
	Zirconium	^{95}Zr	65.2	5.55	150
		^{97}Zr	0.71	5.55	150
	Niobium	^{95}Nb	35	5.55	150
	Lanthanum	^{140}La	1.67	5.92	160
	Cerium	^{141}Ce	32.3	5.55	150
		^{143}Ce	1.38	4.81	130
		^{144}Ce	284	3.145	85

Praseodymium	^{143}Pr	13.7	4.81	130
Neodymium	^{147}Nd	11.1	2.22	60
Neptunium	^{239}Np	2.35	60.68	1640
Plutonium	^{238}Pu	32500	0.002109	0.057

Among all the isotopes in the reactor core, Cs-137 is considered more significant than other isotopes in terms of biological effects [14]. This is due to its considerable half-life, volatility, and the fact that once released into the atmosphere, it will persist in the surface layers of the soil for an extended period, emitting radiation.

Table 3. The amount of Cs-137 and Iodine-131 in the reactor core during the hypothetical accident[5]

	half-life	Activity (Ci)
Cz-137	30 years	4.7x106
I-131	8 days	8.5×107

In this article, we have assumed that in the event of an incident, such as a military attack, all protective and safety systems are disabled, and physical barriers are destroyed. As a result, all isotopes present in the reactor core are released into the open space and dispersed in the environment. Nuclear contaminants (cesium-137) were released at the Bushehr nuclear power plant, located at 50.886944° latitude and 28.828889° longitude, with a release rate of 4.7 MCi/h for one hour, and a release height of 183m was considered. The release height is the altitude at which the contaminants settle after being released into the environment.

Results and discussion

For the calculation of the dispersion and direction of radioactive materials in this study, meteorological data for the specified geographical point were obtained from table number 4 on the meteorological organization's website.

Table 4. Meteorological input data for performing RASCAL code calculations

Date	Time (UTC)	Temperature	Pressure	dew point	Wind speed	Wind direction
01.21.2023	09:00	21°c	1020.30 hPa	11° c	9 m/s	Northwest
01.21.2023	12:00	21°c	1018.50 hPa	12° c	11 m/s	Northwest
01.21.2023	15:00	19°c	1019.10 hPa	11° c	5 m/s	Northwest
01.21.2023	18:00	19°c	1020.00 hPa	11° c	3 m/s	Northwest

The range of atmospheric dispersion of Cs-137 and I-131 isotopes and their biological effects due to a hypothetical incident, such as a military attack on the Bushehr nuclear power plant, where all cesium and iodine radionuclides present in the reactor core are released into the atmosphere within the first hour, along with the relevant meteorological data at the time of the incident until 12 hours afterwards, along with the maximum dose range and related graphs, were obtained using the RASCAL software.

Table 5. The maximum dose (rem) up to a distance of 80 km calculated by the RASCAL code

Dist from release	miles (kilometers)	15 (24.1)	20 (32.2)	30 (48.3)	40 (64.4)	50 (80.5)
	Total EDE	8.8E+01	4.9E+01	2.6E+01	2.0E+01	1.3E+01
	Thyroid CDE	2.5E+03	1.4E+03	7.2E+02	5.5E+02	3.8E+02
	Acute Lung	3.8E+01	2.1E+01	1.1E+01	8.4E+00	5.8E+00
	Total Acute Bone	2.0E+00	1.1E+00	5.7E-01	4.3E-01	3.0E-01
	Inhalation CEDE	7.9E+01	4.4E+01	2.3E+01	1.8E+01	1.2E+01
	Cloud Shine	4.1E-01	2.3E-01	1.3E-01	9.9E-02	7.6E-02
	Period Gnd Shine	1.2E+00	6.4E-01	3.2E-01	2.4E-01	1.6E-01
	4-day Ground Shine	8.7E+00	4.8E+00	2.5E+00	1.9E+00	1.3E+00

Notes:
1. Doses exceeding PAGs are underlined.
2. Early-Phase PAGs: TEDE - 1 rem, Thyroid CDE - 5 rem
3. *** indicates values less than 0.1 mrem
   To view all values - use Detailed Results | Numeric Table
4. Total EDE = CEDE Inhalation + Cloud Shine + 4-Day Ground Shine
5. Total Acute Bone = Bone Inhalation + Cloud Shine + Period Ground Shine Window

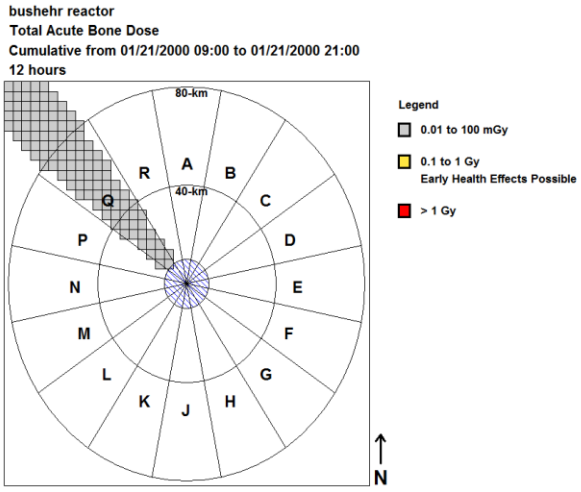

Fig. 1. Total Acute Bone Dose

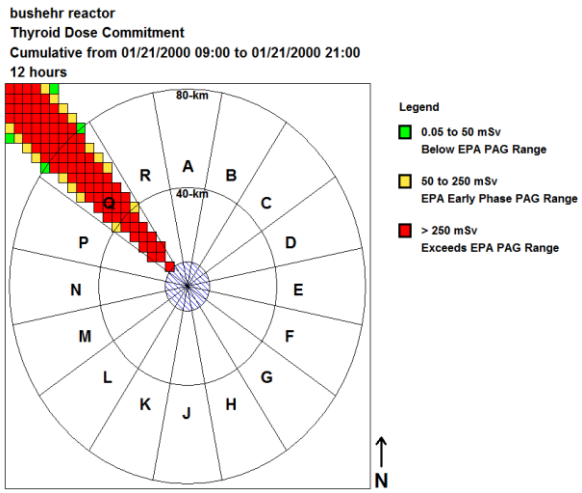

Fig. 2. Thyroid Dose Commitment

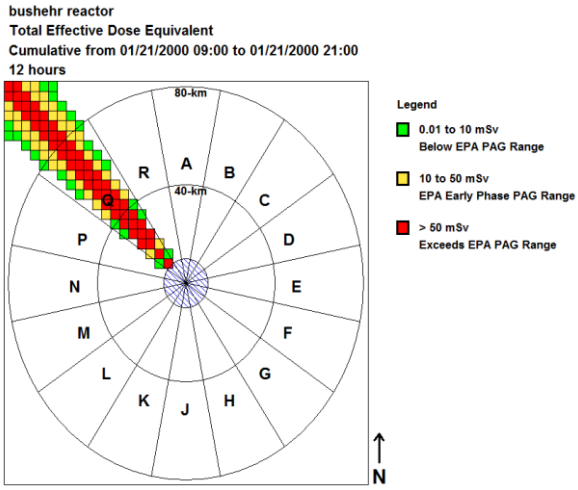

Fig. 3. Total Effective Dose Equivalent

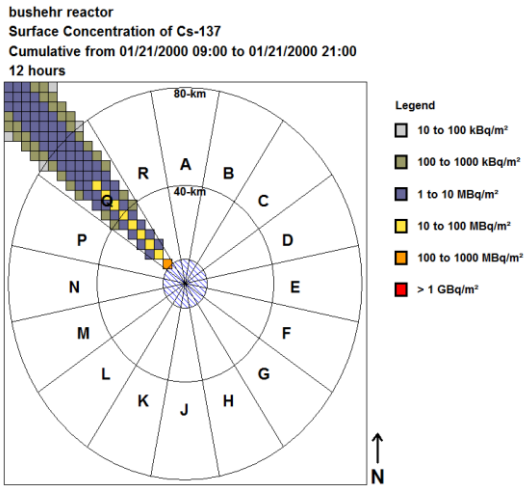

Fig. 4. Surface Concentration of Cs-137

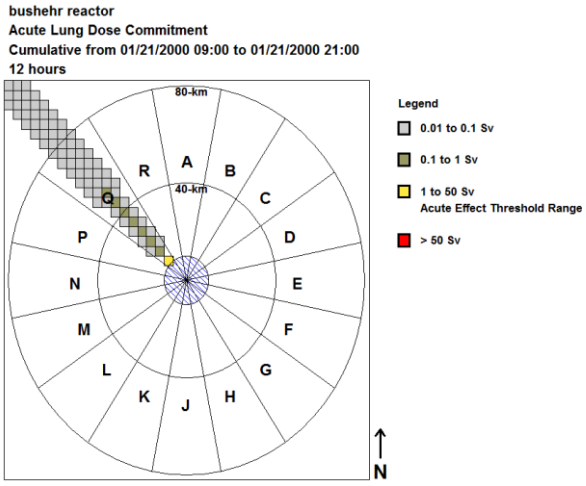

Fig. 5. Acute Lung Dose Commitmen

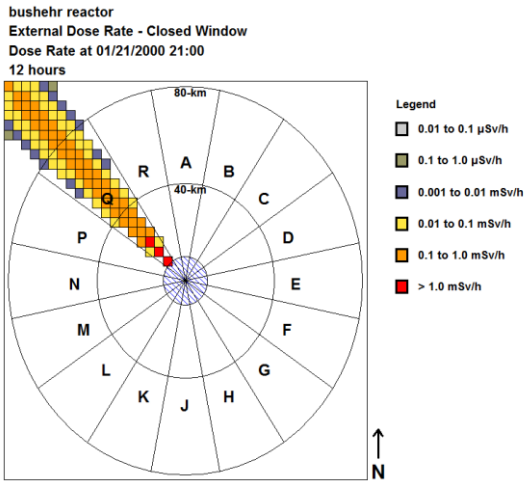

Fig. 6. External Dose Rate-Closed Window

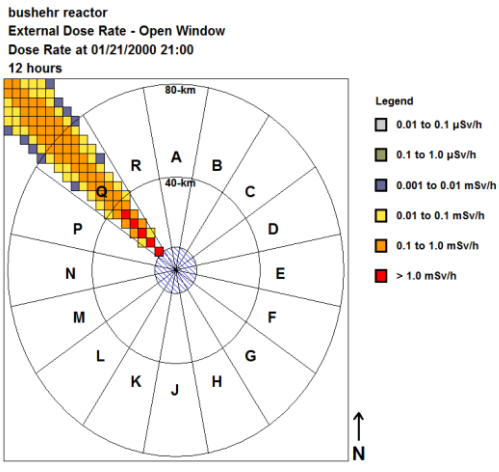

Fig. 7. External Dose Rate-Open

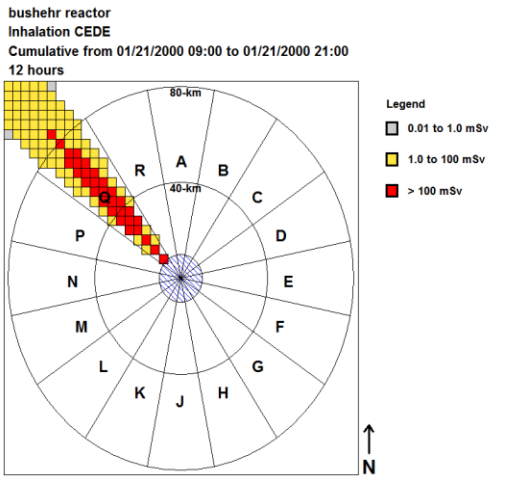

Fig. 8. Inhalation CEDE

Assuming a hypothetical incident and applying weather conditions, the dispersion of cesium-137 was examined using the RASCAL software for a 12-hour period. In this assessment, the trends of changes in the quantities of total effective dose, thyroid dose, inhalation committed effective dose (CEDE), external dose rate - open window, and external dose rate - closed window were calculated and plotted in figures 1 to 8 at a radial distance of 80 kilometers. According to meteorological information, the wind direction at the time of the incident was northwest, and the isotopes were also dispersed in this direction. The results clearly indicate that wind direction is one of the important and determining factors in the dispersion of radioactive materials. The total effective dose in the vicinity of the incident location exceeds 50 mSv, but on average, the dose within an 80-kilometer distance ranges from 0.01 to 10 mSv. The thyroid dose exceeds 250 mSv in close proximity, but on average, it ranges from 0.05 to 50 mSv at greater distances. The average inhalation CEDE dose within an 80-kilometer distance ranges from 1 to 100 mSv. In addition, the received external dose rate was calculated for two scenarios: open window and closed window.

According to the obtained figures, the cesium-137 dose rate decreases with increasing distance, and the trend of changes in the dose rate is clearly visible in the different colors in the figures.

References:

[1] Kasei Azani,A, Investigating the defense role of Bushehr nuclear power plant in the Persian Gulf, National Conference on Passive Defense & Sustainable Development, 3 oct 2016, Ministry of Interior,Tehran,(2016)

[2] Brooks, G. L., & Siddall, E. (1980). An analysis of the Three Mile Island accident (No. AECL-7065). CM-P00067632.

[3] Saenko, V., Ivanov, V., Tsyb, A., Bogdanova, T., Tronko, M., Demidchik, Y., & Yamashita, S. (2011). The Chernobyl accident and its consequences. Clinical Oncology, 23(4), 234-243.

[4] Baba, M. (2013). Fukushima accident: what happened? Radiation Measurements, 55, 17-21.

[5] Karimi,j. Shaisheta,M. Valizadeh,A, Investigation of dispersion of Cs-137 released from a small modular reactor in a hypothetical accident, Proceedings of The 29th Iranian Nuclear Conference, 26 feb 2023, Shahid Beheshti University,Tehran,(2023)

[6] Cai, J., Ip, K. F., Eze, C., Zhao, J., Cai, J., & Zhang, H. (2019). Dispersion of radionuclides released by nuclear accident and dose assessment in the Greater Bay Area of China. Annals of Nuclear Energy, 132, 593-602.

[7] Skrynyk, O., Voloshchuk, V., Budak, I., & Bubin, S. (2019). Regional HYSPLIT simulation of atmospheric transport and deposition of the Chernobyl 137Cs releases. Atmospheric Pollution Research, 10(6), 1953-1963.

[8] Pirouzmand, A., Kowsar, Z., & Dehghani, P. (2018). Atmospheric dispersion assessment of radioactive materials during severe accident conditions for Bushehr nuclear power plant using HYSPLIT code. Progress in Nuclear Energy, 108, 169-178.

[9] G.F.Athey, et.al, RASCAL4.3 User Guide, Prepared for office of nuclear regulatory research U.S Nuclear Regulatory Commission, March 2015

[10] Pelowitz, D.B, (2008), MCNPXTM Uses manual version 2.6.0, Los Alamos national laboratory.

[11] Bushehr Nuclear Power Plant, Final Safety Analysis Report (FSAR) (2003), Technical Report, Chapter 4

[12] Bushehr Nuclear Power Plant (٢٠٠٣), Final Safety Analysis Report (FSAR).

[13] Gianni Petrangeli, (2006), "Nuclear Safety," Elsevier Linacre House, Jordan Hill, Oxford

[14] Nuclear Energy Agency, (2002), "Assessment of Radiological and Health Impact," NEA publications

ICNST 2024
International Conference on Nuclear Science and Technology
6- 8 MAY 2024 | Isfahan, Iran

Preparation and physical investigation of sol-gel derived pure zinc oxide and copper doped zinc oxid samples for gamma shielding purpose (Paper ID: 1438)

Shaddoust M.[1], Bagheri Khatibani A.[1]*, Khoshhal A.R. [2], Nirouei M. [3]
[1] Nano Research Lab, Lahijan Branch, Islamic Azad University, Lahijan, Iran
[2] Department of Nuclear Engineering, Graduate University of Advanced Technology, Kerman, Iran
[3] Faculty of Engineering, Lahijan Branch, Islamic Azad University, Lahijan, Iran

Abstract

The special features of zinc oxide (ZnO) have made it broadly applied in the field of industry and medicine. Within this work, zinc oxide in three forms including pure ZnO and ZnO-Cu (10% and 20%) was successfully synthesized by sol-gel method. The various physical properties of these materials were investigated using the conventional methods of energy dispersive X-ray spectroscopy (EDX), X-ray diffraction (XRD) and field emission scanning electron microscopy (FESEM). XRD result verified hexagonal structure of zinc oxide; however, the addition of copper modified the main structure to some extent. The result of FESEM showed the nanosized quasi-spherical grains and the agglomeration of them. Also the verification of the elemental presence for the all samples were performed through EDX analyze. For these three samples, the protection factors against gamma rays, including mean free path (MFP), mass attenuation coefficients (MAC), tenth value layer (TVL), half value layer (HVL), linear attenuation coefficients (LAC) were calculated. According to these factors, it can be concluded that the use of ZNO, and ZnO-Cu (10% and 20%) as a gamma ray protector can be useful.

Keywords: zinc oxide, copper doping, sol-gel method, gamma shielding

Introduction

Wide use of radiation sources in different situations like as nuclear energy application and radiation therapy sites on the one hand, and its vast utilization in treatment and diagnostic centers on the other hand makes the issue of radiation protection always very important. It is obvious that the health of the employees and patients present in the centers has a high priority. It is quite clear that complete elimination of radiation is not possible. For decreasing the destructive effects of unwanted radiation, it is possible to comply with some cases such as radiation shielding, irradiation time, and distance to the radiation source. Based on these mentioned items, different countries have made radiation protection policies very carefully [1,2].

Zinc oxide, as a famous semiconductor which is widely utilized in various fields, has also shown its effectiveness in the field of radiation. Attractive mechanical, optical, electrical, antimicrobial, Eco-friendly properties of zinc oxide nano-particles with high transparency, great mobility, high binding energy, and

large band-gap makes it seductive. Sometimes it is called the magic substance which, apart from many applications, has shown specific morphologies with unique properties. Exclusively for shielding application, zinc oxide can be used in radiation-retaining glasses and as a protecting material in eyeglasses in X-ray chambers. It can provide more visibility in treatment and diagnostic centers [3,4]. The use of zinc oxide nanoparticles in this issue has been increasing and we have seen an increase in the attention of researchers in using this material. This item is one of the interesting topics which should be examined more carefully.

Considering the increasing growth of the use of nuclear radiation sources in various fields, the use of appropriate protection seems to be fully justified. Although zinc oxide nanoparticles are not the only choice and there is a range of materials in front of us, but the mentioned features and easier synthesis methods compel us to go for them. Eskalen et al., by utilizing combustion technic, prepared zinc oxide nanoparticles and evaluated their morphological and structural features. Zinc oxide nanoparticles added to borate glasses with different percentages have been examined for effective shielding issue. A very important shielding parameter, linear attenuation coefficient (LAC) was calculated through irradiating gamma radiation of gamma sources (65 Zn and 60 Co) to the samples and collecting their data with the NaI (Tl) detector. By aiding of LAC, it was possible to determine other related parameters such as mean- free path (MFP), tenth - value layers (TVL), half- value layer (HVL), and mass attenuation coefficient (MAC) for the prepared samples. Based on the results, they showed that zinc oxide nanoparticles reinforced borate glasses were the right choice for the radiation shielding issue. Accordingly, it was an effective shielding material [5]. Al-Hadeethi et al., also showed that zinc oxide nanoparticles have a decisive role in enhancing the shielding parameters of the ceramic ball clay. It is concluded that using of zinc oxide nanoparticles is more effective [6].

Experimental

Description of the Materials and Methods used in the research

In this research, three samples with 25cc ethanol solution were prepared and then 2.74g of zinc acetate ($Zn(CH3CO2)2{\cdot}2H2O$) was added to each of the samples. 0.24g of copper salt ($CuCl2{\cdot}2H2O$) as a 10% copper dope and 0.53g of copper salt as a 20% copper dope were added to the two of the three solutions mentioned in the current study. In the next step, beaker containing samples of zinc acetate and zinc acetate doped with 10% and 20% copper were placed on the stirrer (Fig. 1. A). Then, after 30 minutes, 1.2 cc of ethanolamine was added to the mentioned samples and then they were stirred for further 90 minutes (2

hours in total) on the stirrer device. In the next step, the beaker containing samples of pure zinc acetate and zinc acetate doped with 10% and 20% copper were poured in crucibles (Fig. 1. B) and annealed in the oven for three hours at 500°C, and then the samples were allowed to cool after annealing. The total process of annealing and cooling the samples took 24 hours, and then the annealed samples were taken out of the oven (Fig. 1. C). Also, in the annealing process, the time to reach the temperature of 500°C was about 25 minutes. In the next step, the powder of the samples taken out of the oven, including pure zinc oxide, zinc oxide doped with 10% copper and zinc oxide doped with copper 20%, were prepared in the laboratory in the form of tablets (Fig. 1. D).

(A) (B) (C) (D)

Fig. 1. Images of Protective production steps

In the next step, the desired samples were placed in the medical radiation laboratory to check their radiation protection properties between the cesium137 point source and a Geiger-Muller type gas detector (Fig. 2). According to the count values obtained from the Geiger-Muller detector, radiation protection parameters of samples including LAC, MAC, HVL, TVL, and MFP have been determined.

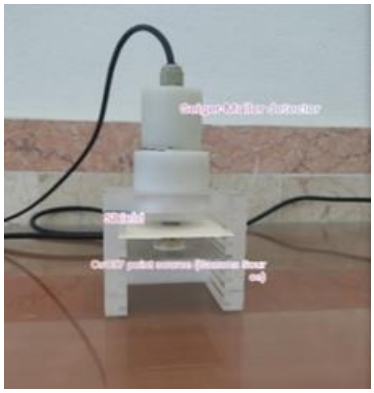

Fig. 2. Image of radiation protection experiment for pure ZnO and ZnO:Cu(10% and 20%)

Also, in this research, the structural and morphological characteristics of pure zinc oxide nanoparticles and zinc oxide doped with 10% and 20% copper were also investigated by performing XRD, EDX, FESEM and UV-visible analyses.

Definition of Radiation shielding parameters

The LAC (μ, linear attenuation coefficient) evaluates an shielding quality of an attenuator for nuclear irradiation. The LAC is determined through the Beer–Lambert relation [1]:

$$\mu = \ln \left({}^{I_0}/_{I} \right)_{x} \qquad (1)$$

Here, x is the thickness of the samples, I and I0is counts of photons with and without the presence of the samples.

The MAC (μm, mass attenuation coefficient) detemines the absorption quality of a material and is obtained from the ratio of LAC on an absorber density. In this research, the MAC values determined with the following [1]:

$$\mu_m = \sum_i w_i (\mu/\rho)_i \qquad (2)$$

wi is the weight fraction, $(\frac{\mu}{\rho})_i$ is the mass attenuation coefficient for an individual element in the compound.

The needed thickness for attenuation the radiation beam to half the value before going through the absorbing material is named as the half value layer (HVL). Hence, this can be evaluted by the following [1]:

$$HLV = \ln 2/\mu \qquad (3)$$

The tenth value layer (TVL) is known as the thickness of an absorbing material that needed to decrease the incident intensity of gamma radiation to its tenth amount at a specific energy [1]:

$$TVL = \ln 10/\mu \qquad (4)$$

The mean free path (MFP) is known the average distance that the gamma ray travels through the medium before any interaction takes place [1].

$$\boldsymbol{MFP = {}^{1}/_{\mu}} \quad (\boldsymbol{cm}) \qquad (5)$$

Results and discussion

Radiation shielding parameters

The linear attenuation amounts obtain noteworthy data about radiation shielding parameters of pure ZnO nanoparticles and ZnO doped with Cu (10 % and 20 %). All the mentioned nanoparticles were prepared in

the form of tablets. All the samples were exposed for 30 seconds to the gamma source of cesium 137 with an activity of 8.7 μci and a gamma energy peak of 0.662 Mev. The acquired data of linear attenuation (μ), mass attenuation coefficient (μm), half value layer (HVL), one-tenth value layer (TVL) and mean free path (MFP) of pure ZnO nanoparticles and ZnO doped with copper (10% and 20%) have been showed in Table 1. It can be seen, different amounts of Cu (10% and 20%) have a positive participation to the shielding parameters. The largest value for linear attenuation coefficient belongs to ZnO doped with 20% cu (2.27cm-1) and the lowest amount belongs to the pure ZnO nanoparticles (2.15cm-1). The Mass attenuation coefficient values of pure ZnO nanoparticles and ZnO:Cu (10% and 20%) were also given in Table 1. The lowest value is 0.392 cm2/g for pure ZnO. It increases as the percentage of Cu starts increasing. The mass attenuation coefficient value has highest value of 0.4 cm2/g for ZnO doped with 20% Cu. The mean free path (MFP), half value layer (HVL) and one tenth Values (TVL) of pure ZnO nanoparticles and ZnO:Cu (10% and 20%) can be observed in Table 1. The half value layer varied from 0.32 cm to 0.3 cm, which depends on the percentage of copper in zinc oxide structure. Also, the one-tenth layer value varied from 1.07 cm to1.01cm. Finally, the mean free path of pure ZnO and ZnO:Cu (10% and 20%) changed from 0.46 cm to 0.44 cm, this reduction has been accompanied by an increase in the amount of copper in the structure of zinc oxide.

Considering that slight structural changes have occurred in the main structure of zinc oxide after the addition of copper. Morphological changes seem to be an important factor in changing the shielding parameters, which is consistent with the FESEM micrographs.

Table 1. Results of radiation protection parameters for pure ZnO and ZnO:Cu (10% , 20%)

Sample	Compositions(%) ZnO-----Cu	LAC(cm^{-1})	MAC(cm^2/g)	MFP(cm)	HVL(cm)	TVL(cm)
ZnO	100%----0	2.15	0.392	0.46	0.32	1.07
ZnO:Cu 10%	90%-----10%	2.19	0.396	0.45	0.31	1.05
ZnO:Cu 20%	90%-----20%	2.27	0.4	0.44	0.3	1.01

XRD results

Fig. 2 shows the XRD data of the sol-gel prepared pure, and copper doped zinc oxide samples which was taken in the 2θ region from 20◦ to 80◦. The miller indices (hkl) of the diffraction planes are also marked. A

very good match between our prepared samples and the standard zinc oxide sample is observed. A standard polycrystalline wurtzite ZnO with the code of 79-0208 was matched.

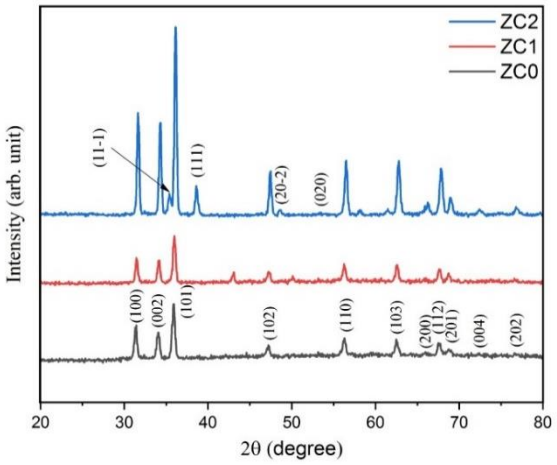

Fig. 3. The XRD Rusults of pure ZnO and ZnO:Cu(10% , 20%)

Lack of attandence of annoying peaks in XRD data for pure zinc oxide verified the presensce of pristine phase of zinc oxide [7]. Copper has a ionic radius of 0.073 nm, which is almost the same radius as of Zn (0.074 nm). Therefore, it is not far from expected that it can replace zinc ions in the structure of zinc oxide, especially in higher amounts of doping [8]. The signs of the presence of copper oxide appeared at larger amount of doping. The possible diffraction peaks are also identified according to JCPDS card CuO: 48-1548. Although these lines are not very strong and have not destroyed the nature of the main lattice. Lattice parameters of three main peaks ((100), (002), (101)) for all samples were calculated and compared with standard values (Table 2). They were decreased due to doping and it seems the lattice parameters become closer to the standard values afer doping. Negligible deviation from the standard values is observed, for example, in the case of unit cell volums, that can be the result of iconicity and instability of the lattice. The ratio of c/a relates to electronegativity of the zinc and oxygen in main structure [9]. Other reasons probably play a role in this deviation such as variation of bond angle, bond length, and twisting of the main structure. It is known that various defects inside the main structure cause to band edge variation process [10].

Table 2. The calculated and standard values of the lattice parameters for three main reflection peaks (i.e. (100), (002), (101)) and other relevant parameters.

Sample	$d=(\overset{\circ}{A})$		$a=b(\overset{\circ}{A})$		$c=(\overset{\circ}{A})$		**Volume of unit cell** $(\overset{\circ}{A})^3$		$\frac{c}{a}$ **ratio**	
	Cal.	**Sta.**	**Cal.**	**Sta.**	**Cal.**	**Sta.**	**Cal.**	**Sta.**	**Cal.**	**Sta.**

ZC0				6	1.602
ZC1				2	1.602
ZC2				4	1.602

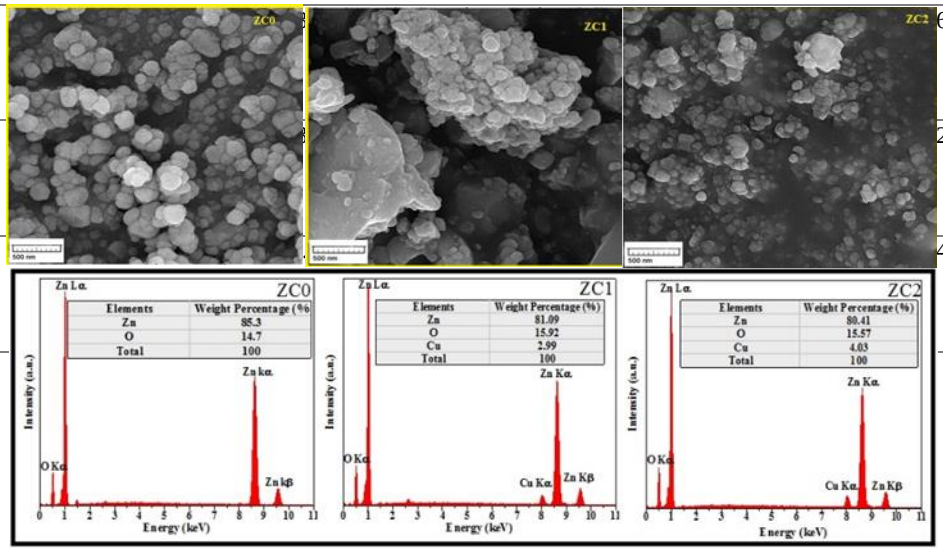

FESEM and EDX results

Fig. 4 presents the micrographs of FESEM of the pure zinc oxide and copper doped (10% and 20%) nanoparticles. All of the micrographs show grains with nano scale amounts, and the aggregation of grains is clear in all samples. adding 10% and 20% Cu doping to ZnO samples increases the aggregation and compression of grains. The EDX spectrum of of the pure zinc oxide and copper doped nanoparticles are brought in Fig. 4 too, which verified the attandance of Zn, O for the undoped sample, along with Cu(10% and 20%) for the Cu doped samples.

Fig. 4. FESEM images of pure ZnO and ZnO:Cu (10% and 20%) along with the EDX spectrum

Conclusions

The powder of pure zinc oxide and copper doped (10%, 20%) ones have been maded through sol–gel technic. Their structural and morphological properties have been evaluated. Based on the XRD data, wurtzite structure of ZnO was confirmed. Even though, the attandance of CuO at larger amount of doping

was inevitable. Due to the FE-SEM information, analogous microstructures, quasi-spherical agglomerated grains in the range of nano scale were observed for all samples. However, after doping, the connection of nanoparticles increased and the sphericity of the grains has decreased. The EDX data has also shown the presence of desirable elements (i.e. Zn, O, and Cu). The radiation shielding properties of the samples (LAC, MAC, MFP, HVL, and TVL) were also calculated. The results showed that copper doped zinc oxide (20%) has good merit as a protector compared to pure zinc oxide. For further study, different experimental setups and arrangements can be provided and zinc oxide nanoparticles can be synthesized in different ways to investigate the radiation protection characteristics and also the absorption characteristics of materials with different particle interactions can be investigated.

References

[1] Eskalen, H., Kavun, Y., Kerli, S. and Eken, S., 2020. An investigation of radiation shielding properties of boron doped ZnO thin films. Optical Materials, 105, p. 109871.

[2] Kavun, Y., Eskalen, H. and Kavgacı, M., 2023. A study on gamma radiation shielding performance and characterization of graphitic carbon nitride. Chemical Physics Letters, 811, p. 140246.

[3] Rashad, M., Tekin, H.O., Zakaly, H.M., Pyshkina, M., Issa, S.A. and Susoy, G., 2020. Physical and nuclear shielding properties of newly synthesized magnesium oxide and zinc oxide nanoparticles. Nuclear Engineering and Technology, 52(9), pp. 2078-2084.

[4] Sarachai, S., Chanthima, N., Sangwaranatee, N.W., Kothan, S., Kaewjaeng, S., Tungjai, M., Djamal, M. and Kaewkhao, J., 2018. Radiation Shielding Properties of BaO-ZnO-B2o3 Glass for X-Ray Room. Key Engineering Materials, 766, pp. 88-93.

[5] Eskalen, H., Kavun, Y. and Kavgacı, M., 2023. Preparation and study of radiation shielding features of ZnO nanoparticle reinforced borate glasses. Applied Radiation and Isotopes, 198, p. 110858.

[6] Al-Hadeethi, Y., Sayyed, M.I., Barasheed, A.Z., Ahmed, M. and Elsafi, M., 2022. Preparation and radiation attenuation properties of ceramic ball clay enhanced with micro and nano ZnO particles. Journal of Materials Research and Technology, 17, pp. 223-233.

[7]Navale, Y.H., Navale, S.T.,. Ramgir, N.S, Stadler, F.J., Gupta, S.K., Aswal, D.K., Patil, V.B., (2017). Zinc oxide hierarchical nanostructures as potential NO2 sensors, Sensors and Actuators B, 251 pp. 551–563.

[8] Wang, C., Yin, L., Zhang, L., Xiang, D., Gao, R., 2010. Metal Oxide Gas Sensors: Sensitivity and Influencing Factors, Sensors, 10(3), pp. 2088–2106.

[9] A. Nandi, R. Majumder, P. Nag, S.K. Datta, H. Saha, S. Majumdar, 2017. Precursor dependent tailoring of morphology and bandgap of zinc oxide nanostructures, J Mater Sci: Mater Electron, 28, pp. 10885-10892.

[10] Bagheri Khatibani, A., Shabankhah, A., 2021. Fabrication and ethanol sensing of sol–gel grown zinc oxide powder: the effect of cobalt and copper doping, Appl. Phys. A, 127, pp. 308.

ICNST 2024
International Conference on Nuclear Science and Technology
6- 8 MAY 2024 | Isfahan, Iran

Simulation of HPGe Detector Spectra Using Monte Carlo Codes and Comparison with Experimental Spectrum (Paper ID: 1457)

Sara Ghanavati[1*], Mohammad Mirzaei[2], Farshid Babapour mofrad [3], Asghar Haddadi[4]
[1] Department of Medical Radiation Engineering, Science and Research Branch, Islamic Azad University, Tehran, Iran
2 Atomic Energy Organization of Iran
3,4 Department of Medical Radiation Engineering, Science and Research Branch, Islamic Azad University, Tehran, Iran

Abstract

Researchers use simulations to understand and optimize the detector's performance. By accurately modeling the detector's response to various gamma-ray energies and interactions, they gain insights into its behavior. Simulations help scientists analyze and interpret experimental data effectively. This leads to improved calibration methods and more accurate measurements. Simulating different detector geometries, materials, and configurations plays a crucial role in designing new detector systems.

In this study, the modeling of the HPGe detector for low to medium-energy gamma rays was carried out, and its validation was conducted through experiments using standard gamma-ray sources. Additionally, a, b, and c as parameters specifying the Full Width at Half Maximum (FWHM) in the GEB option have been extracted to conduct Monte Carlo simulations of germanium detectors. Based on the obtained results, the simulated spectrum showed a good agreement with the experimental spectrum, indicating an accurate representation of the HPGe detector's response to gamma-ray interactions. The similarity between the simulated and real spectra confirms the validity of the simulation approach and enhances confidence in the accuracy of the simulated results.

Keywords: HPGe detector, spectrometry, gamma-ray, MCNP, experimental spectrum, GEB

Introduction

The HPGe detector plays a crucial role in spectrometry due to its high sensitivity and excellent energy resolution. Its ability to accurately detect and measure gamma-rays allows for precise identification and quantification of radioactive isotopes in various samples. the importance of the HPGe detector in spectrometry lies in its capability to provide detailed information about the energy distribution of gamma-rays emitted by radioactive sources. This enables researchers and scientists to study the characteristics of nuclear decay processes, analyze environmental samples for radioisotopes, and perform accurate measurements in fields such as nuclear medicine, environmental monitoring, and materials science.

Various detectors are used for gamma-ray spectrometry, coupled with electronics and data analysis techniques, to identify and measure emitted gamma rays from radioactive sources. Among the detectors used, HPGe detectors have very good energy resolution, making them suitable for accurate gamma-ray spectrometry. The Monte Carlo technique is widely used in radiation-related fields such as medical and industrial research, radiation protection, and nuclear facilities. This tool aids in project development by facilitating the construction of geometries, utilization of detectors, and various energy sources. Consequently, it addresses challenges associated with detector availability, radiation sources, and experimental tests, as it eliminates the need for experimental setups. Therefore, the use of an appropriate modeling that aligns well with experimental results is crucial. Only a limited number of studies address the utilization of germanium detectors in the low- and middle-energy range of gamma rays, a crucial aspect in the realm of activation analysis (1-3).

In this regard, this investigation aimed to present a method for modeling HPGe detectors using the MCNP code with the application of the Eu-152 source, intended for the calibration of such detectors. Furthermore, obtaining the precise response function of the HPGe was pursued to create a simulation that closely mimics reality.

Materials and methods

In this research, the HPGe detector has been simulated using the MCNP code, as depicted in Figure 1. N-type coaxial high purity germanium (HPGe) detector (NIGC-4020) coupled with a multichannel analyzer card system (NIGC1040-, DSG, GMBH). The crystal has a diameter of 61.4 millimeters and a length of 62 millimeters. Additionally, it features a dead layer of 0.3 microns Ge/B and a dead layer of 700 microns Ge/Li. Standard electronics and a multi-channel analyzer with 4096 channels were utilized. The resolution (FWHM) at 1.33 MeV, Co-60 is 2keV and peak-to-Compton ratio, Co-60 is 54:1 and relative efficiency at 1.33 MeV, 60Co is 40%. The GammaVision-7 program was employed for gamma spectrometry. The standard Eu-125 source with a half-life of 13.517 years, a volume of 8 cc, and an activity of ۲,۲۱ microcuries is positioned at 20cm from the HPGe detector.

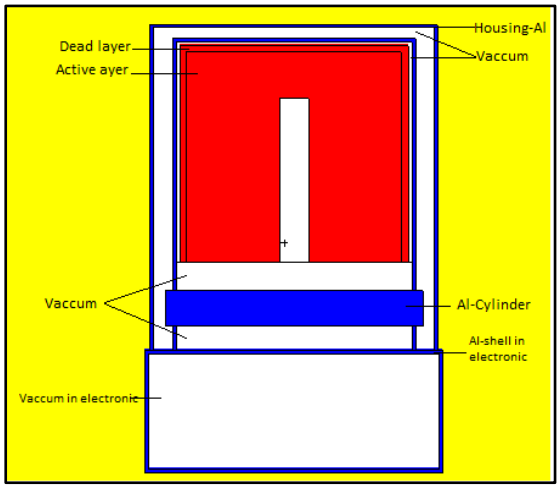

Fig 1. Schematic representation of the simulated HPGe detector.

After conducting the experiment, the Eu-152 spectrum was obtained, as shown in Figure 2. Using this spectrum, the FWHM values for each of the 11 Eu-152 peaks were calculated using Origin software, and Table 1 presents the FWHM and energy values for each peak.

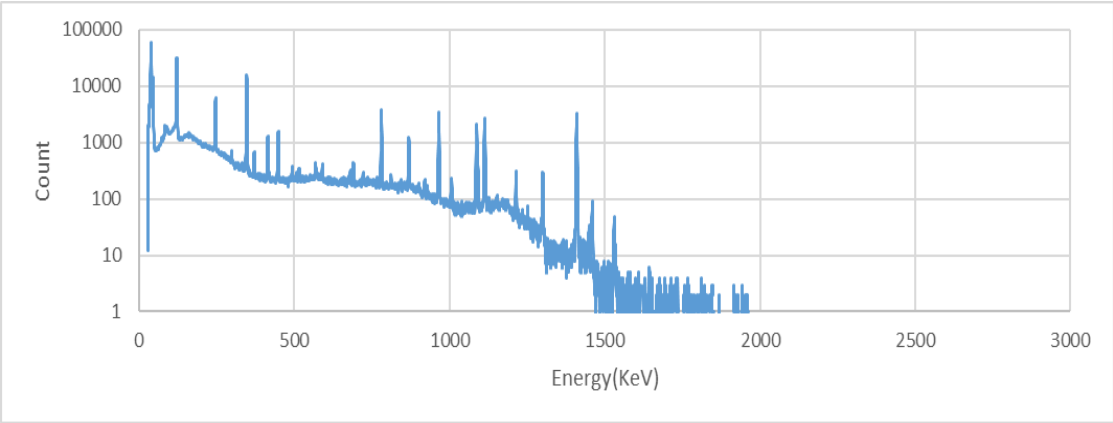

Fig 2. The actual spectrum obtained from Eu-152

Table 1. Calculated Peaks FWHM

Peak Energies (keV)	FWHM(keV)
121/7817	1/99134
244/6975	2/08782
344/2785	2/10049
411/1163	2/05243
443/965	2/16388
778/904	2/30552
867/378	2/30466
964/079	2/4262
1085/869	2/60576
1112/074	2/48503
1408/006	2/68649

In the context of Monte Carlo simulations using the MCNP code, Gaussian Energy Broadening (GEB) serves as a specialized technique for handling tallies. Its purpose is to enhance the simulation of physical radiation detectors, specifically those where energy peaks exhibit Gaussian energy broadening. To apply GEB, users include an 'FTn' card in the input file of MCNP. The tallied energy values are then broadened by sampling from a Gaussian distribution.:(4)

$f\ (E) = Ce$-((E-E0)/A)2

Where E is the broadened energy, $E0$ is the unbroadened energy of the tally, C is a normalization constant, and A is the Gaussian width.

Considering the calculation of Full Width at Half Maximum (FWHM) through Equation 2 and the relationship between FWHM and energy, parameters a, b, and c can be obtained through Equation 3.

$$A=\frac{FWHM}{2\sqrt{Ln2}}$$

$$FWHM = a + b\sqrt{E + cE^2}$$

Figure 3 illustrates the FWHM plot as a function of energy according to the data in Table ١, used to obtain the parameters a, b and c (Table2) to be used in MCNP's GEB command.

Table 2. Values of parameters a, b and c.

a	b	c
١/٩٠٣٤٥٢٧٢09	٠/٠٠٠٦٢١٦٤٥١٨١٧	٠/٧٧٩٠٨٦١٣٣٦٤٩

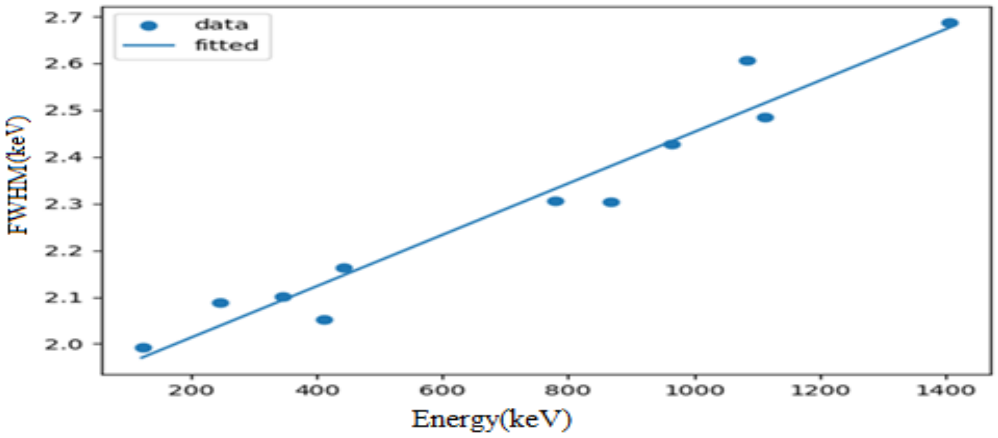

Fig 3. FWHM plot as a function of energy (keV).

Results and Discussion

The HPGe response function to the Eu-152 standard gamma-ray source was experimentally measured and compared with simulated results for validation. Figure 4 illustrates a favorable agreement in the energy range of 11 photoelectric peaks within the Eu-152 gamma-ray spectrum. Despite this overall agreement, minor discrepancies may arise from factors such as scattered radiation from surrounding materials in the room, peak tailing leading to incomplete charge collection, pulse pile-up with electronic noise, or Doppler broadening of inelastically scattered photons that smooth the Compton edges." (5,6).

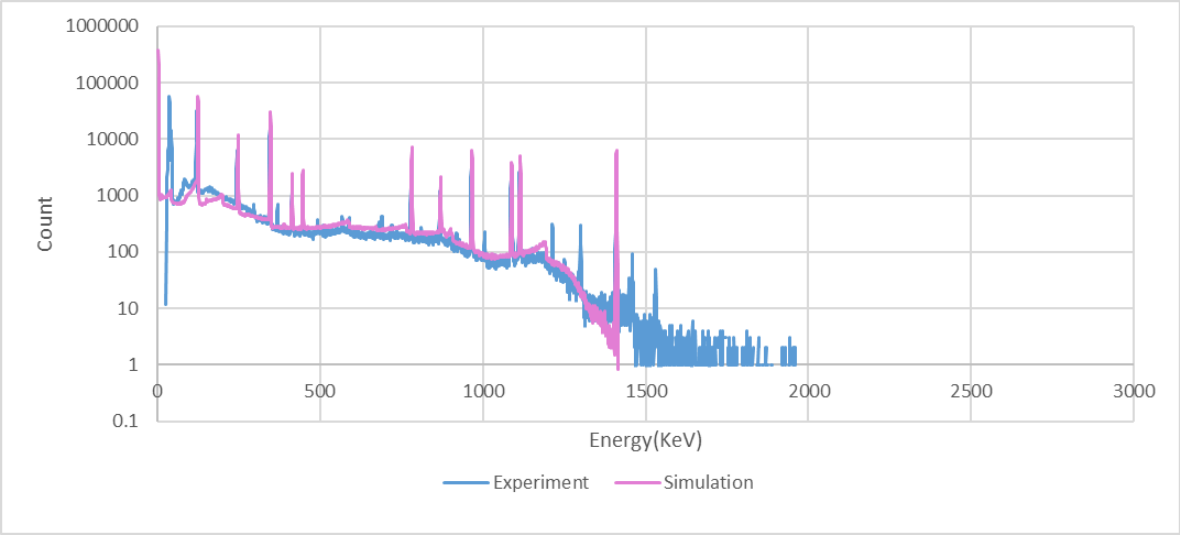

Fig4. Comparison between simulation and experimental gamma-ray spectrum of the Eu-152 point source.

Conclusions

Simulating the detector can offer effective tools for accurately determining the detector's response function, overcoming challenges such as the lack of radiation sources with the necessary photon energies. This study has introduced a method to simulate the response functions of HPGe using GEB as a specific treatment for tallies in MCNPX. The results indicate that MCNPX simulations employing GEB successfully match all Gaussian peaks originating from standard gamma-ray sources across a broad energy range with minor discrepancies. In this study, as part of our future endeavors, the coefficients a, b, and c, as described above, have been extracted to establish a library for delayed gamma neutron activation analysis of cement material using Monte Carlo code. It is important to note that GEB parameters vary for each configuration of the experimental setup.

References

[1] Rahman, M. S., & Cho, G. (2010). HPGe detector energy response function calculation up to 400 keV based on Monte Carlo code. Journal of scientific research, 2(3), 479.

[2] Lépy, M. C., Plagnard, J., & Ferreux, L. (2003). Study of the response function of a HPGe detector for low-energy X-rays. Nuclear Instruments and Methods in Physics Research Section A: Accelerators, Spectrometers, Detectors and Associated Equipment, 505(1-2), 290-293.

[3] Kojima, Y., Ikuta, T., Asai, M., Taniguchi, A., Shibata, M., Yamamoto, H., & Kawade, K. (1997). Measurement of response functions of HPGe detectors for monoenergetic electrons and positrons in an energy range of 6.0–9.0 MeV. Nuclear Instruments and Methods in Physics Research Section B: Beam Interactions with Materials and Atoms, 126(1-4), 419-422.

[4] Pelowitz, D. B. (2005). MCNPXTM user's manual. Los Alamos National Laboratory, Los Alamos, 5, 369.

[5] Pylypchynets, I., Lengyel, A., Parlag, O., Maslyuk, V., & Potoki, I. (2019). Empirical formula for the HPGe-detector efficiency dependence on energy and distance. Journal of Radioanalytical and Nuclear Chemistry, 319, 1315-1319.

[6] El Abd, A., Mostafa, M., & El-Amir, M. (2012). Production of 152,154 Eu mixed sources for calibrations of gamma-ray spectrometers. Journal of Radioanalytical and Nuclear Chemistry, 293(1), 255-260.

ICNST 2024 International Conference on Nuclear Science and Technology
6- 8 MAY 2024 | Isfahan, Iran

Monte Carlo Simulation to Optimize the Design of a Self-Powered Neutron Detector (Paper ID: 1461)

Shoorian S. Correspondent[1*], Heidarinejad M. Co-Author[2]
[1]Nuclear Engineering, Shahid Beheshti University, Tehran, Iran [2]Electrical Engineering, Shahid Beheshti University, Tehran, Iran

Abstract

Self-powered neutron detectors are used as in-core detectors in thermal reactors. These detectors can tolerate the harsh environment of the reactor and are sensitive to both gamma and neutron particles. SPNDs are classified as “prompt” and “delayed” detectors based on their response. In this work, a SPND is simulated by MCNPX Monte Carlo code. The accuracy of the simulation was validated by comparing the results with reported values in reference papers. After validation, the SPND’s sensitivity was studied for different materials as its emitter, insulator and collector. The results indicate that a SPND with Rhodium emitter is more sensitive than one with a Vanadium emitter. Also, regarding the results collector material has no effect on the sensitivity of the SPND. On the other hand, according to the results by selecting Alumina as the insulator, in addition to an improved sensitivity of the SPND, the resistance of Al2O3 stays constant with exposure. In the following, the sensitivity of SPND as a function of the length of the emitter was studied. Due to the calculations, neutron flux in the emitter has an inverse proportionality with the radius of the emitter. On the other hand, with increasing the emitter radius will enhance the absorption of neutrons in the emitter, and finally the sensitivity of SPND improves with the increase of the emitter radius. The results show that changing the insulation thickness does not have a significant effect on the SPND sensitivity. Although, by increasing the thickness of the collector, neutron absorption in the collector increases and will decrease the neutron flux in the emitter. This eventually leads to a deterioration in the sensitivity of SPND.

Keywords: Self-powered neutron detectors, Monte Carlo, Rhodium, Vanadium

Introduction

Self-powered neutron detectors (SPNDs) are used as in-core neutron detectors in thermal reactors [1]. SPNDs can easily operate in-core for long periods of activity and under harsh operational conditions. SPNDs are sensitive to both gamma rays and neutrons [2]

SPNDs are generally designed coaxially, as shown in Fig. 1. The internal electrode is called emitter and is made of materials that can interact with neutrons through absorption (such as Co, V, Rh and Pt), prompt

gamma and/or delayed electron emission. As a result, the signal of a SPND is the sum of a delayed and a prompt response. The outer electrode, usually made of stainless steel, is called collector. An insulator, usually Al2O3 or MgO, is sandwiched between the two electrodes. These non-emitting components are made of materials that do not interact with neutrons and can tolerate the intense radiation and temperature environments inside the reactor.

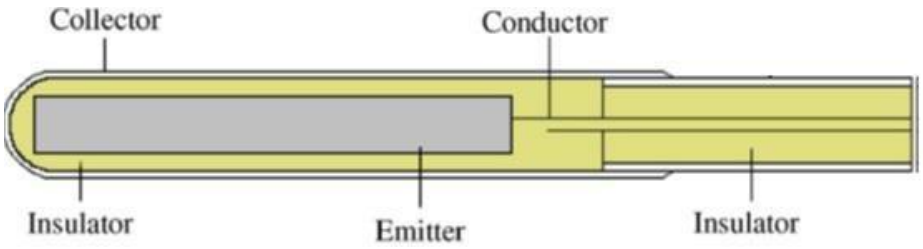

Fig. 1. Cross-section of a typical SPND. The central conductor is called the emitter and is responsible for generating the signal. The external conductor is called the collector and is separated from the emitter by an insulator [3].

SPNDs are divided into two categories: detectors based on beta decay (delayed detector) and detectors based on secondary electrons caused by gamma decay (prompt detector).

Delayed Detectors

Neutron trapping (n, γ) in the emitter leads to the formation of a radioactive nucleus which transform to another state, stable or unstable, by beta decay. The beta decay time, which represents the response of the detector, can vary between a few seconds and several minutes [4]. Some of these emitted beta rays have enough energy to reach the collector, some are stopped after multiple collisions in the emitter, and the rest of them are stopped in the insulator, which causes charge accumulation in the insulator area. These and other possible interactions are shown in Fig. 2 [5]. The generated secondary electrons undergo many interactions before reaching the collector. Electrons that stop at the emitter do not contribute to signal generating. Electrons that can reach the insulator and stop there can make more interactions and cause the accumulation of negative charge. Depending on whether the beta rays are driven into the collector or returned to the emitter, they affect the net current measured by the collector; This should be considered during the analysis.

The emitter of this type of SPNDs must have a neutron absorption cross-section that is neither too high nor too low. A very high absorption cross-section can cause rapid consumption of the emitter material and therefore reduce the lifetime of the detector. On the other hand, the low absorption cross section reduces

the neutron sensitivity of the detector. Also, the electrons produced in this type of detector must have enough energy to pass through the emitter and insulator and reach the collector. The half-life of beta decay should be as short as possible so that the response signal of neutron flux changes is fast enough [6].

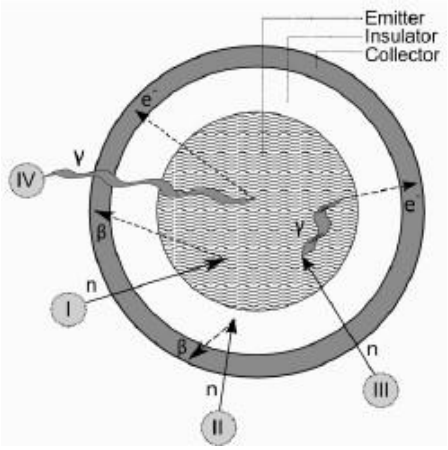

Fig. 2. Possible interactions in a SPND that contribute to detector current signal [5].

Prompt Detectors

Prompt detectors can immediately response to instantaneous changes in reactor operating conditions. The emitter of these detectors is a material with a large neutron absorption cross-section that produces stable or long-lived isotopes. The main signal source of these detectors originates from the electron charge flux produced by gamma due to neutron absorption [4]. Gamma rays may interact with detector materials through the photoelectric effect, Compton scattering, or pair production. As explained above, the electrons transferred from the emitter to the insulator lead to the accumulation of negative charge. The resulting field then pushes the electrons out of the insulator, emitter, or collector.

Selection Emitter Material

Consumption rate of the emitter material is one of the debatable parameters. The signal-to-flux ratio of an SPND changes due to radiation and is not a constant parameter. The emitter material interacts with neutrons and transmutes to another element. As the result of the reduction (or depletion) of the emitter material, the sensitivity of the reactor to the neutron flux decreases [7].

Since the in-core environment is a mixed environment of gamma and neutrons, the selection of the emitter material is based on the cross section of possible nuclear reactions: (n,β-), (n,γ)(γ,e) and (γ,e) in these materials. Emitter material must have a high atomic number to enhance gamma interaction in the emitter [5]. The most known emitter materials used in SPNDs are rhodium, vanadium, cobalt, hafnium, platinum,

and silver. These materials have a relatively high melting point and a large thermal neutron absorption cross-section. Other materials such as cadmium, gadolinium and erbium may also be used as emitters in SPNDs, but these materials are not practical for power reactor applications [8]. Table 2 provides a general description of some of the most important properties of SPND emitter materials used in power reactor applications.

Table 1. Characteristics of some SPND emitter materials [8]

Emitter Material	Thermal Cross-section for Neutron Absorption	Prompt Gamma, Neutron, and Electron	Prompt Gamma and Electron	Applications
Co^{59}	37×10^{-24} cm^2	X	O	LWR Flux Mapping LWR Control Local Core Protection
Pt^{195}	24×10^{-24} cm^2	X	X	LWR Control
Rh^{103}	145×10^{-24} cm^2	-	-	HWR Control LWR Flux Mapping
V^{51}	4.9×10^{-24} cm^2	X	O	HWR Flux Mapping LWR Flux Mapping
HfO_2	115×10^{-24} cm^2	X	O	RBMK* Flux Mapping RBMK* Local Control RBMK Local Core Protection
Ag	64.8×10^{-24} cm^2	-	-	RBMK Flux Mapping

X = Primary Interaction O = Secondary Interaction *Upgraded RBMK LWR - Light Water Reactor HWR - Heavy Water Reactor
RBMK - Graphite Moderated Light Water Reactor RBMK* - Upgraded SPND for RBMK

Methodology

The main parameters determining the gain of a delayed SPND in the reactor core are as follows:

Geometry;

Emitter material;

Emitter sensitivity to neutron flux;

Lifetime of emitter material;

Signal-to-noise ratio of the detector current.

Monte Carlo codes can be applied to simulate SPNDs and check their behavior. In this work, MCNPX code is used to simulate SPNDs. The MCNP code does not follow the history of the unstable activated nucleus created by neutron absorption. These nuclei decay with their specific time characteristics and emit beta and/or gamma rays. To account these effects, which are crucial for sensitivity calculations related to delayed SPNDs, calculations must be performed in two steps:

In the first step, the production rate of activated nuclei is calculated for a specific neutron source.

In the next step, this information is used to define the spatial distribution of an electron source (beta) to calculate electron currents. The initial velocity direction of these secondary particles is considered as a random distribution. The energy distribution for electrons is calculated according to the beta Fermi energy distribution with the appropriate beta energy endpoint [2].

Fig. 3 shows the simulation steps to calculate the sensitivity.

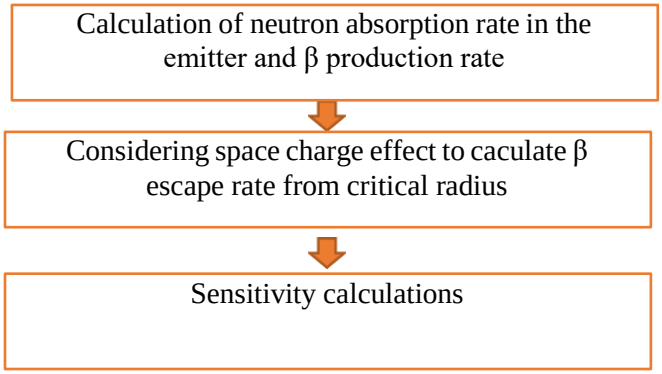

Fig. 3. Roadmap of calculations

In this work, using the MCNPX code, two delayed SPNDs have been modeled in accordance with Table 2, to validate the simulation with the results of [10]. It should be noted that different materials as insulator and collector are investigated and Alumina and Inconel are selected as the final configurations.Several basic assumptions are considered in the modeling. The first assumption is that the incident neutron is isotropic and constant over time [11]. In fact, the neutron flux and its spectrum inside a reactor are not the same: it is higher near the center of the core and lower at the borders [12]. This assumption is crucial for the logical simplification of the problem. The second assumption is that the detector is at the beginning of its operation life, and although the detector material is consumed with time, it is assumed to remain constant during the simulation.

In the first step, to obtain the neutron absorption rate in the emitter, the collector shell is defined as an isotropic thermal neutron source, as shown in Fig. 4, and the neutron absorption rate in the emitter is calculated.

Table 2. Geometry of the simulated SPNDs

Component	Material	Density (g/cm^3)	External Diameter (cm)	Length (cm)
Emitter	Rh	12.4	0.0508	40
	V	6.1		
Insulator	Alumina	1.9	0.1016	40
Critical Radius	-	-	0.0374	40
Collector	Inconel-600	8.44	0.259	40

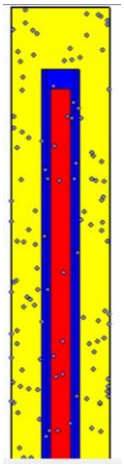

Fig. 4. Cross-sectional representation of the simulated SPND plotted by Visual Editor (Vised).

After calculating the neutron absorption rate in the emitter, it is necessary to define a volume source of beta in the emitter region. The energy spectrum of beta particle with endpoint energy Ei,0 can be calculated from equation 1,

$$p_i(E) = \frac{16}{16} E_{i,0}^{-3.5} \cdot \sqrt{E} \cdot (E_{i,0} - E)^2 \qquad \textbf{Equation 1}$$

The endpoint energy spectrum of beta particles produced by the emitter can be calculated using equation 2,

$$p(E) = \sum_{i=1}^{n} p_i(E) \cdot \eta_i \qquad \textbf{Equation 2}$$

The dominant endpoint energies are 2540, 1207 and 1010 keV, which have the relative intensities of 99.22, 0.57 and 0.12 %, respectively. For 104RH, the dominant endpoint energies are 2440 and 1884 keV with intensities of 98 % and 1.9 % [10].

To calculate SPND sensitivity, the deposited energy by electrons out of the critical radius is calculated using +F8 Tally and is compared with [10] in Table 3.

Table 3. Comparison of the calculated parameters with the reported values in [10]

Tally	Emitter Material	Calculated Value	Expected Value	Relative Error
Neutron Flux in Emitter	^{103}Rh	0.0433 cm^{-2}	0.0433 cm^{-2}	0%
	^{51}V	0.0583 cm^{-2}	0.0614 cm^{-2}	5.0%
Neutron Capture	^{103}Rh	0.0372	0.0372	0%
	^{51}V	0.00174	0.00195	11%
Generated Elc. Cont.	^{103}Rh	33.3%	33.71%	1.3%
	^{51}V	55.5%	57.32%	3.18%
Sensitivity	^{103}Rh	11.4E-22	11.6E-22	1.45%
	^{51}V	6.61E-23	7.4E-23	10.7%

Results and Discussion

Emitter's neutron absorption rate plays an important role in the current drive and sensitivity. As can be seen in Fig. 5, neutron sensitivity increases with the increase of the emitter radius, which follows [13].

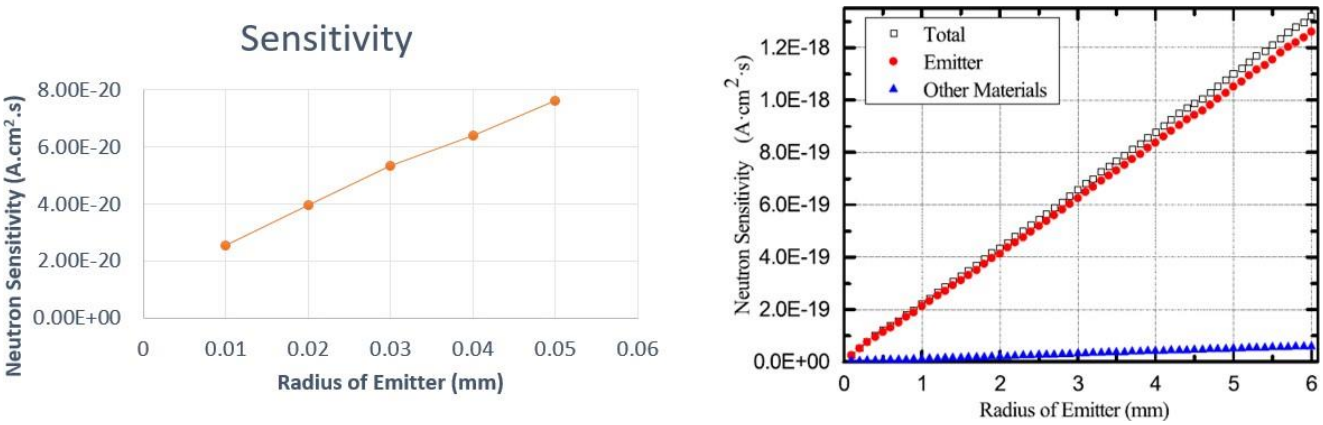

Fig. 5. SPND sensitivity as a function of emitter thickness. Left: Simulation Results, Right: Results reported in [13].

In these simulations, the initial insulation radius was set to 35 mm and increased to the final amount of 75 mm. The detector's sensitivity changes in this radial interval of insulation, as specified in Fig. 6, with the orange box, are almost independent of the thickness of the insulation.

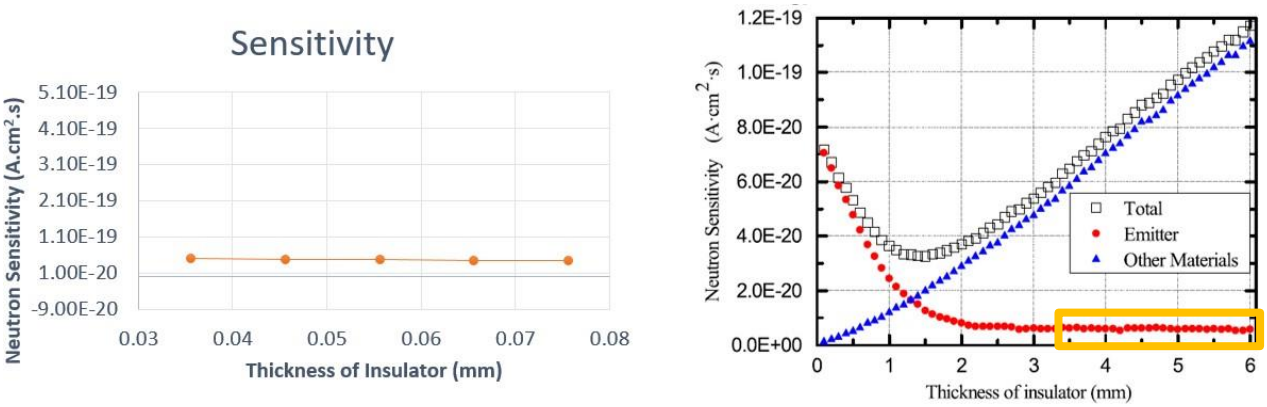

Fig. 6. SPND sensitivity as a function of insulation thickness. Left: Simulation Results, Right: Results reported in [12].

Increasing the thickness of the collector reduces the sensitivity, Fig. 7, but these changes do not affect the neutron sensitivity slope significantly, and can be neglected in the intervals of this study.

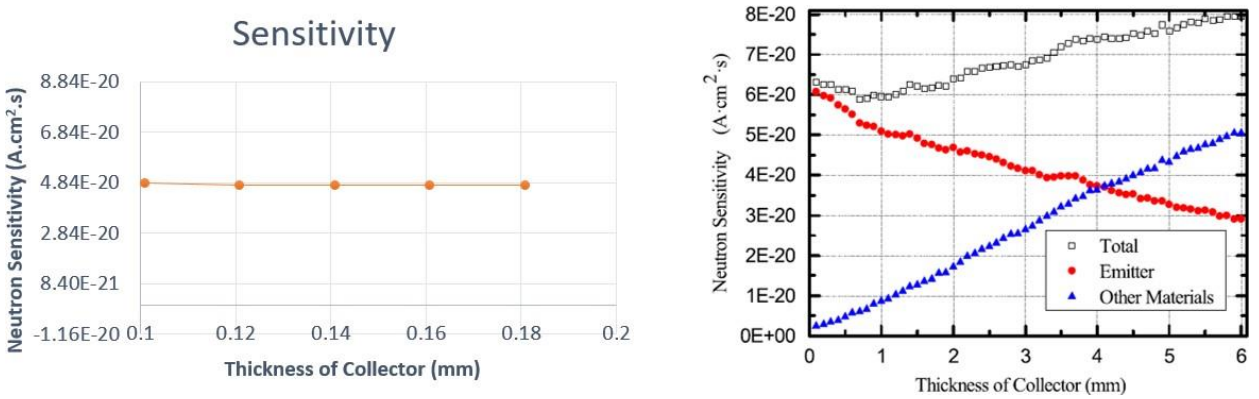

Fig. 7. SPND sensitivity as a function of collector thickness. Left: Simulation Results, Right: Results reported in [12].

Sensitivity changes due to SPND length have also been studied. The results indicate that in lengths below 10 cm, the neutron flux in emitter shows a catastrophic drop by increasing the length of SPND, and after that, the neutron flux in the emitter becomes almost independent of the detector's length. Finally, as shown in Fig. 8, from 10 cm up, the detector's sensitivity is almost independent of its length.

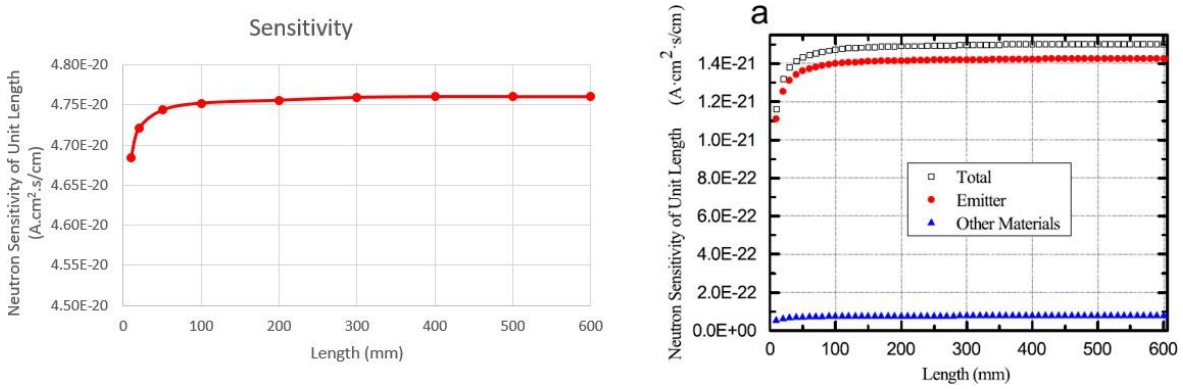

Fig. 8. SPND sensitivity as a function of detector's length. Left: Simulation Results, Right: Results reported in [12].

Conclusions

In this paper, the simulated SPND was validated by comparing the results of the simulation with the results presented in [10]. Then, the SPND sensitivity for different materials of the emitter, insulation and collector was investigated. As reported in Table 3, the rhodium emitter is more sensitive to neutron than the vanadium emitter. Also, the use of stainless-steel or Inconel as the SPND collector will not affect the sensitivity of this detector. By selecting aluminum oxide as the insulator, in addition to increasing SPND sensitivity, resistance of Al2O3 against radiation is also effective, unlike the MGO resistance.

The SPND sensitivity was then examined in terms of emitter length. According to the calculations, the neutron flux in the emitter decreases with the increase of the emitter radius. On the other hand, with the increase in the emitter radius, the absorption of neutrons in the emitter increases, and ultimately the sensitivity of the SPND improves with the increase in the emitter radius. Also, the insulation thickness, as shown in Fig. 6, has no significant effect on SPND sensitivity. Changing the thickness of the collector over the simulated interval has no significant effect on SPND sensitivity. As the collector's thickness increases, the absorption of neutrons in the collector region increases follows a neutron flux decrease in the emitter and as shown in the right of Fig. 7 leads to the reduction of SPND sensitivity. In the end, the effect of the change of the detector's length on its sensitivity has been studied. As the SPND length increases, the neutron flux decreases in the emitter. But as the absorbed neutrons in the emitter increases by SPND length, as shown in Fig. 8, one can conclude that the detector's sensitivity is almost independent of the length of the detector.

Acknowledgements

Special thanks to Dr. Majid Khorsandi for his consultation as my professor.

References

[1] Knoll, G.F., Radiation Detection and Measurement. 4 ed. 2010, John Wiley & Sons.
[2] Vermeeren, L., Neutron and gamma sensitivities of self-powered detectors: Monte Carlo modelling. 2015 4th International Conference on Advancements in Nuclear Instrumentation Measurement Methods and their Applications (ANIMMA), 2015: p. 1-5.
[3] Alex, M. and M.D. Ghodgaonkar, Development of an Inconel self-powered neutron detector for in-core reactor monitoring. Nuclear Instruments and Methods in Physics Research Section A: Accelerators, Spectrometers, Detectors and Associated Equipment, 2007. 574(1): p. 127-132.
[4] Verma, V., et al., Feasibility study of self powered neutron detectors in fast reactors for detecting local change in neutron flux distribution. 2015. 1-4.
[5] Verma, V., et al., Self powered neutron detectors as in-core detectors for Sodium-cooled Fast Reactors. Nuclear Instruments and Methods in Physics Research Section A: Accelerators, Spectrometers, Detectors and Associated Equipment, 2017. 860: p. 6-12.
[6] Yu, J., Simulation of Dynamic Response of Self-Powered-Inconel-Neutron-Detector Lead Cables Using a Semi-Empirical Model, in Faculty of Energy Systems and Nuclear Science. 2013, Ontario Institute of Technology.
[7] COMPANY, B.W., Rhodium In-Core Detector Sensitivity Depletion. 1980.
[8] Todt, W.H., Sr., Characteristics of self-powered neutron detectors used in power reactors. 1998, Switzerland: European Nuclear Society.
[9] Ulybkin, A., et al., Compton (prompt-response) neutron detectors: Comparison of emitter materials through the nuclear transmutation model. Sensors International, 2020. 1: p. 100020.
[10] Cui, T., et al., A Monte-Carlo simulation method for the study of self-powered neutron detectors. Nuclear Instruments and Methods in Physics Research Section A: Accelerators, Spectrometers, Detectors and Associated Equipment, 2020. 954: p. 161383.
[11] Warren, H.D. and N.H. Shah, Neutron and Gamma-Ray Effects on Self-Powered In-Core Radiation Detectors. Nuclear Science and Engineering, 1974. 54(4): p. 395-415.
[12] Yue, S., et al. Imaging radioactive components inside a CANDU reactor using gamma radiation scanning. in Atoms for Power, Health and the Environment 31st annual conference of the Canadian Nuclear Society and 34th annual conference of the Canadian Nuclear Society and Canadian Nuclear Association. 2010. Canada: Canadian Nuclear Society.
[13] Zhang, Q., et al., Numerical optimization of Rhodium Self-Powered Neutron Detector. Annals of Nuclear Energy (Oxford), 2018: p. 519-525.
[14] Bozarth, D. and H .Warren. Leakage Characteristics of Magnesia-insulated and Alumina-insulated SPNDs in B and W Reactors. in transactions of the American Nuclear Society. 1976. Harpers Magazine Foundation 666 Broadway, New York, NY 10012.

ICNST 2024 International Conference on Nuclear Science and Technology
6- 8 MAY 2024 | Isfahan, Iran

Evaluation of Strategies/Options for Implementing the Decommissioning Project of the WWER Nuclear Power Plant (Paper ID: 1462)

B. Khosrowpour[1*], V. Jmashidi[1], S.H. Hosseini[1]
[1]*Faculty of Engineering, Ofogh Consultant Engineers, Tehran, Iran*
[*]*Email Address: behzad.khosrowpour@gmail.com*

Abstract

The decommissioning of a nuclear power plant (NPP) involves activities aimed at reaching a specified final state of the NPP to ensure safety and environmental protection after removing nuclear fuel and materials. Considering legal and regulatory documents, the planning and management of NPP decommissioning are responsibilities of operating companies. Making decision for decommissioning is affected by some factors such as depletion of the main components' service life, economic impracticability, potential hazards to personnel or the environment, and non-compliance with modern safety requirements. In accordance with requirement No. 8 of the IAEA GSR part 6 document, the licensee must select a decommissioning strategy consistent with national radioactive waste management policy, and justify the chosen strategy. Decommissioning begins with obtaining a regulatory license for the initial stage and ends upon completing all works outlined in the decommissioning project, as per the specified strategies/options. The best, safest, and most cost-effective strategy should be chosen from different options based on specific requirements and decontamination technologies following the issued license. "Liquidation - Immediate Dismantling" represents the optimal strategy for decommissioning WWER reactors in international publications.

Keywords: Decommissioning, Option, Strategy, Decontamination

Introduction

By the end of 2022, there were 411 operational nuclear reactors worldwide, with a decrease of 26 compared to the previous year. In 2022, construction of eight new NPPs began globally. Recrded data from 1959 shows a significant increase in the number of operable reactors, reaching 420 within 30 years; however, since 1989, the number of reactors has remained relatively stable, with a peak of 450 in 2018 [1,2]. Aging of many reactors will likely lead to an increase in decommissioning activities in the coming years, adding to the large number of inactive reactors. The purpose of a NPP decommissioning is to ensure reaching safe status and environmental protection after removing nuclear fuel and materials [2].

Research Theories

The process of decommissioning a NPP involves a complex set of actions aimed at addressing the following issues [2, 3]:

Developing technologies and technical resources for all decommissioning operations;

Protecting the environment, personnel, and the public from radioactive contamination;

Maximizing the use of "clean" equipment, with metals being dismantled and other material resources being released after decontamination during the NPP decontamination process;

Minimizing material, radiation, and financial expenses for the decommissioning works of the NPP, considering social and other factors;

Establishing the necessary regulatory, technical, and informational infrastructure;

To ensure safety during the decommissioning process, a technical database should be established containing required information determined by regulatory authority. The primary purpose of this database is to accumulate, store long-term, sequence, search, and present information on the business objects required for and influencing the works at the decommissioning stages, as well as information on the results of the works at the NPP decommissioning stage [1]. The general principles and requirements for ensuring the safety of NPP decommissioning are as the following [3]:

The safety criteria for NPP decommissioning are established by the codes and regulations for the use of nuclear energy, developed while considering recommendations from the IAEA and other international organizations.

The operating organization is responsible for ensuring the safety of decommissioning, including measures to prevent accidents, mitigate their consequences, record, control, and physically protect nuclear materials, radioactive substances, and nuclear waste; Additionally, it is responsible for environmental protection and monitoring within the industrial site and the sanitary protection zone.

Technical and organizational decisions should be validated by previous experience, tests, necessary studies, or experience working with prototypes.

Before commencing NPP decommissioning works (before obtaining a license), the operating organization establishes organizational NPPs responsible for the direct activities to ensure safety during decommissioning; these NPPs have the necessary rights and allocated financial, material, and human resources;

When preparing for and executing the decommissioning of an NPP and throughout the decommissioning process, irrespective of the chosen decommissioning option/strategy, the following main activities are conducted [3,4]:

Operation of safety-critical systems and equipment, including ensuring the safe operation of other at the NPP site.

Decontamination of NPP systems, equipment, premises, and site areas, along with reutilization decontamination.

Preparation for dismantling and actual dismantling of NPP equipment and building structures.

Management of generated waste, including nuclear and decommissioning materials.

The extent of implementing the above activities, as well as the list of systems and equipment used for decommissioning depends on the chosen decommissioning strategy/option, the stage of work, and is determined by the "NPP decommissioning project"; comprehensive inspections should be conducted according to a specific program, including [4,5]:

Assessing the radiological conditions on the premises and at the industrial site, creating charts for radioactive contamination and/or dosage rates.

Surveying the condition of structures, systems, equipment, buildings, and facilities to be dismantled to estimate their strength and residual life, considering long-term observations of natural processes' effects and phenomena on building and structure foundations, including the hydrographic features of the site state.

Surveying the condition of facilities, equipment, and systems required for decommissioning to estimate their operability and reliability during decommissioning.

Determining the radionuclide composition and physical and chemical condition of radioactive materials, their activities, localization zones, and the nature of their generation.

Estimating the radiation characteristics of spills and fragments of nuclear fuel resulting from accidents and remaining in the core section and other technological systems.

NPP Decommissioning strategies/Options

The selection of an appropriate decommissioning strategy/option for a specific NPP should be based on a multifactor analysis, taking into account various factors that are applicable to the entire NPP; these factors encompass considerations related to safety, environmental protection, and public health, the cost of the work, the socioeconomic impact on the regional situation, and the availability of necessary financial,

technical, material, and human resources [4]. In line with the IAEA's stance, there are three primary strategies/options for NPP decommissioning [2, 3, 5]:

Immediate dismantling;

Deferred dismantling, also known as secure enclosure;

Entombment;

The decommissioning strategies/options considered for NPPs in the USA are:

Safe storage ("SAFSTOR");

Entombment ("ENTOMB");

Decontamination ("DECON");

Figures 1-6 depict examples of activities associated with the aforementioned strategies [2-11]:

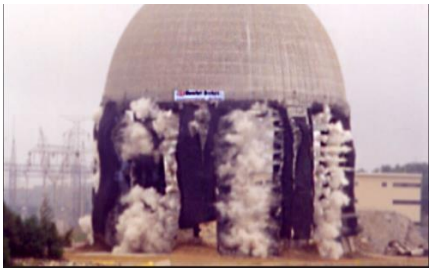

Fig. 1. The strategy: immediate dismantling

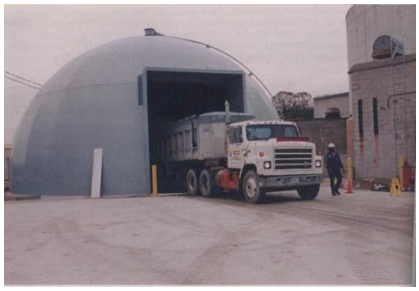

Fig. 2. The strategy: safe storage

Fig. 3. The strategy: deferred dismantling, also called secure enclosure

Fig. 4. The strategy: safe storage

Fig. 5. The strategy: entombment

Fig. 6. The strategy: Decontamination

Currently, the "Decommissioning Option/Strategy for Nuclear Facilities, Radiation Sources, and Storage Facilities," which is approved by authorize Nuclear Organization, is being proposed for implementation. The term "option" in this context is conceptually similar to the IAEA term "strategy" [5]. Following IAEA recommendations [5], and considering the requirements of the document [6], the "Decommissioning Option/Strategy for Nuclear Facilities, Radiation Sources, and Storage Facilities" adopted by the State Corporation Russian Nuclear Institutes is proposed [4]. During the preliminary stage of technical design development, the decommissioning strategy/option of "NPP liquidation" is proposed as the fundamental strategy/option for the NPP, aligning with the immediate dismantling strategy – "Liquidation – Immediate Dismantling." Figure 7, illustrates the diagram of the Concept of NPP decommissioning under these strategies/options [4].

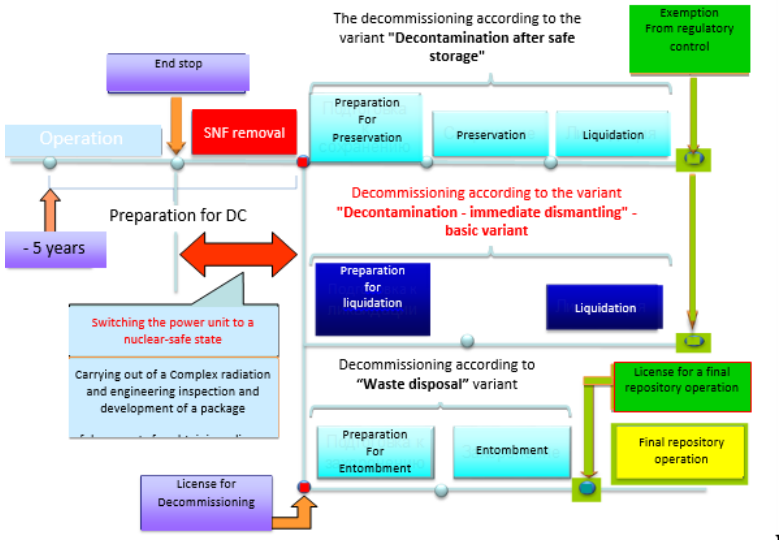

Fig. 7. Diagram of the NPP decommissioning Options/Strategies

Due to its complexity, the decommissioning (DC) process can be divided into multiple stages and may involve the long-term safe storage of the NPP under supervision. This aims to reduce the facility's radiation hazard level due to the decay of radioactive substances while ensuring the maintenance of safety barriers at an appropriate level; the stages of the decommissioning process are characterized and defined by the final states of the facility achieved upon completion of the stage works; when selecting the decommissioning option/strategy for the NPP, the "conversion" (diversion) option/strategy cannot be disregarded [7]. Hence, the following factors can be considered as supporting arguments for choosing a particular option/strategy [6]:

The presence or absence of a storage building for the permanent disposal of the reactor components and the availability of necessary financial resources for permanent disposal.

Reduction of radioactive waste processing and conditioning expenses due to the decrease in radioactivity.

Potential utilization of NPP operational personnel experience, plant infrastructure, and process equipment.

Licensing conditions;

Avoidance of facility monitoring and maintenance expenses in the case of choosing a safe preservation strategy.

Re-use of the NPP industrial site;

The main criteria for the successful completion of any decommissioning option/strategy are as follows [8, 11]:

Compliance with all codes and regulations, ensuring the completion of all works and activities outlined in the Decommissioning Project.

Achievement of the decommissioning project's objective.

Fulfillment of all decommissioning project licensing requirements.

NPP Decommissioning, strategy of "Liquidation after Storage under Supervision"

Decommissioning commences with the acquisition of a decommissioning works license from a regulatory body for the NPP and concludes upon the fulfillment of the entire scope of works outlined by the NPP decommissioning project in accordance with the "Liquidation after Storage under Supervision" option. This variant is divided into three stages [5, 7]:

Stage 1: Preparing for storage under supervision; Stage 2: NPP storage under supervision;

Stage 3: NPP decontamination;

During Stage 1, "Preparing for Storage under Supervision," various engineering designs, production, and organizational-methodical documentation are developed to encompass all emerging aspects in carrying out the works at this stage. This includes [7]:

Updating technological normative rules for NPP equipment and systems operation.

Compiling an inventory of equipment and systems supporting the NPP flow processes, indicating their operational status.

Compiling an inventory of dismantled equipment systematized according to the radioactivity level, further use, form of storage, disposal, entombment, and other factors, indicating residual life, residual value, and other essential characteristics.

According to the aforementioned stages, the following process control and management measures are to be implemented:

Removal of radioactive working environment and deactivation of equipment and systems not used at the NPP decommissioning stages.

Justification of the necessary number of personnel for the NPP decommissioning.

Localization of highly active NPP equipment in line with the decommissioning project.

Modernization of the radiation monitoring system (Figure 8 [11]).

Installation and setup of a radioactive waste handling complex (decontamination, pressing, etc.).

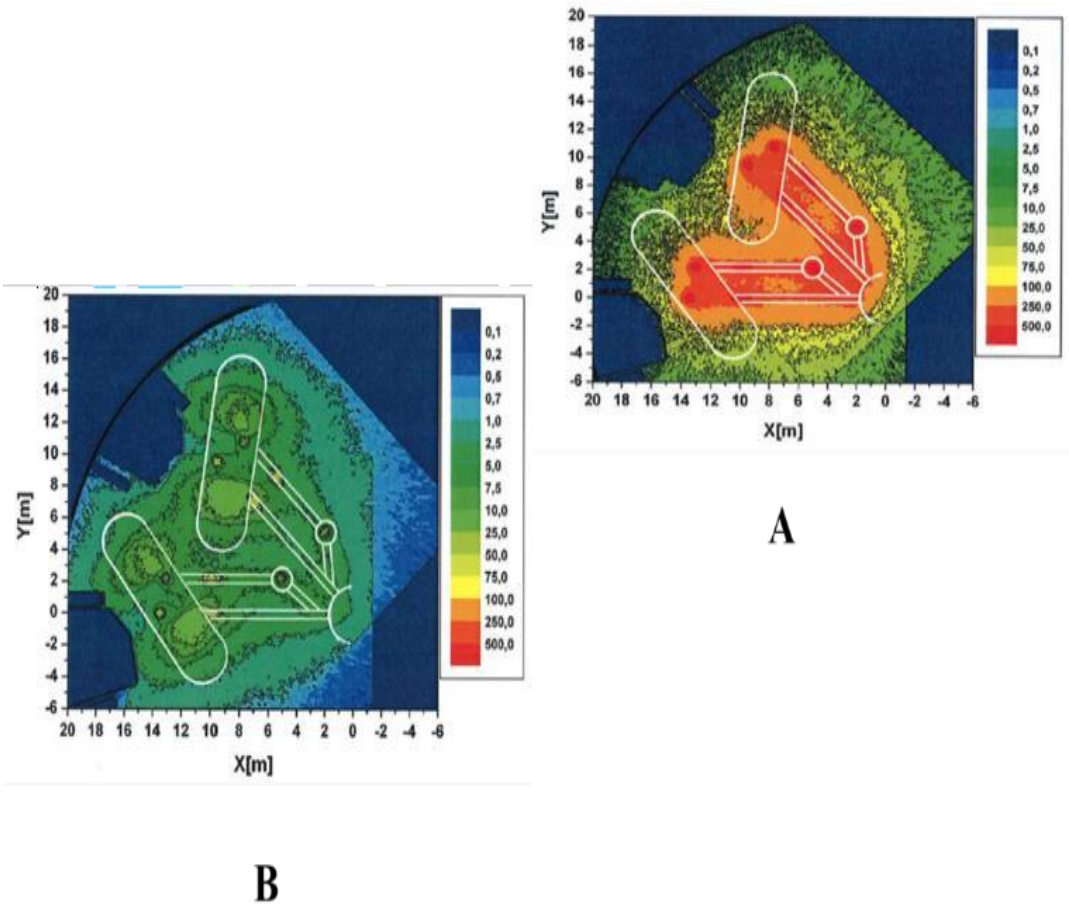

Fig. 8. Radiation Monitoring in Decommissioning Projects

In the second stage of NPP decommissioning, "NPP Storage under Supervision," which is the longest stage ranging, from 30 to 70 years, the following main activities and works are conducted [4-5]:

Operation of operable equipment, systems, buildings, and structures at this stage.

Ensuring reliable operation of necessary equipment, systems, and engineering structures, including renovation, modernization, and repair if required.

Dismantling of "clean," mildly, and medium-contaminated process systems equipment followed by utilization or processing.

Decontamination of equipment, structures, and premises being dismantled.

Radioactive waste processing.

Developing technologies, design documentation, and preparing equipment and tools for NPP decontamination works.

Maintaining a database on the NPP decommissioning.

Developing and documenting a procedure for the operation of the NPP equipment and systems at the "Clearance of the NPP" stage.

Radiation environmental monitoring.

The third stage commences with a decision by the operating organization on the completion of the second stage works, and the initiation of the third stage works; at this stage, the following main works and activities are planned [1-6]:

Complete dismantling of radioactive equipment and structures localized and not dismantled at previous stages.

Decontamination of NPP buildings and structures and their transfer from a "radiation" facility state to a "non-radiation" facility state.

Processing and removal of all radioactive waste to the final isolation facility for storage or entombment.

Dismantling of unused NPP buildings and structures, if necessary.

Re-planning the cleared industrial site territory, if necessary.

During this stage, the remaining NPP equipment and systems are operated in accordance with the developed operation technology regulations for this stage, and radiation monitoring systems and safety barriers and systems are decommissioned and dismantled, ensuring safety for personnel and the environment; this stage concludes upon receiving documents from supervisory authorities confirming the rescinding of NPP classifications as a "radiation facility" [4].

NPP Decommissioning, Option/Strategy of "Liquidation - Immediate Dismantling"

Clearance with immediate dismantling involves the placement of both low-radioactive and highly radioactive waste, including highly active in-vessel internals, into burial grounds or temporary waste storage facilities; plant equipment, structures, and parts containing radioactive substances are either removed or decontaminated to a level allowing the site to be deregistered for unrestricted use and the license to be revoked [4]. Advantages of the immediate dismantling option are [1-9]:

Proper removal or elimination of all radioactivity exceeding specified levels;

Potential for the site to be used for other purposes shortly after shutdown.

Ability for operational personnel with in-depth knowledge of the NPP to plan and perform decommissioning works.

Feasibility of using existing on-site infrastructure for radioactive waste management.

Utilization of existing premises for waste burial, eliminating uncertainty about future locations.

Potential cost savings due to anticipated future price increases.

Elimination of uncertainties associated with the legal framework and availability of funds.

Drawbacks of the immediate dismantling strategy:

Potential increase in personnel radiation exposure due to less time for radioactive decay.

More significant initial investments of financial resources and immediate need for accessibility of facilities for waste disposal or storage.

This option/strategy is divided into two stages [2]:

Stage 1: "Preparation for Liquidation - Immediate Dismantling";

Stage 2: "NPP Liquidation - Immediate Dismantling";

During Stage 1, similar to the "Liquidation after Storage under Supervision" option/strategy, design, process, and organizational-methodical documentation are developed; this includes various activities such as adjusting the process schedule for NPP equipment and systems operation, modifying equipment and systems operation instructions, compiling inventories, developing coordination plans for decommissioning works distribution, and developing quality assurance programs for contractors [2].

In Stage 2, activities include operating equipment, systems, buildings, and structures for safe NPP conditions during decommissioning, dismantling of systems and equipment, organizing areas for dismantled equipment and radioactive waste processing, decontamination, recycling and conditioning of radioactive waste, radiation monitoring, updating operation technology regulations, developing design documentation, and maintaining a database on the NPP decommissioning [2].

The decommissioning of the NPP according to the Option/Strategy, “Entombment”

The purpose of this decommissioning option/strategy is to establish a final isolation facility (near-surface entombment) based on the structures of the NPP being decommissioned; this facility is designed to accommodate and localize equipment components with radioactive contamination, building structures, and conditioned radioactive waste on-site; it involves constructing physical barriers to prevent unauthorized access to the localization zone and ensure the radiation safety of personnel, the

population, and the environment throughout the potential radioactive waste hazard period [5]. This decommissioning option is divided into two stages [2-3]:

Stage 1: Preparing NPP for disposal;

Stage 2: Disposal of the NPP;

Stage 1, "Preparing NPP for disposal", involves activities such as the complete dismantling of non-radioactive equipment, dismantling of low-contaminated and low-activated NPP equipment and systems, processing, and preparation of all radioactive waste for disposal, establishing confinement areas, transferring buildings and structures to non-radiation-dangerous status, and setting up monitoring and control systems for safety barriers integrity and radiation monitoring [2-3].

Stage 2, "NPP Disposal" includes creating final isolation for radioactive waste, dismantling unused NPP buildings and structures, preparing the cleared site for unlimited industrial use, re-grading the site territory if necessary, and obtaining a license for the new facility operation [2-3]. The main types of work carried out during the "NPP Liquidation - Immediate Dismantling" stage under the approved NPP Decommissioning Project include operating equipment, complete dismantling of equipment and NPP systems, decontamination of NPP facilities, processing and conditioning of generated radioactive waste, dismantling of building structures, site reclamation, and radiation monitoring of works and the environment [2-3].

NPP Decommissioning, Strategy/Option of "Conversion"

Furthermore, in addition to the previously mentioned NPP decommissioning options/strategies, the NPP may also undergo decommissioning according to the "Conversion" option/strategy; the term "conversion" refers to the NPP decommissioning option/strategy in which its designated use and process profile are entirely changed; under this option/strategy, the facility is transitioned from being nuclear- or radiation-hazardous to a conventional site; this transformation involves the replacement of main process equipment and complete removal of all radioactive materials, substances, and waste from the industrial site; while old NPP systems, equipment, and building structures may be partially repurposed to create a new similar installation, it is essential to determine the future use profile before commencing decommissioning under this option/strategy [3].

Safety

The decommissioning of nuclear power plants (NPPs) is a growing concern worldwide, driven by factors such as economic viability, public acceptance, and political considerations. To achieve sustainable decommissioning, it is crucial to prioritize radiation safety for personnel, the public, and the environment. This paper reviews existing research on decommissioning strategies, emphasizing the need for a systematic approach. Moreover, decommissioning strategies and their associated influencing factors were reviwed and the importance of outlining the organizational structure responsible for radiation safety during NPP decommissioning, including the goals, tasks, and qualifications of the radiation safety subdivision were highlited. By understanding these critical aspects, effective and safe decommissioning strategies that align with sustainable practices can be developed [8].

As part of the organizational and technical measures for radiation safety assurance during the decommissioning of the NPP, the following works should be prioritized [8-11]:

Inspection and technical examination of protective barriers to assess the remaining life for further operation or replacement.

Replacement of radiation monitoring system equipment that has reached the end of its service life.

Establishment and commissioning of a measuring complex for radiation monitoring of materials intended for re-use.

Development of methods for the radiation monitoring of materials intended for unrestricted and limited re-use.

Equipping a decontamination point transport and containers with waste at the building exits or inside the NPP buildings.

Renovation of exhaust ventilation systems to ensure proper airflow direction and ventilation.

Retaining premises zoning during dismantling and adjusting ventilation characteristics based on survey results.

Decontamination of internal surfaces of exhaust ventilation systems ducts. Considering 60 years of NPP operation and the potential activation of structural elements, significant reactor building components may contain radioactive sources; the SuperMC software has been utilized to simulate the calculation of emitted doses from key concrete structure elements; figure 9 to 11 show some of these calculations [10]:

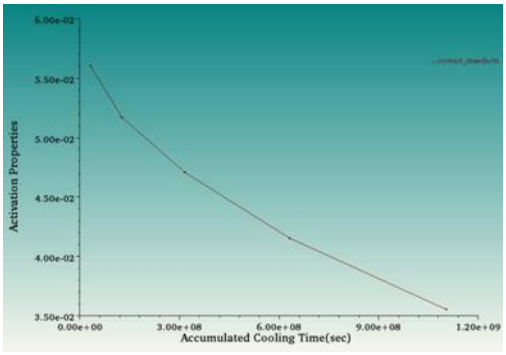

Fig. 9. The diagram of the received dose from gamma radiation emitted by 56Fe for 60 years of reactor operation and cooling times of 1, 2, 3, 4, and 5 years.

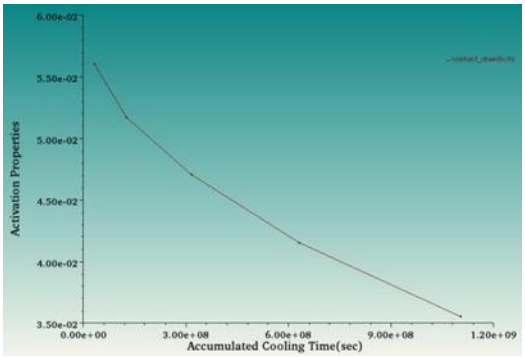

Fig. 10. The diagram of the received dose from gamma radiation emitted by 58Ni for 60 years of reactor operation and cooling times of 1, 2, 3, 4, and 5 years.

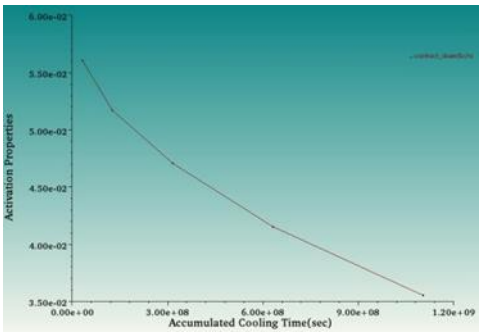

Fig. 11. The diagram of the received dose from gamma radiation emitted by 54Fe for 60 years of reactor operation and cooling times of 1, 2, 3, 4, and 5 years.

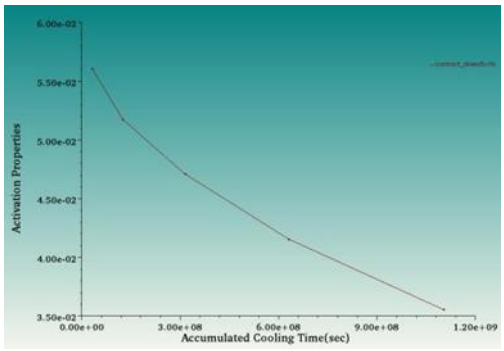

Fig. 12. The diagram of the received dose from gamma radiation emitted by 59Co for 60 years of reactor operation and cooling times of 1, 2, 3, 4, and 5 years.

Results and discussion

Based on the results of radiation safety measurements, the strategy of decommissioning the NPP after 60 years of operation and five years of cooling time was proposed as a suitable strategy, considering a radiation protection approach; furthermore, following an analysis of materials, IAEA recommendations, and the options/strategies for decommissioning nuclear facilities, radiation sources, and storage facilities, the "Liquidation - Immediate Dismantling" is proposed as the fundamental strategy for the decommissioning of the NPP.

References

[1] NP-091-14 Ensuring safety when decommissioning nuclear facilities. General provisions.

[2] IAEA, (1999). WS-G-2.1 Decommissioning of Nuclear Power Plants and Research Reactors. – IAEA Safety Guide No. WS-G-2.1.

[3] NP-012-16 Rules of safety provision at decommissioning of the nuclear plant unit.

[4] "Rosenergoatom" (2019), acknowledged the urgency of completing a new "Methodology decommissioning.

[5] IAEA, GSR Part 6 Decommissioning of Facilities. General Safety Requirements.

[6] National Policy and Strategy for Radioactive Waste Management in I.R.Iran, (2005) no. DO0094 issued by IRWA Co. in February.

[7] I.A.Engovatov, Vestnik MGSU(2013), Integrated Engineering and Radiation Inspection in NPP Units Decommissioning Problem . No.1. p. 125-132.

[8] SP 2.6.1.2612-10, (2010), "General sanitary rules of radiation safety"

[9] A.D. Zimon, V.K. Pikalov, M.: IzdAT (1994). Decontamination. 336 pages.

[10] V. Jamshidi, S.H. Hosseini, J. Emami, B. Khosrowpour (2020). Calculation of elements activation in concrete of reactor building for the decommissioning of a nuclear power plant by Chebyshev method. 6 th. International Reliability and safety Engineering Conference.

[11] Elagin, Yu. P. Atomnaya Tekhnika za Rubezhom (2007) Regulation of NPP Decommissioning Processes. - N 3. - Pp. 1-12.

ICNST 2024 International Conference on Nuclear Science and Technology
6- 8 MAY 2024 | Isfahan, Iran

Monte Carlo Calculation of Pulse Height Distribution of a Neutron Proportional Counter (Paper ID: 1480)

Peiman Rezaeian[*1], **Sepideh Shafiei**[1]
[1]*Radiations Application Research School, Nuclear Science and Technology Research Institute, AEOI, Tehran, Iran*

Abstract

In this study, the pulse height distribution of a neutron-proportional counter was simulated using the Monte Carlo method. The proportional counter consists of a layer of A-150 with a thickness of 1070 µm and a propane gas region with a thickness of 2000 µm. Incident neutrons undergo elastic scattering with a hydrogen nucleus in A-150, and the recoil proton enters the gas region, depositing some energy in this region. The response of the detector is defined as the energy deposition normalized to one incident particle. Furthermore, the response of the detector at different neutron energies was calculated for various energy deposition thresholds. The calculation results showed that setting an energy deposition threshold on counts provides a detector response that is less energy-dependent. A detector with weak energy dependency can be used as an ideal dosimeter.

Keywords: Monte Carlo Calculations, Neutron Proportional Counter, Dosimeter, Energy Deposition, Threshold

Introduction

Neutrons have no electrical charge, and the mechanism for detecting them is based on an indirect method [1]. Therefore, neutron detectors rely on a conversion process where an incident neutron interacts with a nucleus to produce secondary charged particles. These particles are then directly detected, and the presence of neutrons is deduced from them. Neutrons can have elastic or non-elastic interactions with the nucleus of materials [2]. The elastic interaction of neutrons is efficient for fast neutrons interacting with light nuclei such as hydrogen and helium. Various types of neutron detectors utilizing elastic or non-elastic interactions include gas-filled detectors [3], scintillators [4], semiconductors [5], solid state detectors [6], and polymers [7]. Neutrons will interact with atomic nuclei through several mechanisms. The type of interaction depends on the neutron energy. So, different methods can be used for neutron detection. Gas-filled detectors using BF3 or 3He gas are employed to detect thermal neutrons [8]. Detectors with 4He or CH4 gas can be used for fast neuron detection [9]. Additionally, nuclear track detectors like CR-39 and boron-doped CR-39 are applied for fast and thermal neutron detection, respectively [10, 11]. Although different methods or detectors are used in each energy region, neutron detectors still exhibit some energy dependency [12, 13].

In this paper, the pulse height distribution of a neutron proportional counter was simulated using a Monte Carlo method. The investigated detector consisted of a layer of A-150 plastic and a gas region filled with propane gas. Protons generated due to the elastic interaction of neutrons with the nucleus of the A-150 layer enter the propane gas and deposit their energy in this region. The response of the detector is defined as the deposit energy per one incident neutron. Simulation results indicated that the response of the detector depends on the incident neutron energy. To reduce the energy dependency of the response, an energy deposition threshold was set on pulse counting. The results reveal that considering an energy threshold deposition can be useful to decrease the energy dependency.

Research Theorie

In this study, the A-150 is considered a converter. Elastic scattering dominates the interactions of fast neutrons with A-150 plastic. The incident neutrons undergo elastic scattering with hydrogen nuclei in A-150, and the recoil proton enters the gas region (propane) and deposits some energy in the gas region. This energy is proportional to the pulse height of the detector.

Calculation Method

The C++ program tracks the histories of incident neutrons, generated protons in the A-150 layer with, and the energy deposition in the gas region. The atomic composition of the A-150 layer is extracted from [13]. According to its composition the fraction weight of Carbon and Hydrogen is 77% and 10%, respectively. The detector's response, in this case, is defined as the energy deposition distribution normalized to one incident particle. The Geometry configuration of the simulations is depicted in fig. 1.

The charged particle generating due to carbon interactions have very small ranges (less than 10 μm [13]). So, these particles are stopped in the A-150. So, these particles have no effect in the pulse height distribution of the detector.

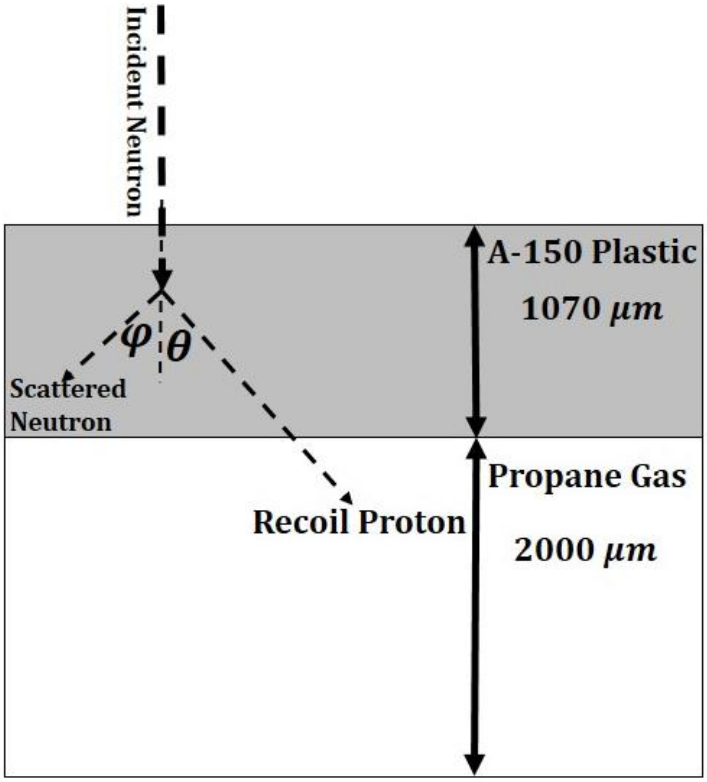

Fig. 4. The geometry configuration of the simulations

In simulations, the position of the generated protons in A-150 plastic (x) is determined using equation. 1.

$$x = -\frac{1}{\Sigma_t} ln(1-\xi) \qquad 0 < \xi < 1 \qquad (1)$$

Where Σ_t and ξ are the macroscopic cross-section of neutrons in A-150 plastics and a random number with a uniform distribution between 0 and 1, respectively. Due to the domination of elastic scattering in neutron interactions with protons, only elastic interactions are taken into account to determine Σ_t.

In the written code, if the position of the interaction is less than the length of the A-150 plastic, the scattering angle of the generated proton is calculated by

$$\theta = \cos^{-1}(2\zeta - 1) \qquad 0 < \zeta < 1 \qquad (2)$$

Where ζ is a random number with a uniform distribution between 0 and 1. This equation is used by considering that the energy distribution of protons after elastic interactions with neutrons is isotropic in the center of mass system of the two particles.

By knowing the scattering angle of protons, their energies are determined, utilizing:

$$E_p = E_n(\cos\theta)^2 \qquad (3)$$

Using the value of the recoiled proton energy, the range in the converter is extracted from the PSTAR library [13]. If this range is enough for the proton to enter the propane, the energy of the proton when it enters the propane is determined

$$E_{EP} = E_p - \int_0^{L_{A-150}} \left(\frac{dE}{dx}\right)_{A-150} dx \quad (4)$$

Where LA-150 and $\left(\frac{dE}{dx}\right)_{A-150}$ are the distance traveled by the proton and the stopping powers of protons in A-150 plastic, respectively. In the next step, it is determined whether the proton stops or passes through the propane gas. If the proton stops in the propane, the energy deposited in the gas is equal to the proton's energy when entering the gas region. If the proton crosses through the gas region, the deposited energy using the distance traveled by the proton, L_{Pr}, and its stopping power in propane gas, $\left(\frac{dE}{dx}\right)_{Pr}$, is determined as follows:

$$E_D = E_{Ep} - \int_0^{L_{Pr}} \left(\frac{dE}{dx}\right)_{Pr} dx \quad (5)$$

Using the values of energy deposited by protons in propane gas, the pulse height distribution and the response of the detector are calculated.

Results and Discussion

Fig. 2 shows the simulated results of the pulse height distribution of various neutron energies.

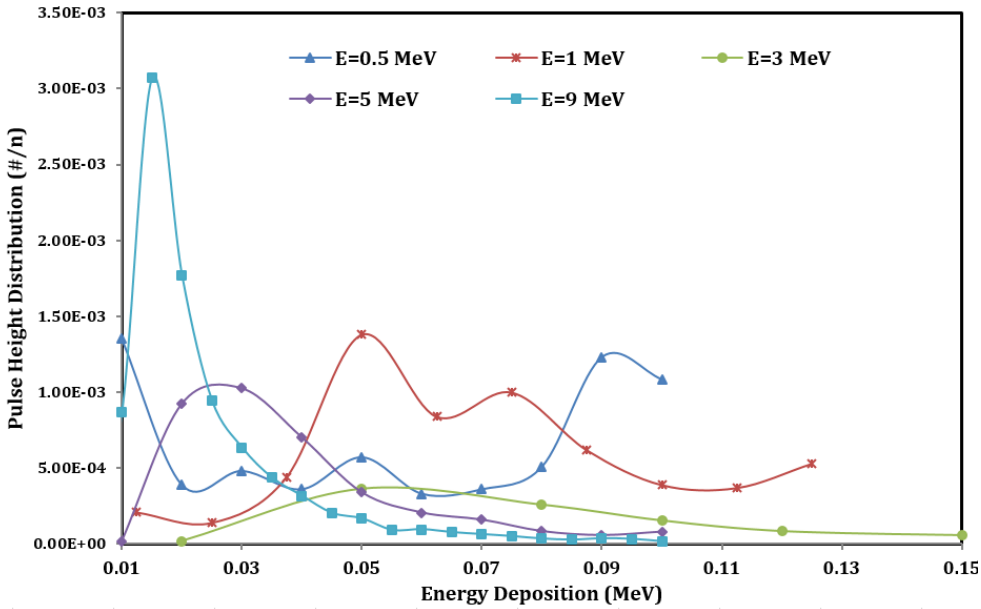

Fig. 5. Pulse height distribution of the simulated detector for various neutron energies.

As indicated, the response is represented as the energy deposition distribution normalized to one incident neutron. It shows that low-energy neutrons deposit more energy in the gas than high-energy neutrons and that the detection efficiency (i.e., counts n-1) increases as neutron energy increases. The former can be explained by the stopping power effect. That is, the stopping power of a proton increases as the proton energy decreases, and therefore, the recoil protons produced by neutrons of low energies

tend to deposit more energy. The latter can be explained by the proton-range effect. That is, the energetic recoil protons produced in A-150 by high-energy neutrons tend to have longer ranges than those produced by low-energy neutrons and therefore have a higher probability of reaching the gas region.

The pulse height distribution for neutron sources 241Am-Be and 252Cf was simulated as shown in Fig. 4. The used spectrum for 241Am-Be and 252Cf are shown in Fig. 3[14]. Sampling was performed using the cumulative distribution function.

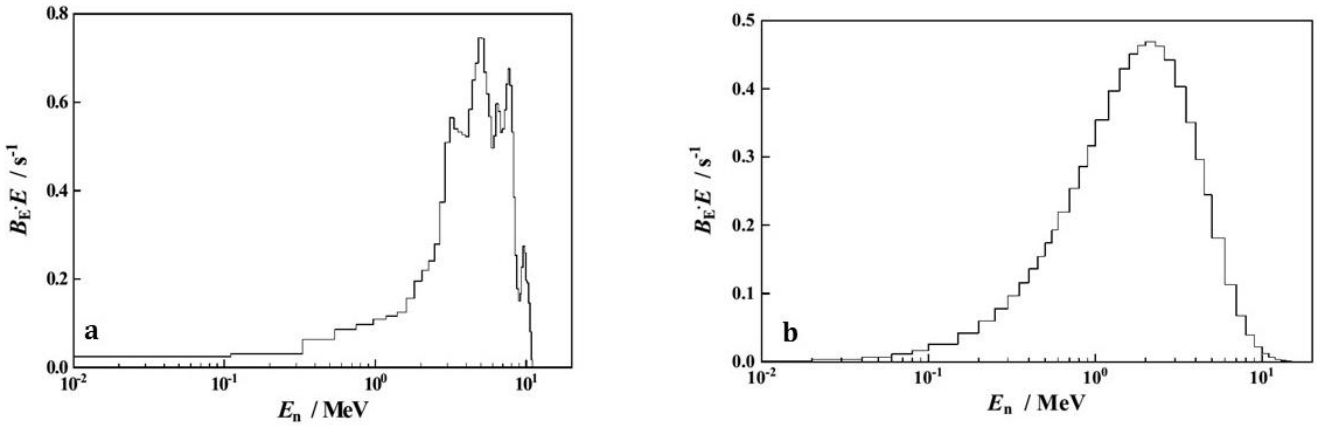

Fig. 3. The neutron spectrum of a: ^{241}Am-Be and b: ^{252} Cf [14].

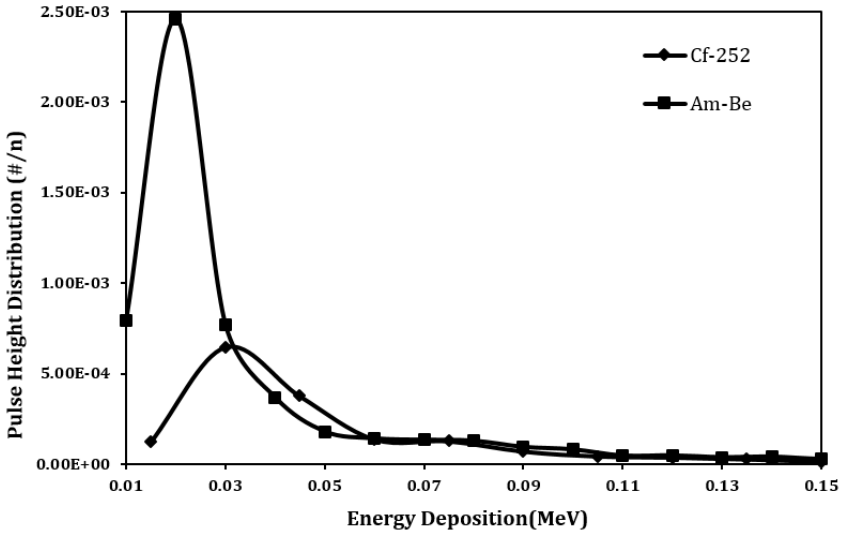

Fig. 4. Pulse height distribution calculation for 241Am-Be and 252Cf neutron sources.

As shown in both cases, most neutron events have energy depositions less than 0.05 MeV. The few events that exceed 0.05 MeV are attributed to the protons that have very long tracks in the gas region. Also, the detection efficiency of 241Am-Be neutrons is higher than that of 252Cf neutrons, and the energy depositions are lower for 241Am-Be neutrons compared to 252Cf neutrons. These observations

are consistent with the fact that 241Am-Be neutrons are, on average, more energetic than 252Cf neutrons.

To evaluate the calculations, the obtained results have been compared with experimental results reported in reference [15]. These results are depicted in Fig. 5. As shown in this picture, the simulation results are in agreement with the experimental data.

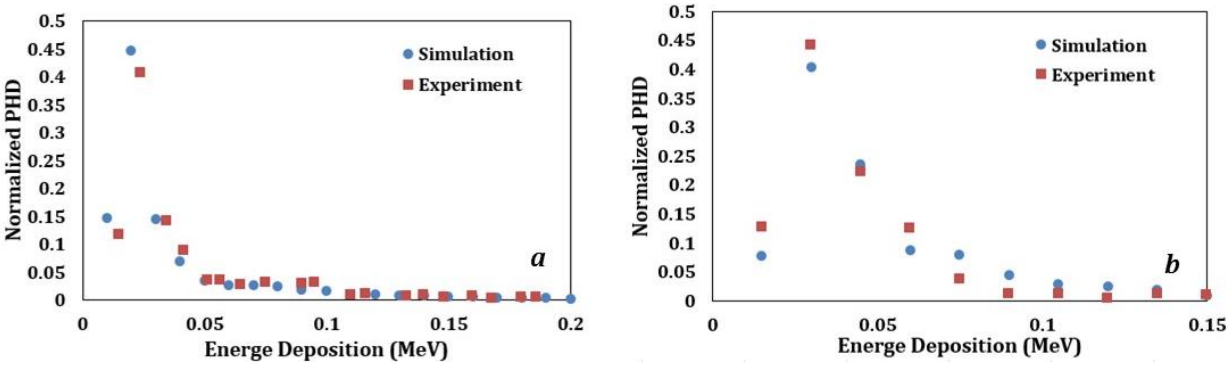

Fig. 5. Evaluation the simulation results with experimental data reported in reference [14]. a: ^{241} Am-Be,b: ^{252}Cf .

In Fig. 6 the number of pulses as a function of energy at different energy deposition thresholds is depicted. These curves were obtained from Fig. 2 by integrating the counts that have energy depositions above the corresponding threshold value.

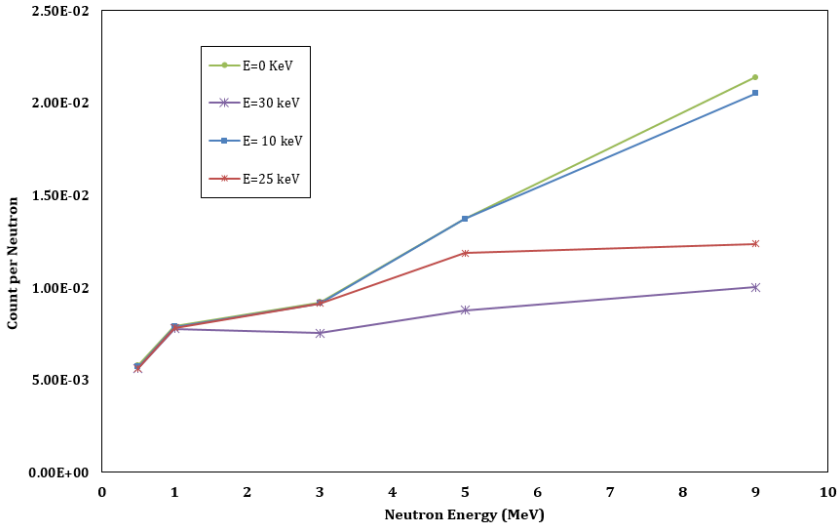

Fig. 6. Count per incident neutron as function of neutron energy in differnet energy threshold.

As shown in this figure, by increasing the deposition energy threshold, the number of counts at higher energies decreases. Since the energy deposition decreases as neutron energy increases, setting an energy deposition threshold would suppress the response of high-energy neutrons, and the detector's response is independent of neutron energy.

Conclusions

In this study, the pulse height distribution of a neutron-proportional counter is simulated using the Monte Carlo method. The simulated detector, like any detector, suffers from some energy dependencies in its responses.

Improvements to the energy response of the simulated proportional-counter have been made by setting an energy deposition threshold on the response of the detector. The results indicate that the proportional counter can be made less energy-dependent by using an energy deposition threshold.

Since the energy of the radiation is usually unknown, a detector with a weak energy dependence on its response would be ideal. These types of detectors can be used as dosimeters. The results of this study can be used to design neutron dosimeters with an ideal response curve.

References

[1] G. F. Knoll, ”Radiation Detection and measuremnts”,3rd edition, John Wiley & Sons. Inc, 1999.

[2] J. R. Lamarsh, ” Introducton to nuclear reactor Theory”,Addison-Wesley Reading, MA(1966).

[3] A.D. Mullen et al, ” Simulating gas-filled neutron detector response with DRiFT”, Nuclear Instrument and Methods in Physics Reserch A, 106(2024), 169194.

[4] J. A. Harvey and N. W. Hill, ” Scintillation detectors for neutron physics research”, Nuclear Instrument and Methods in Physics Reserch A, 162(2024)507-529.

[5] Frank H. Ruddy, ” A Review of the Effects of Fast-Neutron Irradiation on the Performance of 4H-SiC Schottky Barrier Detectors”, IEEE Transactions on Nuclear Science, 17 (2024).

[6] Gary W. Phillips et al, ” Neutron spectrometry using CR-39 track etch detectors”, Radiation Protection dosimetry, 120 (2006)457-460.

[7] P. Rezaeian et al., ” Development of a new pressure dependent threshold superheated drop detectro for neutrons”, Nuclear Instrument and Methods in Physics Reserch A, 11(2015), 50-56.

[8]T. W. Crane, “Gas Mixture Evaluation for 3He Neutron Detectors,” Nuclear Safeguards Research and Development program Status Report, LOSAlamos Scientific Laboratory report LA-7030-PR (March 1978), p. 39.

[9]T. L. Atwell and H. O. Menlove, “Measurement ofthe Time Resolution of Several ‘He and CH4 Proportional Counters “, Nuclear Safeguards Research Program Status Reporg September-December 1973, Los Alamos Scientific Laboratory report LA-5557-PR (February 1974).

[10] A. M. Abdalla et al.,” Fast neutron detection in CR 39 and DAM-ADC nuclear track detectors”, Nuclear Instrument and Methods in Physics Reserch A, 108(2015), 24-28.

[11]Takao Tsuruta and Norimichi Juto, ”Neutron Dosimetry with Boron-Doped CR-39 Plastic”, Journal of Nuclear Science and Technology, 21(1984)871-876.

[12] G. M. Hassib, S. A. Kasim and E. Piesch, ”Neutron energy dependence of different track etch detectors”, Radiation Effects, 45, 1-2, (1979)57-60.

[13] Berger, M. , Coursey, J. and Zucker, M. (1999), ESTAR, PSTAR, and ASTAR: Computer Programs for Calculating Stopping-Power and Range Tables for Electrons, Protons, and Helium Ions (version 1.21), http://physics.nist.gov/Star, [online], http://physics.nist.gov/Star (Accessed March 9, 2024)

[14] ISO/DIS 8529-1 Intrenational Standard, Refernce Neutron Radiation, Part 1, Characteristics and Method of Production. 2000.

[15] C-K. Chris Wang, M. Seidaliev and A. Mandapaka, Development and Test of a GEM-Based TEPC for neutron Protection Dosimetry, Health Physics, 2007.

International Conference on Nuclear Science and Technology
ICNST 2024
6- 8 MAY 2024 | Isfahan, Iran

Simulation of 60Co standard source using electrodeposition method: Effect of electrolyte conductivity on thickness (Paper ID: 1481)

Meisam Fathinejad[1*], Hamid Reza Shakur[1], Mostafa Najafi[2], Taher Hossienzade Kebria[1]
[1]Science and Technology Center of Physics, Imam Hossein Comprehensive University, Tehran, Iran.
[2] Science and Technology Center of Chemistry, Imam Hossein Comprehensive University, Tehran, Iran.

Abstract

An appropriate standard source for particle spectroscopy should be thin, possess a homogeneous distribution on a flat and smooth substrate, and exhibit suitable activity to achieve better energy resolution spectra. Electrodeposition, being one of the most common methods for preparing standard sources for high-resolution spectroscopy, is employed to meet these requirements. To fabricate a high-quality standard source using electrodeposition method, numerous parameters need optimization, including electrolyte type, electrode type (Cathode quality), geometric shape of the anode, electrolyte pH, temperature control, deposition mass, current density, and deposition time. Simulation of standard sources using the COMSOL software allows us to quantitatively determine the final layer thickness formed on the cathode substrate in the electrodeposition process with minimal experimental work. In this paper a mathematical model to predict the electrodeposition of cobalt on stainless steel as cathode in an electrochemical cell with platinum electrodes and cobalt acetate as the electrolyte was developed. Moreover, thickness of deposited layer as a function of electrolyte conductivity was studied. Results showed that with decrease in the electrical conductivity of the electrolyte a decreasing trend in the simulated thickness coatings was observed. The model accurately predicts the trend of effect of electrolyte conductivity on coating formation. The model can thus be used as a starting point to predict effect of process parameters on electrodeposition thickness.

Keywords: Electrodeposition, 60Co Standard Source, Electrolyte conductivity, Thickness dependence, COMSOL.

Introduction

Radioactive sources are employed across various scientific and technical domains, including physics, chemistry, geology, medicine, industry, agriculture, environmental education, and research. These radioactive sources may vary significantly, possessing different characteristics such as origin (type of radiation), activity level, mass, chemical properties, physical shape, and dimensions. Consequently, the production of radioactive sources encompasses a broad spectrum, categorizing them into two primary qualitative and quantitative groups. While the first group focuses on specific features of the source, such as shape, thickness, and uniformity, the second group, in addition to these characteristics, also

requires determining the quantity of radioactive materials [1]. Various methods exist for producing standard sources for calibrating nuclear detectors, including Electroplating, Molecular plating, Vacuum sublimation, Precipitation, Electrospraying, Electrostatic precipitation, and Electrodeposition. Each of these methods has its own strengths and weaknesses. An ideal standard source for particle spectroscopy should be thin, have a homogeneous distribution on a flat and smooth substrate, and possess suitable activity to achieve better energy resolution spectra. The spectral characteristics of particles always hold greater significance in nuclear data measurements than any other form of measurement [2]. Electrodeposition is one of the most common methods for preparing high-resolution particle sources for spectroscopy. Electrodeposition is a process that, using electric current in an electrodeposition cell, forms a dense, uniform, and adherent layer on a metal surface. This process of deposition is primarily used to alter the surface properties of a substance. In a metallic electrodeposition cell, the metal onto which the layer is to be deposited is placed on the cathode bed, and oxidation occurs in the anode while reduction reaction occurs at the cathode, resulting in the formation of a layer on the cathode bed. An electrodeposition cell comprises a cylindrical cell (typically made of Teflon or polyethylene), a flat metal cathode made of stainless steel, and an anode made of platinum, usually in the form of a meshed disk with a diameter smaller than that of the cathode [3]. To manufacture a high-quality particle source, numerous parameters in the electrodeposition cell must be optimized, including the type of electrolyte, type of electrode (cathode quality), geometric shape of the anode, electrolyte pH, temperature control, deposition mass, current density, and deposition time. Electrolyte conductivity is important parameter for an electrodeposition system as they dictate the overall efciency of flow of ions in the electrolyte system and thus optimization of this parameter is necessary. In this manuscript we report the development of a mathematical model to predict the electro deposition of cobalt in an electrochemical cell with stilnes steel as the electrode. Therfore, the aims of this research is to predict the thickness of a standard 60Co source layer and evaluate the effect of electrolyte conductivity on the thickness of the electrodeposition process layer using COMSOL software. The model can thus be used as a starting point to predict effect of process parameters on electrodeposition thickness.

Theoretical Description and Model Development

In this research, the development of a mathematical model for simulating electrodeposition cell to construct a standard 60Co source has been studied. Simulation using the mathematical model serves as a tool for assessing the performance of a studied system used over time. Simulations are conducted under specific input conditions, and the output of the model is compared with the actual system [4].

The software COMSOL, fundamentally, is a comprehensive simulation toolkit capable of solving differential equations using the finite element method (FEM) in a graphical simulation environment. Therefore, the following assumptions were proposed for the development of the mathematical model:

1) Dilute Solution Theory was applied, which indicates the existence of negligible interactions between species in the solution.

2) Physical transport and convective parameters throughout the solution are constant.

3) The solution is homogeneous.

4) No homogeneous chemical reactions occur in the electrolyte.

5) The current density distribution on the electrode surface is uniform.

The current density distribution is represented by the Butler-Volmer equation, expressing the current dependence on the electrolyte solution composition in the vicinity of the electrode surface and the relative activity of solid-state species, as well as the exponential dependence of the current on the potential difference. This equation represents the difference in current intensity between anodic and cathodic processes and is formulated as follows.

$$I = i_0\left[exp\left(-\frac{\alpha F\eta}{RT}\right) - exp\left(\frac{(1-\alpha)F\eta}{RT}\right)\right] \quad (1)$$

Where I- Electric current density (A/cm²), i_0- Exchange current density (A/cm²), α- Transfer coefficient ($0< \alpha <1$), η- Overpotential (V), F- Faraday's constant (96485 C/mol), R- Ideal gas constant (8.314J/molK), T- Absolute temperature (K). Mass transport of charge carriers in the electrodeposition process occurs first due to the migration of charge carriers in an electric field, secondly due to diffusion driven by concentration gradients, and thirdly due to convection in a fluid field [5]. Therefore, the mass transport equation, which is expressed based on the flux of ion species in the solution and is famous as the Nernst-Planck equation, is formulated using the following relationship.

$$N_i = -Z_i U_i F C_i \nabla\varphi_L - D_i \nabla C_i + V_i C_i \quad (2)$$

In the expressed equation Ni denotes the molar flux, Zi represents the charge number, Ui stands for mobility, F signifies Faraday's constant, Ci pertains to concentration, Di signifies diffusivity, φ_L represents the potential within the electrolyte, and Vi symbolizes velocity[6]. Additionally, the velocity of species i can be approximated linearly as follows.

$$Vi = - Ui\ \nabla\mu i \quad (3)$$

Where Ui represents the mobility, thus the density of species fluxes is obtained accordingly.

$$Ji = ciVi = - Uici\ \nabla\mu i = -\nabla\mu i \quad (4)$$

The Einstein relationship between mobility and diffusion coefficient is expressed as follows, where in this relationship, R is the universal gas constant.

$$Di = UiRT \quad (5)$$

When an electric field E is imposed within an electrodeposition cell, positive charge carriers are driven towards the cathode surface at a velocity V along the direction of the field E. Consequently, both the current density and the velocity of the charge carriers can be determined accordingly.

$$J = \frac{I}{A} = \frac{Ne}{AT} = \frac{NeL}{ATL} = \frac{N}{AL} \times \frac{L}{T} \times e = nVe = neV \quad (6)$$

The direction of J is aligned with the direction of the motion of charges, and if the charges are negative, it is opposite to their direction. Additionally, in this equation, ne represents the charge carrier density.

Electrolyte conductivity

Electrolyte conductivity is a crucial parameter in the electroplating process, as the conduction of ion flow within the electroplating cell relies on the electrolyte. Additionally, the electrolyte serves as a medium for the movement of electrons in the electroplating cell, hence optimizing these parameters is essential. The conductivity of a solution due to the movement of negative ions towards the anode and positive ions towards the cathode in an electroplating cell results in an applied potential, indicating the solution's ability to conduct current. The resistance of a solution containing a constant concentration of an electrolyte, at a constant temperature, is directly proportional to the distance between two electrodes L and inversely proportional to the cross-sectional area of the electrodes A, and it is calculated through the following relationship.

$$R = \rho L/A \quad (7)$$

In this equation, R (Ω) is expressed in ohms as a function of the unit proportionality constant ρ (Ω-m) in meters, known as resistivity. Since the ability of a solution to conduct electricity decreases with an increase in its electrical resistance, the conductivity of a solution is defined as the inverse of resistivity, with its unit being siemens per meter [7].

$$\sigma = \frac{1}{\rho} = \frac{J}{E} \quad (8)$$

$$J = \frac{I}{A} = \frac{V}{RA} = \frac{VL}{RAL} = \frac{L}{RA} \times \frac{V}{L} \quad (9)$$

$$J = \frac{1}{\frac{RA}{L}} \times \frac{V}{L} = \frac{1}{\rho} E = \sigma E \quad (10)$$

Thus, the density of deposition current in the electrodeposition cell can be expressed through Ohm's Law.

$J = \sigma E$; $E = -\nabla\varphi \rightarrow id = -\sigma l \nabla \varphi l$ (11)

Where σl denotes the electrolyte conductivity.

Thickness of deposition

The amount of deposition is expressed by Faraday's laws of electrolysis, which state that the quantity of substance deposited on an electrode is proportional to the amount of electric charge passing through that electrode, which can be calculated by the following equation.

$m = Q / nF$ (12)

In the expressed equation, m represents the mass of the deposited substance (g), Q denotes the amount of electric charge passing through the system (Coulombs), n signifies the number of electrons exchanged per ion, F represents Faraday's constant, which is equal to 96485 C/mol. Therefore, the cumulative charge utilized in the electrodeposition process can be computed by multiplying the current (Amperes) passing through the electrode by the deposition time (seconds), provided that the deposition current remains constant. If the current fluctuates during the deposition process, it can be determined as follows:

$Q = \int_0^t I(t)dt$ (13)

In the electrodeposition process, the deposit weight, w(g), can be determined by the product of the number of moles of the reduced metal and the atomic weight of the deposited metal (g/mol), as follows:

$W = \frac{M}{nF} \int Idt$ (14)

And also, the thickness of the deposited layer, d (cm), can be expressed by the following equation:

$d = \frac{IMt}{\rho AnF}$ (15)

Where ρ is the density of the metal (g /cm3) and A is the area of deposition (cm2).

Results AND Discussion

Figure 1 illustrates a depiction of the simulation geometry of the electrodeposition process. The COMSOL finite element method software was utilized to simulate and predict the thickness of the layer formed on the cathode substrate with various electrolyte conductivity values. The simulation was set up in a (3D) and time-dependent manner. In this simulation, deposition occurs on the cathode substrate, while oxidation processes take place on the anode. Throughout the electrodeposition process, we neglected the free convection component based on our assumption that the solution is stagnant. Additionally, in this simulation, the electrodeposition process was considered a time-dependent phenomenon, and metal deposition progressed over time.

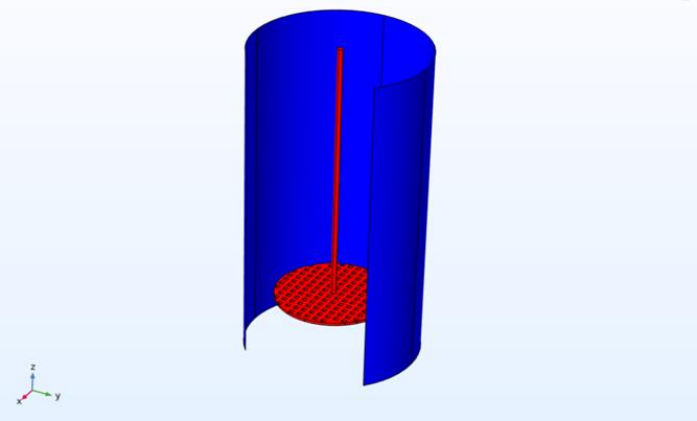

Fig. 1. A schematic of the electrodeposition cell with a grid platinum anode designed using COMSOL.

For evaluating the influence of electrolyte conductivity on the thickness of the deposition layer and conducting the stages of electrodeposition process simulation in the COMSOL software environment with different electrolyte conductivities of 0.0884 S/m, 0.884 S/m, 1.326 S/m, 1.768 S/m, 2.21 S/m, and 2.65 S/m over a period of 45 minutes and applying a voltage of 9 volts on a cathode substrate with a contact surface area of 2.2 cm^2 were investigated. The electrolyte consists of 4 ppm Co as Oxalate salt in 2.4 M aqueous ammonia solution. The electrolyte volume in the electrodeposition process was 5 mL, and a platinum anode was selected for this cell. To achieve a standard source with excellent energy resolution using the electrodeposition method, all relevant parameters involved in the source fabrication must be optimized. These parameters include electrolyte pH, solution temperature control, and current density. The distance between the anode and the cathode is another important parameter. However, simulated set up for electrodeposion process in this work is based on the experimental work of P. Sahoo and et al. in 1998 [8]. According to the above reference, the distance between the anode and cathode was set to 0.5 cm to facilitate the deposition of electrodeposits. This process was simulated at a temperature of 70°C. Changing the layer thickness on the cathode substrate as a function of electrolyte conductivity presented in Figure 2. As evident from Figure 2, an increasing trend in the thickness of simulated layers is observed with increasing electrolyte conductivity. According to Ohm's law, an increase in electrolyte conductivity, with other parameters held constant, results in a higher electrical current in the solution. This increase in electrical current implies a faster migration rate and deposition of ions on the electrode surface. The accelerated deposition rate of particles leads to a thicker deposition layer, and this increased rate can enhance the adhesion of deposited particles to each other. Consequently, the elevated adhesion of deposited particles improves the strength of the deposition layer. From another perspective, there is a direct correlation between electrolyte conductivity and the concentration of dilute solutions. Thus, as electrolyte conductivity increases, we observe a rise in solution concentration. Solution concentration is directly proportional to the number of ions (electric

charge carriers) per unit volume of the solution. Therefore, as the number of ions in the solution increases, so does the thickness of the layer on the cathode substrate. Additionally, a representation of the thickness of the deposited layer on the cathode substrate in a sample of electrolyte conductivity with a value of 0.0884 S/m is depicted in Figure 3

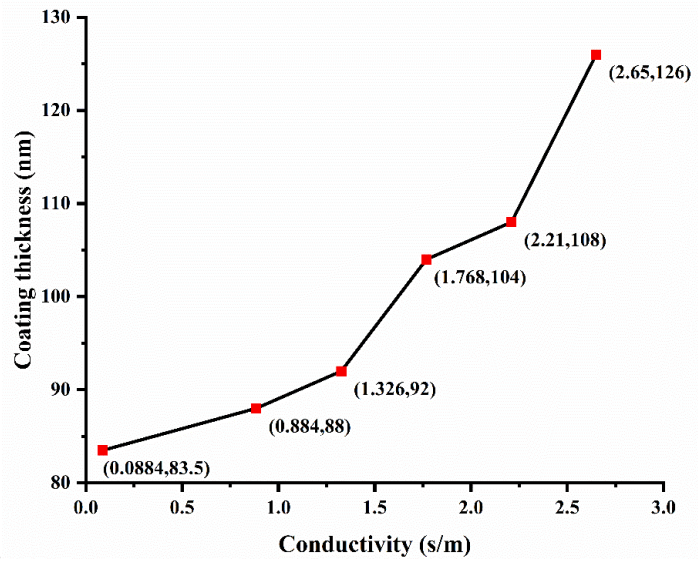

Fig. 2. Trend of increasing layer thickness on the cathode substrate with increasing electrolyte conductivity.

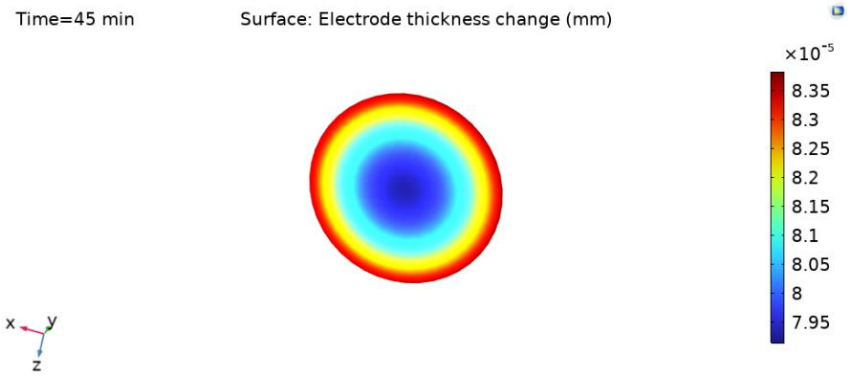

Fig. 3. A graphical representation of the thickness of the deposited layer on the cathode substrate in the COMSOL software at an electrolyte conductivity of 0.0884 S/m.

Electrolyte conductivity and surface roughness are two significant parameters in the electrodeposition process, as illustrated in Figure 4, directly affecting the uniformity of the deposited layer on the cathode substrate. In the electrodeposition process, the uniform distribution of electrical current plays a key role in the quality of the deposited layer on the cathode substrate. A uniform distribution of electrical current in the electrodeposition process leads to reduced roughness and increased uniformity of the layer surface on the cathode substrate. Therefore, achieving surface uniformity on the cathode substrate may be due to the reduction in layer resistance. Consequently, the reduction in resistance results in a

more uniform distribution of electrical current across the layer surface. As indicated by the trend in the graph, increasing the surface roughness and height in different electrolyte conductivities signifies a reduction in the uniformity of the layer formed on the cathode substrate.

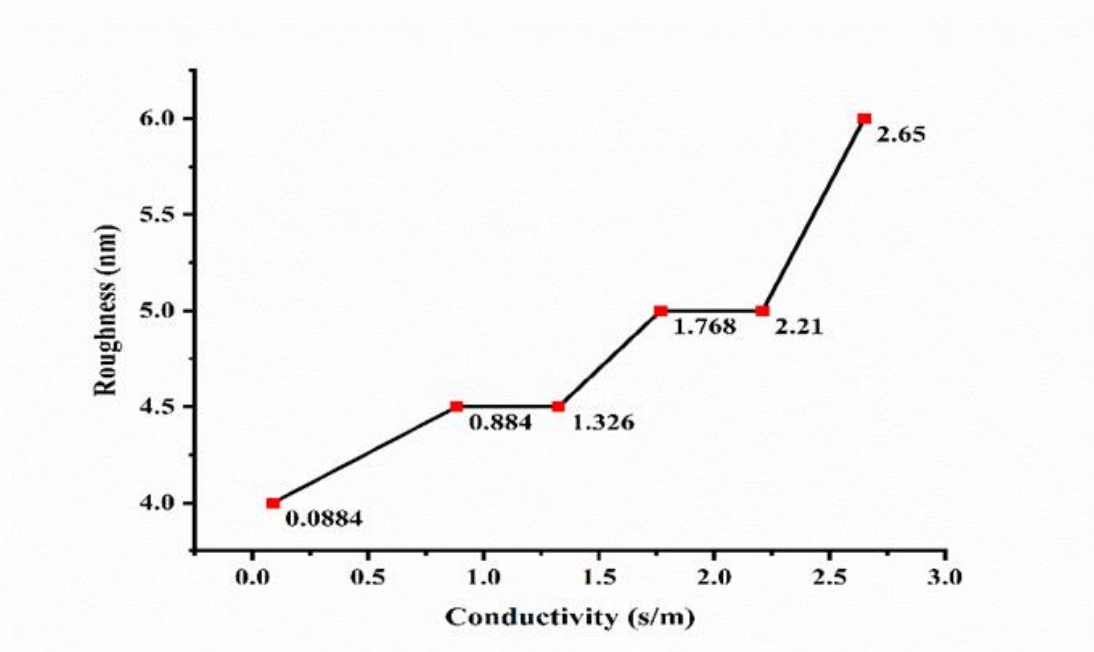

Fig. 4. The effect of electrolyte conductivity on the surface roughness and thickness of layers formed on the cathode surface in the electrodeposition process.

Fig. 5. illustrates the mass deposition as a function of time in the electrodeposition process. With an increase in the current, according to Equation 14, the rate of mass deposition also increases. This phenomenon is due to the increase in the number of metal ions deposited per unit time at the cathode substrate. Therefore, selecting an appropriate current depends on various factors such as the concentration of the solution, solution temperature, pH of the electrolyte, and desired thickness for deposition. Generally, higher currents can be used for faster deposition. However, using higher currents may reduce the quality of the deposition. High currents can increase defects in the deposition such as cracking and flaking. By utilizing these curves, the process parameters of electrodeposition can be adjusted to achieve maximum efficiency and effectiveness.

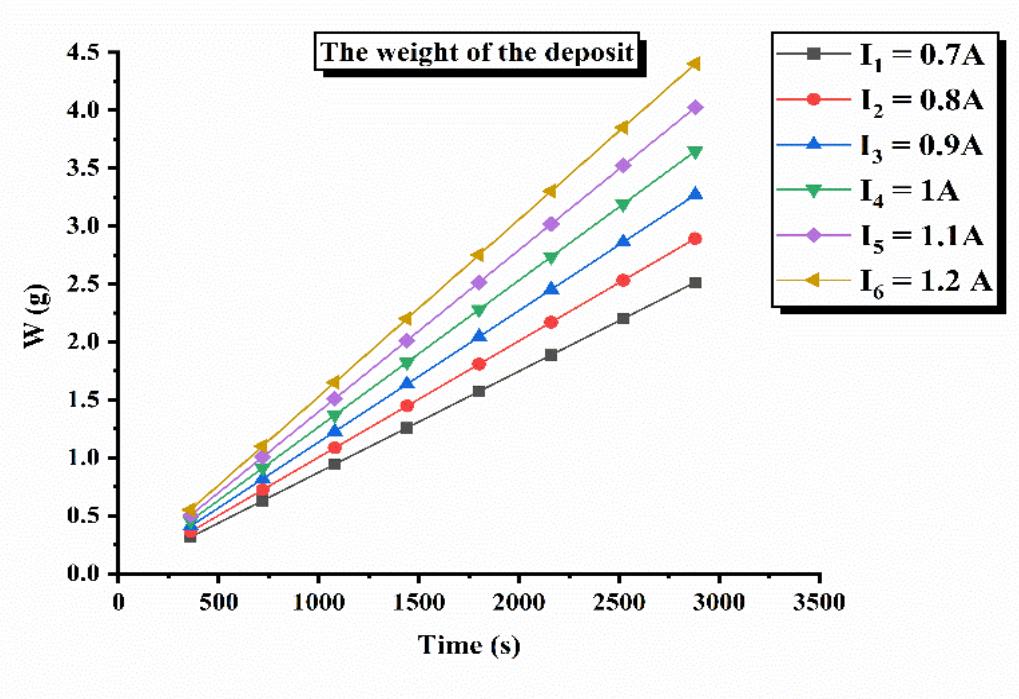

Fig.5. The effect of different current densities on the mass deposition in an electrolyte conductivity of 0.0884 s/m in the electrodeposition process.

Conclusions

We have successfully developed a mathematical model to simulate the electrodeposition process for fabricating standard cobalt sources and examined the impact of increasing electrolyte conductivity on the thickness of the layer on the cathode substrate. Consequently, simulating standard sources using the electrodeposition method and COMSOL software allows us to determine the final layer thickness on the cathode substrate with minimal experimental effort, only by measuring the conductivity of the standard source solutions. Hence, knowing the electrolyte conductivity parameter (σ) is crucial in the simulation process of standard source formation. This model accurately predicts the trend of the effect of electrolyte conductivity on layer formation on the cathode substrate. Therefore, it can serve as a starting point for predicting the impact of electrodeposition process parameters on layer thickness.

Refrence

[1] Goedele. Sibbens, and Timotheos Altzitzoglou. "Preparation of radioactive sources for radionuclide metrology." Metrologia 44, no. 4 (2007): S7

[2] N.Tsoulfanidis, and S. Landsberger, ."Measurement and detection of radiation.". (2021): CRC press.

[3] Young Gun. Ko, "Preparation and characterization of electrodeposited layers as alpha sources for alpha-particle spectrometry." Journal of Radioanalytical and Nuclear Chemistry 326, no. 2 (2020): 861-877.

[4] Anil. Mahapatro, and Santosh Kumar Suggu. "Mathematical modeling of the electrodeposition process." ECS Transactions 61, no. 26 (2014): 23.

[5] Bard, A.J, L.R. Faulkner, and H.S. White, " Electrochemical methods: fundamentals and applications". (2022): John Wiley & Sons.

[6] N. Obaid, R. Sivakumaran, J. Lui, and A. Okunade. "Modelling the electroplating of hexavalent chromium." In COMSOL Conference. Boston 2013. (2013).

[7] B.H. Vassos, "Electroanalytical Chemistry". Wiley-Interscience, (1983).

[8] P. Sahoo, and S. V. Narasimhan. "Electrodeposition of Cobalt at Trace Levels with a Special Reference to Preparation of 60Co Source." Radiochimica Acta 81, no. 3 (1998): 157-162.

ICNST 2024
International Conference on Nuclear Science and Technology
6- 8 MAY 2024 | Isfahan, Iran

Investigation of Pyrolytic graphite single-crystal (002) plane fine tuning effect on the reflected monochromatic neutron spectra (Paper ID: 1522)

Z. Gholamzadeh, R. Ebrahimzadeh*
Safety and Nuclear Research Reactor School, Nuclear Science and Technology Research Institute, Tehran, Iran,
E-mail for correspondence author: rebrahimzadeh@aeoi.org.ir

Abstract

Single-crystal graphite grown in highly preferred orientation of (002)-planes known as pyrolytic graphite is used in many research centers to make monochromatic neutron beam the exited neutrons from the radial beam channels of the research reactors. Simulation methods could be effectively used to predict the crystal behavior before time-consuming and high-cost experimental tests. The present work aims to investigate the effect of the PG(002) crystal fine tuning on the reflected neutron spectra quality in Tehran Research Reactor (TRR) D channel neutron beam line. Hence, Vitess3.4 and McStas neutron optic-based computational codes were used in the present work to study the mentioned parameter. To evaluate the obtained code data accuracy a benchmark study was carried out in the present work. The obtained simulations showed that fine adjustment of the crystal angle than the parallel incident neutron beam is very important. In addition, the crystal mosaic spread has noticeably effect on the reflected neutron intensity so that its change from 1.0° to 0.5° decreases the monochromatic neutron peak intensity about 12%. In addition, the simulations showed the crystal reflectivity change from 1 to 0.7 could decrease the monochromatic neutron peak intensity about 43%. Comparison of the experimental monochromatic reflected beam from PG(002) crystal with the carried out simulations showed there is good agreement between the two obtained spectra.

Keywords: PG(002) crystal, Neutron reflection, Vitess3.4, McStas, computational method

Introduction

It should be taken in attention nowadays the use of polycrystalline materials and pyrolytic graphite (PG) has led to a considerable improvement in neutron diffraction techniques. PG has been in use for about 30 years as a filter. Since in PG, crystallites are preferentially oriented along the hexagonal c-axis. The transmission of neutrons thru PG with c-axis parallel to the beam versus neutron wavelength, exhibits "absorption" lines due to Bragg scattering [1].

It was proven [2] that, it is possible to tune the PG plates for optimum scattering of second-order neutrons in a continuous wavelength range by varying the angle between the c-direction and the

incident neutron beam. If this angle is denoted by ψ, and if the mosaic spread is negligible in comparison with ψ, the lattice planes hkl will scatter neutrons in the following wavelength intervals:

$$2d_{hkl}\sin(\theta_{hkl}-\psi) \le \lambda \le 2d_{hkl}\sin(\theta_{hkl}+\psi) \quad for\ \theta_{hkl} \ge \psi$$

$$0 \le \lambda \le 2d_{hkl}\sin(\theta_{hkl}+\psi) \quad for\ \theta_{hkl} < \psi$$

On the other hand, the filter should be transparent for first-order neutrons. This region was found to cover the wavelength interval 1.12Å<λ/2<4.25Å [1].

The integrated reflectivity of the monochromatic neutrons from PG crystals cut along its c-axis is high within a wavelength band from 1 Å up to 6.5 Å. The monochromatic features of PG crystal is detailed in terms of the optimum mosaic spread, crystal thickness and reactor moderating temperature for efficient integrated neutron reflectivity within the wavelength band.

The distribution of the reflected neutrons P_{002}^{θ} from PG crystal cut along c-axis, as a function of mosaic spread were calculated by Adib et al. (2012), assuming the following input parameters: PG thickness t: 2 mm set at glancing angle 23.45°, FWHM of incident beam divergence is 0.4° and the wavelength band was from 0.01 Å to 4 Å. The result of calculation is displayed in Figure 1. As it is seen, the mosaic spread less than 0.5° could obtain favorable monochromatic FWHM [3].

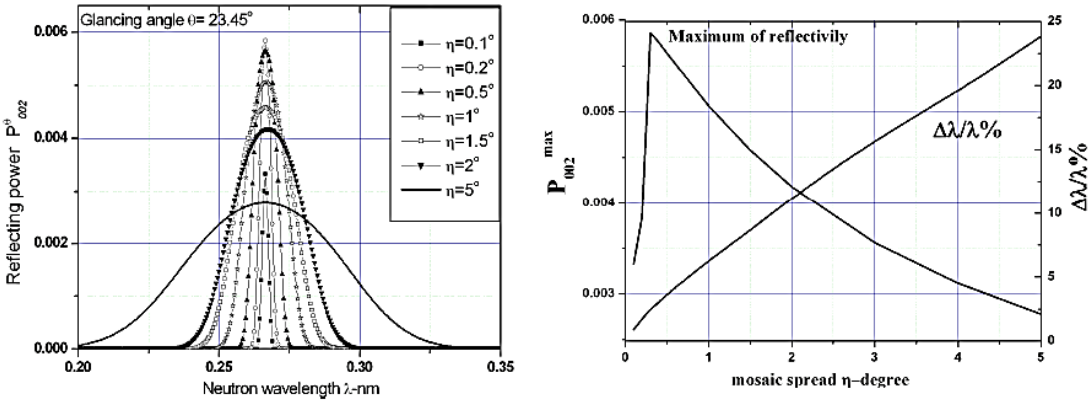

Fig.1. The wavelength distribution of the reflectivity from PG at various η, as well as the $\frac{\Delta\lambda}{\lambda}$ [3]

They theoretically showed that the integrated reflected neutron intensity of 2nd and 3rd orders that thermal reactor flux are even higher than that from the 1st order one. Therefore, the use of PG crystal as an efficient neutron monochromator is limited. To improve such case a neutron filter is essential. While, the intensities of higher order reflections from cold reactor flux are too small with respect to the 1st order one. So, for the neutron flux which exit from a channel of a steady state reactor with neutron gas temperature close to hydrogen one, if available, there is no need to use a neutron filter [3].

In Figure 4, reflection from a surface is presented.

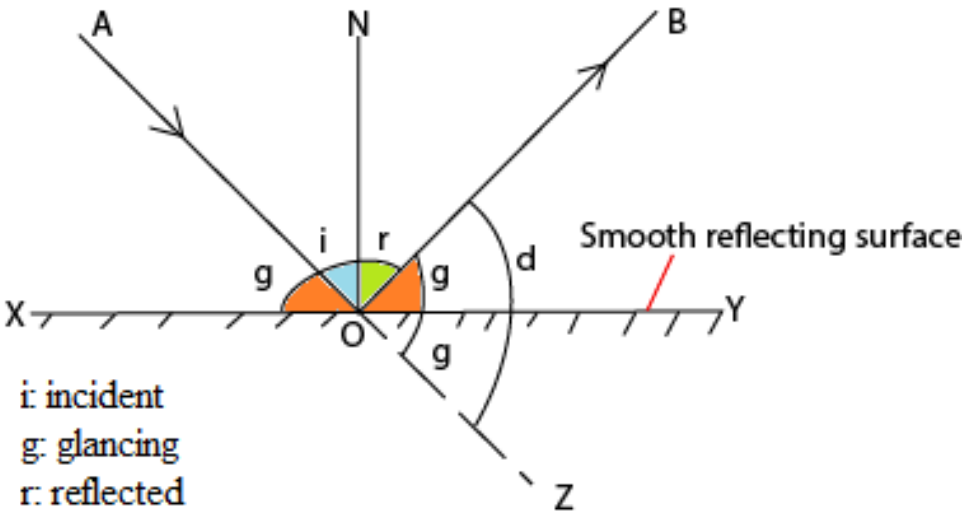

Fig.2. Reflection from a surface

The NPD facility of the 5 MW Tehran Research Reactor was simulated in the [4] study using Monte Carlo based programs. The outcomes of the simulation and the experimental data were contrasted. Theoretical results demonstrated good agreement with experimental data, suggesting that the Vitess 3.3a code performed satisfactorily in the neutron optic calculation part. In the study [5], two double axis neutron diffractometers, KARL and KANDI-II, which are situated at the Israel Research reactors IRR-1 and IRR-2, respectively, are modeled in order to validate the Monte Carlo ray-tracing simulation program McStas. These instruments' straightforward construction and limited component count make them ideal for simulation. Using the McStas neutron ray-tracing program, a detailed virtual model of the cold triple-axis spectrometer RITA-II at PSI, Switzerland, was developed in the [6] study. The virtual instrument's characteristics were meticulously adjusted in comparison to actual trials. The paper's findings demonstrate that, for a range of samples, virtual trials may replicate experimentally reported linewidths within 1-3 percent. It has also been demonstrated that quantitative estimations of linewidth broadening arising from finite domain widths in single-crystal samples, may be made using the detailed knowledge of the instrumental resolution discovered from virtual experiments, including sample mosaicity.

Tehran research reactor (TRR) is a pool-type thermal U3O8Al plate-type fueled research reactor which its D radial channel has been equipped to neutron diffraction. PG crystal with 2×50×75 mm3 dimension is used to make the incident neutron spectrum as monochromatic. The crystal glancing angle of 11° has been selected for TRR facility. The present study aims to investigate the PG crystal fine-tuning effects on the reflected monochromatic neutron beam quality using some optic computational codes. Finally, the obtained results are compared with the experimental results.

Research Theories

Construction of the light water Tehran Research Reactor (TRR) began in 1960, while it first achieved criticality and operation began in 1967. This reactor was designed to produce a thermal power of 5 MW. The normal operation mode of the reactor core involves 22 to 33 fuel assemblies. This reactor is equipped with 8 radial beam channels called A, B, C, D, E, F, H (tangential one which is considered as two beam channel). Beam channels A, D, E, and H have a diameter of 6 inches and are arranged radially at an angle of about 30° (Fig.3). Beam channels B and F have diameters of 12 inches and 8 inches, which are respectively arranged radially and as directly-faced toward the reactor core [7].

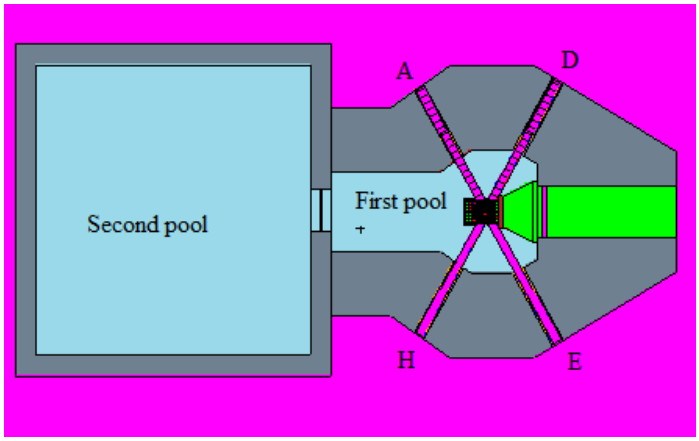

Fig.3. Schematic view of TRR pool and position of its four radial channels (A, D, E, H)

Vitess is a software widely used for simulation of neutron scattering experiments. Although originally motivated by instrument design for the European Spallation Source, all major neutron sources are available. Existing as well as future instruments on reactor or spallation sources can be designed and optimized, or simulated in a virtual experiment to prepare a measurement, including basic data evaluation. This note gives an overview of the Vitess software concept and usage [8].

McStas is a general tool for simulating neutron scattering instruments and experiments. It is actively supported by DTU Physics, NBI KU, ESS, PSI and ILL. McStas software commemorated its 25th year since the release of version 1.0 in October 1998. McStas is based on a compiler that reads a high-level specification language defining the instrument to be simulated and produces C code that performs the Monte Carlo Simulation. The system is very fast in use, both when setting up the instrument definition and when doing calculations. Typical figures are 500000 neutron histories per second on a fast PC. McStas supports triple-axis, time-of-flight instruments, and polarized neutrons. It comes with a comprehensive manual and a library of well-tested components that include most standard elements of neutron scattering instruments, including steady-state and pulsed sources, monochromators/analysers,

guides, collimators, vanadium and powder samples, velocity selectors and choppers, and a variety of detectors [9].

The present work aims to use the mentioned optic codes to investigate TRR PG(002) crystal behavior in front of the parallel neutron beam exited from the first TRR soller collimator.

Simulation

Simulation results using Vitess 3.4 and McStas 3.2 computational code would be presented in this section as the following:

Results and Discussion

The TRR neutron beam was introduced in the Vitess 3.4 and McStas input file on wavelength (Å) according to the Fig.4.

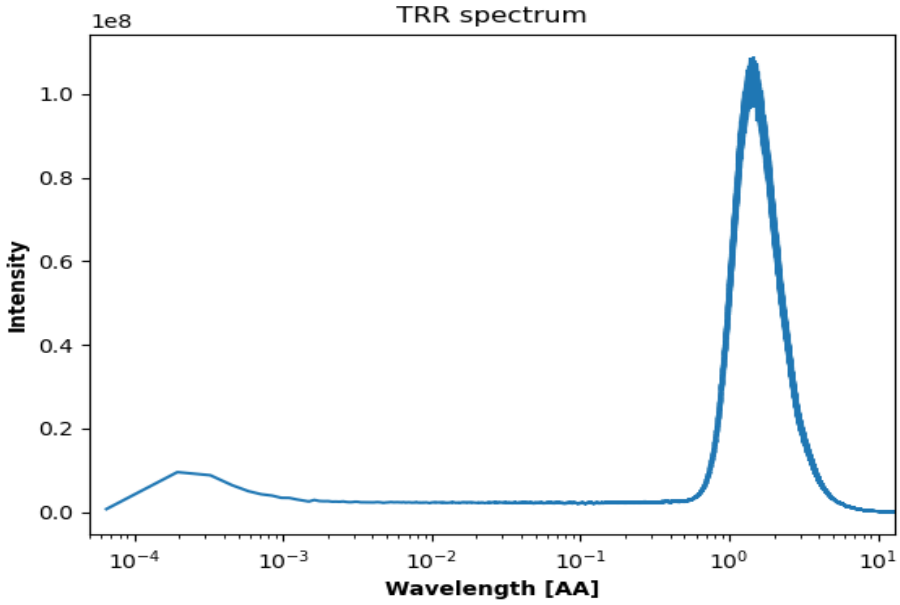

Fig.4. Neutron beam spectrum of TRR in D channel after sapphire crystal

Vitess code results showed for PG reflectivity of 1 and mosaic spread of 1°, selection of the glancing angle of 13° or the crystal angle than horizontal plan (77°) would result the highest intensity for the monochromatic reflected beam while the peak for the monochromatic beam is 1.5 Å. The second highest intensity belongs to the crystal angle of 79° or the glancing angle of 11°, which the peak for the monochromatic beam is 1.3 Å. The neutron flux peak of the first mentioned monochromatic beam is 24% higher than the second investigated one. in Fig.5 is shown Vitess output for the reflected neutrons from PG(002) crystal with 1° mosaic spread and reflectivity of 1.

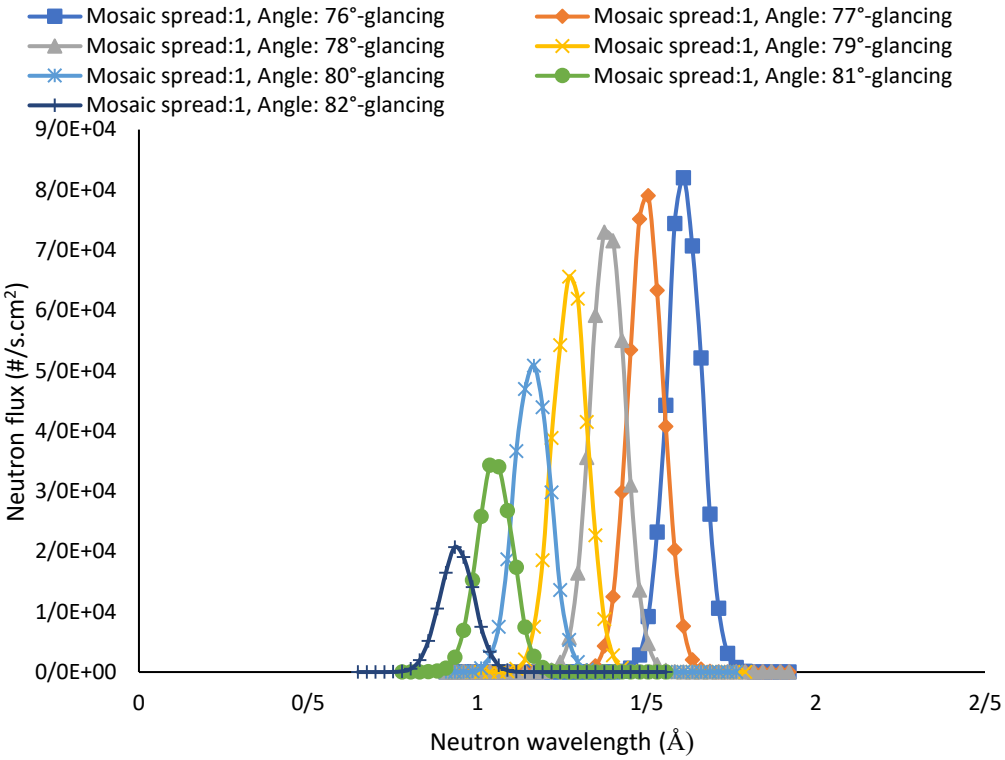

Fig.5. Vitess output for the reflected neutrons from PG(002) crystal with 1° mosaic spread and reflectivity of 1.

At next stage, the same situation was kept and the crystal mosaic spread was changed to 0.8° in the Vitess input. The same behavior was observed from the Fig.6 while the neutron flux peak of the 13°-glancing monochromatic beam is 19% higher than the 11°-glancing.

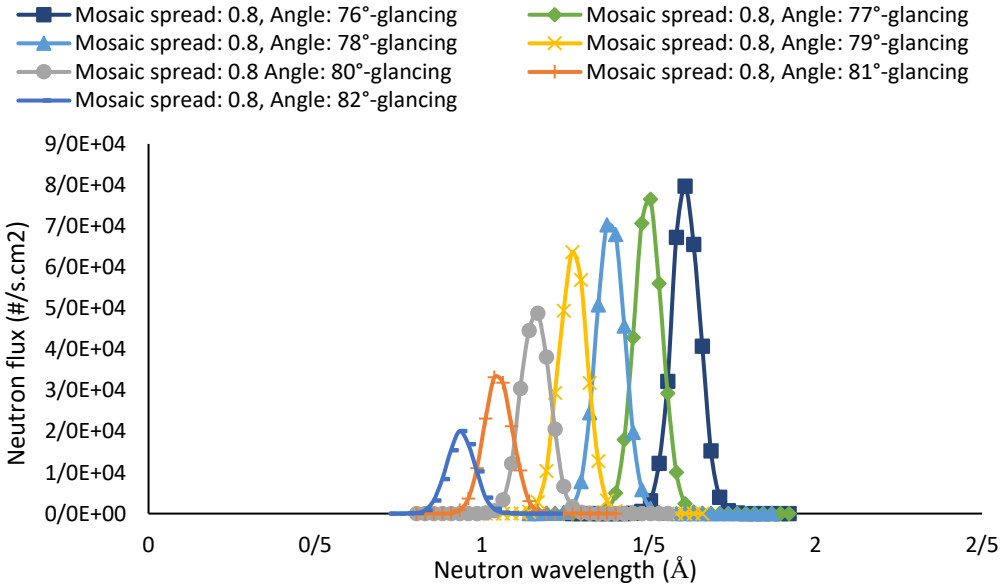

Fig.6. Vitess output for the reflected neutrons from PG(002) crystal with 0.8° mosaic spread and reflectivity of 1.

The crystal behavior was investigated for 0.5° mosaic spread as it is depicted in Fig. 7. Again, the neutron flux peak of the 13°-glancing monochromatic beam is 22% higher than the 11°-glancing.

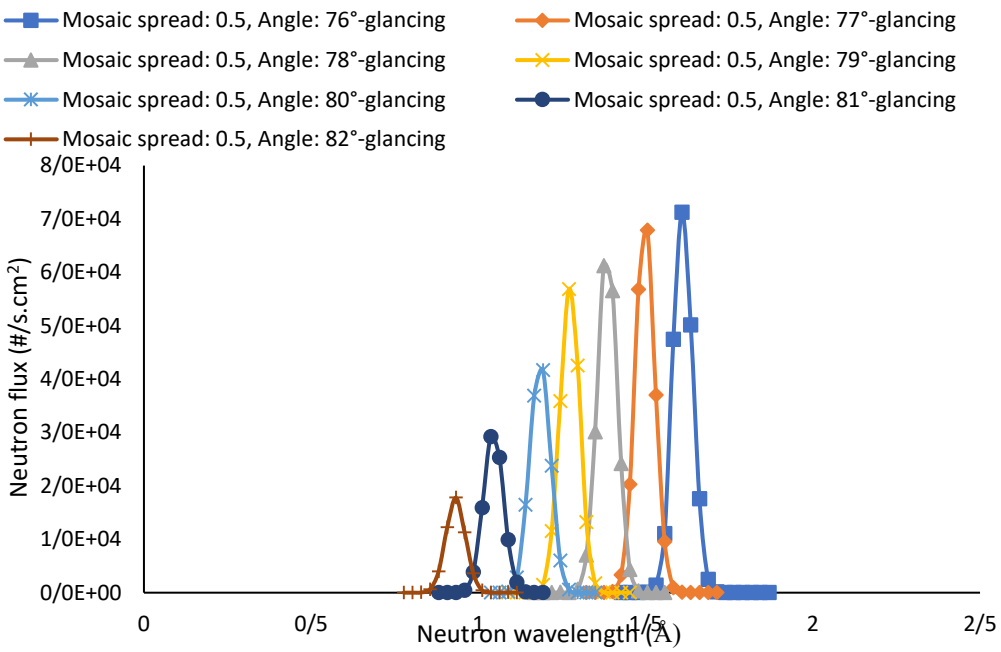

Fig.7. Vitess output for the reflected neutrons from PG(002) crystal with 0.5° mosaic spread and reflectivity of 1.

Fig.8 shows the optical equipment installed along the TRR D channel simulated by the McStas code.The behavior of the crystal for 1° mosaic spread was investigated in McStac code at different angles and the results are shown in Fig. 9.

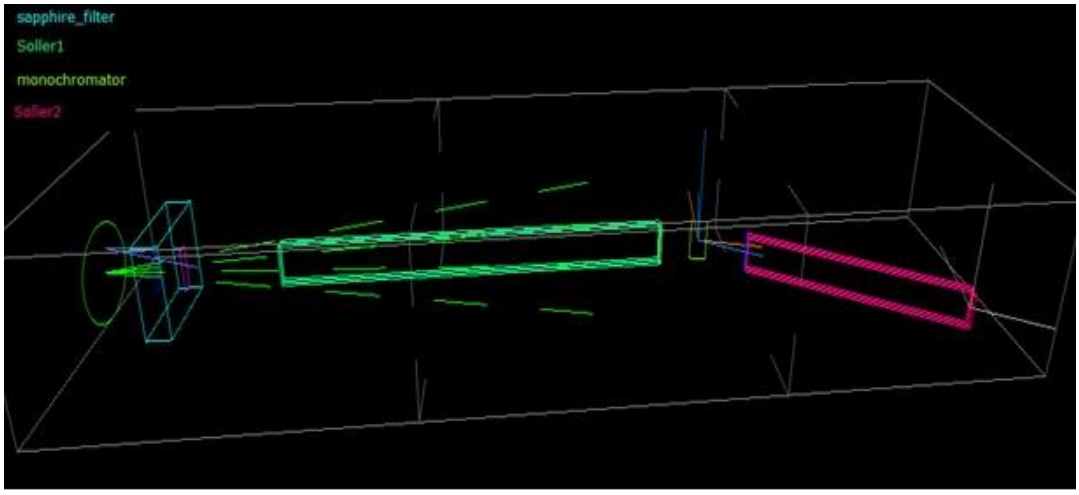

Fig.8. Optical equipment installed along the TRR D channel.

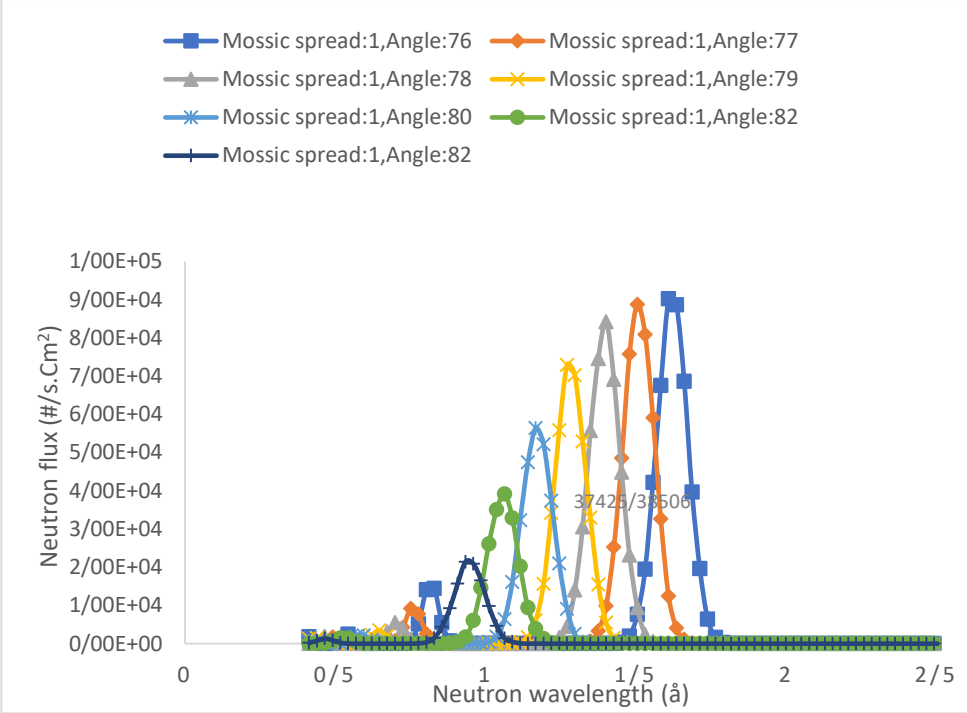

Fig.9. McStac output for the reflected neutrons from PG(002) crystal with 1° mosaic spread and reflectivity of 1.

The results of the McStac and Vitess code for the reflected neutrons from the PG(002) crystal with a mosaic spread of 1° and a reflectivity of 1 is shown in Fig.10.

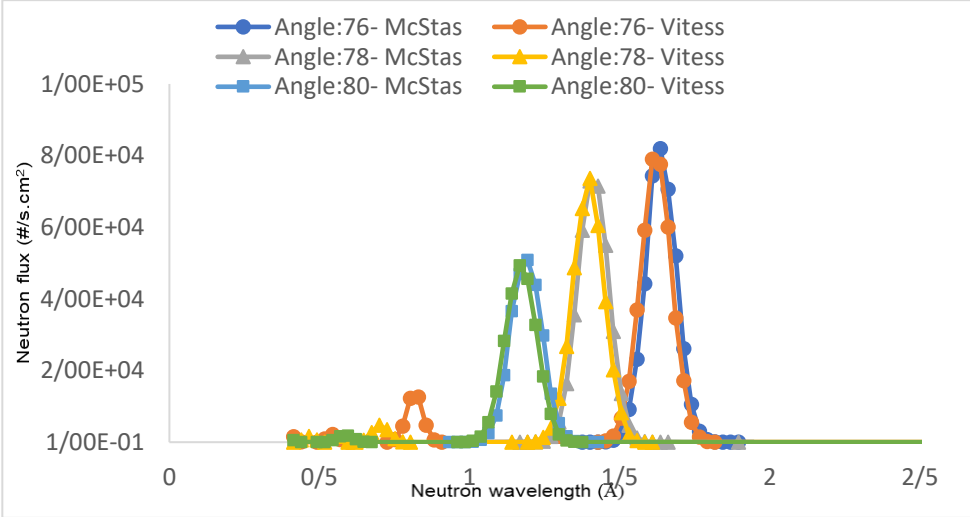

Fig.10. McStac and Vitess output for the reflected neutrons from PG(002) crystal with 1° mosaic spread and reflectivity of 1.

For crystal reflectivity of 1, the mosaic spread effect on the reflected neutron spectra was compared for glancing angle 11°. The obtained results showed, by mosaic spread reduction the reflected neutron intensity reduces but FWHM of the monochromatic beam improves (Fig.11). This result is in

agreement with the theoretical investigation depicted in Fig.1. In the case of 0.5 Mosaic spread than 1 there would be about 12% reduction of the monochromatic beam peak.

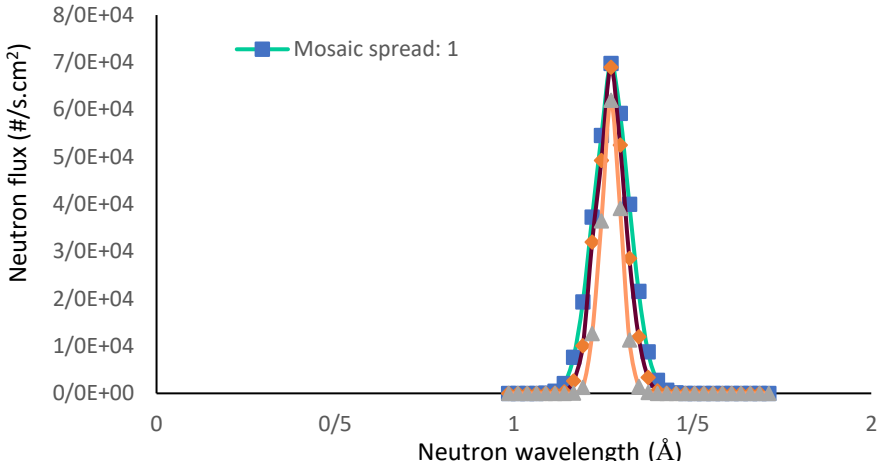

Fig.11. Vitess output for the reflected neutrons from PG(002) crystal with 11° glancing angle and reflectivity of 1.

At the next step, the crystal mosaic spread was selected as 0.5° and the crystal reflectivity was investigated using Vitess code for the crystal glancing angle of 11°. The obtained results showed reduction of the crystal reflectivity from 1 to 0.7 causes about 43% reduction in reflected neutron flux peak (Fig.12).

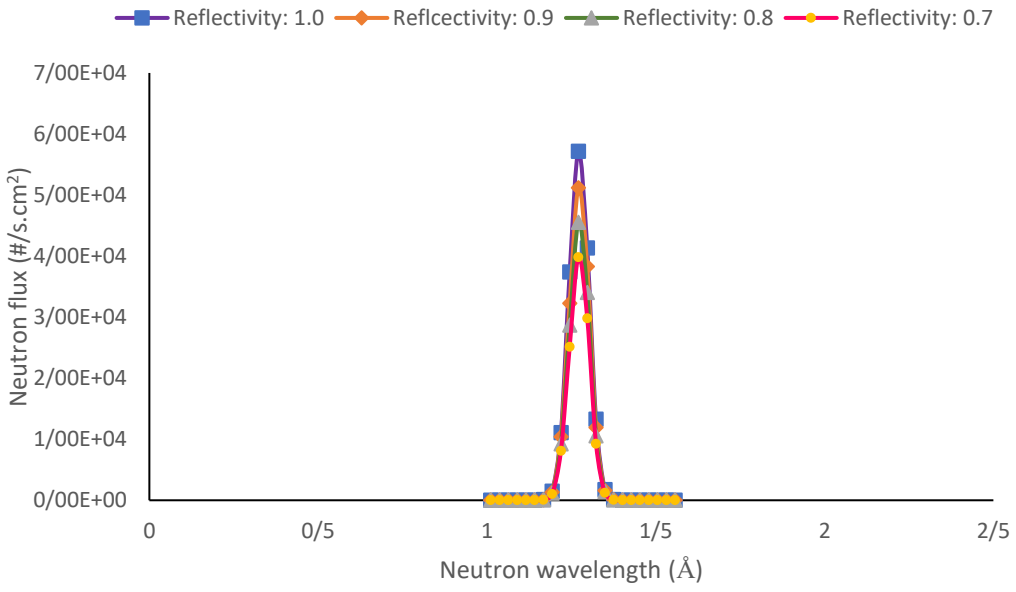

Fig.12. Vitess output for the reflected neutrons from PG(002) crystal with 11° glancing angle and different reflectivity values, Mosaic spread of the crystal: 0.5.

A comparison with Vitess3.4 output and an available PG experimental data was carried out (Fig.13). As the figure shows there is good comformity between the theoritical calculations and the experimental data.

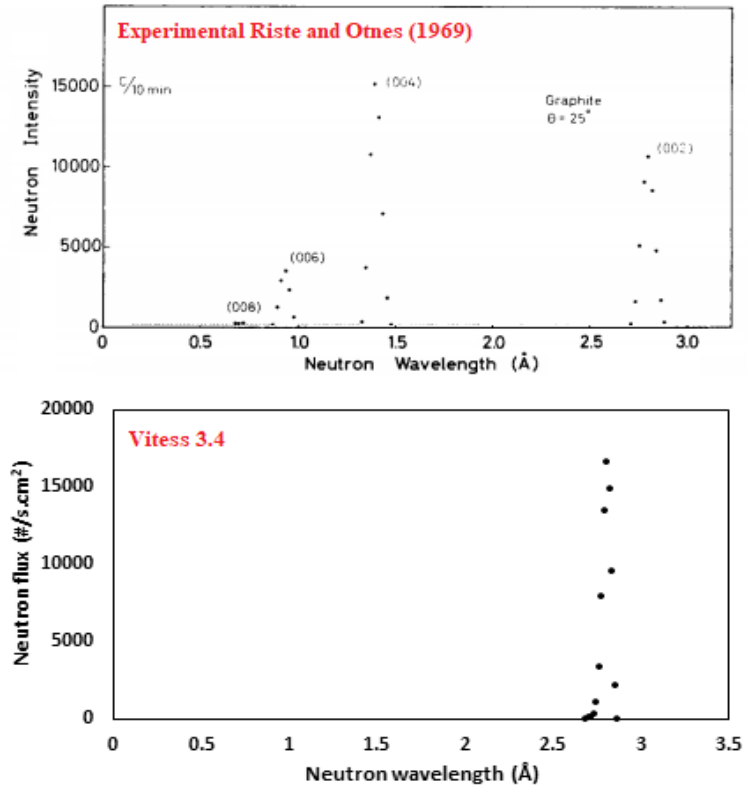

Fig.13. Comparison of Vitess output for the reflected neutrons from PG(002) crystal with 25° glancing angle and the available experimental data for PG crystal [10].

Conclusions

In the present study, fine tuning effect of single neutron monochromator of PG(002) was investigated. Vitess and McStas code calculations show that the decrease in reflectivity of the crystal reduces the flux of the monochromatic neutron beam. Also, reducing the mosaic spread of the crystal also reduces the single beam neutron flux. The results obtained by Vitess and McStas code also show their similar behavior regarding the crystal reflection angle changes. It was also in Fig.7 shown that the simulation results are in very good agreement with the experimental results.

The results of this study can be used to fine tuning of pyrolytic graphite single-crystal (002) plan on the quality of the reflected neutron spectra, including neutron imaging, neutron diffractometry, and neutron scattering facilities. In addition, this work verified the effectiveness of the Vitess and McStas code in modeling and analyzing the optical components of neutron facilities.

References

[1] Adib, M., (2009). Pyrolytic graphite as tunable second order neutron filter, Proceedings of the 7th Conference on Nuclear and Particle Physics, 1-15 Nov., Sharm El-Sheikh, Egypt

[2] Frikkee, E., (1975). Application of pyrolytic graphite as a tunable neutron filter, Nucl. Instr. & Meth., 125: 307-312.

[3] Adib, M., Habib, N., El-Mesiry, M. S., Fathallah, M., (2012). Characteristics of Pyrolytic Graphite as a Neutron Monochromator, Energy and Environment Research, 2(1), 35-43.

[4] Gholamzadeh, Z., Bavarnegin, E., Rachti, M. L., Mirvakili, S. M., Dastjerdi, M. C., Ghods, H., ... & Hosseini, M. (2018). Modeling of neutron diffractometry facility of Tehran Research Reactor using Vitess 3.3 a and MCNPX codes. Nuclear Engineering and Technology, 50(1), 151-158.

[5] Potashnikov, D., Pesach, A., Rivin, O., Ozeri, O., Yungrais, Z., Bertelsen, M., & Caspi, E. N. (2024). Verification of the McStas code using two double axis neutron diffractometers. Nuclear Instruments and Methods in Physics Research Section A: Accelerators, Spectrometers, Detectors and Associated Equipment, 169291.

[6] Udby, L., Willendrup, P. K., Knudsen, E., Niedermayer, C., Filges, U., Christensen, N. B., ... & Lefmann, K. (2011). Analysing neutron scattering data using McStas virtual experiments. Nuclear Instruments and Methods in Physics Research Section A: Accelerators, Spectrometers, Detectors and Associated Equipment, 634(1), S138-S143.

[7] Aslani Menarebazari, Z., Jafari, H. and Gholamzadeh Z., (2023). The design and construction of a collimator holder to equip beam tube D of the Tehran Research Reactor, Nuclear Engineering and Design, 405(15):112226

[8] Zendler, C., Lieutenant, K., Nekrassov, D., Fromme, M., (2014). VITESS 3 – Virtual Instrumentation Tool for the European Spallation Source, Journal of Physics: Conference Series 528: 012036.

[9] https://www.mcstas.org/about/

[10] Riste, T., Otnes, K., (1969). Oriented graphite as a neutron monochromator, Nucl. Inst and meth. 75: 197-202.

ICNST 2024
International Conference on Nuclear Science and Technology
6- 8 MAY 2024 | Isfahan, Iran

Reducing displacement damage caused by space radiations in electronic components of satellites (Paper ID: 1548)

Vahedi Z. Correspondent[1*], Ezzati A. Co-Author[2]
[1]*Department of physics, Tabriz university, Tabriz, Iran*
[2] *Department of physics, Tabriz university, Tabriz, Iran*

Abstract

As the number of satellites increases and their parts become smaller and more sensitive, the need for innovation in the field of radiation shields is felt more. In this research, 3 shields consisting of side layers of polyethylene, lithium hydride and lithium tetra-borate and middle layers of tungsten, respectively, with abbreviated representation with PE+W+PE, LiH+W+LiH and Li2B4O7+W+Li2B4O7 were studied. These shields were placed in front of protons trapped in Low Earth Orbit (LEO) to reduce the Displacement Damage Dose (DDD) caused by them and secondary neutrons. In order to optimize the performance of the shields, different percentages of tungsten of the total mass were investigated and the thickness of the side layers in the shields is considered the same. For this purpose, MCNP code was used for simulation and a silicon piece was considered as a sensitive semiconductor device. In order to make a comparison between the performance of different shields, the mass of all shields was considered 1.5 $\mathbf{g/cm^2}$. The efficiency of the examined shields was compared with AL+W+AL shield. It was shown that in masses of 0.1, 0.2, 0.3, 0.4, 0.5 of tungsten, LiH+W+LiH shield is the best option with more than 7% reduction in DDD compared to AL+W+AL shield and 3% compared to Li2B4O7+W+Li2B4O7. In higher thicknesses, PE+W+PE shield works better. Therefore, LiH+W+LiH and PE+W+PE shields are introduced as the optimal shields among these 4 shields as a better reducer of displacement damage.

Keywords: Shield, Satellite, Damage, MCNP, Trapped.

Introduction

In order to ensure the survival of a satellite in orbit, it is important to evaluate its surrounding environment. In the outer space of the earth's atmosphere, there are space radiations that have 3 sources as follows: Galactic Cosmic Rays (GCRs), Solar Energetic Particles (SEPs) and particles trapped in the earth's radiation belts [1]. Cosmic rays are high-energy particles originating from outside the solar system and are considered as background radiation in space. The major part of cosmic rays consists of protons [2]. The second source of space particles is the sun. During the process of solar flares and winds, the sun accelerates electrons, protons, alpha particles and heavy nuclei to the extent of several

mega electron volts. Therefore, solar particles are very active in space and fluctuate in a very large range [3, 4]. Meanwhile, many solar particles are trapped in the magnetic field around the earth and form the third source of particles. The earth's magnetic field oscillates these particles in a spiral path and prevents them from reaching the earth. As a result, two distinct regions of particles called Van-Allen belts are formed around the earth [1, 5-8] .These radiations leave adverse effects on sensitive electronic parts of satellites. The effects of radiations are divided into two categories: cumulative and individual. Total ionizing dose and displacement damage are cumulative effects, and single events are individual effects .Currently, reducing these effects has become a serious challenge. In this regard, materials are designed as shields to protect the electronic components of satellites. These materials should interact with space particles in a favorable way and be affordable in terms of mass and cost. By using these shields, the amount of damage caused by primary and secondary particles in electronic parts of satellites is reduced. Without the presence of shields between the parts of the satellites, there is a possibility of processing error or even disconnection with the ground stations, and it is possible that the satellite will not be able to fulfill its mission. Therefore, the effort to introduce the best shield with less weight and more efficiency continues. For this purpose, it is necessary to know how protons interact with materials. Proton interaction with materials is carried out in the following three ways are as follows:

Non-elastic Coulomb interactions

The repulsive Coulomb elastic scattering from the nuclei

Inelastic nuclear interaction [9]

During the elastic and inelastic interactions of protons with the lattice atoms of the target material, an energy loss occurs, which we denote by the quantity Non-Ionising Energy Loss (NIEL). The result of these interactions is the displacement of atoms from their place in the target material and leaving a hole in its place. The displaced atom is placed among the lattice atoms. when the energy of the incoming particles is high; several atoms are displaced from their lattice positions, these atoms can displace other atoms and finally they can create a cluster of lattice defects in the target material, which is called displacement damage. Protons, electrons, neutrons and heavy ions can cause displacement damage in the target material. Since the population and energy of protons in space is greater than other particles, in this work, we have focused on the displacement damage caused by trapped protons in LEO up to 300 MeV.

To do this, simulation with MCNP code was used. In addition to the ability to transport particles, this code can also determine the cross-section interactions [10]. In Monte Carlo methods, sampling is done

randomly and statistically and a numerical result is obtained. Therefore, solving a complex problem with long calculations is done with the help of a random method [11-14]. In this simulation, a software called OMERE was used to obtain the space data. OMERE is a free software for space environment and radiation effects which was developed for industrial development and calculates the space constraints for a satellite in orbit [15]. In this work, by using the data of OMERE software and setting up the geometry of the shield and the silicon piece behind it, we obtained the DDD caused by space protons and neutrons at the place of the piece. This research is presented with the aim of reducing displacement damage, which is achieved by using the right choice of materials for the radiation shield. Therefore, we used different materials in the structure of multi-layer shields with specific mass. According to reports, the protection of electronic parts of satellites was usually done using an aluminum frame. This material produces too many neutrons and does not provide adequate radiation protection for electronic components [10]. Therefore, at the moment, layered heterogeneous shields are used, of which we discussed the efficiency of some samples here.

Research Theories

This research is to introduce the optimal shield with the approach of reducing Displacement Damage caused by space protons and secondary neutrons. DDD is obtained using relation 1 [16].

$$DDD = \int_{E_{min}}^{E_{max}} \left(\frac{\partial \varphi}{\partial E}\right) NIEL(E) dE \qquad \left({}^{Kev}/_{g} \ \ or \ {}^{Mev}/_{g}\right) \tag{1}$$

The quantity of φ refers to the particle flux. Non-Ionization Energy Loss (NIEL) is a measure of the energy lost by particles during nuclear Coulomb, elastic and inelastic interactions in the process of producing interstitial-hole pairs. NIEL Can be calculated as relation 2.

$$NIEL(E) = \frac{N_A}{A} \int_{T_d}^{T_{max}} Q(T) T \left(\frac{d\sigma}{dT}\right)_E dT \qquad {}^{Mevcm^2}/_{g} \tag{2}$$

which in this relation: NA is Avogadro's number, A is the atomic mass of the lattice atom, E is the kinetic energy of incident particle, T is the kinetic energy transferred to the target atom, Q(T) is Lindhard partition function, (dσ/dT) is the differential cross section (Coulombic and nuclear elastic/inelastic) for atomic displacements. Td is the threshold energy for displacement and Tmax is the maximum energy which can be transferred by the incident particle to target atoms .

The Damage Reduction Factor (DRF) of the introduced shields was expressed based on the performance of the AL+W+AL shield. This quantity can be defined by relation 3.

$$DRF = \frac{DDD(AL + W + AL)}{DDD(other\ shields)} \tag{3}$$

Experimental

In this research, at first, the flux of trapped protons was obtained using OMERE software. For this purpose, the STS-31 shuttle orbital data was used. The shuttle had an apogee of 615km, a perigee of 613km and an inclination of 28.5 degrees, which is in the range of LEO. These quantities were entered as orbital parameters in the mission tab of OMERE software, and then the flux of trapped protons was obtained from the environment tab according to Figure 1. The standard used to calculate this flux is AP8. The AP8 trapped proton Models are empirical models of the omnidirectional proton flux in Earth's magnetosphere. The models were derived from measurements accumulated by numerous satellites in the 1960s and 1970s [15, 17, 18]. In this research, flux differential with respect to energy that was called differential flux was used for the simulations.

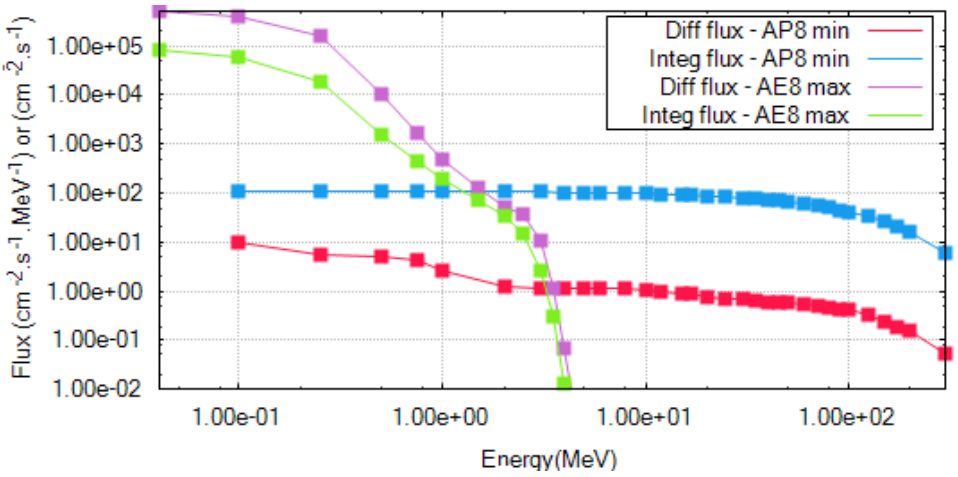

Fig. 1. Differential, and integral flux of trapped protons

Another quantity to calculate the displacement damage was NIEL. This quantity for protons got from the SR-NIEL web calculator and for neutrons from Figure 2 [15].

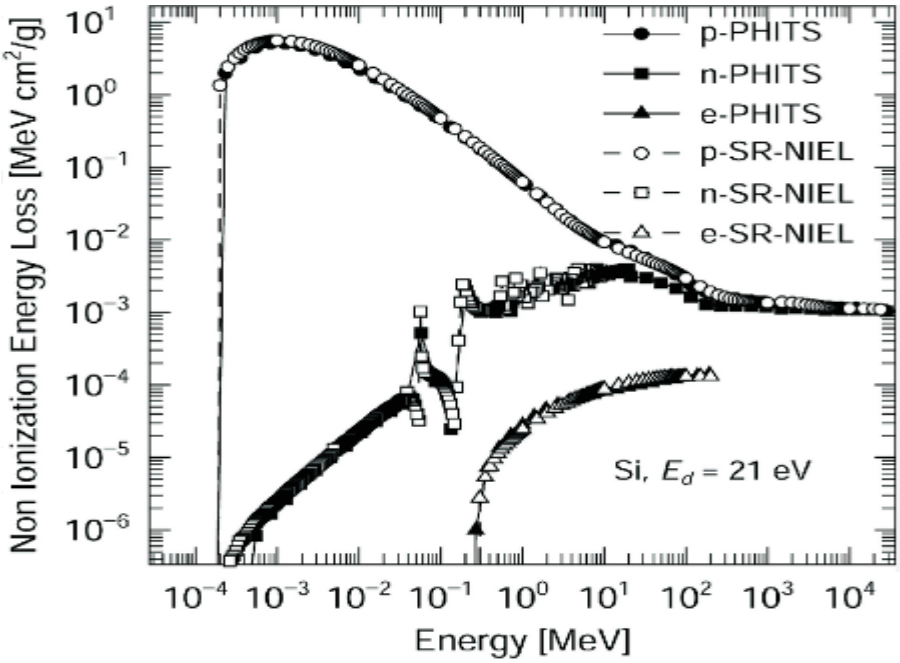

Fig. 2. Non-Ionization Energy Loss vs. Energy

The schematic representation of the geometry of the problem with a three-layer shield in front of the silicon piece is shown in Figure 3. This figure is drawn using the graphical interface of the MCNP code. The source of particles was considered on the outer surface of layer1.

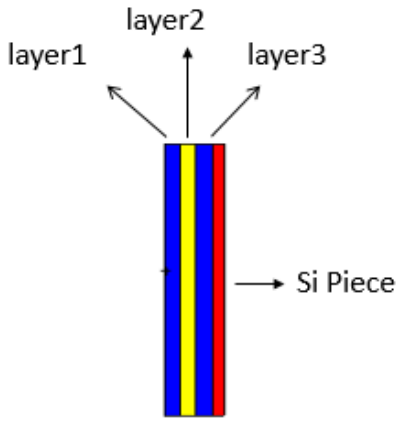

Fig. 3. Schematic representation of silicon piece and shield

Flux values according to the respective energies were entered as source information in the code. The NIEL values were entered as dose function in the data card of the relevant code, and finally the displacement damage was calculated by using Tally type 4. The thickness of the shields is considered to be 1.5 g/cm^2. The amount of displacement damage was calculated for the thicknesses of 0.1, 0.2,... and 1 of tungsten and the results are presented in Figure 4. Finally, in order to introduce the optimal

shield with the approach of reducing displacement damage, the DRF values of the shields under investigation were obtained according to Figure 5.

Results and Discussion

To validate the MCNP code simulation set-up, the conditions of the space environment, geometry and materials were simulated according to reference [19]. The particle flux was obtained from Figure 2 of reference [19] and entered as source information in the code. The dimensions of the layers of the shields were considered 10 m by 10 m with a mass of 1.5 $\mathbf{g/cm^2}$ Due to the repetition of the geometry in reference [19] with different materials, we chose two shields PE+PE+Ta, PE+PE+Pb of them and obtained the total ionizing dose deposited in the silicon piece placed behind these shields. Dose values in krad are presented in Table 1. The error of the obtained values was less than 3% and the results were in good agreement with the reference values. With this match, the correctness of the simulation set-up was confirmed.

Table 1. The three-layer shielding material with total shielding depth 1.5 g/cm^2 and each layer 0.5 g/cm^2

	Shielding layers			Ionising Dose [krad]
Rank	A	B	C	Total Dose
		Article values		
1	PE	PE	Pb	0.506
2	PE	PE	Ta	0.511
		Obtained values		
1	PE	PE	Pb	0.490
2	PE	PE	Ta	0.509

DDD in silicon piece caused by trapped protons and secondary neutrons

Figure 4 shows the DDD in the silicon piece with a thickness of 0.5 mm behind the 4 shields AL+W+AL, Li2B4O7+W+Li2B4O7, PE+W+PE and LiH+W+LiH in terms of different thicknesses of tungsten. It can be seen that by changing the percentage of tungsten and accordingly, the percentages of side materials as shown in the Figure 4, the DDD also changes. Comparing DDD values in different percentages of tungsten leads us to the best thickness among the introduced thicknesses. Undoubtedly, infinite combinations with different percentages of materials can be chosen, of which we have examined only 10 of them for each shield.

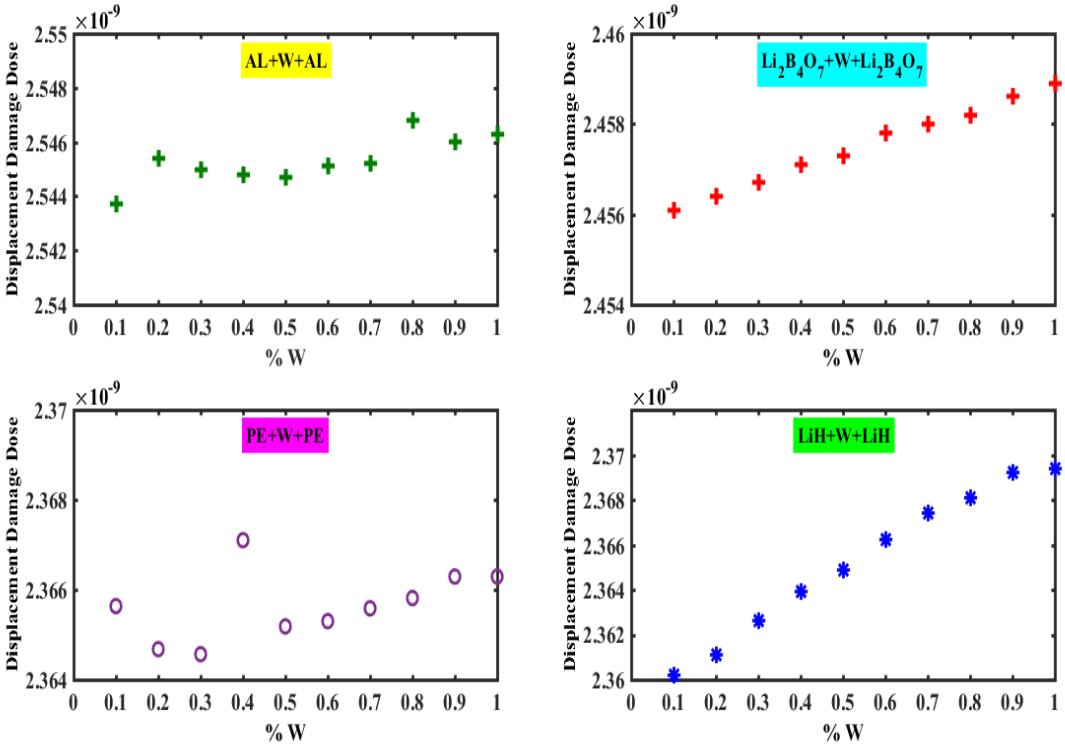

Fig. 4. DDD in silicon piece as a function of tungsten percentage

DRF of the provided shields compared to AL+W+AL shield

To compare the performance of the investigated shields, the damage reduction factor for Li2B4O7+W+Li2B4O7, PE+W+PE and LiH+W+LiH shields compared to AL+W+AL was calculated in different percentages of tungsten and the results are presented in Figure 5. It can be seen that PE+W+PE and LiH+W+LiH shields have a higher reduction factor than Li2B4O7+W+Li2B4O7 shield. This means that the performance of these shields against space radiation will be better than Li2B4O7+W+Li2B4O7, and by placing them against the silicon piece, we will have less displacement damage in it.

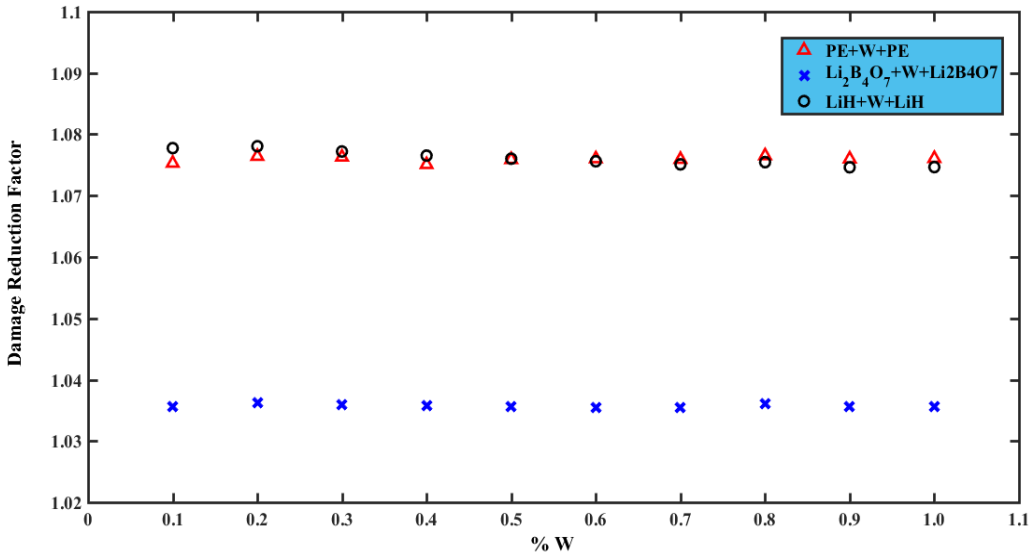

Fig. 5. Damage Reduction Factor for introduced shields vs. percentages of tungsten

Although aluminum is widely used as a common material in the construction of the body of satellites and or as a common shield, it does not work well against radiation due to the production of secondary particle [10]. For this reason, currently, finding materials with higher efficiency and lower mass has become a challenge. One of the things done in this field is the use of layered shields made of different materials. In this context, two, three, five, and seven-layer shields have been introduced. In the work done in the reference [20] seven-layer shields were found to be optimal, however, due to the higher mass and its low difference with the efficiency of three-layer shields, it was preferred to use three-layer shields [20] . Of course, contrary to previous claims based on superiority of three-layer shields of three materials with different atomic numbers, it was shown that limiting the materials to two different types increases their efficiency against radiation [19].

According to the literature, materials with low density are used to reduce the adverse effects of protons and materials with high density are used to reduce secondary particles effects. Therefore, a combination of low and high density materials is considered as the best option for the structure of shields[21]. Furthermore, materials with high hydrogen content are the best for shielding protons[22] and, lithium is considered a neutron absorber [21]. Therefore, various shield materials were introduced considering the above. This information led us to choose the introduced materials for the shields.

Conclusions

We studied the performance of several materials to reduce the displacement damage of space radiations. The results showed that the three-layer shield of lithium hydride with 0.1% tungsten and the shield made of polyethylene with 0.3% tungsten were better against protons and neutrons. All three

shields were superior to aluminum plus tungsten shield. Quantitatively, the lithium hydride and polyethylene shields showed more than 7% reduction in damage compared to the aluminum shield, and the lithium tetra borated shield with tungsten was more than 3% superior to the aluminum plus tungsten shield. Considering the challenges in assigning the right amount of mass to different shield materials, the use of existing algorithms to find the exact amount of those materials is one of the interests of the authors.

References

[1] Vainio, R., et al., Dynamics of the Earth's particle radiation environment. Space science reviews, 2009. 147: p. 187-231.

[2] Gaisser, T.K., R. Engel, and E. Resconi, Cosmic rays and particle physics. 2016: Cambridge University Press.

[3] Jiggens, P., et al., The solar accumulated and peak proton and heavy ion radiation environment (SAPPHIRE) model. IEEE Transactions on Nuclear Science, 2017. 65(2): p. 698-711.

[4] Sturrock, P.A., Physics of the Sun: Volume II: The Solar Atmosphere. 2013.

[5] Van Allen, J. and L. Frank, Radiation Around the Earth to a Radial Distance of 107,400 kilometers, Nature, 183, 430. 1959b. Radiation Measurements to, 1959. 658.

[6] Li, W. and M. Hudson, Earth's Van Allen radiation belts: From discovery to the Van Allen Probes era. Journal of Geophysical Research: Space Physics, 2019. 124(11): p. 8319-8351.

[7] Van Allen, J.A., Radiation belts around the Earth. Scientific American, 1959. 200(3): p. 39-47.

[8] Königstein, T., et al., Design considerations for the use of laser-plasma accelerators for advanced space radiation studies. Journal of Plasma Physics, 2012. 78(4): p. 383-391.

[9] Newhauser, W.D. and R. Zhang, The physics of proton therapy. Physics in Medicine & Biology, 2015. 60(8): p. R155.

[10] Yang, D., Effectiveness of Polymer Composites as Radiation Shield Against Galactic Cosmic Rays. 2019, Rice University.

[11] Wilson, J.W., et al., Standardized radiation shield design method: 2005 HZETRN. SAE Transactions, 2006: p. 263-276.

[12] Li, X., D. Warden, and Y. Bayazitoglu, Analysis to evaluate multilayer shielding of galactic cosmic rays. Journal of Thermophysics and Heat Transfer, 2018. 32(2): p. 525-531.

[13] Raychaudhuri, S. Introduction to monte carlo simulation. in 2008 Winter simulation conference. 2008. IEEE.

[14] Waters, L.S., et al. The MCNPX Monte Carlo radiation transport code. in AIP conference Proceedings. 2007. American Institute of Physics.

[15] Adams Jr, J., et al., Revolutionary concepts of radiation shielding for human exploration of space. 2005.

[16] Srour, J., C.J. Marshall, and P.W. Marshall, Review of displacement damage effects in silicon devices. IEEE transactions on nuclear science, 2003. 50(3): p. 653-670.

[17] Daly, E., et al., Problems with models of the radiation belts. IEEE Transactions on Nuclear Science, 1996. 43(2): p. 403-415.

[18] Fung, S., Recent development in the NASA trapped radiation models. Radiation Belts: Models and Standards, 1996. 97: p. 79-91.

[19] Fetzer, A., et al., Total ionising dose multilayer shielding optimisation for nanosatellites on geostationary transfer orbit. Advances in Space Research, 2024. 73(1): p. 831-845.

[20] Daneshvar, H., et al., Multilayer radiation shield for satellite electronic components protection. Scientific reports, 2021. 11(1): p. 20657.

[21] Zeynali, O., et al., The design and simulation of the shield reduce ionizing radiation effects on electronic circuits in satellites. Electr. Electron. Eng., 2011. 1(2): p. 112-116.

[22] Yang, D. and Y. Bayazitoglu, Polymer composites as radiation shield against galactic cosmic rays. Journal of Thermophysics and Heat Transfer, 2020. 34(2): p. 457-464.

---

[i] IAEA (2016), Safety of Nuclear Power Plants: Design, IAEA Safety Standards, Specific Safety Requirement NO. SSR-2/1.

[ii] IAEA (2008), Radiation. Radioactive Waste Management in the Design and Operation of Research Reactors, IAEA Safety Standard Series No. NS-G-4.6.

[iii] M. Hannan Bahrin, etc. (2019), The design of a Hot Cell with interlocking concrete wall, IOP Conf. Series: Materials Science and Engineering 555.